

The Pennsylvania State University

The Graduate School

Department of Aerospace Engineering

**AN EXPERIMENTAL STUDY OF THE VISCOUS FLOWFIELD
AROUND A LOW-SPEED AIRFOIL AT HIGH ANGLE OF ATTACK
WITH ACTIVE FLOW CONTROL IMPLICATIONS**

A Thesis in

Aerospace Engineering

by

Robert Todd Klaput

©1997 Robert Todd Klaput

Submitted in Partial Fulfillment
of the Requirements
for the Degree of

Master of Science

December 1997

We approve the thesis of Robert Todd Klaput.

Date of Signature

Cengiz Camci
Associate Professor of Aerospace Engineering
Thesis Advisor

Dennis K. McLaughlin
Professor of Aerospace Engineering
Head of the Department of Aerospace Engineering

Mark D. Maughmer
Associate Professor of Aerospace Engineering

I grant The Pennsylvania State University the nonexclusive right to use this work for the University's own purposes and to make single copies of the work available to the public on a not-for-profit basis if copies are not otherwise available.

Robert T. Klaput

ABSTRACT

Active control of flow separation can be beneficial for many fluid flow systems. Inlet diffusers become more efficient if separation is reduced. Vehicle drag can be lessened leading to better fuel efficiency. Airfoil lift can be enhanced creating higher maximum lift coefficients and lower stall speeds. Runway distances could then be shortened. Propellers and windmills would be more efficient with separation control.

It is possible that separation control may be achieved through enhancement of the mixing process in the separated free shear layer. The naturally existing large-scale coherent vortical structures in the separated shear layers can be artificially excited and strengthened. The entrainment of free stream fluid will then be increased. The separated free shear layer will be drawn toward the surface, be it that of an airfoil or any other surface over which the flow is separated. An argument involving the Coanda effect can be used as a possible explanation for this flow reattachment phenomenon.

This thesis presents necessary background work for the active control of flow separation on a low speed airfoil under stalled conditions. Initial work involved determining the viscous flow regions on the suction surface of the airfoil. This information is necessary so that the location at which to put control actuators can be discerned. Two experimental methods were used to document these surface viscous flow regions: fluorescent oil flow visualization and a heat transfer study which utilized thermochromic liquid crystals to generate heat transfer coefficient maps. Work then progressed to examining the nature of the large-scale vortical structures that are created and shed from the airfoil under stalled conditions. Time-accurate surface shear stress gauges and single sensor hot-wire probes were used to determine the frequencies at which the large-scale flow structures were shed.

The heat transfer study was found to compliment the conventional oil flow visualization. Using both methods in conjunction revealed more detail of the viscous flow near the airfoil surface than was found by using either method alone. The accuracy of the heat transfer data was verified numerically, thus providing confidence in the use of the heat transfer data as a baseline solution for the development of better heat transfer/viscous

flow solvers. The qualitative shear stress measurements along the chord of the airfoil served to instill more confidence in the trends of the heat transfer results but failed to reveal dominant flow instability frequencies. In effect, the flow recirculating region acts as a buffer to shield the dominant frequencies of the coherent structures that exist in the separated shear layer from detection by the surface shear stress gauges. Wake profile hot-wire anemometry measurements easily captured the frequencies of these large-scale coherent structures. In addition, velocity fluctuation skewness measurements and smoke flow visualization verified the existence of the large-scale flow structures. These flow structures were seen to not only dominate the flow physics away from the airfoil, but also to cause significant increases in the convective heat transfer and turbulence levels on the surface near the trailing edge of the airfoil.

A limited examination of the use of piezoelectric films as surface actuators was performed and revealed possible difficulties in using the films to excite the coherent flow structures of the separated shear layer. As a result of the work presented in this thesis, a reasonable active control strategy may now be developed and pursued for separation control on the SM701 airfoil under stalled conditions at low Reynolds numbers.

TABLE OF CONTENTS

1	INTRODUCTION	1
2	EXPERIMENTAL MODEL AND FACILITIES	4
	2.1 The Airfoil Definition	4
	2.2 The Axisymmetric Wind Tunnel (ASWT)	9
	2.3 The Low-Speed Low-Turbulence Wind Tunnel (LSLTT)	10
3	BOUNDARY LAYER PREDICTIONS ON THE AIRFOIL SUCTION SIDE	12
	3.1 Potential Flow	12
	3.2 Boundary Conditions	17
	3.2.1 Initial Considerations	17
	3.2.2 Starting Velocity Profile	19
	3.3 The Boundary Layer Code STANS	25
4	EXAMINATION OF VISCOUS FLOW REGIONS ON SM701 AIRFOIL	29
	4.1 Fluorescent Oil Flow Visualization	29
	4.1.1 Oil Flow Visualization Objective	29
	4.1.2 Oil Flow Visualization Procedure	29
	4.1.3 Oil Flow Visualization Results	31
	4.1.4 Conclusions from Oil Flow Visualization	41
	4.2 Liquid Crystal Thermography	43
	4.2.1 Objectives of the Heat Transfer Experimentation	43
	4.2.2 Liquid Crystal History and Properties	44
	4.2.3 Types of Heat Transfer Experiments	50
	4.2.3.1 Transient Technique	50
	4.2.3.2 Steady State Technique	53
	4.2.4 Importance of the Convective Heat Transfer Coefficient, h	55
	4.2.5 Past Heat Transfer Work Using Liquid Crystals	57
	4.2.6 Experimental Determination of the Thermal Conductivity of the Wing Material	59
	4.2.7 The Image Processing System	65
	4.2.8 Modifications to Model Prior to ASWT Heat Transfer Experimentation	65
	4.2.9 ASWT Setup for Heat Transfer Experimentation	67
	4.2.10 ASWT Experimental Procedure	70
	4.2.11 Problems Discovered and Knowledge Gained During ASWT Tests	72
	4.2.12 Modifications to the Model Prior to LSLTT Heat Transfer Experimentation	74
	4.2.12.1 Fabrication of the Wing Extensions	74
	4.2.12.2 Model Changes Due to Knowledge Gained from ASWT Tests	83
	4.2.13 LSLTT Setup for Heat Transfer Experimentation	84

4.2.14 Calibration of the Liquid Crystals	88
4.2.15 LSLTT Experimental Procedure	91
4.2.16 LSLTT Heat Transfer Results	92
4.2.17 Conclusions from LSLTT Heat Transfer Measurements	109
4.2.18 LSLTT Heat Transfer Error Analysis	110
5 EXAMINATION OF POST-STALL FLOW INSTABILITIES	113
5.0.1 Fluid Instability	113
5.0.2 Importance of Separation Control	115
5.0.3 Approaches To Separation Control	115
5.0.4 Past Work in Control of Separated Shear Layers	120
5.0.5 Keys to Controlling the Separated Shear Layer	124
5.1 Qualitative Shear Stress Measurements	126
5.1.1 Objectives of Qualitative Shear Stress Experimentation	126
5.1.2 Past Work with Shear Stress Gauges	127
5.1.3 Setup for Qualitative Shear Stress Measurements	128
5.1.4 Description of Data Acquisition and Data Reduction Codes	130
5.1.5 Procedure for Qualitative Shear Stress Measurements	131
5.1.6 Qualitative Shear Stress Results	132
5.1.7 Conclusions from Qualitative Shear Stress Measurements	146
5.2 Hot-Wire Flowfield Measurements	147
5.2.1 Objectives of Hot-Wire Flowfield Experimentation	147
5.2.2 Experimental Setup for Hot-Wire Flowfield Measurements	147
5.2.3 Description of Data Acquisition and Data Reduction Codes	152
5.2.4 Verification of Experimental Setup	154
5.2.5 Procedure for Hot-Wire Flowfield Measurements	156
5.2.6 Hot-Wire Flowfield Measurements Results	157
5.2.7 Conclusions from Hot-Wire Flowfield Measurements	188
6 SIMPLE ACTIVE CONTROL TEST USING PIEZOELECTRIC FOIL	191
6.1 Background on Piezoelectric Materials	191
6.2 The Experiment	192
7 CONCLUSIONS	197
8 SUGGESTIONS FOR FUTURE WORK	199
APPENDIX A: ASWT Turbulence Intensity Information	203
APPENDIX B: Numerical Predictions Input Information	204
APPENDIX C: Heat Transfer Codes	208
APPENDIX D: Hot-Wire Anemometry Codes	229
BIBLIOGRAPHY	254

LIST OF FIGURES

Figure		Page
2.1	: SM701 Airfoil Shape	6
2.2	: Sandwich Panel Construction of the Test Model Skin	6
2.3	: Leading Edge Spar of the Airfoil	7
2.4	: The Airfoil Model	8
2.5	: Axisymmetric Wind Tunnel (ASWT)	9
2.6	: Low-Speed Low-Turbulence Wind Tunnel (LSLTT)	10
3.1	: Verification of Panel.f	13
3.2	: Potential Flow C_p Distribution for $\alpha = 0^\circ$	14
3.3	: Nondimensional Velocity Distribution for $\alpha = 0^\circ$	15
3.4	: The Boundary Layer (B.L.) Coordinate System	16
3.5	: Outer Flow Velocity Distribution in B. L. Coordinate System	17
3.6	: Setup for Falkner-Skan Wedge Flow Solution	19
3.7	: Determination of m for $\alpha = 0^\circ$	22
3.8	: Falkner-Skan Similarity Profile for SM701 at $\alpha = 0^\circ$	23
3.9	: Comparison of STAN5 C_f Results and Blasius Solution	27
3.10	: Comparison of STAN5 δ_99 Results and Blasius Solution	28
4.1a	: $\alpha = 0^\circ$, Re = 315,000, ASWT	32
4.1b	: $\alpha = 0^\circ$, Re = 315,000, LSLTT	32
4.1c	: $\alpha = 0^\circ$, Re = 750,000, LSLTT	32
4.2a	: $\alpha = 5^\circ$, Re = 315,000, ASWT	33
4.2b	: $\alpha = 5^\circ$, Re = 315,000, LSLTT	33
4.2c	: $\alpha = 5^\circ$, Re = 750,000, LSLTT	33
4.3a	: $\alpha = 10^\circ$, Re = 315,000, ASWT	34
4.3b	: $\alpha = 10^\circ$, Re = 315,000, LSLTT	34
4.3c	: $\alpha = 10^\circ$, Re = 750,000, LSLTT	34
4.4a	: $\alpha = 15^\circ$, Re = 315,000, ASWT	35
4.4b	: $\alpha = 15^\circ$, Re = 315,000, LSLTT	35
4.4c	: $\alpha = 15^\circ$, Re = 750,000, LSLTT	35
4.5a	: $\alpha = 18^\circ$, Re = 315,000, ASWT	36
4.5b	: $\alpha = 18^\circ$, Re = 315,000, LSLTT	36
4.5c	: $\alpha = 18^\circ$, Re = 750,000, LSLTT	36
4.6a	: $\alpha = 20^\circ$, Re = 315,000, ASWT	37
4.6b	: $\alpha = 20^\circ$, Re = 315,000, LSLTT	37
4.6c	: $\alpha = 20^\circ$, Re = 750,000, LSLTT	37
4.7	: Sketch of a Laminar Separation Bubble	40
4.8	: Two Regions of Laminar Separation Bubble	40
4.9	: Smectic Liquid Crystal Molecular Structure	45
4.10	: Nematic Liquid Crystal Molecular Structure	46

4.11	: Cholesteric Liquid Crystal Molecular Structure	47
4.12	: Clarification of Transient Heat Transfer Method	52
4.13	: The Composite Heater Element	53
4.14	: Various Flow Regimes in Which h Can Validate Codes	56
4.15	: Sketch of Wing Material Being Tested	60
4.16a	: k Test Piece	62
4.16b	: Side View of k Test Piece	62
4.16c	: Insulation Material	62
4.16d	: Insulating the Test Piece	62
4.16e	: Assembly of Insulating Box	62
4.16f	: Insulation Complete	62
4.16g	: Final k Testing Setup	62
4.17	: Experimental Determination of k_{wall}	64
4.18	: Inconel Before Painting	67
4.19	: The Model in the ASWT	68
4.20	: Schematic of ASWT Heat Transfer Experimentation Setup	70
4.21	: Edge Effects on The Heater Strip Color Pattern	73
4.22	: Sketch of Inside of Model for ASWT Tests	73
4.23	: Rectangular Indexing Table Mount	75
4.24a	: Top Wing Extension (lower surface view)	76
4.24b	: Bottom Wing Extension (lower surface view)	77
4.25	: Model with Extensions Mounted in LSLTT	78
4.26	: Wing Extension Pieces Before Assembly	79
4.27a	: Aligning Load-Carrying Beams	80
4.27b	: Aligning Load-Carrying Beams (cont.)	80
4.28a	: Beginning Wing Extension Assembly	80
4.28b	: Mating Extension to Wing	80
4.28c	: Attachment of First Foam Piece	81
4.28d	: Attachment of Final Foam Piece	81
4.28e	: Extension After Sanding	82
4.28f:	: Completed Extensions Before Covering	82
4.29	: Calibration of the Nine Thermocouples	85
4.30	: Model Mounted to Rotary Indexing Table	86
4.31	: Rotary Bearing Mount Above Test Section	86
4.32	: Model Mounted in LSLTT Test Section (view of upper surface)	87
4.33	: Schematic of LSLTT Heat Transfer Experimentation Setup	88
4.34	: Liquid Crystal Calibration Graph	90
4.35	: Hue Versus Intensity Check for Liquid Crystal Calibration	91
4.36	: h Map for $\alpha = 0^\circ$, $Re = 315,000$	94
4.37	: h Map for $\alpha = 0^\circ$, $Re = 750,000$	94
4.38	: h Map for $\alpha = 5^\circ$, $Re = 315,000$	95
4.39	: h Map for $\alpha = 5^\circ$, $Re = 750,000$	95
4.40	: h Map for $\alpha = 10^\circ$, $Re = 315,000$	96
4.41	: h Map for $\alpha = 10^\circ$, $Re = 750,000$	96

4.42	: h Map for $\alpha = 15^\circ$, Re = 750,000	97
4.43	: h Map for $\alpha = 18^\circ$, Re = 750,000	98
4.44	: h Map for $\alpha = 20^\circ$, Re = 750,000	99
4.45	: Velocity Distribution over a Separation Bubble	101
4.46	: C_f Trend After Flow Reattachment	102
4.47	: Convective Heat Transfer in a Separation Bubble	103
4.48	: Schematic Interpretation of Streamwise Vortices at Reattachment	105
4.49	: Evidence of Longitudinal Vortices at Reattachment	106
4.50	: Comparison of Heat Transfer Results to Cylinder-in-Crossflow	107
4.51	: Heater Strip Negative Affect on Flow	108
5.1	: The Coanda Effect (Surface Located Near a Jet)	117
5.2	: Airfoil Flow Separation	118
5.3	: Summary of the Two Main Separation Control Approaches	119
5.4	: Flow Reattachment Caused by Sound	120
5.5	: Schematic of Setup for Qualitative Shear Stress Measurements	129
5.6	: The DISA 55M01, Krohn-Hite Filter, and Techkor Amplifier	129
5.7	: $\alpha = 0^\circ$, Re = 315,000	133
5.8	: $\alpha = 5^\circ$, Re = 315,000	133
5.9	: $\alpha = 10^\circ$, Re = 315,000	136
5.10	: $\alpha = 15^\circ$, Re = 315,000	136
5.11	: $\alpha = 18^\circ$, Re = 315,000	138
5.12	: Coherent Vortical Structures in Separated Shear Layer	138
5.13	: Separated Flow Region Streamlines, $\alpha = 20^\circ$, Re = 315,000	139
5.14	: Separated Flow Region Velocity Vectors, $\alpha = 20^\circ$, Re = 315,000	139
5.15	: Turbulent Kinetic Energy Along Airfoil Surface, $\alpha = 20^\circ$	141
5.16	: Enhanced Trailing Edge Heat Transfer (ASWT, $\alpha = 20^\circ$)	141
5.17	: Visualization of Coherent Vortical Structures, $\alpha = 20^\circ$	142
5.18	: $\alpha = 20^\circ$, Re = 315,000	144
5.19	: $\alpha = 22^\circ$, Re = 315,000	144
5.20	: $\alpha = 25^\circ$, Re = 315,000	145
5.21	: $\alpha = 20^\circ$, x/c = 70%	145
5.22	: Schematic of Setup for Flowfield Measurements	149
5.23	: Traverse Calibration	150
5.24	: Calibration of Hot-Wire Against Pitot-Static Probe	151
5.25	: Hot-Wire Calibration Polynomial and Its Repeatability	152
5.26	: Simple Propeller Test for Hot-Wire Measurement System	155
5.27	: Velocity Profile and Wake Survey Locations for $\alpha = 15^\circ$	158
5.28	: $\alpha = 15^\circ$; Re = 315,000; x/c = 80%	159
5.29	: $\alpha = 15^\circ$; Re = 315,000; x/c = 90%	160
5.30	: $\alpha = 15^\circ$; Re = 315,000; 0.75c Wake	162
5.31	: Wake Survey Location for $\alpha = 18^\circ$	163
5.32	: $\alpha = 18^\circ$; Re = 315,000; 0.75c Wake	164
5.33	: $\alpha = 18^\circ$; 0.75c Wake	166

5.34	: $\alpha = 18^\circ$; Re = 315,000; 0.75c Wake	167
5.35	: Velocity Profile and Wake Survey Locations for $\alpha = 20^\circ$	169
5.36	: $\alpha = 20^\circ$; Re = 315,000; x/c = 25%	170
5.37	: $\alpha = 20^\circ$; Re = 315,000; x/c = 50%	171
5.38	: $\alpha = 20^\circ$; Re = 315,000; x/c = 70%	172
5.39	: Hot-Wire Rectification in 1D Reversing Flowfield	173
5.40	: $\alpha = 20^\circ$; Re = 315,000; 0.25c Wake	175
5.41	: $\alpha = 20^\circ$; Re = 315,000; 0.75c Wake	176
5.42	: $\alpha = 20^\circ$; Re = 315,000	177
5.43	: Wake Survey Location for $\alpha = 22^\circ$	181
5.44	: $\alpha = 22^\circ$; Re = 315,000; 0.75c Wake	182
5.45	: Wake Survey Location for $\alpha = 25^\circ$	183
5.46	: $\alpha = 25^\circ$; Re = 315,000; 0.75c Wake	184
5.47	: Dominant Instability Frequency as Function of Alpha	186
5.48	: Modified Strouhal Number as Function of Alpha	186
5.49	: Summary of Important Hot-Wire Experimentation Conclusions	190
6.1	: Piezoelectric Film	192
6.2	: Attachment Location of PVDF Film Element	193
6.3	: The Function Generator with Digital Oscilloscope	193
6.4	: The Microphone Above the PVDF Element	195
8.1	: Synthetic Jet Actuator	201
A.1	: ASWT Turbulence Intensity Level	203

LIST OF TABLES

Table		Page
2.1	: SM701 Airfoil Coordinates	5
2.2	: LSLTT Description Summary, (Brophy, 1994)	11
3.1	: Information Required for Dimensional Starting Profile Calculations	24
4.1	: Fluorescent Oil Flow Visualization Summary	42
4.2	: Selected Samples of Thermal Conductivity Values of Insulators	64
4.3	: Estimates of Uncertainties in Measured Quantities	110
4.4	: Summary of Heat Transfer Uncertainty Analysis	112
5.1	: Test Matrix for Qualitative Shear Stress Experimentation	132
5.2	: Test Matrix for Hot-Wire Experimentation	156
5.3	: $St_{\sin \alpha}$ Results for Various High-Angle-of-Attack Airfoil Experiments	188
B.1	: Inputs for panel.f for Angle of Attack = 0 degrees	204
B.2	: STAN5 Input File - SM701 Airfoil; $\alpha = 0^\circ$; $Re=315000$	205

NOMENCLATURE

A	: area
c	: airfoil chord, also specific heat at constant pressure
c_l	: section lift coefficient
C_f	: skin friction coefficient
C_p	: pressure coefficient
D	: van Driest damping function
e'	: fluctuation voltage
E	: mean voltage
f	: dependent variable in Falkner-Skan similarity solution
$f_{excitation}$: excitation frequency
f_s	: dominant flow instability frequency (shedding frequency)
h	: convective heat transfer coefficient
i^*	: fluctuation stagnation enthalpy
I^*	: mean stagnation enthalpy
k	: thermal conductivity
l	: mixing length
Ma	: Mach number
p	: local static pressure
p_∞	: free stream static pressure
q''	: heat flux per unit area
R	: electrical resistance
Re	: Reynolds number based on airfoil chord
s	: arc length coordinate from airfoil leading edge stagnation point in boundary layer coordinate system
St	: Strouhal number based on airfoil chord
$St_{\sin \alpha}$: modified Strouhal number ($= St \cdot \sin \alpha$)
t	: time
T	: absolute temperature
Tu	: turbulence intensity
u'	: fluctuation velocity in boundary layer in x-direction
U	: mean velocity in boundary layer in x-direction
U_*	: inviscid velocity at outer edge of boundary layer in boundary layer coordinate system
U_∞	: free stream velocity
$U_{INVISCID}$: inviscid velocity at airfoil surface in x-y coordinate system
v'	: fluctuation velocity in boundary layer in y-direction
V	: mean velocity in boundary layer in y-direction
x, y	: coordinates of airfoil surface point location in Cartesian coordinate system
y	: also coordinate normal to airfoil surface in boundary layer coordinate system

$\overline{()}$: time averaged quantity

Greek

α	: angle of attack with respect to airfoil chordline
δ, δ_{99}	: 99% boundary layer thickness
ε	: emissivity
ε_M	: eddy diffusivity for momentum
η	: independent variable in Falkner-Skan similarity solution
κ	: von Karman constant
μ	: air viscosity
μ_t	: turbulent viscosity
ν	: air kinematic viscosity
ρ	: air density
σ	: Stefan-Boltzmann constant

Subscripts

<i>air</i>	: quantity pertaining to air
<i>avg</i>	: average value
<i>initial</i>	: initial value
<i>rms</i>	: root-mean-square value
<i>wall</i>	: quantity pertaining to wall of model
∞	: free stream quantity

ACKNOWLEDGEMENTS

Many people have helped to make my time at Penn State enjoyable. First I must thank my advisor Dr. Cengiz Camci for his time and help throughout my work. Also important are Dr. Dennis McLaughlin and Dr. Mark Maughmer who always had helpful and insightful comments on my research.

I must thank Cris Bosetti for teaching me about the operation of low-speed wind tunnels and for the rides in the Thing. Chris McLean was very helpful regarding instrumentation and deserves my gratitude. Thanks to Todd Wolownik for assisting in the setup for the hot-wire anemometry experiments and the signal analysis. Also, without Rick Auhl and Mark Saussure my research effort would have been much more difficult. In addition, I want to thank Ms. Sheila Corl as well as the other secretaries for always being helpful. Thanks to Eric Donahoo for the interesting conversations over the years and to Oğuz Uzol for performing the computer flowfield simulations.

My friends and family have also been very important to me during my time at Penn State. Thanks to my friends for the comic relief they provide: Manny Wolfe, Tim Malec, Dave Cribbs, Drew Fennell, and all those I can not name. I must thank my parents, Robert and Donna, and my sister Melanie for their continued support throughout the years. In addition, thanks to my grandparents who were always there for me, especially my grandfather Edward Klaput, for the interest he showed in all of my work that has culminated with this thesis.

1 INTRODUCTION

The subject of active control of separated flow regions has become a popular research topic since the discovery in the mid 1970's that large-scale coherent structures dominate the development of turbulent mixing layers. A coherent structure is defined by Hussain as a large-scale turbulent fluid mass with phase-correlated vorticity which transports significant amounts of mass, momentum, and energy (Hussain, 1983). Before coherent structures were understood to dominate turbulent flow regions, the flow was regarded as random motion of fluid particles at all scales which could only be studied by statistical analysis. However, today, with the understanding of deterministic coherent structures, it is generally believed that appropriate aerodynamic excitation can enhance the strength of the naturally occurring coherent structures in a separated turbulent mixing layer and thus influence the turbulent mixing layer growth. By affecting the turbulent mixing layer growth, any separated flow region beneath the mixing layer will also be altered.

Separation control has many applications in all fields of fluid mechanics. Through separation control, propellers, windmills, inlets, and diffusers could be made more efficient. Increased $c_{l_{max}}$ and α_{stall} of airfoils, improved axial flow compressors, reduced engine noise, shorter runways and reduced approach speeds, supermaneuverability, better stall control, and lower drag on automobiles, ships, and aircraft could also be achieved (Gad-el-Hak and Bushnell, 1991). Fuel consumption could be lessened. At the heart of all of these examples lies the common problem: interaction with and enhancement of the coherent flow structures which exist in the separated flow mixing layer regions produced by the object in question.

This thesis provides initial steps toward that ultimate goal of separation control. Many experiments are presented that were performed on the SM701 airfoil. Detailed objectives for the different experiments that were performed are given in the relevant sections of the thesis prior to discussing the work. A general idea of the objectives follows.

Before separation control can be realized, an extensive study of the viscous flow around the airfoil must be conducted. The locations and extent of laminar, transitional,

turbulent, and separated regions must be ascertained for different angles of attack and for different Reynolds numbers.

To determine the flow regions, qualitative fluorescent oil surface flow visualization was first performed and is discussed in Section 4.1. A steady-state heat transfer approach, Section 4.2, was then examined as a means of corroborating the results of the oil flow visualization. The heat transfer approach utilized thermochromic liquid crystals to measure surface temperature distributions. The temperature information allowed convective heat transfer coefficients along the chord of the SM701 airfoil to be calculated under different experimental conditions. The heat transfer results were compared to the oil flow visualization results in an attempt to determine how well the heat transfer method would reveal the location and extent of the viscous flow regions over an airfoil. This line of research was felt to be of value not only to verify oil flow visualization results for the current airfoil, but if successful, to provide a method of flow visualization when the fluorescent oil technique is not practical. Such situations include spinning turbomachinery and flight testing.

Besides being used to verify the oil flow visualization results and being examined as a flow visualization tool, the heat transfer research was conducted for other reasons not related to the goal of active flow control. First, results of the heat transfer experiments could be used as a benchmark solution in the development of better heat transfer prediction codes. Second, experimental heat transfer information for airfoils in low turbulence environments is not particularly abundant; therefore, the data generated in the heat transfer experiments would add to the existent database. The heat transfer method was verified numerically by running a boundary layer code as described in Chapter 3.0.

Once the viscous flow regions on the SM701 model were studied, work began on understanding the naturally occurring coherent structures of the separated flow regions for different experimental conditions. Section 5.1 discusses qualitative shear stress tests made using McCroskey type shear stress gauges. It was hoped that the dominant flow instability frequencies could be measured near the surface of the airfoil by the shear stress gauges.

Single sensor hot-wire measurements were then conducted. Boundary layer profiles and wake surveys were examined and analyzed for frequency content. The locations of the hot-wire sensor where the flow instability frequencies were best revealed were also studied. Results of these hot-wire tests are contained in Section 5.2.6.

Once the frequencies of the coherent structures were better understood, a simple test in active control was attempted using a polyvinylidene fluoride (PVDF) piezoelectric film attached to the upper surface of the airfoil. The film could be made to vibrate normal to the surface by application of a square wave voltage signal. Chapter 6.0 discusses these simple tests and offers possible reasons why they were ineffective in controlling the separated flow region on the SM701 airfoil. Conclusions are given in Chapter 7.0. Suggestions are then given in Chapter 8.0 for future heat transfer, shear stress, hot-wire, and active control research.

Because of the complexity of this flow control problem, ultimate success was not achieved in controlling the separated flow on the SM701 airfoil. Due to this shortcoming, an effort was made to provide extensive background information and extreme detail throughout this thesis. After reading this work, any future experimenter should have a much clearer idea as to the problems to be solved to make active control a success. The systems (hardware and software) are now in place to quickly study the frequency of naturally occurring coherent structures formed in the separated mixing layer region of any airfoil. Future time can thus be better allocated to the active control problem itself.

2 EXPERIMENTAL MODEL AND FACILITIES

This chapter will describe the model that was tested during the course of this study. In addition, the two different experimental facilities that were used will be discussed.

2.1 The Airfoil Definition

The airfoil used for the test model was the SM701, a 16% thick, laminar-flow airfoil designed for World Class sailplanes by Mr. Dan M. Somers of Airfoils, Incorporated and Dr. Mark D. Maughmer of The Pennsylvania State University. The primary objectives of their design were high maximum lift and low profile drag with restrained pitching moment and docile stall characteristics. Details on predicted performance characteristics of the SM701 airfoil (Somers and Maughmer, 1990 and 1991) and experimental verification of those characteristics (Nicks, et. al., 1991 and Althaus and Würz, 1991) are available. Table 2.1 contains the coordinates of the SM701 airfoil. Figure 2.1 is a sketch of those coordinates.

Table 2.1: SM701 Airfoil Coordinates

Upper Surface		Lower Surface	
x/c	y/c	x/c	y/c
0.00168	0.00771	0.00016	-0.00212
0.00736	0.01910	0.00435	-0.00981
0.01701	0.03121	0.01501	-0.01632
0.03055	0.04344	0.03127	-0.02244
0.04794	0.05534	0.05277	-0.02800
0.06915	0.06648	0.07923	-0.03294
0.09417	0.07658	0.11036	-0.03726
0.12295	0.08544	0.14575	-0.04101
0.15541	0.09296	0.18488	-0.04418
0.19133	0.09914	0.22722	-0.04670
0.23041	0.10397	0.27222	-0.04849
0.27229	0.10746	0.31929	-0.04943
0.31654	0.10964	0.36784	-0.04938
0.36268	0.11055	0.41726	-0.04803
0.41019	0.11018	0.46727	-0.04488
0.45853	0.10853	0.51811	-0.03983
0.50714	0.10557	0.56979	-0.03340
0.55548	0.10120	0.62191	-0.02623
0.60323	0.09517	0.67386	-0.01887
0.65041	0.08760	0.72497	-0.01182
0.69676	0.07903	0.77446	-0.00553
0.74171	0.06990	0.82144	-0.00041
0.78466	0.06055	0.86497	0.00324
0.82498	0.05125	0.90406	0.00526
0.86207	0.04221	0.93768	0.00567
0.89529	0.03348	0.96489	0.00463
0.92431	0.02493	0.98462	0.00262
0.94922	0.01669	0.99624	0.00073
0.96999	0.00946	1.00000	0.00000
0.98605	0.00405		
0.99640	0.00095		
1.00000	0.00000		

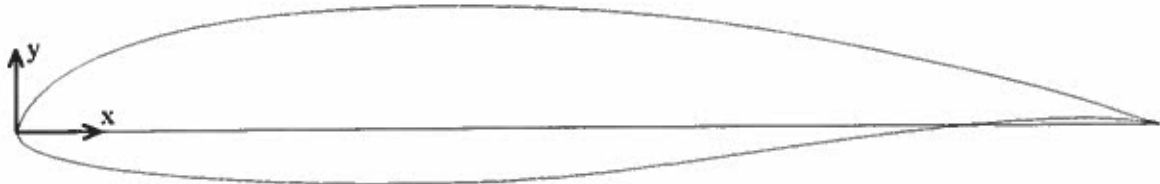


Figure 2.1: SM701 Airfoil Shape

The test model was fabricated by a group of Penn State aerospace engineering students as part of a senior project. Members of the group were Louis Centolanza, Chris Dunn, Patrick Papay, Duk Park, Robert Smith, and Thomas Thibodeau. The group decided to construct a composite model with a 12 inch chord and a 30 inch span. One-half inch wooden end caps were used to seal the ends of the model, increasing the overall span to 31 inches and the aspect ratio to 2.58.

The group's design included fabricating the upper surface and the lower surface of the model separately and screwing the pieces together with 10 screws along the span of both a main spar and a trailing edge spar. This design feature would allow easy access to the inside of the model during future experimentation.

To fabricate the skin of the model, an existing mold was used. Centolanza et al. used a wet lay-up of E-glass and EPON epoxy resin with EPI-CURE as the hardener. A layer of three ounce E-glass was first laid up, followed by two layers of six ounce E-glass. A layer of Owens Corning Foamular 150 foam was then added, followed by two layers of six ounce E-glass and one layer of three ounce E-glass, Figure 2.2. This sandwich panel construction was then vacuum-bagged to increase the final quality of the composite by pressing the layers together and removing excess voids (Centolanza et al., 1995).



Figure 2.2: Sandwich Panel Construction of the Test Model Skin

A main spar and a trailing edge spar were machined from 6061-T6 aluminum. Figures 2.3 and 2.4 show the final model.

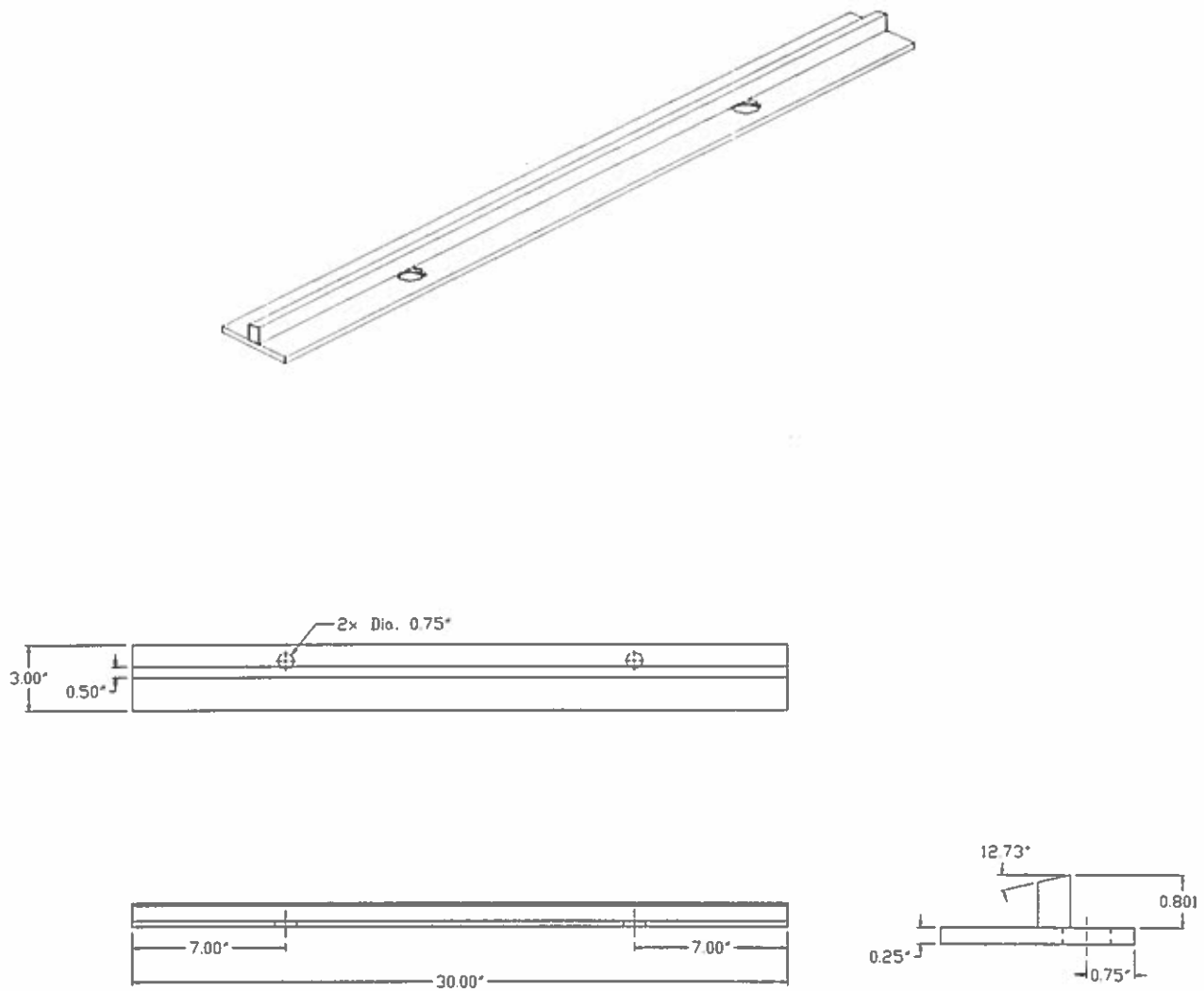


Figure 2.3: Leading Edge Spar of the Airfoil

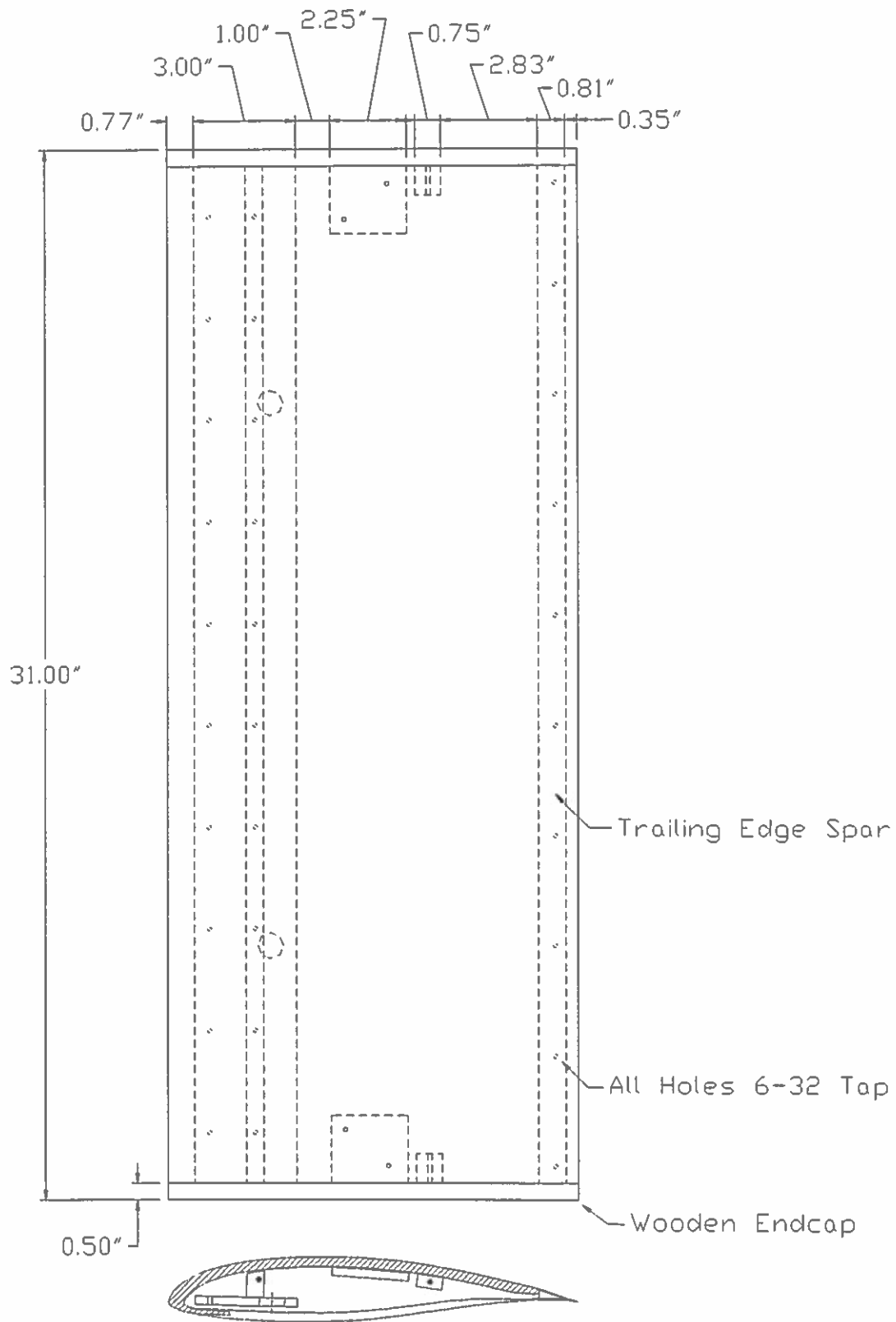


Figure 2.4: The Airfoil Model

2.2 The Axisymmetric Wind Tunnel (ASWT)

The ASWT is an open-return wind tunnel with overall dimensions of 32 x 11 feet. Fiberglass construction was used for the contraction section and test section. The ASWT, Figure 2.5, is located in 31 Hammond Building at The Pennsylvania State University.

The tunnel fan is powered by a 35 hp electric motor through a direct drive shaft. The motor and fan are located inside the wind tunnel downstream of the test section. A specially designed acoustic cone protrudes into the diffuser section at the flow outlet to provide noise control.

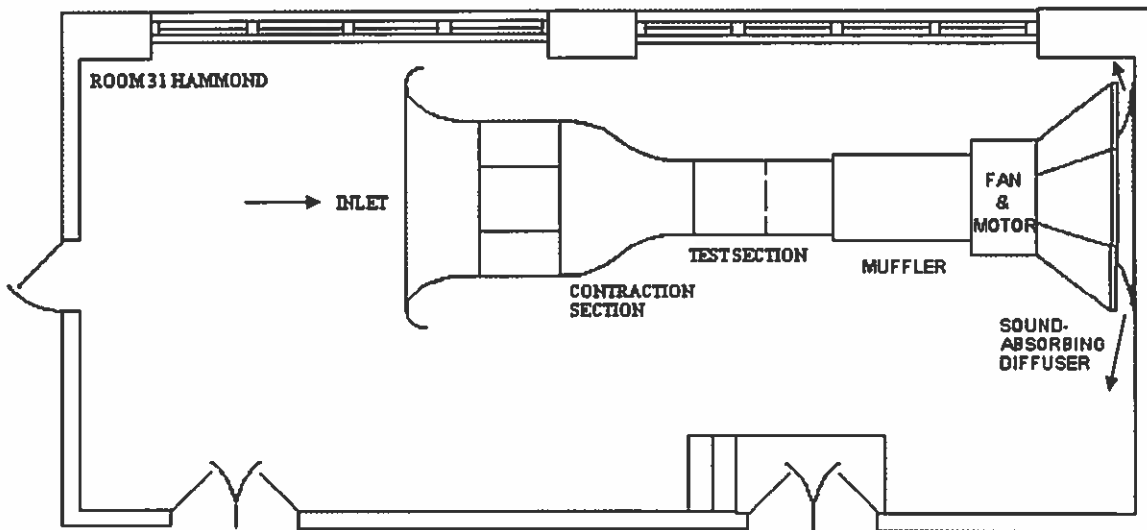


Figure 2.5: Axisymmetric Wind Tunnel (ASWT)

The test section has a circular cross-section three feet in diameter, and the contraction section accelerates flow through a 4:1 area ratio. Access to the test section is via a side window. To provide turbulence management, a fine cloth and a screen are used at the inlet. This is followed by honeycomb and a series of screens between the inlet and the contraction section. The original design of the tunnel considers the test objects as axisymmetric objects. Hot-wire measurements of the streamwise turbulence intensity in the test section found a representative value of 0.25% over the tunnel operating speed range of zero to 60 ft/s (see Figure A.1 in Appendix A for more detailed ASWT

turbulence intensity information). A two-component strain gauge balance is situated below the test section allowing the measurement of lift and drag.

2.3 The Low-Speed Low-Turbulence Wind Tunnel (LSLTT)

The LSLTT, Figure 2.6, located in 117 Academic Projects Building at The Pennsylvania State University is a high-quality research facility. A detailed description of this facility is given in Brophy, 1994. The most important facility statistics are presented here. It should be noted that Brophy's documentation of the dimensions of the test section used for finite model testing are slightly in error. The correct dimensions are presented in this section.

The LSLTT is a closed-return wind tunnel constructed over a 75 x 25 foot area. A three-phase, 300 hp electric motor powers the eight-bladed 6.5 foot diameter tunnel fan through a belt and drive shaft arrangement. The motor is held at a constant 1100 rpm. An in-line magnetic clutch allows the fan rotation rate to be varied from 150 to 1100 rpm.

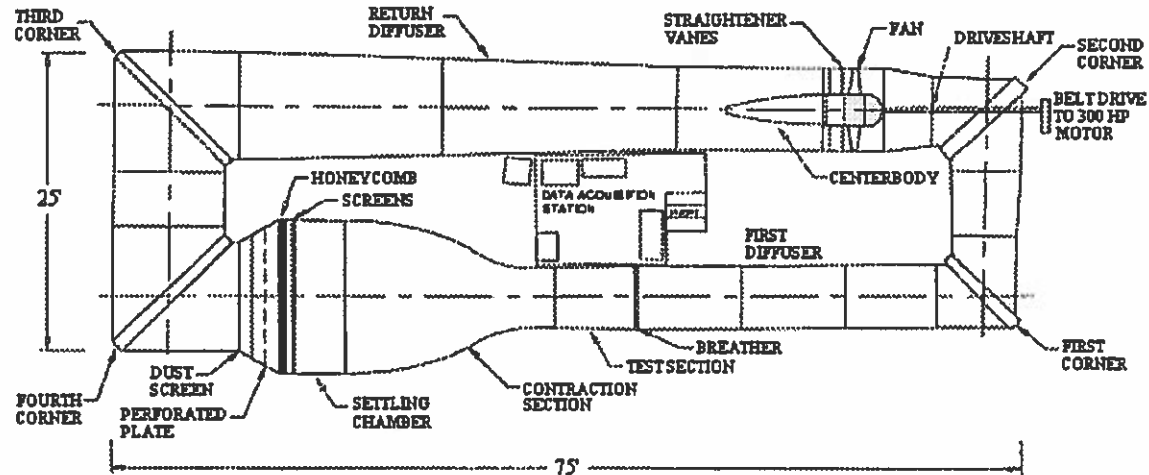


Figure 2.6: Low-Speed Low-Turbulence Wind Tunnel (LSLTT)

The dimensions at the entrance to the test section are 39.5 inches high by 57.25 inches wide. At the end of the test section, the dimensions are 41 inches high by 59 inches wide. Thus the test section floor and ceiling diffuse at a total angle of 1.2° , and the test section

side walls diffuse at a total angle of 1.4°. This feature is used to offset the effect of the growing displacement thickness in the test section. A breather slot 1.0 inch wide is located at the end of the test section to ensure atmospheric static pressure at that position (Brophy, 1994).

Honeycomb and a series of screens are used in the settling chamber for turbulence management. Brophy reports a streamwise turbulence intensity value of less than 0.06% over the operating speed range of the wind tunnel (Brophy, 1994). The tunnel can be used for both finite model testing and infinite airfoil testing. For the former, a six-component pyramidal balance can be used to measure the forces acting upon a model. For the latter, a wake survey system and surface static pressure measurements can be used for determining coefficients of lift, drag, and moment. The contraction section of the LSLTT has a 9.3:1 area ratio. Table 2.2 provides many details of the LSLTT.

Table 2.2: LSLTT Description Summary (Brophy, 1994)

Device	Description
Fan	8 blades and 13 stators, max RPM = 1100
Motor	Three phase-300 hp, belt driven
Turning Vanes	
First & Second corners	Single Wall, 8" chord, 3/16" thick
Third & Fourth corners	Double Wall, 6" chord, 9/16" max thickness at .5 chord
Dust Screen	46 mesh, .0045 wire diameter, $\beta = .6288$
Perforated Plate	3/8" holes, 3/32" thickness, $\beta = .62$
Settling Chamber Screens	
First	16 mesh, .009" wire diameter, $\beta = .7327$
Second	43 mesh, .005" wire diameter, $\beta = .6162$
Third	46 mesh, .0045" wire diameter, $\beta = .6288$
Rapid Expansion	2:1 Area ratio
Contraction Section	9.3:1 Area ratio, tapered corner fillets
Test Section	Closed section w/fillets, 6'1" length; max speed, 220 ft/s
First Diffuser	1.9:1 Area ratio
Return Diffuser	2.2:1 Area ratio

3 BOUNDARY LAYER PREDICTIONS ON THE AIRFOIL SUCTION SIDE

In order to gain insight into the viscous flow behavior on the upper surface of the airfoil, two-dimensional theoretical boundary layer predictions were made. Values of the convective heat transfer coefficient, h , were computed along the chord of the SM701 airfoil at various angles of attack and two Reynolds numbers. This process involved three basic steps: calculating the potential flow around the SM701 airfoil for a given experimental configuration, determining the proper boundary conditions, and invoking a two-dimensional differential boundary layer code to solve for the details in the boundary layer at the airfoil's surface. Predictions were made for three angles of attack: 0, 5, and 10°. Reynolds numbers studied were 315,000 and 750,000. The details of the prediction process will now be illustrated using the zero degree angle of attack case at a Reynolds number of 315,000.

3.1 Potential Flow

A two-dimensional panel code was used for the potential flow calculations. The code is named Panel.f and was written by Dr. G. S. Dulikravich and several of his students at The Pennsylvania State University. The code requires the x/c and y/c airfoil coordinates to be listed in an input file. The coordinate points should be listed beginning at the trailing edge, proceeding along the pressure surface of the airfoil to the leading edge, and continuing along the suction surface back to the original starting point making sure to repeat this original point. The x/c and y/c points for the SM701 airfoil were listed in Table 2.1 of Section 2.1. Note that a third column should be included in this input data file consisting simply of values of 1.0. The first line of the input file should be a value that is the total number of x/c, y/c points in the input file.

The panel code inputs the desired number of panels from the user into which the airfoil's surface is then divided. Initially a value of 43 panels was chosen. Calculations for the pressure coefficient at each panel are then performed. The pressure coefficient is defined as

$$C_p = \frac{p - p_\infty}{\frac{1}{2} \rho U_\infty^2}. \quad (3.1)$$

Table B.1 in Appendix B contains all of the inputs used to execute Panel.f for the case currently being discussed.

Since the accuracy of Panel.f was not known, a C_p comparison was made to the potential flow results obtained by Mr. Dan M. Somers and Dr. Mark D. Maughmer who used the well-known and well-tested Eppler Airfoil Program System for their calculations on the SM701 airfoil. The Eppler results are trusted since the Eppler Airfoil Program System has been used to design and analyze many other airfoils with experiments verifying the results (Somers and Maughmer, 1990). Somers' and Maughmer's C_p predictions are tabulated in their report entitled "The SM701 Airfoil" (Somers and Maughmer, 1990) and are plotted for an angle of attack of 13° in Figure 3.1. Results of Panel.f for the same angle of attack are plotted for comparison.

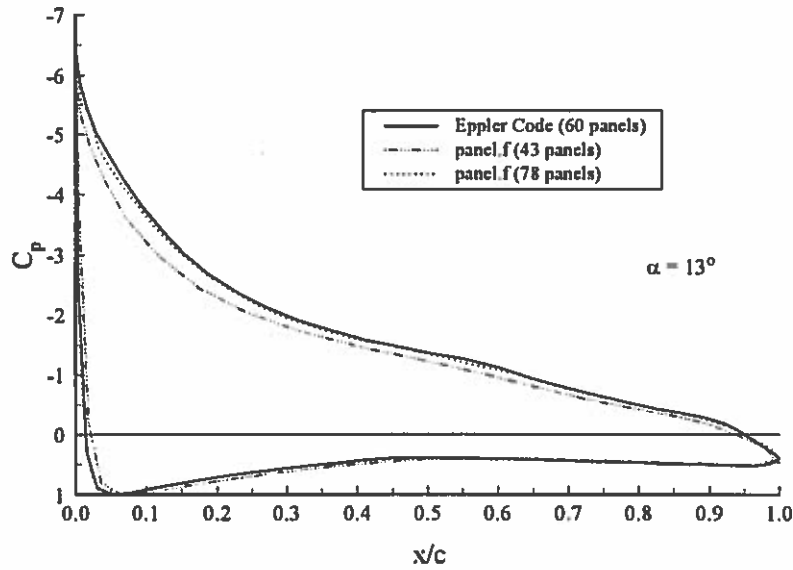


Figure 3.1: Verification of Panel.f

Note that the C_p prediction made by Panel.f using 43 panels is poor along the upper surface of the airfoil. Because of the poor agreement between Panel.f and the Eppler code, Panel.f was re-run with the number of panels increased to 78. These results are also shown in Figure 3.1. Notice the good agreement between Panel.f and Eppler C_p predictions. A value of 78 for the number of panels was obtained by repeatedly running Panel.f while increasing the number of panels from 43 until no further improvement was obtained for the agreement between Panel.f results and those of the Eppler code.

Two other angles of attack were analyzed and compared to Eppler code results. These angles were 6° and 11° . Good agreement was again obtained. Because of these comparisons, Panel.f was felt to be trustworthy for use in the prediction of boundary layer characteristics including convective heat transfer coefficients, the ultimate goal of this theoretical study.

The code Panel.f was then run for a zero degree angle of attack. Pressure coefficient results are plotted in Figure 3.2.

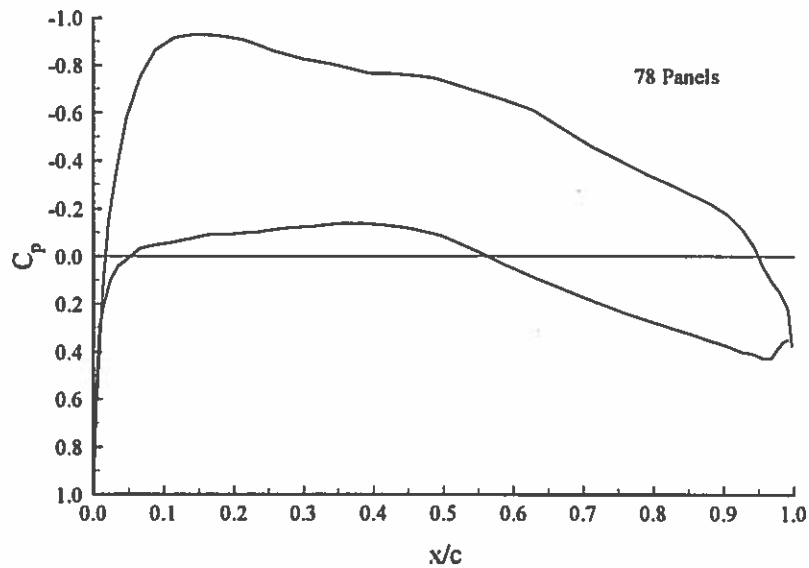


Figure 3.2: Potential Flow C_p Distribution for $\alpha = 0^\circ$

These C_p values were converted to nondimensional velocity values by using equation 3.2 derived from Bernoulli's equation for steady, incompressible, irrotational flow. Results are seen in Figure 3.3.

$$\frac{U_{INVISCID}}{U_\infty} = \sqrt{1 - C_p} \quad (3.2)$$

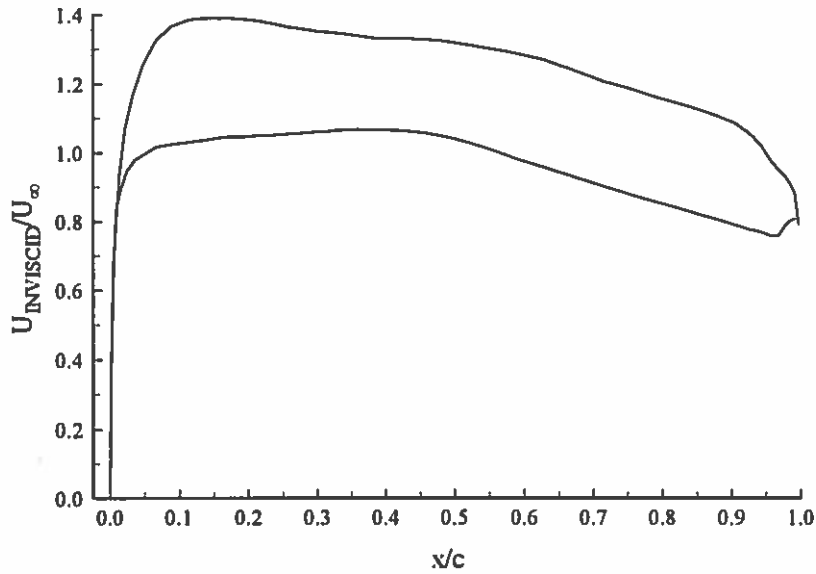


Figure 3.3: Nondimensional Velocity Distribution for $\alpha = 0^\circ$

From this nondimensional velocity distribution, the stagnation point can be located at the x/c location at which $U_{INVISCID}/U_\infty$ goes to zero. Referring to Figure 3.3, the stagnation point for this case is estimated to occur at $x/c = 0.0$. With knowledge of the stagnation point location, the calculated nondimensional inviscid velocity distribution about the SM701 airfoil may be translated into the boundary layer coordinate system which begins at the stagnation point and proceeds along the arc length of the upper surface of the airfoil. See Figure 3.4.

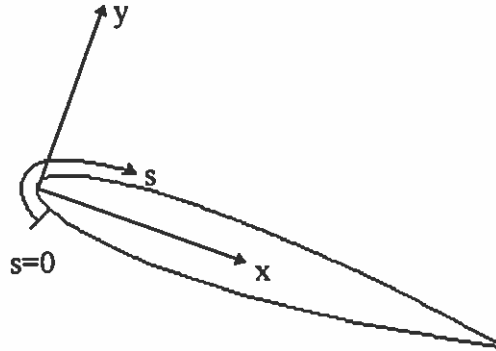


Figure 3.4: The Boundary Layer (B.L.) Coordinate System

The calculated inviscid velocity distribution will hereafter be referred to as the “outer flow velocity distribution” when presented in the boundary layer coordinate system. In addition, the variable $U_{INVISCID}$ will be replaced by U_e . This outer flow velocity distribution will be used by the boundary layer code as the boundary condition velocity values at the outer edge of the boundary layer. The outer flow velocity distribution calculated for an angle of attack of zero degrees is shown in Figure 3.5.

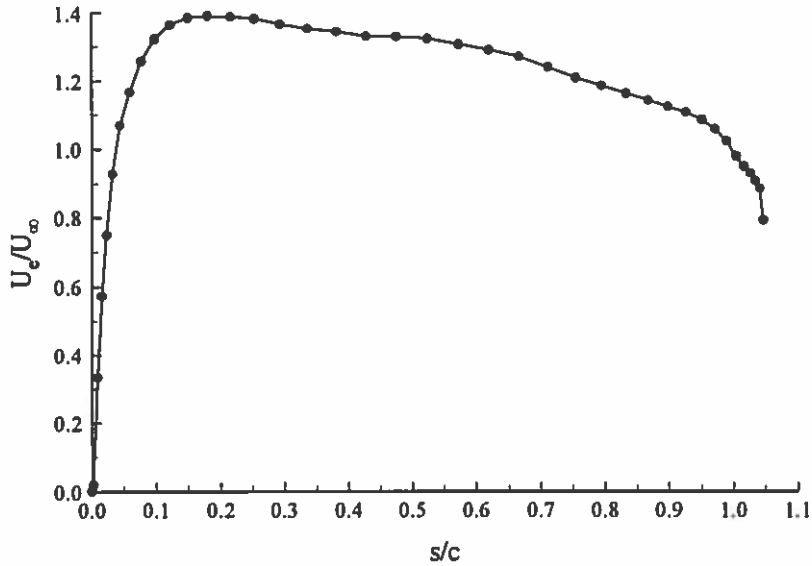


Figure 3.5: Outer Flow Velocity Distribution in B. L. Coordinate System for $\alpha = 0^\circ$

3.2 Boundary Conditions

3.2.1 Initial Considerations

Calculating the boundary layer development at the surface of an airfoil requires solving the continuity, s-momentum, and energy equations simultaneously. The time-averaged, incompressible, boundary layer form of these equations are presented as equations 3.3, 3.4, and 3.5, respectively, in the boundary layer coordinate system. Gravity is neglected (Crawford and Kays, 1975).

$$\frac{\partial U}{\partial s} + \frac{\partial V}{\partial y} = 0 \quad (3.3)$$

$$U \frac{\partial U}{\partial s} + V \frac{\partial U}{\partial y} = U_e \frac{\partial U_e}{\partial s} + \frac{\partial}{\partial y} \left[V \frac{\partial U}{\partial y} - \bar{u}' v' \right] \quad (3.4)$$

$$\rho U \frac{\partial^* U}{\partial s} + \rho V \frac{\partial^* U}{\partial y} = \frac{\partial}{\partial y} \left[\frac{k_{air}}{c_{air}} \frac{\partial^* U}{\partial y} - \rho \bar{u}'^* v' + \frac{\mu}{g_c J} \frac{\partial}{\partial y} \left(\frac{U^2}{2} \right) \right] + S \quad (3.5)$$

The dependent variables in these equations are U , V , $\overline{u'v'}$, I^* , and $\overline{i^*v'}$. However, modeling the Reynolds stress term and the $\overline{i^*v'}$ term reduces the dependent variables to the mean velocities (U , V) and the stagnation enthalpy (I^*). Equations 3.3 to 3.5 then reveal the necessary boundary conditions. From the continuity equation it is seen that U must be specified at a given s location for all y locations; this requires specification of a *starting velocity profile*. Continuity also reveals that V must be specified at a given y location for all s locations; the no-slip boundary condition can be used to satisfy this requirement.

$$V(s,0) = 0 \quad \text{----- no-slip} \quad (3.6)$$

The s -momentum equation adds to the current boundary conditions since it contains a second order partial derivative of U with respect to y . Thus U must be specified at two y locations for all s locations. These boundary conditions may be expressed mathematically as

$$\begin{aligned} U(s,0) &= 0 & \text{----- no-slip} \\ \lim_{y \rightarrow \delta_{99}} U(s,y) &= U_e(s) & \text{----- edge condition} \end{aligned} \quad (3.7)$$

The values of $U_e(s)$, containing pressure gradient information outside the boundary layer, were determined previously in Section 3.1 by use of a panel code.

The energy equation reveals the required boundary conditions on stagnation enthalpy. The first term reveals that I^* must be specified at a given s location for all y locations. This requires a *starting profile for stagnation enthalpy*. The energy equation also shows through its second partial derivative of I^* with respect to y that I^* must be specified at two y locations for all s locations. This is handled by calculating the stagnation enthalpy I^* at the airfoil surface ($y = 0$) and also at the edge of the boundary layer ($y = \delta_{99}$) based on the respective average absolute temperatures. This is an approximation since the airfoil surface temperature and boundary layer edge temperature will be functions of s , but the temperatures will both be considered constants for calculation of the stagnation enthalpy boundary conditions.

From this discussion the only unresolved boundary conditions are the starting profiles for U and I^* . The starting profile for stagnation enthalpy I^* is simply modeled as varying linearly between the airfoil surface value of stagnation enthalpy and the boundary layer edge value (as suggested by Crawford and Kays, 1975), both of which are specified as constants in s as previously discussed. The starting velocity profile is somewhat more complex and is now discussed in detail.

3.2.2 Starting Velocity Profile

A simple linear starting profile for U could have been specified and used as a boundary condition in the solution of the continuity, s -momentum, and energy equations (as suggested by Crawford and Kays, 1975). However, a more correct method was chosen to calculate a velocity profile which could be used as the starting profile. This involved a similarity solution of the continuity and x -momentum boundary layer equations where the velocity at the edge of the boundary layer was assumed to be of the form of equation 3.8. Refer also to Figure 3.6.

$$U_e(x) = C_1 x^m \quad (3.8)$$

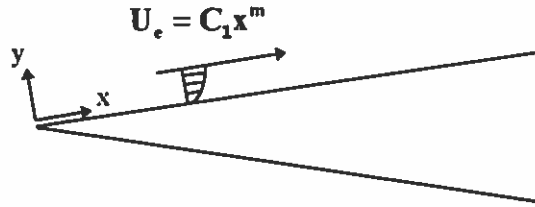


Figure 3.6: Setup for Falkner-Skan Wedge Flow Solution

The similarity solution process for this form of $U_e(x)$ is commonly referred to as the Falkner-Skan wedge flow solution since the assumed velocity distribution can be shown to come directly from the complex potential function $w(z) = Az^{m+1}$ for flow about a two-dimensional wedge; this complex potential function represents the inviscid velocity distribution at the wedge surface with the $x = 0$ point at the wedge vertex. It should be noted that if $m = 0$, the complex potential and assumed velocity distribution revert to

forms for flow over a flat plate. If $m = 1$, the complex potential and velocity distribution represent two-dimensional stagnation point flow. The physical case of flow near the stagnation point on an airfoil falls between the case of a flat plate and that of a two-dimensional stagnation point. Thus, the case of wedge flow where m falls between zero and one is used to generate a starting profile.

The equations to be solved for this similarity solution are the two-dimensional, steady, incompressible continuity and x -momentum boundary layer equations. Gravity is neglected.

$$\frac{\partial U}{\partial x} + \frac{\partial V}{\partial y} = 0 \quad (3.9)$$

$$U \frac{\partial U}{\partial x} + V \frac{\partial U}{\partial y} = U_e \frac{\partial U_e}{\partial x} + \nu \frac{\partial^2 U}{\partial y^2} \quad (3.10)$$

Making the similarity assumption that the two dependent variables (U, V) which are functions of the two independent variables (x, y) can be combined into a single dependent variable (f) which is a function of a single independent variable (η), the following substitutions are made.

$$U = U_e(x)f'(\eta) \quad (3.11)$$

$$\eta = \frac{y}{\delta(x)} \quad (3.12)$$

With these substitutions and after some rearranging and integration by parts, the continuity equation becomes

$$V = U_e \frac{d\delta}{dx} \eta f' - \frac{d}{dx}(U_e \delta) f \quad (3.13)$$

Substituting equations 3.11 to 3.13 into the x -momentum equation 3.10, the following similarity equation is obtained

$$f''' + \alpha f f'' + \beta [1 - (f')^2] = 0 \quad (3.14)$$

where $\alpha = \frac{\delta}{\nu} \frac{d}{dx}(U_e \delta)$ and $\beta = \frac{\delta^2}{\nu} \frac{dU_e}{dx}$. Taking the assumed form of $U_e(x)$ for wedge flow, equation 3.8, and assuming $\delta(x) = \sqrt{\frac{\nu x}{U_e}}$, the following results are obtained via

substitution for the coefficients α and β .

$$\alpha = \frac{1}{2}(m+1) \quad (3.15)$$

$$\beta = m \quad (3.16)$$

Using equations 3.15 and 3.16, the similarity equation becomes

$$f''' + \frac{1}{2}(m+1)ff'' + m[1 - (f')^2] = 0 \quad (3.17)$$

recalling that $U_e(x) = C_1 x^m$

$$\delta(x) = \sqrt{\frac{\nu x}{U_e}}. \quad (3.18)$$

The boundary conditions are given by

$$f(0) = 0 \quad (3.19)$$

$$f'(0) = 0 \quad (3.20)$$

$$f'(\infty) = 1 \quad (3.21)$$

It should be emphasized now that the similarity equation 3.17 is a combination of the continuity and x-momentum boundary layer equations. Solution of equation 3.17 with the boundary conditions (equations 3.19 to 3.21) will yield a profile $f'(\eta)$. This profile can be dimensionalized by using equations 3.11, 3.12, and 3.18 to obtain $U(y)$ for use as a starting velocity profile in the solution of equations 3.3, 3.4, and 3.5 of Section 3.2.1.

A fourth order Runge-Kutta code was used to solve the similarity equation 3.17 after it was first broken into three first order differential equations. The value of m that was used in the equation was obtained by fitting an exponential curve through the first few $U_e(s)/U_\infty$ outer flow velocity values near the stagnation point at a zero degree angle of attack; these velocity values were calculated via a panel code as explained in Section 3.1. See Figure 3.7.

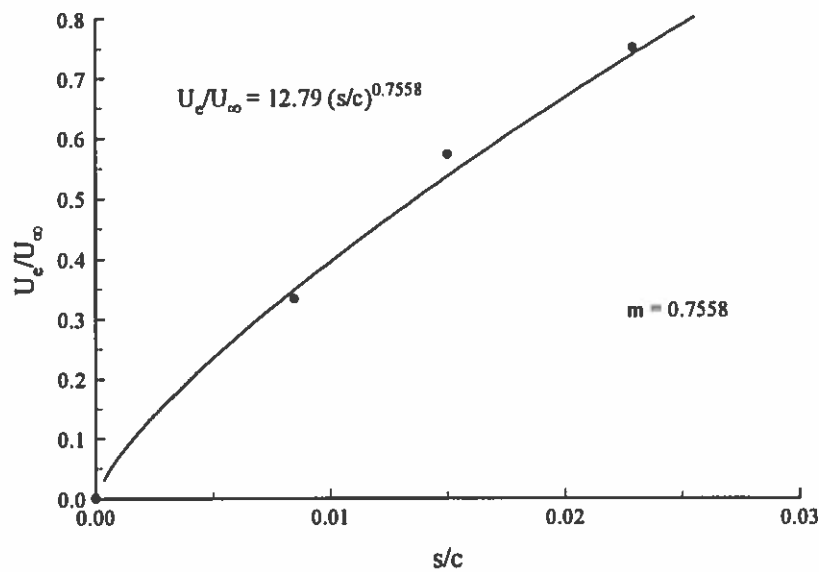


Figure 3.7: Determination of m for $\alpha = 0^\circ$

Using the value for m determined in Figure 3.7, solution to the similarity equation 3.17 yields the following similarity profile in Figure 3.8.

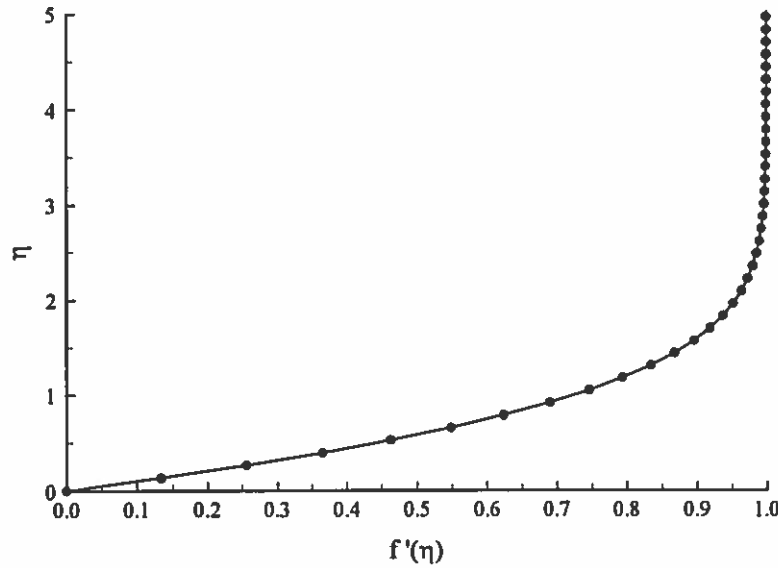


Figure 3.8: Falkner-Skan Similarity Profile for SM701 at $\alpha = 0^\circ$

Finally, to dimensionalize this profile, values of $U_e(s)$, ν , and s must be known for the experimental runs at $\alpha = 0^\circ$. $U_e(s)$ and s are obtained from the panel code discussed in Section 3.1, and $\nu = \frac{\mu}{\rho}$ is obtained from experimental data. The value of viscosity is calculated using Sutherland's law and experimentally measured free stream temperatures. Table 3.1 summarizes the information used to calculate the dimensional starting profile for the zero degree angle of attack case, along with data for all other experimental runs. The experimental data listed in the table (μ_{AVG} , ρ_{AVG} , $U_{\infty AVG}$, $T_{wallAVG}$, and $T_{\infty AVG}$) were obtained during experimentation as will be discussed in Section 4.2.

Table 3.1: Information Required for Dimensional Starting Profile Calculations

Data Determined Through Experimentation							From Panel Code	
α (deg)	Re	μ_{avg} ($N \cdot s/m^2$)	ρ_{avg} (kg/m^3)	$U_{\infty, avg}$ (m/s)	$T_{wall, avg}$ (K)	$T_{\infty, avg}$ (K)	$S_{first\ node\ after\ stagnation\ point}$ (m)	$U_e \left(S_{first\ node\ after\ stagnation\ point} \right)$ (m/s)
0	315,000	1.8282x10 ⁻⁵	1.174	15.87	303.15	295.10	0.000835	0.020347
0	750,000	1.8851x10 ⁻⁵	1.120	40.48	316.15	304.41	0.000835	0.020347
5	315,000	1.8660x10 ⁻⁵	1.151	16.28	316.15	296.28	0.002159	0.297676
5	750,000	1.8868x10 ⁻⁵	1.117	40.78	316.15	305.29	0.002159	0.297676
10	315,000	1.8652x10 ⁻⁵	1.152	16.31	316.15	295.99	0.001326	0.032894
10	750,000	1.8872x10 ⁻⁵	1.123	40.61	316.15	305.35	0.001326	0.032894
15	750,000	1.8886x10 ⁻⁵	1.125	40.72	316.15	306.07	0.003467	0.052077
18	750,000	1.8882x10 ⁻⁵	1.122	40.79	316.15	305.91	0.005771	0.101089
20	750,000	1.8844x10 ⁻⁵	1.124	40.56	316.15	304.31	0.005522	0.077840

Using equations 3.11, 3.12, and 3.18 and substituting $x = s_{\text{first node after stagnation point}}$, a dimensional starting profile is obtained to be used as a boundary condition in the solution of equations 3.3, 3.4, and 3.5. All necessary boundary conditions have now been specified, and solution to the governing equations may now continue.

3.3 The Boundary Layer Code STAN5

Now that all necessary boundary conditions have been set for the solution of the continuity, s-momentum, and energy equations inside the boundary layer of the SM701 airfoil at a zero degree angle of attack, a boundary layer solver can be invoked to calculate the convective heat transfer coefficient along the chord of the airfoil. For this purpose STAN5, a boundary layer code developed at Stanford University, was used. STAN5, developed from the Patankar/Spalding program which is discussed in their book (Patankar and Spalding, 1967), is “a program for numerical computation of two-dimensional internal/external boundary layer flows” (Crawford and Kays, 1975). These flows are described by the parabolic boundary layer equations which include the continuity, momentum, and stagnation enthalpy equations. The time averaged form of these equations have already been presented as equations 3.3 to 3.5 in Section 3.2.1.

STAN5 is able to solve both laminar and turbulent boundary layers and includes a provision to allow transition based on a momentum thickness Reynolds number criterion (Crawford and Kays, 1975). Viscous dissipation in the energy equation is included, and the eddy diffusivity concept is used to model the Reynolds stresses.

$$-\overline{u'v'} = \varepsilon_M \frac{\partial U}{\partial y} = \frac{\mu_t}{\rho} \frac{\partial U}{\partial y} \quad (3.22)$$

The Prandtl mixing-length model is used to model the eddy diffusivity.

$$\varepsilon_M = l^2 \left| \frac{\partial U}{\partial y} \right| \quad (3.23)$$

The mixing length, l , is modeled as

$$l = \kappa y \quad \text{near wall region} \quad (3.24)$$

$$l = \kappa y D \quad \text{viscous sublayer} \quad (3.25)$$

where κ is the von Karman constant ($\kappa = 0.41$), and D is the exponential Van Driest damping function. STAN5 uses freestream velocity $U_\infty(s)$ rather than pressure as the boundary condition at the edge of the boundary layer and invokes a finite-differencing scheme to solve the continuity, s-momentum, and energy equations simultaneously.

To execute STAN5 an input file must first be created. The STAN5 manual (Crawford and Kays, 1975) contains details regarding the construction of the input file. Table B.2 in Appendix B lists the input file used for the SM701 airfoil at a zero degree angle of attack and a Reynolds number of 315,000. The bold faced comments in the table do not appear in the actual input file.

Before using STAN5 to perform calculations on the SM701 airfoil, a simple test case was first run to verify that STAN5 was functioning properly. This test was deemed important since the version of STAN5 that was used was slightly modified from the original STAN5 code to run on a PC instead of on a Digital/VAX computer. The well-known Blasius flat plate equation for skin friction was used to calculate the C_f distribution over a flat plate with the following test values.

$$C_f = \frac{0.664}{\sqrt{\frac{U_\infty x}{\nu}}} \quad (3.26)$$

$$\begin{aligned} U_\infty &= 10 \frac{m}{s} \\ \mu &= 1.8 \times 10^{-5} \frac{N \cdot s}{m^2} \\ \rho &= 1.225 \frac{kg}{m^3} \end{aligned} \quad (3.27)$$

An input file was then created for STAN5. The starting profile required by the input file was calculated by the method described in Section 3.2.2 with $m = 0$. STAN5 was run, and the calculated skin friction coefficient distribution is presented in Figure 3.9.

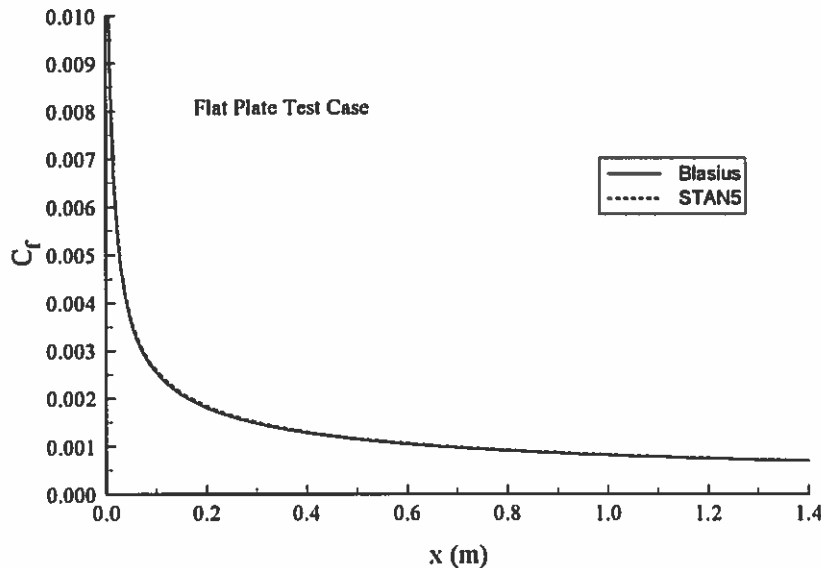


Figure 3.9: Comparison of STAN5 C_f Results and Blasius Solution

As can be seen, STAN5 results agree well with the analytic Blasius solution. As a further check, the 99% boundary layer thickness was also obtained from velocity profiles calculated by STAN5 along the flat plate and compared to the analytically predicted values from the following equation. This equation also stems from the classical Blasius solution.

$$\delta_{99} = 4.92 \sqrt{\frac{vx}{U_e}} \quad (3.28)$$

The results can be seen in Figure 3.10. The δ_{99} values never differ by more than 3% for any of the points calculated.

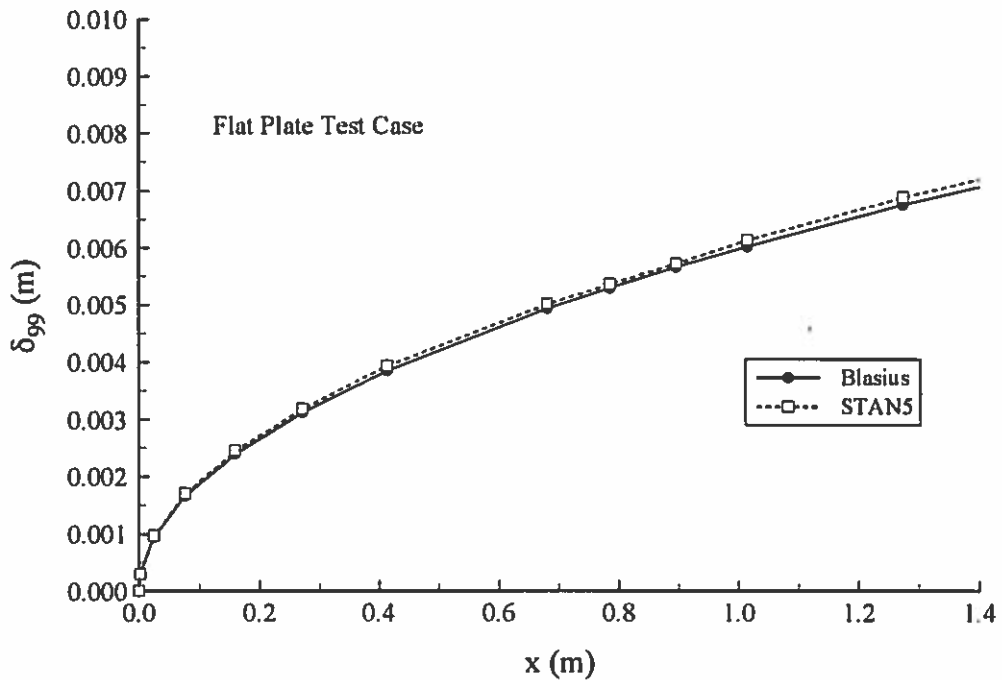


Figure 3.10: Comparison of STAN5 δ_{99} Results and Blasius Solution

From these two checks (C_f and δ_{99}), the STAN5 code appeared to be functioning properly. Because of the confidence in the code, it was then run for the cases of interest involving the SM701 airfoil. These numerical predictions are presented in Section 4.2.16 along with the experimental heat transfer results.

4 EXAMINATION OF VISCOUS FLOW REGIONS ON SM701 AIRFOIL

This chapter discusses the experimentation that was performed to gain an understanding of the viscous flowfield over the SM701 airfoil under various experimental conditions. The existence and locations of the laminar, transitional, turbulent, and separated/reattached regions on the airfoil are explored using two different methods: fluorescent oil flow visualization and liquid crystal thermography.

4.1 Fluorescent Oil Flow Visualization

The following sections describe the fluorescent oil flow visualization tests and present qualitative results as a series of pictures for experiments performed in Penn State's Axisymmetric Wind Tunnel (ASWT) and Low-Speed Low-Turbulence Wind Tunnel (LSLTT) at two different Reynolds numbers and several different angles of attack. Models tested were two-dimensional. The two Reynolds numbers were 315,000 and 750,000. ASWT results are only for a Reynolds number of 315,000 due to the lower maximum flow speed of that facility. Angles of attack studied were 0, 5, 10, 15, 18, and 20°. Angle of attack is referenced with respect to the chord of the airfoil. LSLTT tests include a heater strip located on the surface of the model. This heater strip will be discussed in detail in Section 4.2.

4.1.1 Oil Flow Visualization Objective

The objective of the conventional fluorescent oil flow visualization tests is to determine the locations and extent of the various flow regions on the upper surface of the SM701 airfoil under different experimental conditions. These tests will provide a baseline with which to compare the liquid crystal thermography results of Section 4.2.

4.1.2 Oil Flow Visualization Procedure

All lights illuminating the model were replaced with ultraviolet "black lights." Three mixtures of aviation oil (Shell Aeroshell W 100 ashless dispersant SAE 50) and kerosene were prepared.

- A. 1:2 (oil:kerosene)
- B. 1:3
- C. 1:4

A fine paintbrush was used to apply a thin coat of an oil/kerosene mixture to the upper surface of the SM701 model. The tunnel was operated at the desired Reynolds number, and the flow of the oil on the model surface was noted. If the oil was washed away too quickly, a thicker mixture was used. Between tests the model was wiped clean with a rag and a small amount of kerosene.

A Pentax P30T 35mm camera was used operating on the bulb setting to take 35mm pictures of the resulting patterns that formed on the airfoil. Super HG Fujicolor 1600 speed color film was used. All tests were performed at night to ensure the best conditions for viewing the fluorescent oil patterns.

A good reference regarding this surface oil flow visualization method is an AGARDograph compiled by R. L. Maltby (Maltby, 1962). Several important conclusions are reached by L. C. Squire in this compilation regarding the interpretation of oil flow visualization results. Squire's conclusions are as follows:

- A. "The oil follows the boundary layer surface streamlines except near separation where it tends to form an envelope upstream of the true separation envelope. This early indication of separation is ... less marked for turbulent than laminar layers. The distance by which separation is apparently altered depends on the oil thickness, and the model size, but it is independent of the oil viscosity ..."
- B. "The effect of the oil flow on the motion of the boundary layer ... is very small in most practical cases but increases as the oil viscosity decreases."
- C. "Results at low Reynolds number should be treated with caution as transition could be erroneously interpreted as separation."

4.1.3 Oil Flow Visualization Results

Figure 4.1 compares results from both facilities for $\alpha = 0^\circ$. Figure 4.1a is of poorer quality than Figures 4.1b and 4.1c due to less available “black” light in the test section of the ASWT. The ASWT results indicate a laminar separation bubble existing on the upper surface between 59-75% chord for $Re = 315,000$. At the same Reynolds number, Figure 4.1b shows that a laminar separation bubble exists between 57-75% in the LSLTT. At $Re = 750,000$, Figure 4.1c shows that the laminar separation bubble has shifted forward and exists from 61-68%. The upper edge of the heater strip is seen to be affecting the downward flow of the oil due to gravity. Flow is seen to be very two-dimensional for the test conditions in Figure 4.1.

Figure 4.2 presents oil flow visualization results for $\alpha = 5^\circ$. In Figure 4.2a, a weak laminar separation bubble is seen between 35-50% in the ASWT at $Re = 315,000$. It is difficult to accurately pinpoint the location of this weak bubble since the points of laminar separation and flow reattachment are somewhat ambiguous. Figure 4.2b indicates a more distinct laminar separation bubble from 29-45% in the LSLTT at $Re = 315,000$. Turbulent separation is also seen in Figure 4.2b at approximately 97%. For $Re = 750,000$, Figure 4.2c is somewhat ambiguous. Either a weak laminar separation bubble exists from 21-34%, or natural transition is occurring. Turbulent separation is at 95%. Two-dimensionality is again seen to be a prominent feature for the test conditions of Figure 4.2.

Figure 4.3 contains results for $\alpha = 10^\circ$. The ASWT results in Figure 4.3a indicate a laminar separation bubble from 12-25% and turbulent separation at 85%. Although visible to the eye during experimentation and in the original photograph, unfortunately these features are not very evident in the reproduced photograph that is Figure 4.3a. In the LSLTT at the same Reynolds number, Figure 4.3b shows the laminar separation bubble is from 11-23% with turbulent separation at 86%. In Figure 4.3c for $Re = 750,000$, the laminar separation bubble has shortened and is located from 12-18% with turbulent separation at 83%. The flow patterns seen on the upper surface of the airfoil remain two-dimensional for the test conditions in these figures, especially near the heater strip.

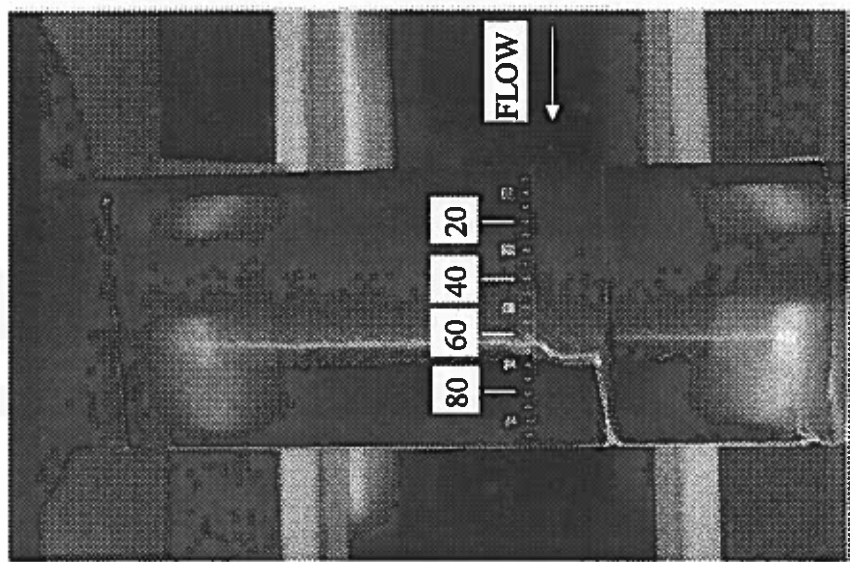


Figure 4.1c: $\alpha = 0^\circ$, $Re = 750,000$
LSLTT

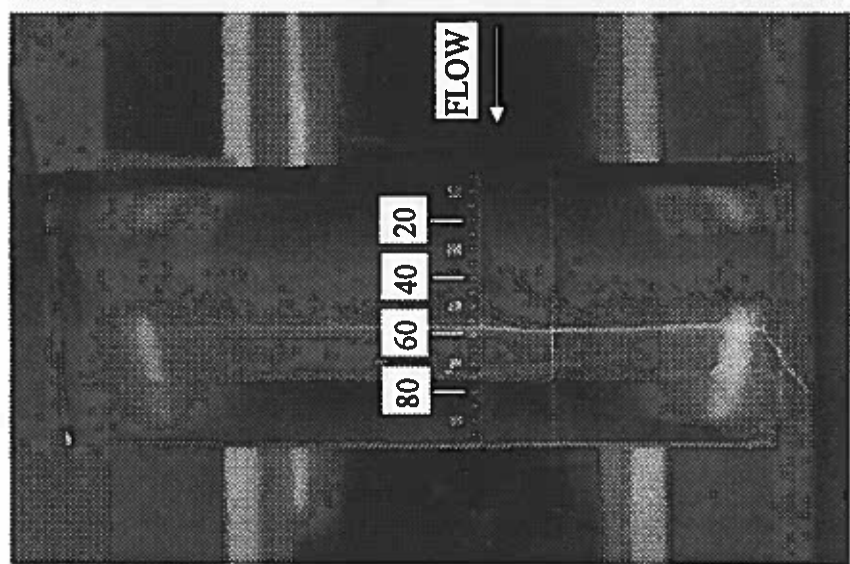


Figure 4.1b: $\alpha = 0^\circ$, $Re = 315,000$
LSLTT

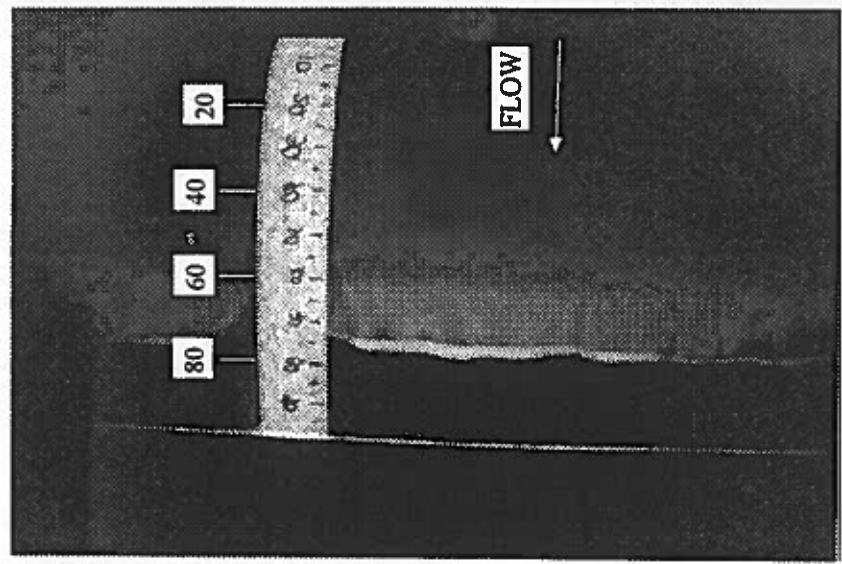


Figure 4.1a: $\alpha = 0^\circ$, $Re = 315,000$
ASWT

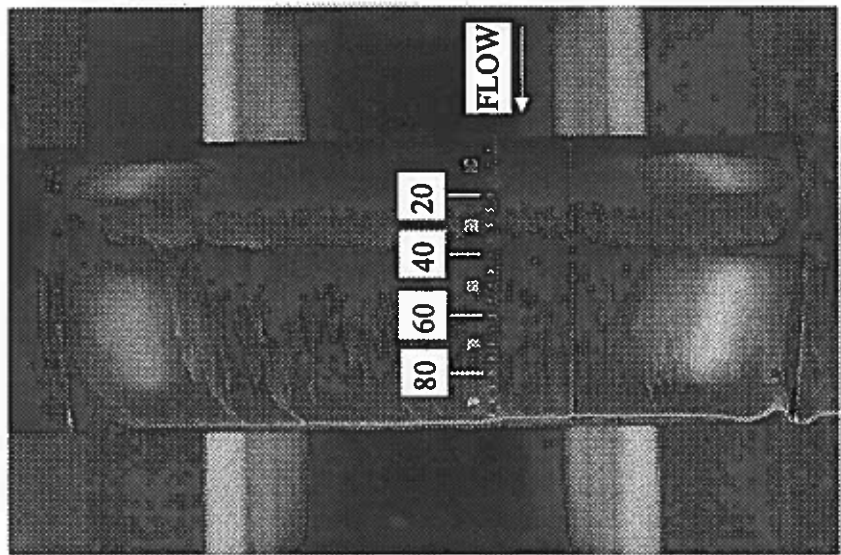


Figure 4.2c: $\alpha = 5^\circ$, $Re = 750,000$
LSLT

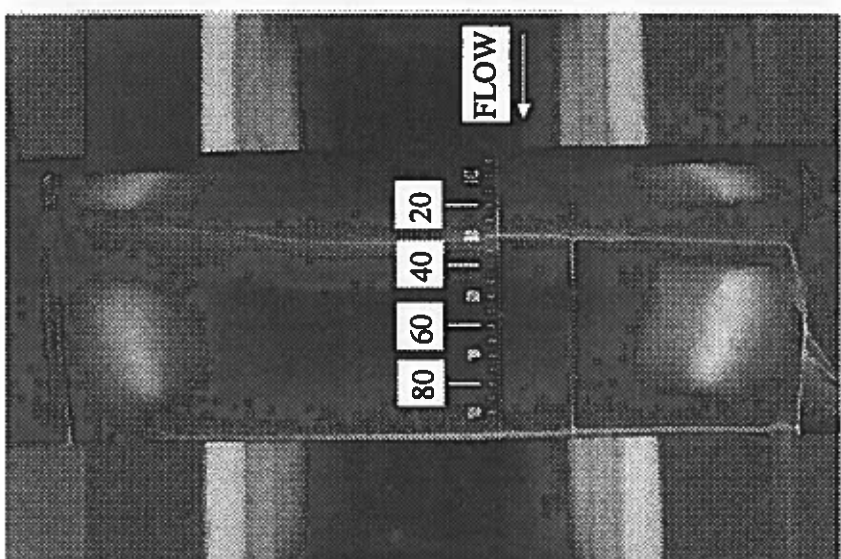


Figure 4.2b: $\alpha = 5^\circ$, $Re = 315,000$
LSLT

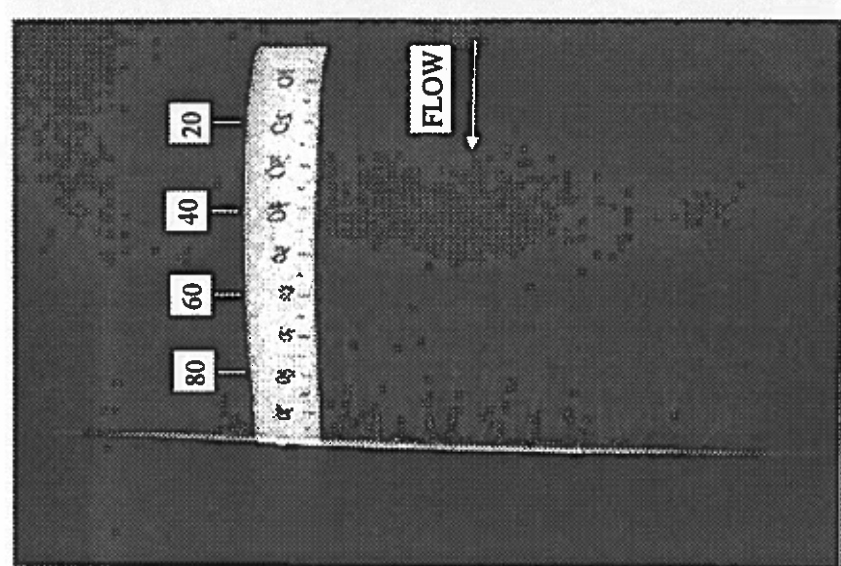


Figure 4.2a: $\alpha = 5^\circ$, $Re = 315,000$
ASWT

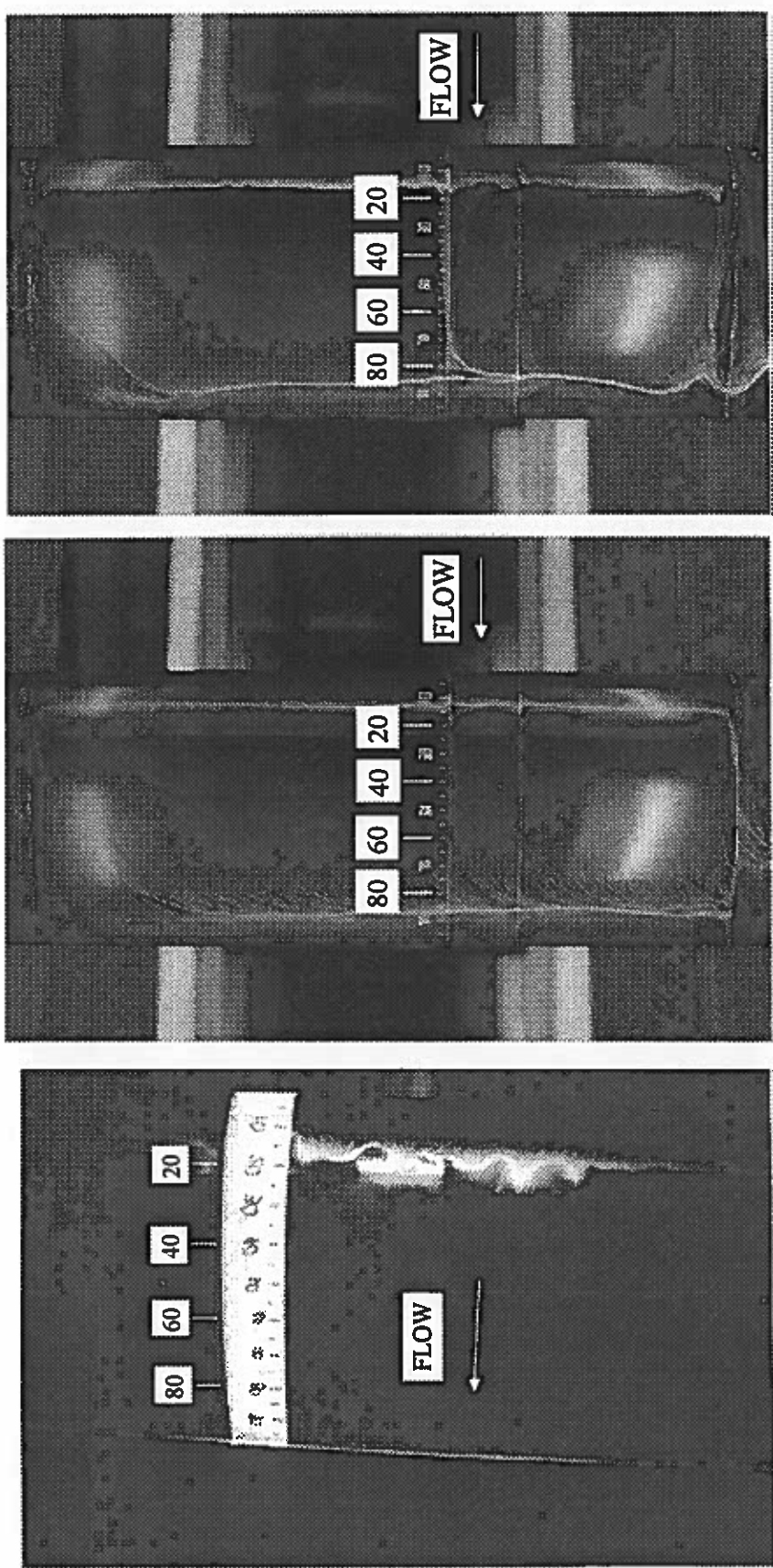


Figure 4.3a: $\alpha = 10^\circ$, Re = 315,000
ASWT

Figure 4.3b: $\alpha = 10^\circ$, Re = 315,000
LSLTT

Figure 4.3c: $\alpha = 10^\circ$, Re = 750,000
LSLTT

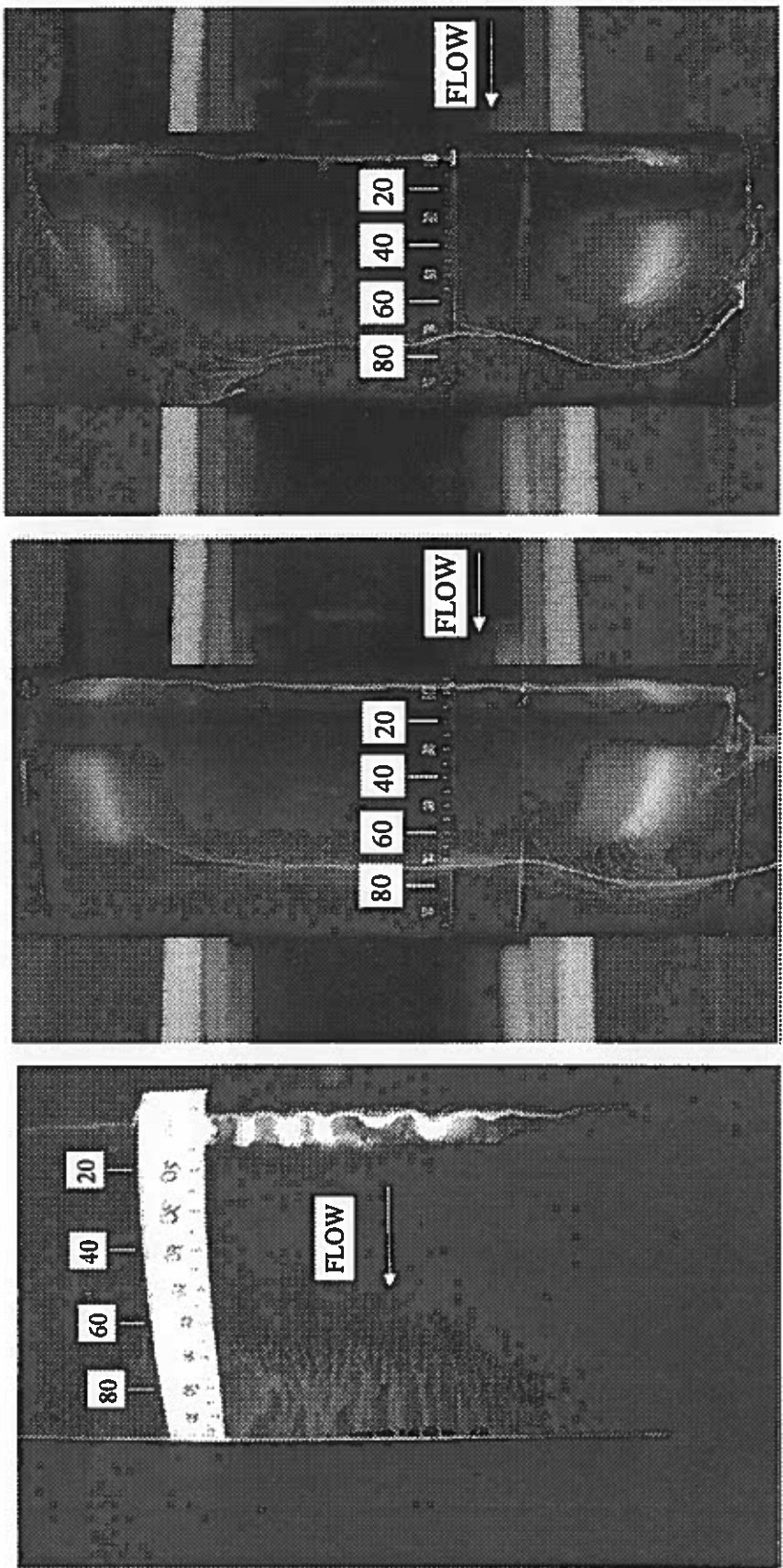


Figure 4.4a: $\alpha = 15^\circ$, $Re = 315,000$
ASWT

Figure 4.4b: $\alpha = 15^\circ$, $Re = 315,000$
LSLTT

Figure 4.4c: $\alpha = 15^\circ$, $Re = 750,000$
LSLTT

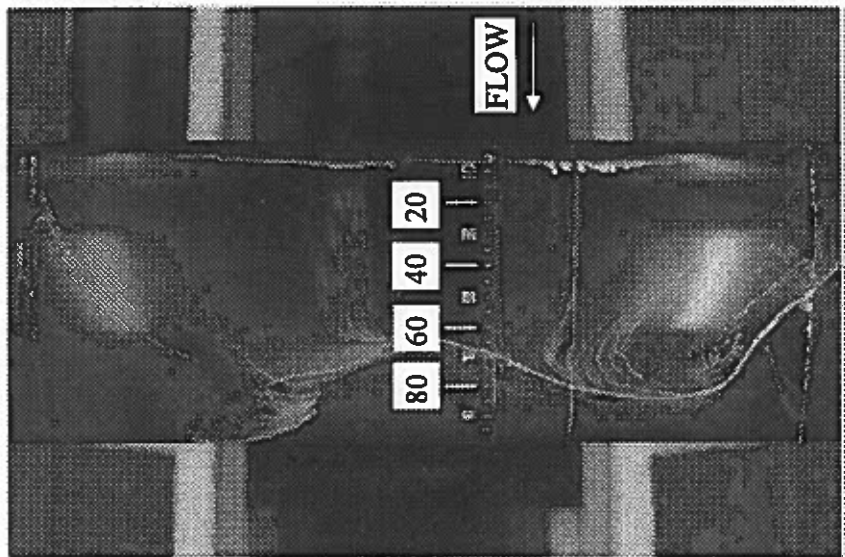


Figure 4.5c: $\alpha = 18^\circ$, $Re = 750,000$
LSLTT

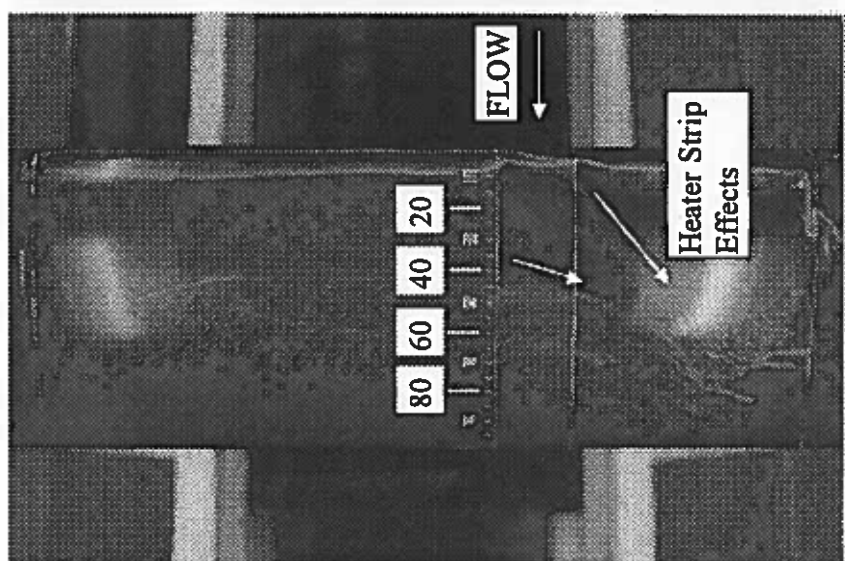


Figure 4.5b: $\alpha = 18^\circ$, $Re = 315,000$
LSLTT

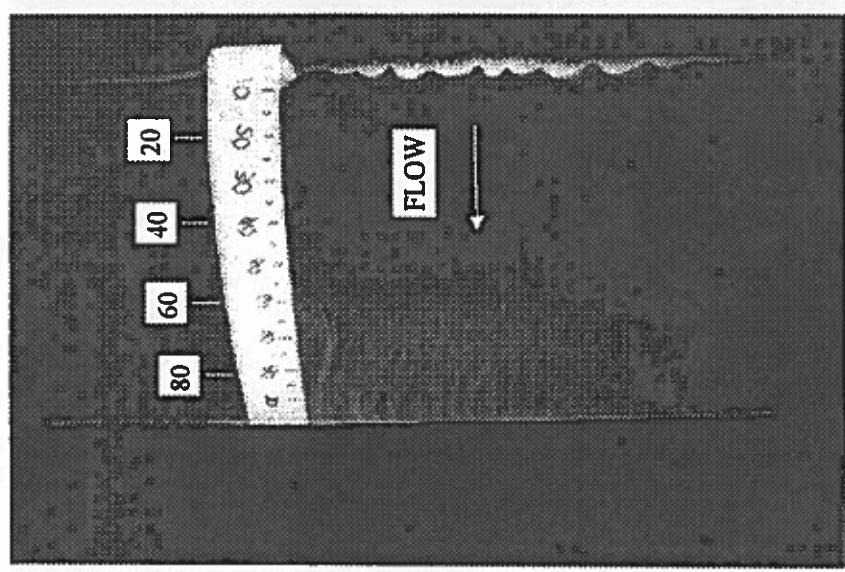


Figure 4.5a: $\alpha = 18^\circ$, $Re = 315,000$
ASWT

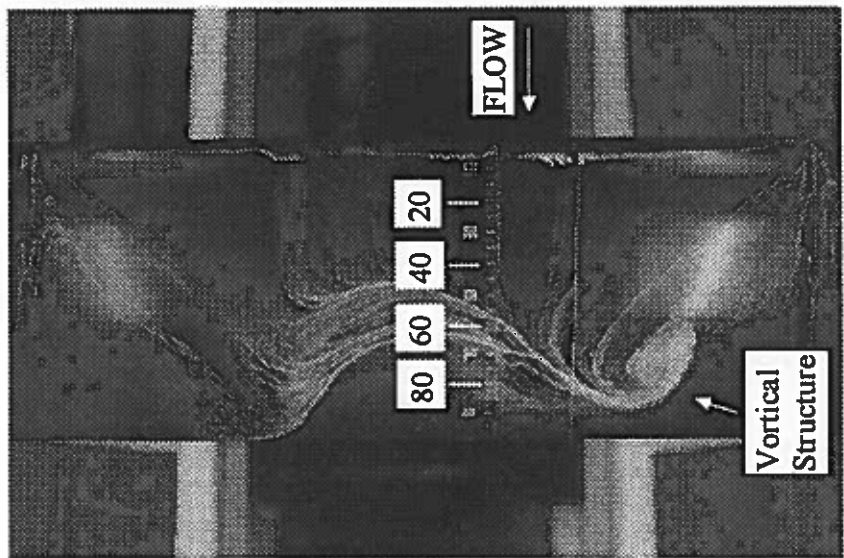


Figure 4.6c: $\alpha = 20^\circ$, $Re = 750,000$
LSLTT

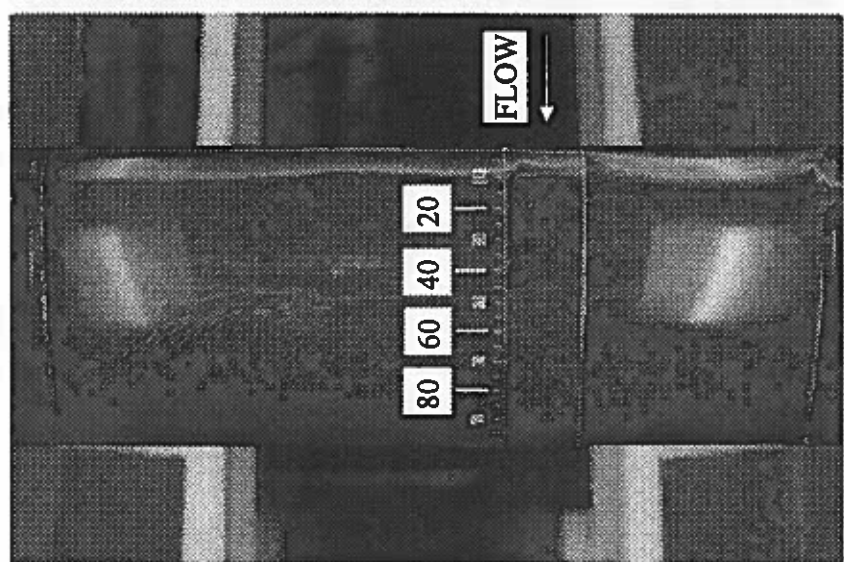


Figure 4.6b: $\alpha = 20^\circ$, $Re = 315,000$
LSLTT

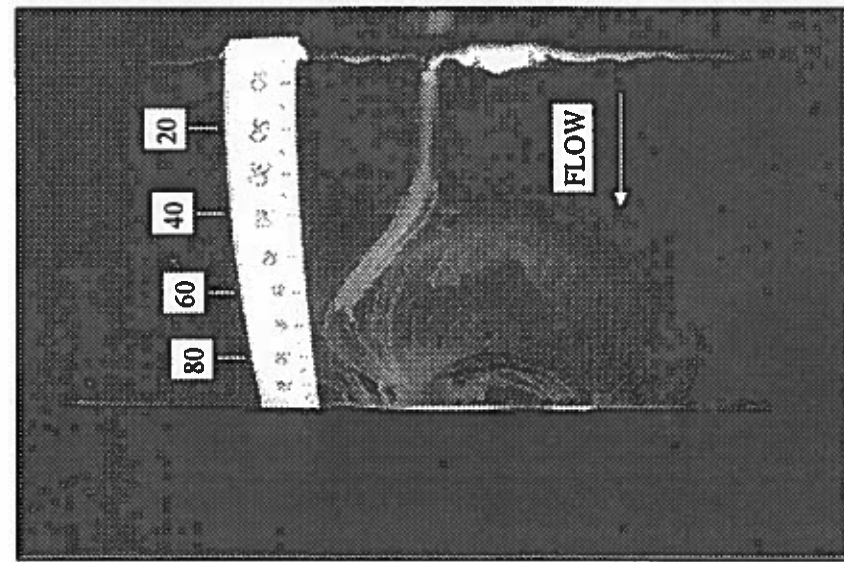


Figure 4.6a: $\alpha = 20^\circ$, $Re = 315,000$
ASWT

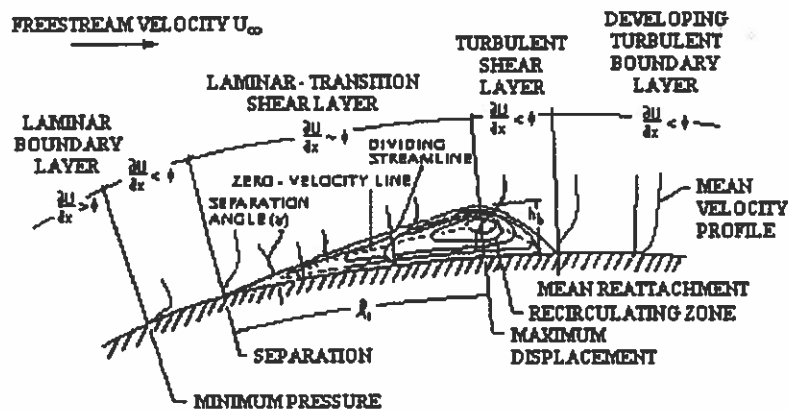
The results for $\alpha = 15^\circ$ are shown in Figure 4.4. This angle of attack is very near the angle of maximum lift coefficient for the SM701 airfoil. The ASWT results of Figure 4.4a reveal a laminar separation bubble from 6-15% and turbulent separation around 65 to 70% for a Reynolds number of 315,000. Figure 4.4b shows that at the same Reynolds number in the LSLTT, the laminar separation bubble is also from 6-15% with turbulent separation around 68 to 72%. Figure 4.4c shows that the laminar separation bubble for $Re = 750,000$ has moved to 9-11% with turbulent separation at 70%. The flow patterns on the airfoil surface are still fairly two-dimensional at the heater strip location for the test conditions of these figures. Away from the heater strip toward the tunnel walls, three dimensionality of the flow patterns is beginning to appear, especially at $Re = 750,000$. The ASWT results of Figure 4.4a also show some flow effect that is limiting the oil patterns to the midspan region of the model. This effect is not seen in the LSLTT results and might possibly be attributed to the circular cross-section of the ASWT and the corresponding larger blockage effect of the model in that smaller cross-section.

Figure 4.5 contains results for $\alpha = 18^\circ$. Figure 4.5a shows a laminar separation bubble at 5-10% with turbulent separation around 60%. From Figure 4.5b, it appears that a laminar separation bubble exists from 2-3%, followed by turbulent separation at about 10%. On the heater strip in this figure, however, the flow appears to be turbulent back to around 45% before separating. The heater strip thus appears to be affecting the surface flow patterns at this high angle of attack for $Re = 315,000$. It will be seen in the liquid crystal thermography results section that this heater strip effect for $Re = 315,000$ and $\alpha = 18^\circ$ made taking meaningful heat transfer data impossible for this experimental configuration. For $Re = 750,000$, Figure 4.5c shows the laminar separation bubble from 6-10% and turbulent separation around 70 to 80%. While the laminar separation bubble remains two-dimensional for these test conditions, the turbulent separation is extremely three-dimensional, especially far from the strip.

Figure 4.6 shows results for $\alpha = 20^\circ$. From Figure 4.6a, the laminar separation bubble in the ASWT at $Re = 315,000$ is located from 3-7%. The location of turbulent separation is more difficult to ascertain. From Figure 4.6a, it appears that turbulent separation occurs around 40% when examining the midspan region. However, after performing hot-wire

velocity profile surveys at the midspan (Section 5.2), it is known that the flow is separated by 25% chord. Thus an estimate of the turbulent separation location is around 20% chord. The turbulent separation is seen to be extremely three-dimensional. For the LSLTT at this same Reynolds number, Figure 4.6b shows what seems to be a laminar separation bubble at 2-3% followed by turbulent separation at 9%. The heater strip is again seen to be having some effect for these experimental conditions. Back to around 45%, the heater strip oil pattern is affected. For $Re = 750,000$, Figure 4.6c shows a laminar separation bubble at 5-7% with turbulent separation around 60 to 80%. Turbulent separation is extremely three-dimensional. A three-dimensional vortical structure near the airfoil surface is seen below the heater strip. Its development can be traced through Figures 4.1c to 4.6c.

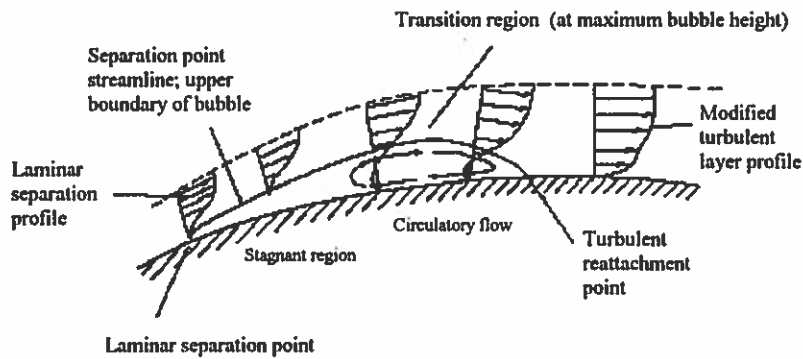
As an additional note, an apparent characteristic of laminar separation bubbles for the Reynolds numbers tested is observed. The separation bubble in Figure 4.1b seems to have two distinct regions associated with it. This is most evident from examining the upper portion of the span away from the heater strip in the figure. This trait is somewhat difficult to see in the figure reproduced for this thesis; however, the original photographs showed this characteristic very clearly. As already mentioned, the laminar separation bubble spans from 57 to 75% of the chord. However, upon closer inspection of Figure 4.1b, it seems that the oil has remained much thicker on the surface from 57 to 62%. The oil from 62 to 75% is much more scrubbed away. It appears that the aft portion of the laminar separation bubble has much more circulation than the forward portion, causing the oil to be cleaned more effectively. This division of the laminar separation bubble can also be seen in Figure 4.2b where the bubble exists between 29 and 45% chord, with the division occurring at about 35% chord. This apparent trait of the laminar separation bubble was also observed for the cases of Figures 4.3b and 4.4b and for some of the higher Reynolds numbers cases in the original flow visualization photographs; the reproduced photographs are not very clear in showing this division of the separation bubble. Gad-el-Hak and Bushnell give a sketch of a laminar separation bubble that shows what has just been mentioned: a thin forward portion of the bubble and a recirculating zone at the aft of the bubble (Gad-el-Hak and Bushnell, 1991). See Figure 4.7.



Source: Gad-el-Hak and Bushnell, 1991

Figure 4.7: Sketch of a Laminar Separation Bubble

In addition, after performing this flow visualization work, a reference was found that discussed the division of a laminar separation bubble into two regions. Figure 4.8 is taken from *Aerodynamics for Engineering Students*, 4th edition (Houghton and Carpenter, 1993). Houghton and Carpenter report, “Within the bubble, ..., two regimes exist. In the upstream region a pocket of stagnant fluid at constant pressure extends back some way and behind this a circulatory motion develops ...”



Source: Houghton and Carpenter, 1993

Figure 4.8: Two Regions of Laminar Separation Bubble

4.1.4 Conclusions from Oil Flow Visualization

Table 4.1 presents a summary of the fluorescent oil flow visualization results. Included in the table are results for all angles of attack tested for both Reynolds numbers and both facilities. As would be expected, for a fixed Reynolds number as the angle of attack is increased, the laminar separation bubble moves forward toward the leading edge and becomes smaller. In addition, for a fixed angle of attack, as the Reynolds number is increased the laminar separation bubble moves aft towards the trailing edge and becomes smaller.

It appears from the data of Table 4.1 that for a given Reynolds number and angle of attack, the laminar region of flow over the airfoil is slightly longer in the ASWT than in the LSLTT. It must be mentioned, however, that the differences were minor and probably fall within the accuracy of the oil flow visualization method. Although if this longer laminar trend in the ASWT is indeed valid, it should be mentioned that it was not expected to be the case. The streamwise turbulence intensity of the ASWT is much larger than that of the LSLTT (0.25% compared to 0.06%). Because of this higher level of turbulent fluctuations, the ASWT laminar flow region was expected to be shorter than the laminar flow region in the LSLTT. An explanation for this longer laminar flow region in the ASWT may be found when blockage effects and related three-dimensional flow patterns near the ends of the airfoil are considered. The blockage in the ASWT is greater than the blockage in the LSLTT because of the smaller test section cross-section of the ASWT. Thus, the flow could be accelerated locally near the airfoil causing longer laminar flow regions in the ASWT. Existence of three-dimensional vortical flow structures near the airfoil ends could also induce core flow variations near the midspan of the airfoil.

The region of turbulent separation is much less in the ASWT than in the LSLTT. For angles of attack of zero and five degrees, the ASWT results do not show any turbulent separation while the LSLTT results indicate turbulent separation near the trailing edge. For $\alpha = 15^\circ$ and 20° , turbulent separation occurs near midchord in the ASWT but around 10% chord in the LSLTT. These differences are dramatic. Again, blockage effects could be playing a role by constraining the flow in the ASWT and not allowing it to separate as it would in a less-restricted test environment.

Table 4.1: Fluorescent Oil Flow Visualization Summary

α (deg.)	Re	Laminar Flow		Laminar Separation Bubble		Turbulent Flow		Turbulent Separation	
		0-5%	5-7%	59-75%	57-73%	75-100%	71-93%	96-100%	99-100%
0	315,000	0-5%	0-5%	59-75%	57-73%	75-100%	71-93%	96-100%	99-100%
	750,000	0-5%	0-5%	61-63%	68-69%	68-69%	68-69%	96-100%	99-100%
5	315,000	0-3.5%	0.22%	3.5-5.0%	29.45%	50-100%	45.97%	97.100%	97.100%
	750,000	0-3.5%	0.21%	0.21%	21.34%	21.34%	34.93%	95.00%	95.00%
10	315,000	0-1.2%	0.11%	1.2-2.5%	11.23%	25-85%	21.16%	85-100%	86-100%
	750,000	0-1.2%	0-1.2%	0-1.2%	12.18%	12.18%	13.44%	83-100%	83-100%
15	315,000	0-0.6%	0-0.6%	6-15%	6-15%	15-68%	15-68%	68-100%	70-100%
	750,000	0-0.6%	0-0.6%	0-0.9%	9-11%	9-11%	11.71%	70-100%	70-100%
18	315,000	0-0.5%	0-0.5%	5-10%	2-1%	10-60%	3-10%	60-100%	10-100%
	750,000	0-0.5%	0-0.5%	0-0.5%	6-10%	6-10%	10.75%	75-100%	75-100%
20	315,000	0-0.3%	0-0.2%	3-7%	2-3%	7-20%	3-10%	20-100%	20-100%
	750,000	0-0.3%	0-0.3%	0-0.5%	5-7%	5-7%	7.76%	70-100%	70-100%

ASWT (no heater strip) =

LSLT (with heater strip) =

Finally, the turbulent separation in the ASWT can be seen to be less dramatic than the turbulent separation in the LSLTT. Compare Figure 4.4a to Figure 4.4b. The smeared oil pattern in the ASWT case of Figure 4.4a does not show a distinct turbulent separation location. The turbulent separation location in the LSLTT as seen in Figure 4.4b is more obvious. Note the accumulation of oil at a distinct separation line. Figures 4.3a and 4.3b also show this turbulent separation characteristic. These differences can be attributed to the unequal free stream turbulence intensity levels of the two wind tunnels, tunnel blockage effects, three-dimensional flow structures near the ends of the airfoil, and the horizontal ASWT versus the vertical LSLTT mounting orientation of the model.

This flow visualization study has shown the heater strip to have little effect on the surface flow patterns for most of the tests. However, at angles of attack equal to 18° and 20° at a Reynolds number of 315,000, the strip did seem to be having an undesired effect. This strip effect will be seen again in Section 4.2.16 during the heat transfer studies.

A baseline now exists for the locations of the various flow regions on the SM701 airfoil. Six angles of attack were examined at two different Reynolds numbers. Flow regions were seen to be two-dimensional except for turbulent separation at high angles of attack ($\alpha > 15^\circ$). This flow two-dimensionality is important because the heat transfer method that will now be discussed involves constructing a two-dimensional heat transfer map. Results from the heat transfer experiments will be compared to the oil flow visualization findings.

4.2 Liquid Crystal Thermography

The following sections give a detailed account of the flow visualization work based on liquid crystal thermography that was performed for the current research. An introduction to liquid crystal thermography is given, and related past work is discussed.

4.2.1 Objectives of the Heat Transfer Experimentation

Several reasons exist for conducting liquid crystal thermography experiments. The main objective is to provide a comparison to the qualitative fluorescent oil flow visualization results. By comparing the heat transfer results to the fluorescent oil flow

visualization results, the heat transfer method will be examined as a flow visualization tool. If the heat transfer method yields the same information about the flow regions on an airfoil that the fluorescent oil method provides, the heat transfer method could then be used for flow visualization in situations where fluorescent oil flow visualization is not practical. Examples of such instances include spinning turbomachinery and flight testing. It is thus hoped that the heat transfer method will confirm the existence and locations of the laminar, transitional, turbulent, and separated flow regions on the SM701 airfoil under various experimental conditions. Only when these flow regions are well defined can work begin on actively trying to control the separated zones.

A second objective of this heat transfer research is to generate experimental convective heat transfer data for an airfoil with low free stream turbulence conditions. According to Poinsatte and Van Fossen of the NASA Lewis Research Center, limited heat transfer data exist for airfoils operating in a low free stream turbulence environment (Poinsatte and Van Fossen, 1990). Also, the data generated during this investigation can serve as a benchmark solution for the development of better viscous flow/heat transfer codes. Development of heat transfer prediction tools capable of handling large transitional zones currently requires high-quality high-resolution heat transfer measurements.

4.2.2 Liquid Crystal History and Properties

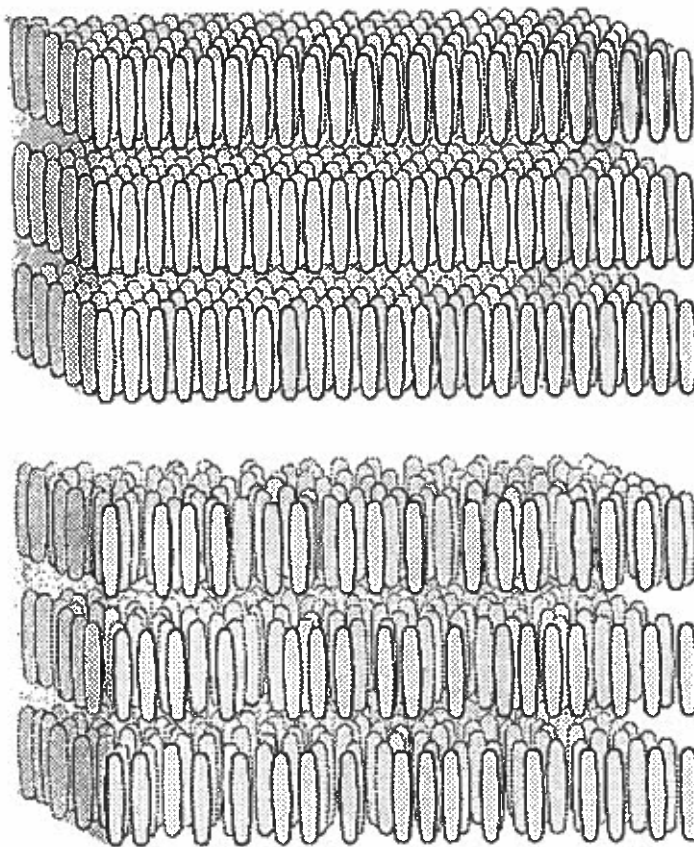
The substance today known as liquid crystals was first discovered in 1888 by Austrian botanist Friedrich Reinitzer who observed that the organic compound cholesteryl benzoate appeared to have two distinct melting points (Ferguson, 1964). The first melting point occurred when the solid phase turned to a cloudy liquid phase. This has since been called the “mesophase.” The second melting point occurred when the cloudy liquid turned to a clear liquid.

A short time after Reinitzer noticed this property of cholesteryl benzoate, German physicist O. Lehmann termed the distinct compounds with two melting points as “liquid crystals” since the intermediate phase contained areas that appeared to have crystal-like molecular structures. This name makes sense since the liquid crystal phase exhibits the

fluid nature of a liquid while at the same time maintaining a degree of anisotropic and ordered structure like a crystalline solid (Fergason, 1964).

Liquid crystals are thus organic compounds that exhibit a unique molecular structure. Slight differences in molecular structure divide liquid crystals into three categories: smectic, nematic, and cholesteric. These classes were proposed by G. Friedel in 1922 and are described by Fergason (Fergason, 1964).

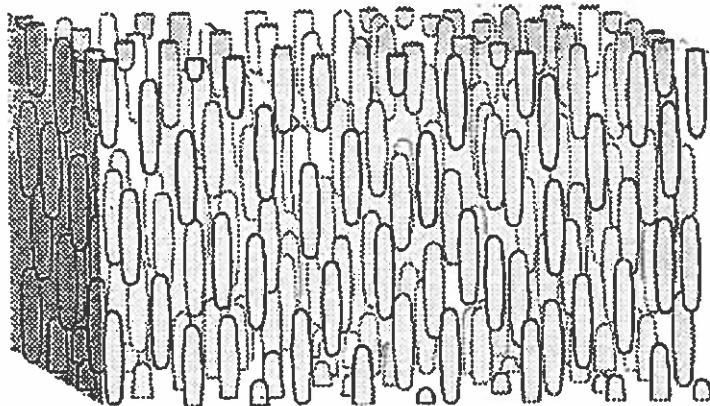
Smectic liquid crystals get their name from the Greek word for soap. They exhibit cigar-shaped molecules arranged side-by-side in layers which are one molecule thick. The long axes of the molecules are parallel to each other and are perpendicular to the plane of the layer. See Figure 4.9. The molecules may either be arranged in rows (top of Figure 4.9) or randomly (bottom of Figure 4.9) in the layers. An example of a smectic liquid crystal substance is a soap bubble.



Source: Fergason, 1964

Figure 4.9: Smectic Liquid Crystal Molecular Structure

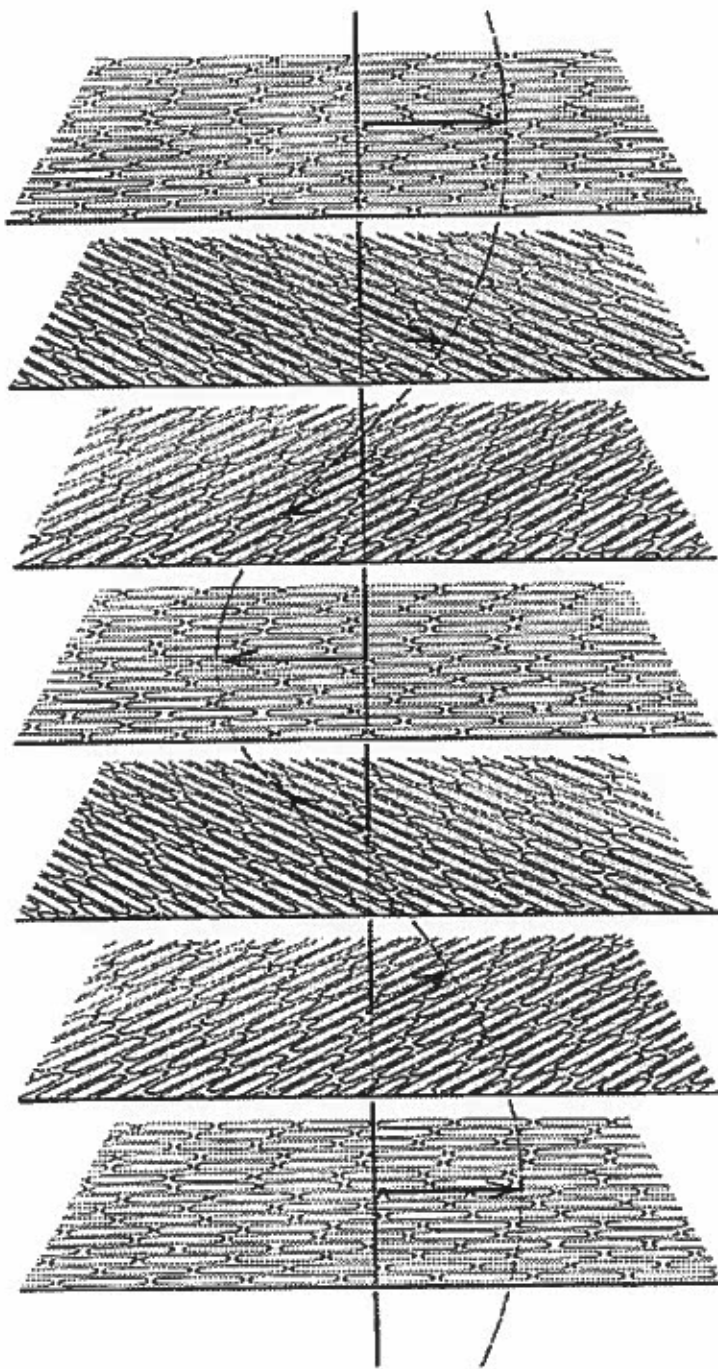
The name for nematic liquid crystals comes from the Greek word for thread. This name is appropriate because nematic liquid crystals contain microscopic thread-like structures floating freely or attached to the surface of the container. The molecules are arranged with long axes parallel, but no layers exist. The molecular structure of nematic liquid crystals is not as ordered as that of smectic liquid crystals. Figure 4.10 shows the nematic liquid crystal molecular structure.



Source: Fergason, 1964

Figure 4.10: Nematic Liquid Crystal Molecular Structure

The third type of liquid crystals is termed “cholesteric.” This name stems from the fact that their molecular structure is characteristic of a large number of compounds that contain cholesterol. The molecules are arranged in layers with the long axes of the molecules parallel to the plane of the layers. In each layer the long axes of the molecules are slightly rotated with respect to adjacent layers thereby creating a helical pattern. This pattern can be seen in Figure 4.11.



Source: Fergason, 1964

Figure 4.11: Cholesteric Liquid Crystal Molecular Structure

An interesting property of smectic and nematic liquid crystals is that when applied in a thin film and viewed through a dielectric material such as glass, the liquid crystals appear

opaque when subjected to an electric field. When the electric field is removed, the liquid crystals appear transparent (Cooper, Field, Meyer, 1975).

The distance between aligned molecular layers of liquid crystals affects the color that the liquid crystal projects. For pure liquid crystals, the distance between aligned molecular layers can be altered by temperature and shear stress as well as chemical vapors, ultraviolet light, and magnetic and electric fields. An example of electric fields altering smectic and nematic liquid crystals was described in the previous paragraph. These many factors affecting the pure liquid crystal molecular structure made scientific experimentation with pure liquid crystals difficult. For instance, a color change in the liquid crystals could not be directly related to any one parameter. Temperature and shear stress effects as well as contributions by ultraviolet light, chemical vapors, and electric and magnetic fields had to be examined. Separating the effect of merely temperature on the liquid crystal molecular structure and thus its projected color was extremely difficult.

Advanced fabrication techniques have solved this dilemma. The process of microencapsulation allows gelatin in a polyvinyl alcohol binder to form spheres 10 to 40 microns in diameter around very small amounts of the liquid crystal mixture. The liquid crystals are then referred to, appropriately enough, as encapsulated liquid crystals and are greatly shielded from the effects of shear stress, chemical vapors, and ultraviolet light. Microencapsulation thus creates a substance that is affected primarily by temperature, a quantity to which the projected color of the liquid crystals can be directly related.

Encapsulated liquid crystals are available in two forms. They can be obtained on a precoated, blackened substrate of paper or as a water-based slurry. The slurry form allows more freedom in that it may be airbrushed onto any surface regardless of the geometry.

As a result of the microencapsulation process, liquid crystals are very useful in the determination of surface temperature. Liquid crystals provide a way to obtain local temperature measurements at a high resolution over a model surface without obstructing the flow or local heat flux. This is in contrast to thermocouples which are point sensors and may protrude into the flow. Liquid crystals have a color response time of no more

than a few milliseconds (Ireland and Jones, 1987) which is of the same order as a typical thermocouple.

As already mentioned, liquid crystals scatter light at different wavelengths depending on the sensed temperature. This property is caused by the temperature affecting the distance between molecular layers of the liquid crystal. This color/temperature relationship can be calibrated to enable precise surface temperature distributions to be obtained by using liquid crystals. The distributions are continuous, unlike the results of thermocouple arrays, and also qualitatively reveal the thermal patterns and isotherm lines on a given test surface.

Another attractive feature of liquid crystals is their ability to respond to slight temperature variations. For narrow band crystals these variations may be as small as 0.15 °C. Liquid crystals also have good resolution on the order of 0.1 °C. Liquid crystal substrates can be mixed to achieve event temperatures from -40 to 285 °C and bandwidths from 0.1 to 50 °C. (The event temperature is the temperature at which the liquid crystal mixture first begins to display a reddish color. The bandwidth is the temperature range over which all the colors of the visible spectrum are displayed by the liquid crystals. For instance, a liquid crystal mixture with an event temperature of 30 °C and a bandwidth of one °C will display color from 30 °C to 31 °C).

Reversibility is also an important property of liquid crystals. As the liquid crystals are heated through their color range, they show a continuously changing color spectrum from colorless to red, yellow, green, blue, violet, and again colorless. As the liquid crystals cool, the reverse color order is seen. Thus the surface on which the liquid crystals are sprayed may be reoriented or flow conditions in a test may be changed without having to restart the experiment. Colors, regardless of when or in what order they appear, will always correlate to the same precise temperature values.

Practicality also makes liquid crystals a valuable temperature measuring tool. Tests involving liquid crystals can be conducted at room temperature conditions. This provides a great reduction in cost from testing turbine blades, for example, at their normally high operating temperatures. Liquid crystals are also much cheaper to use than infrared thermography cameras which also yield continuous temperature distributions. This is

because infrared image sensors must be cryogenically cooled during operation, and the test section viewing window must be made of a special material to allow infrared radiation transmission.

Finally, it must be emphasized that liquid crystals have two primary uses. First, they may be used as a flow visualization tool to qualitatively see the thermal patterns (isotherms) on a surface. Laminar and turbulent flow regions, for instance, could be distinguished due to their different heating rates. Liquid crystals may also be used to measure continuous surface temperature distributions, thus allowing calculation of continuous convective heat transfer distributions. This second use of liquid crystals which is quantitative and reasonably accurate is extremely useful due to the possibility of validating analytical and computational viscous flow/heat transfer models and new turbulence models. It is the job of the experimenter to decide how to best utilize liquid crystals for his or her work.

4.2.3 Types of Heat Transfer Experiments

Liquid crystals may be used in convective heat transfer research through the use of two different techniques. These methods are the transient technique and the steady state technique. Both techniques are now discussed.

4.2.3.1 Transient Technique

To use this technique, the test model should be constructed from an insulating material such as Plexiglas. A step change in the convective heating must then be created, either by impulsively starting the flow over the model or by rapidly injecting a (e.g. hot) model into a (e.g. relatively cold) flow. The surface temperature distribution is monitored using a coating of liquid crystals, the colors of which are recorded with a video camera. The model's wall is assumed to be a semi-infinite medium, meaning that the thermal energy during the transient test does not penetrate far into the wall such that it reaches the other side of the wall. Therefore, the heat conduction may be assumed one-dimensional.

The convective heat transfer coefficient, h , may then be deduced from this time history of temperature by solving the 1D transient heat conduction equation analytically. The 1D transient heat conduction equation is as follows:

$$\frac{\partial^2 T}{\partial y^2} = \frac{\rho_{wall} c_{wall}}{k_{wall}} \frac{\partial T}{\partial \alpha} \quad (4.1)$$

An analytic solution to equation 4.1 results (equation 4.2) if the thermal properties and gas temperature are assumed to be constant. Refer to Jones and Hippensteele (1988), Camci, Kim, and Hippensteele (1992), Camci, Hippensteele, and Poinsatte (1993), and Kim (1991) for detailed discussion of the analytical solution process. Carslaw and Jaeger (1959) also discuss analytically solving equation 4.1.

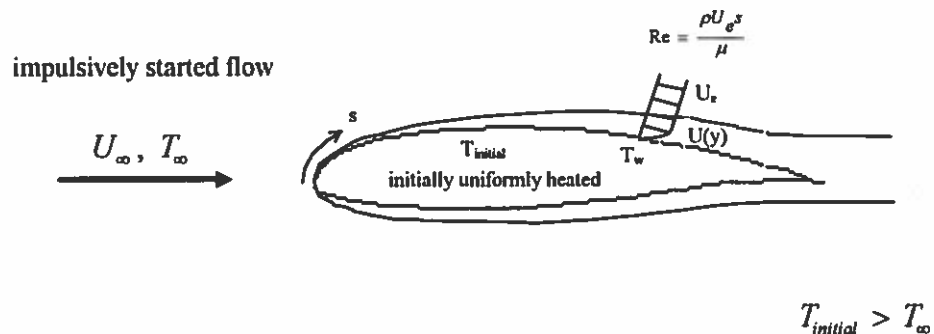
$$\frac{T_{wall} - T_{initial}}{T_{\infty} - T_{initial}} = 1 - e^{\gamma^2} erfc(\gamma) \quad (4.2)$$

where	γ	=	$\frac{h\sqrt{t}}{\sqrt{\rho_{wall} c_{wall} k_{wall}}}$
	T_{wall}	=	surface wall temperature of model at time t
	$T_{initial}$	=	initial wall temperature of model (constant)
	T_{∞}	=	gas temperature (constant)
	ρ_{wall}	=	density of wall of model
	c_{wall}	=	specific heat of wall of model
	k_{wall}	=	thermal conductivity of wall of model

Thus by knowing the model wall temperature and the corresponding time, the convective heat transfer coefficient, h , may be calculated for a substrate with known $\sqrt{\rho_{wall} c_{wall} k_{wall}}$. Figure 4.12 should help to further clarify the transient heat transfer method.

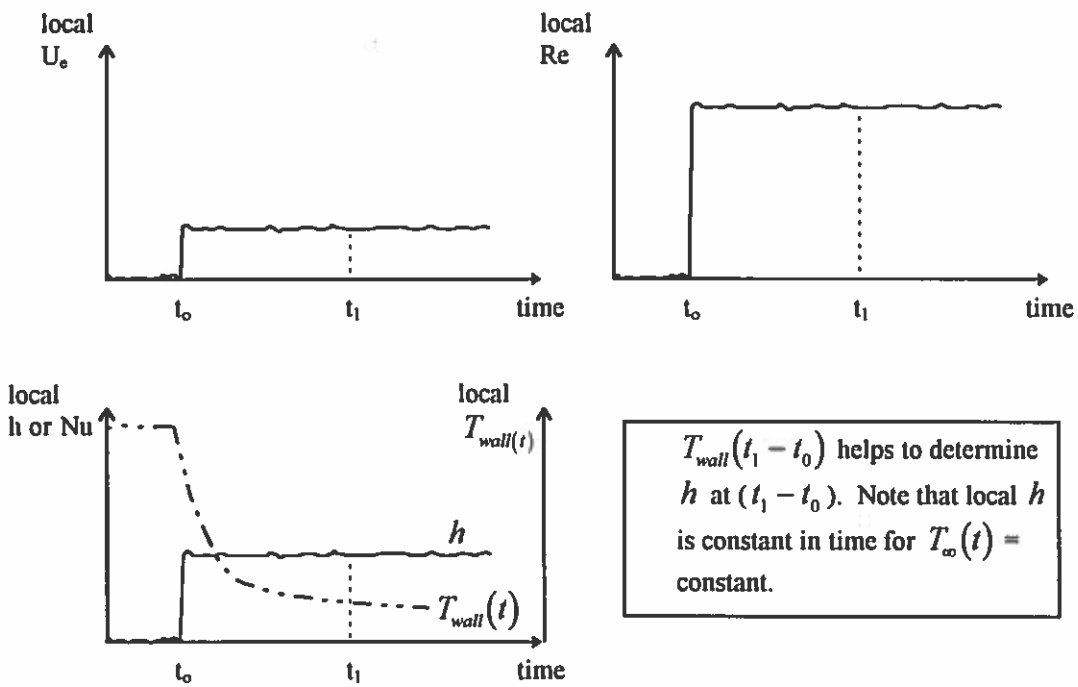
h is a measure of the ability of the viscous layer to transfer heat by forced convection

In incompressible flow **h** and skin friction coefficient C_f are analogous.



$$T_{initial} > T_\infty$$

As soon as the main stream flow starts, the model begins to cool.



$T_{wall}(t_1 - t_0)$ helps to determine h at $(t_1 - t_0)$. Note that local h is constant in time for $T_\infty(t) = \text{constant}$.

Figure 4.12: Clarification of Transient Heat Transfer Method

4.2.3.2 Steady State Technique

This method of heat transfer research requires the use of a heater element attached to the surface of the test model. Refer to Wiedner (1994) and Hippensteele and Russell (1988) for information on this method. The basic assumption is that the metallic heater surface (such as Inconel 600) does not change its electrical resistance due to local temperature variations in the experimental temperature range. The attachment of the heater element is usually performed by using a double-sided tape. The model with heater strip is then spray painted black to provide the best color contrast for the liquid crystals. After the black paint is applied, a very thin coating of liquid crystals is sprayed onto the heater strip. A typical composite heater element is shown in Figure 4.13.

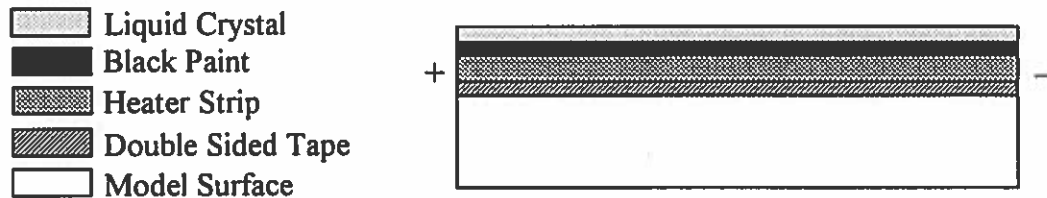


Figure 4.13: The Composite Heater Element

The model is then exposed to the flow, and a DC voltage is applied across the heater strip. The DC voltage is increased until color bands appear. At this point steady state conditions are allowed to be reached, and then an image of the heater strip is recorded with an image processor. The colors on the heater strip directly yield temperature information. The power to the heater strip is then increased causing a shifting of the color bands. Again steady state is allowed to be realized, and an image is recorded. This process is repeated until the color bands have covered the entire heater strip surface.

Knowing the temperature information at the various power settings, the convective heat transfer coefficient is calculated via Newton's Law of Cooling.

$$h = \frac{q''_{\text{TOTAL GENERATED}} - q''_{\text{COND}} - q''_{\text{RAD}}}{T_{\text{wall}} - T_{\infty}} \quad (4.3)$$

For simple Joulean heating,

$$q''_{\text{TOTAL GENERATED}} = \frac{V_{\text{heater strip}}^2}{R_{\text{heater strip}} A_{\text{heater strip}}} \quad (4.4)$$

where

$V_{\text{heater strip}}$ = voltage across heater element

$R_{\text{heater strip}}$ = resistance of heater element

$A_{\text{heater strip}}$ = area of heater element

One should notice that equation 4.4 is valid only for rectangular heater geometries with any aspect ratio. For heater surfaces having arbitrarily specified boundaries, a more elaborate technique is required for the accurate calculation of $q''_{\text{TOTAL GENERATED}}$. Details of such a technique are given in Wiedner and Camci (1996).

The conduction loss term is approximated as one-dimensional.

$$q''_{\text{COND}} = k_{\text{wall}} \frac{T_{\text{wall}} - T_2}{t_{\text{wall}}} \quad (4.5)$$

where

T_{wall} = surface wall temperature of model

T_2 = temperature on side of wall opposite to where T_{wall} is measured

t_{wall} = model wall thickness

The radiation loss term, which is relatively small when T_{wall} and T_{∞} are close in magnitude, is estimated by using a black body assumption.

$$q''_{\text{RAD}} = \sigma \epsilon_{\text{wall}} T_{\text{wall}}^4 - \sigma \epsilon_{\infty} T_{\infty}^4 \quad (4.6)$$

where

σ	=	Stefan-Boltzmann constant
ε_{wall}	=	model wall emissivity
ε_∞	=	wind tunnel wall emissivity
T_∞	=	free stream static temperature

This composite heater strip method is recognized by Hippensteele and Russell to have simplicity, to be readily applied using commercially available products, and to provide continuous and high-resolution heat transfer maps (Hippensteele and Russell, 1988). A disadvantage of this steady state technique is that the model shape must be conducive to allowing the attachment of the heater element. For the transient technique, the model geometry may be very complex since the liquid crystals are merely sprayed onto the model surface. Care must also be taken with the steady state technique to ensure the heater strip has a minimal effect on the model geometry and thus on the flow. The heater strip composite construction should be as thin as possible, and the edges of the strip should smoothly blend in with the model surface, if possible.

These two methods are used to obtain high-resolution convective heat transfer data. The next section will give some insight as to why it is important to have methods to accurately calculate convective heat transfer coefficient values.

4.2.4 Importance of the Convective Heat Transfer Coefficient, h

This section presents several examples in which accurate convective heat transfer information is necessary. These are but a few of the many areas in engineering in which heat transfer is important.

Relating back to one of the objectives of the current study, accurate h distributions are needed to improve viscous flow/heat transfer tools that use the Navier-Stokes equations. The h distributions can be used as benchmark data against which to compare the computational methods. These prediction tools must be able to handle many complicated flow situations. See Figure 4.14.

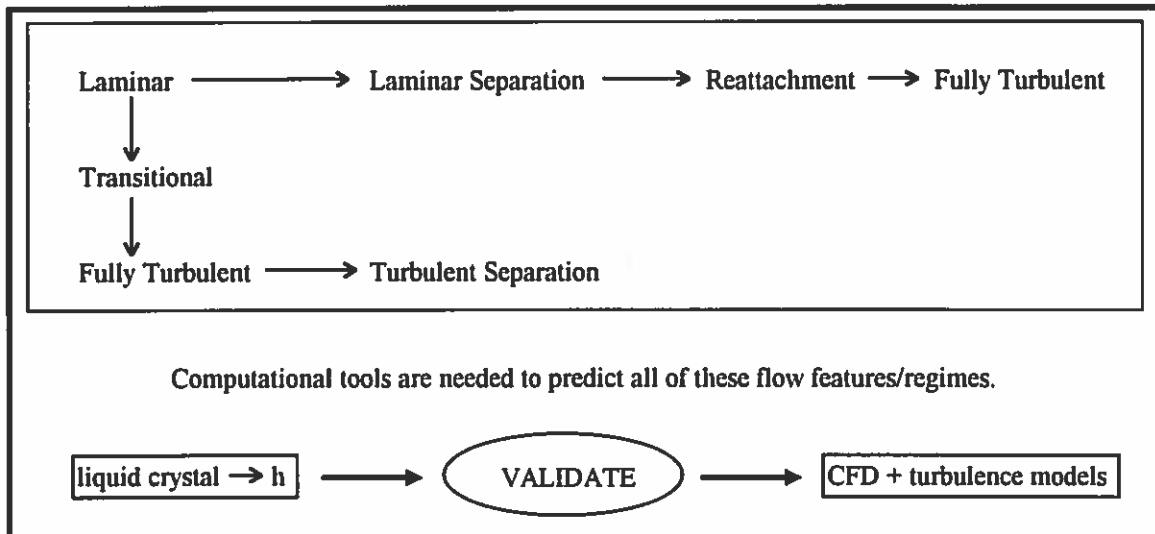


Figure 4.14: Various Flow Regimes in Which h Can Validate Codes

As a use in aircraft aerodynamics, Klein points out that convective heat transfer rate may be used to calculate local skin friction (Klein, 1968). Through integration of the skin friction over the aircraft surface, an accurate value of total drag may be obtained. Convective heat transfer information is also very important in specifying structural materials for high speed aircraft.

In the field of turbomachinery there is a constant desire to increase engine efficiencies. To achieve this goal, gas turbine inlet temperatures and pressures must be increased. Thus the heat loads to the turbine blades must necessarily increase. If this is to become a reality, more effective cooling needs to be developed for turbine blades to provide acceptable metal temperatures and blade life. To precisely predict blade temperatures, accurate convective heat transfer coefficients must first be obtained (Hippensteele, Russell, and Torres, 1985).

Another important area of engineering involving heat transfer is the field of de-icing research. Ice formations on a wing add weight, increase drag, reduce lift, and can affect the normal operation of control surfaces. This accumulation of ice can be fought in two ways. First, the ice can be broken, and aerodynamic forces will cause it to shed. This method of dealing with icing can present problems such as the shedding ice striking other parts of the aircraft or populated regions on the ground. The second method to fight icing

on wings is to stop it before it has a chance to form. This may be accomplished by heating the wing surface at locations where the ice is going to form. In order to predict where ice will first begin to accumulate for given environmental and flow conditions, it is very important to have accurate knowledge of the heat transfer on the wing's surface.

Specifically, an energy balance shows that convective and evaporative cooling are the dominant heat loss terms as an airplane flies through cool air containing supercooled liquid water droplets. If these heat loss mechanisms overcome the warming due to kinetic and viscous effects, ice will form on the aircraft. Thus it is seen why convective heat transfer information is critical for accurately predicting icing (Poinsatte and Van Fossen, 1990).

The following section gives many examples of past instances where liquid crystals were employed to obtain experimental convective heat transfer data. Both transient and steady state experiments are discussed.

4.2.5 Past Heat Transfer Work Using Liquid Crystals

The first person to use liquid crystals as a tool for aerodynamic research was Enrique J. Klein in 1968. He used pure (unencapsulated) liquid crystals to study transition on a wind tunnel model of a supersonic airplane of symmetric cross section at a zero degree angle of attack. The turbulent boundary layer existing on the model caused the liquid crystals to display colors different from the colors associated with regions of laminar flow due to variations in surface temperature caused by the differing boundary layer flow characteristics. Klein's work was qualitative in nature only since the effects of temperature and shear stress are combined for pure liquid crystals. Klein noted that, "It is therefore clear that liquid crystals must be shielded from mechanical shear to obtain good quantitative results" (Klein, 1968). This statement was realized when microencapsulation became possible.

Quantitative convective heat transfer data were first obtained five years after Klein's work in 1973 by Vennemann and Bütfisch (Simonich and Moffat, 1984). They coated models with liquid crystals and aerodynamically heated them in a high-speed flow. A transient technique was used to calculate the convective heat transfer coefficient.

The first steady state experiments using liquid crystals were performed by den Ouden and Hoogendoorn a year later in 1974. They used a constant temperature heat source and measured stagnation heat transfer from a jet impinging on a flat plate (den Ouden and Hoogendoorn, 1974). Hippensteele, Russell, and Torres also performed steady state heat transfer experiments. This group used the steady state method and liquid crystals to calculate convective heat transfer coefficients on the midchord of a turbine blade airfoil in a static cascade. They achieved a maximum uncertainty in h of 6.2% (Hippensteele, Russell, and Torres, 1985).

Blade cooling passages have also been studied with liquid crystal research. Ireland and Jones used a transient technique to calculate convective heat transfer coefficient values. Specifically, they examined the effect of rib heat transfer promoters on the complicated flow in a representative blade trailing edge passage (Ireland and Jones, 1985).

An interesting study was performed by Jones and Hippensteele in 1988. They performed both transient and steady state experiments using liquid crystals to calculate convective heat transfer coefficients on a model duct wall. Results from both methods were consistent. For the transient tests, they combined two different liquid crystal mixtures with differing event temperatures into a single liquid crystal mixture. This is possible since the liquid crystals are encapsulated, and each different liquid crystal mixture in the combination will act as though independent. Jones and Hippensteele used this combination of two different liquid crystal mixtures to eliminate the problem of determining an initial surface temperature at each point on the model. They call this technique the "double crystal method" (Jones and Hippensteele, 1988).

Mee et al. used liquid crystal thermography to study the location of transition in a flat plate boundary layer (Mee et al., 1991). The destabilizing effect of introducing heat into a gas boundary layer was examined. This destabilizing effect causes a measurement of the transition region location that is actually nearer the leading edge than the actual transition region location that occurs when no heat is applied.

Camci and Glezer performed a liquid crystal heat transfer study on a rotating disk (Camci and Glezer, 1997). Their work showed that encapsulated liquid crystals do not respond to wall shear stress.

Michael Anbar discussed the value of thermography to the medical community in his paper entitled "Clinical Applications of Computerized Thermography" (Anbar, 1988). Because of the interesting nature of this topic, it is briefly discussed here. Clinical thermology is the science of studying local changes in skin temperature that are a function of subcutaneous blood supply. Among the factors affecting subcutaneous blood supply are the patency of the arteries bringing blood into the region, the rate of blood flow, and the vasodilation or constriction of the subcutaneous arterioles. Thermography using liquid crystals may reveal abnormalities in local heating of the skin. Anbar mentions the following as possible medical uses of thermography: checking for asymmetric temperature distributions caused by spinal cord injuries, aiding in the diagnosis of migraine headaches, helping to assess the severity of inflammation of joints, and revealing areas of poor circulation.

Another qualitative use of liquid crystals is in the area of non-destructive testing (Parsley, 1991). Structural imperfections may be located by spraying liquid crystals onto a surface and applying heat. Imperfections will conduct heat at a different rate than their surroundings. Thus imperfections will be a different temperature than the surrounding material, and the liquid crystals will show a different color.

In addition to non-destructive testing, liquid crystals may also be used as indicators for chemical leaks or hazards. This is possible since liquid crystals, especially in the pure state, will react to certain chemical vapors by changing colors. Liquid crystals can be mixed so that a chemical hazard will change an indicator from green to red, for instance.

These past uses of liquid crystals in the engineering community show the types of experiments that have been performed in which convective heat transfer information was desired. The next section begins the discussion of the experimental determination of convective heat transfer coefficients on the SM701 airfoil. The steady state technique was chosen for this study.

4.2.6 Experimental Determination of Thermal Conductivity of the Wing Material

To estimate thermal conduction losses while using the steady state technique, the thermal conductivity, k , of the material through which the losses are occurring must be

known. For this experiment, the material in question is the composite wing material. Since this material is composed of a layer of Owens Corning extruded polystyrene Foamular 150 sandwiched with layers of E-glass in an epoxy matrix, an estimate of the thermal conductivity could have been made based on the properties of those elements. However, it was felt that to minimize experimental error, the value of k should be experimentally determined.

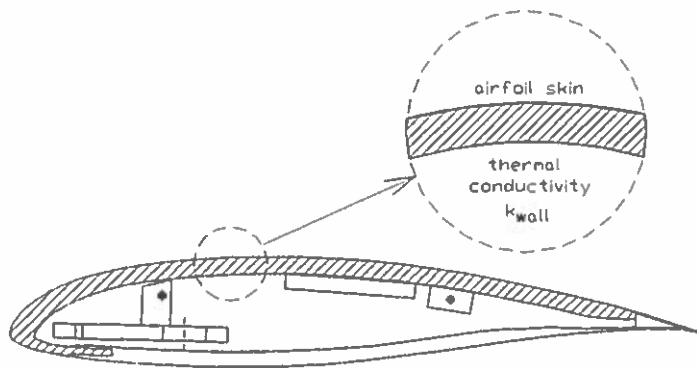


Figure 4.15: Sketch of Wing Material Being Tested

To accomplish this goal, a scrap piece of the wing material was cut into a rectangular section 1 x 3 inches. Figure 4.15 gives insight into the material being tested. A piece of Inconel 600 foil was taped to one surface of the test piece using double-sided tape, and copper bus bars were attached. The double-sided tape was 0.005 inches thick. Inconel foil was used for the heater strip because its resistance does not change in the experimental temperature range in which it was used. Figure 4.16a shows the test piece. A Keithley 580 micro-ohmmeter was used to measure the resistance of the heater strip to an accuracy of four decimal places. The wire leads marked "A" were used to apply a voltage across the heater strip using a Hewlett Packard 6261B DC power supply. The leads marked "B" were connected to a Fluke 77 multimeter so that the voltage across the heater strip could be measured. The wire coming from the center of the test piece is for a K-type cement-on thermocouple which was placed immediately below the Inconel foil. A second thermocouple was attached to the surface opposite the heater strip. These two

thermocouples allowed the temperature difference through the wing material test piece to be measured.

Figure 4.16b shows a side view of the test piece. Using micrometers, the average thickness of the test piece was measured to be 0.362 inches (0.919 cm) based on ten separate locations. Measurements were performed before attachment of the heater strip.

A piece of space shuttle tile manufactured by Rockwell International Corporation was used to insulate the test piece. Insulation was important to minimize radiation and convection losses during the tests. Figures 4.16c and 4.16d show the insulating material and how the test piece was situated, respectively. In Figure 4.16e more insulating material was added to form sides of what would be an enclosing insulating box. The lid of the box can also be seen in the figure.

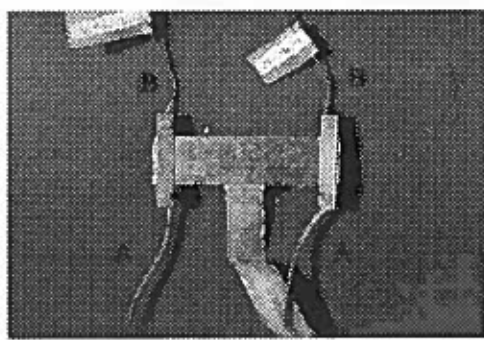


Figure 4.16a: k Test Piece

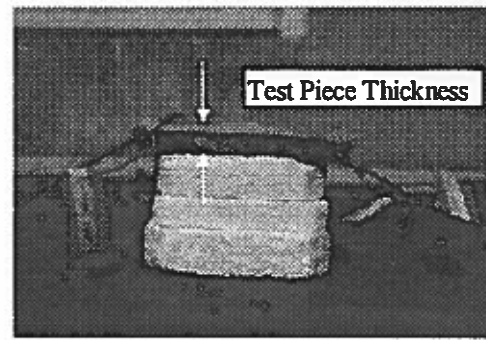


Figure 4.16b: Side View of k Test Piece

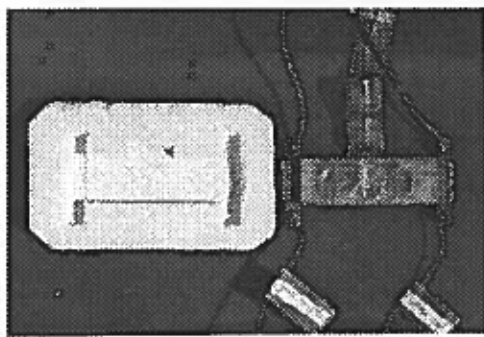


Figure 4.16c: Insulation Material

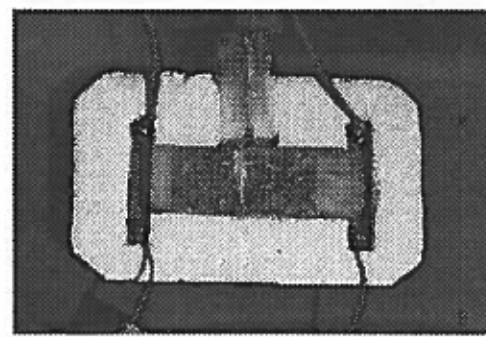


Figure 4.16d: Insulating the Test Piece

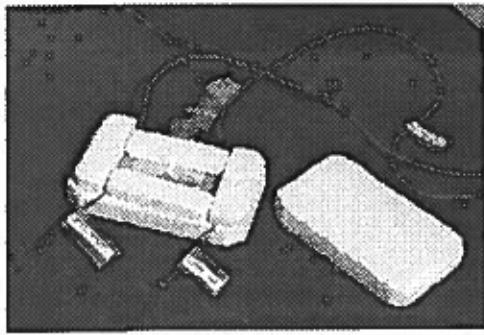


Figure 4.16e: Assembly of Insulating Box

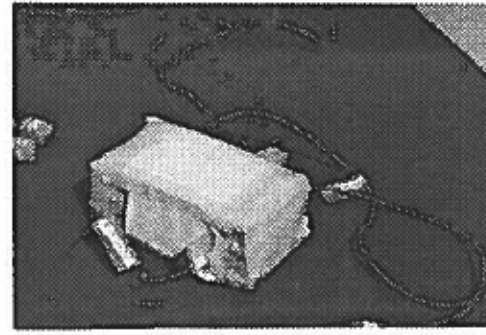


Figure 4.16f: Insulation Complete

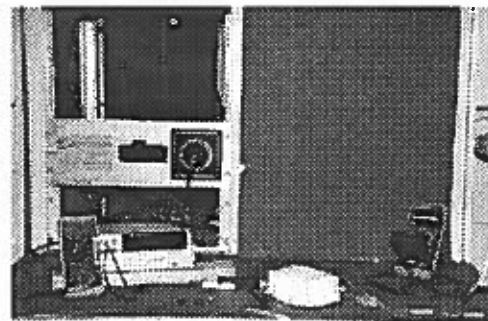


Figure 4.16g: Final k Testing Setup

After putting the lid on the insulating box, the entire assembly was wrapped in five layers of paper towels and secured with masking tape. This final assembly can be seen in Figure 4.16f. The entire experimental setup is shown in Figure 4.16g. The power supply had been attached to the appropriate leads, and the multimeter had been connected to measure the voltage across the heater strip. A second multimeter, a Fluke 45 Dual Display, had been connected to an Omega-CJ cold junction compensator which in turn was attached to the thermocouples through a mechanical voltage scanner. By applying a series of voltages to the heater strip and recording the temperature difference across the wing material test piece, the thermal conductivity was determined from equations 4.4 and 4.5. Combining those two equations and noticing that the conductive heat flux equals the total heat flux generated due to the insulating enclosure, the following expression is obtained.

$$\frac{V_{\text{heater strip}}^2}{R_{\text{heater strip}} A_{\text{heater strip}}} = k_{\text{wall}} \frac{T_{\text{wall}} - T_2}{t_{\text{wall}}} \quad (4.7)$$

The thermal conductivity is the slope of the graph of the total generated heat flux versus temperature gradient though the wing material test piece. Tests were performed on four separate days, and the average slope was determined. Figure 4.17 presents the results for the thermal conductivity experiments.

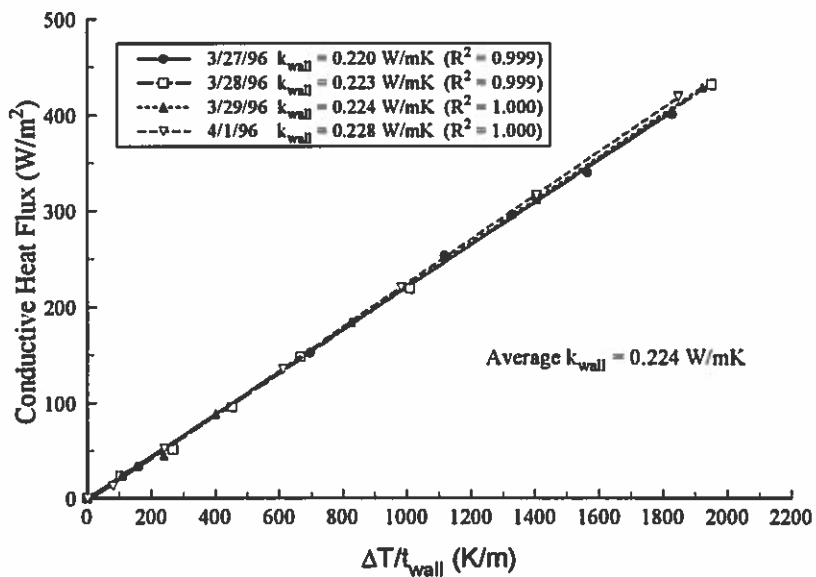


Figure 4.17: Experimental Determination of k_{wall}

An estimate of the uncertainty in k_{wall} was made using the method of Kline and McClintock (1953). It was found that $\delta k_{wall} = \pm 8.9\%$ was a good representative value of the experimental uncertainty in the measurement.

To verify that the results of this testing made sense, the value of the thermal conductivity of the wing material was compared to that of several insulators taken from Appendix B, Properties of Solids, of Adrian Bejan's *Heat Transfer* (Bejan, 1993).

Table 4.2: Selected Samples of Thermal Conductivity Values of Insulators

Material	T (°C)	k (W/mK)
Asbestos (sheet)	20	0.74
Bakelite	20	0.230
Brick (cement)	10	0.34
Fat	20	0.17
Plexiglas	20	0.184
Rubber (soft)	20	0.2

From these examples, the experimentally determined value of k for the wing material is seen to be of the correct order of magnitude and can be used with confidence to calculate the conduction losses through the wing material.

4.2.7 The Image Processing System

To record the liquid crystal colors and to convert the colors to quantitative temperature information, an image processor was used. The image processor is an NTSC (National Television System Committee) standard 24-bit color system which converts RGB (red, green, blue) information to HSI (hue, saturation, intensity) information for each pixel of a 512 x 480 image (Wiedner, 1994).

Hue corresponds directly to the dominant wavelength of the light entering the image processor sensor for the visible spectrum. *Saturation* refers to color purity, or in other words, the amount of white contained in a specific color. *Intensity* refers to the relative brightness of a color (Kim, 1991).

The RGB attributes were captured by the CCD sensor inside a standard 8mm video camera. Complete images were acquired at a rate of 30 frames per second. The RGB attributes were then multiplexed and sent to the image-capturing board made by Data Translation. The image processor system uses three eight-bit video A/D converters, which means that each RGB or HSI attribute varies between 0 and 255.

The hue attribute is used to determine the temperature at a given pixel location. The intensity attribute is used as a filtering device for a given pixel location. If the intensity value of a pixel falls below 50, the hue value becomes unstable, and the pixel can not be used to produce an accurate temperature value (Kim, 1991). Also, if the intensity value of a pixel exceeds 200, the hue value becomes less accurate due to the saturation of the CCD sensor in the video camera.

4.2.8 Modifications to Model Prior to ASWT Heat Transfer Experimentation

This section describes the modifications that were made to the original SM701 wing model to enable heat transfer experimentation in the ASWT. The intent of testing in the ASWT was to work out any difficulties and unforeseen problems in experimentally

measuring convective heat transfer coefficients with the existing laboratory equipment. Any problems that would arise would be addressed and corrected before final experimentation would take place in the higher-flow-quality (less turbulence, more two-dimensional test section flow) LSLTT.

The ASWT tests were conducted with a finite aspect ratio 2.58 model since fluorescent oil flow visualization results showed that the flow was two-dimensional on the surface of the wing at its midspan even though the wing was finite. The model was first painted with Pittsburgh Paints spray enamel quick dry flat black to provide maximum color contrast for the liquid crystal images. The next step in preparing the model was to construct two bus bars inside of the wing that would provide electrical connections for the heater strip to be used in the steady state heat transfer technique that was chosen for experimentation. The bus bars were made out of sheet copper 1/16 inches thick. Two wires were attached to each bus bar using Circuit Works conductive epoxy. One wire on each bus bar would be used to apply constant DC voltages across the heater strip during experimentation. The other wire on each bus bar would provide leads for a multimeter to measure the applied voltage directly across the heater strip. This second set of wires eliminates the need to calculate the voltage drop across the power leads had the multimeter been used only to record the voltage supplied by the DC power supply.

The heater strip was then cut from a piece of Inconel 600 foil, the resistance of which is constant in the temperature range encountered during experimentation. The heater strip was cut as a rectangle with dimensions of $25\frac{1}{4} \times 1$ inch and had a thickness of 0.025 mm. The heater strip length allowed a $\frac{1}{2}$ inch excess on either end of the strip with which to make the bus bar connection (the total length of the strip from bus to bus was $24\frac{1}{4}$ inches). A strip of double-sided tape 0.005 inches thick was attached to the wing upper surface at the midspan where the heater strip would lie. The heater strip was then rolled onto the tape strip taking care to avoid trapping air bubbles beneath the foil. Figure 4.18 shows the heater strip attached to the upper surface of the model. The Inconel strip was then sprayed black in preparation for the liquid crystal coating.

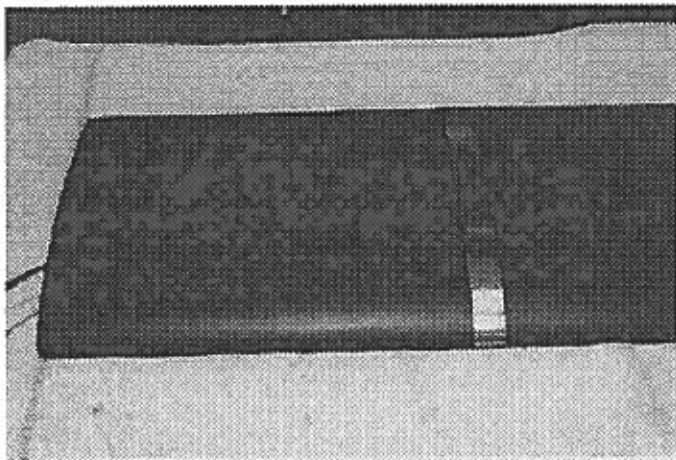


Figure 4.18: Inconel Before Painting

A slurry of thermochromic liquid crystals with an event temperature of 30 °C was sprayed onto the strip using an airbrush. The slurry was dried carefully between successive coatings by using a heat gun. Several coats were applied until very distinct color patterns were seen.

Finally, a single K-type cement-on thermocouple was attached inside the wing to the lower surface at approximately a 60% chordwise location. The purpose of this thermocouple was to record the model's internal temperature (T_2 in equation 4.5) to be used in calculating conduction losses from the heat flux generated by the heater strip.

4.2.9 ASWT Setup for Heat Transfer Experimentation

Before installing the model into the ASWT for testing, the wind tunnel first had to be calibrated. A pitot-static probe was positioned along the centerline of the empty test section. Two 0.125 psi Validyne differential pressure transducers, each connected to a Validyne Model CD15 Carrier Demodulator, were then calibrated using a Meriam Instrument hand pump and a Dwyer Instruments, Inc. manometer. TSI integrating voltmeters were used to read the pressure transducer output voltages. One of the pressure transducers was next connected to the total and static ports of the pitot-static probe. The other transducer was connected to static pressure ports located before and after the contraction section of the ASWT. By varying the tunnel speed, a calibration plot of the

test section dynamic pressure versus the contraction pressure drop was constructed. The calibration slope was determined to be 1.0452 Pa/Pa.

The model was then installed in the test section of the ASWT. Two struts supported the model, and a metal rod connected to the lower surface of the model near the trailing edge provided a means for angle of attack adjustment. These features can be seen in Figure 4.19.

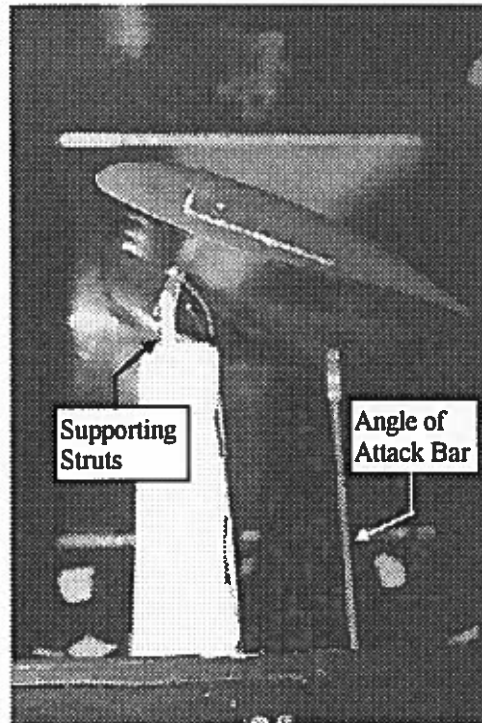


Figure 4.19: The Model in the ASWT

A Mitutoyo Pro 360 digital protractor was attached to the wing tip using an angle iron bracket. The bracket was carefully positioned along the chordline so that the protractor readout would display the angle of attack. The digital protractor has a resolution of $\pm 0.1^\circ$. A Maxwell Electronics Inc. x-y stepping motor controller was used to drive the angle of attack adjust motor.

A K-type cement-on thermocouple was attached to the tunnel wall immediately upstream of the model to allow measurement of the free stream temperature. The leads

from this thermocouple as well as the thermocouple leads coming from the model were connected to a mechanical voltage scanner. The single set of leads coming from the mechanical voltage scanner was connected to an Omega-CJ cold junction compensator that provided a zero °C reference point electronically. The voltage from the compensator was read from a Fluke 45 Dual Display multimeter.

A Hewlett Packard 6261B DC power supply was used to apply a voltage across the heater strip. A TSI integrating voltmeter was used to display the voltage that was applied across the heater strip. A discussion of the actual wiring for the heater strip is available in Section 4.2.8.

A Sony 8mm video camera was mounted above the test section. The camera viewed the heater strip on the upper surface of the model through a five inch wide Lucite window that was built for that specific purpose. The camera was positioned so that the heater strip would be horizontal in the image. The camera video output was connected to the Data Translation image processor which was inside a 386 personal computer. Two 200 Watt incandescent light bulbs in reflectors were positioned on either side of the test section to provide illumination for the liquid crystal coated heater strip. Direct radiative heating of the liquid crystal coated surface was avoided by only illuminating the lights when data were being taken.

The liquid crystals were calibrated to obtain a hue versus temperature relationship. Details regarding liquid crystal calibration are available in Section 4.2.14 in which the calibration for the LSLTT tests is described. Figure 4.20 summarizes the ASWT setup.

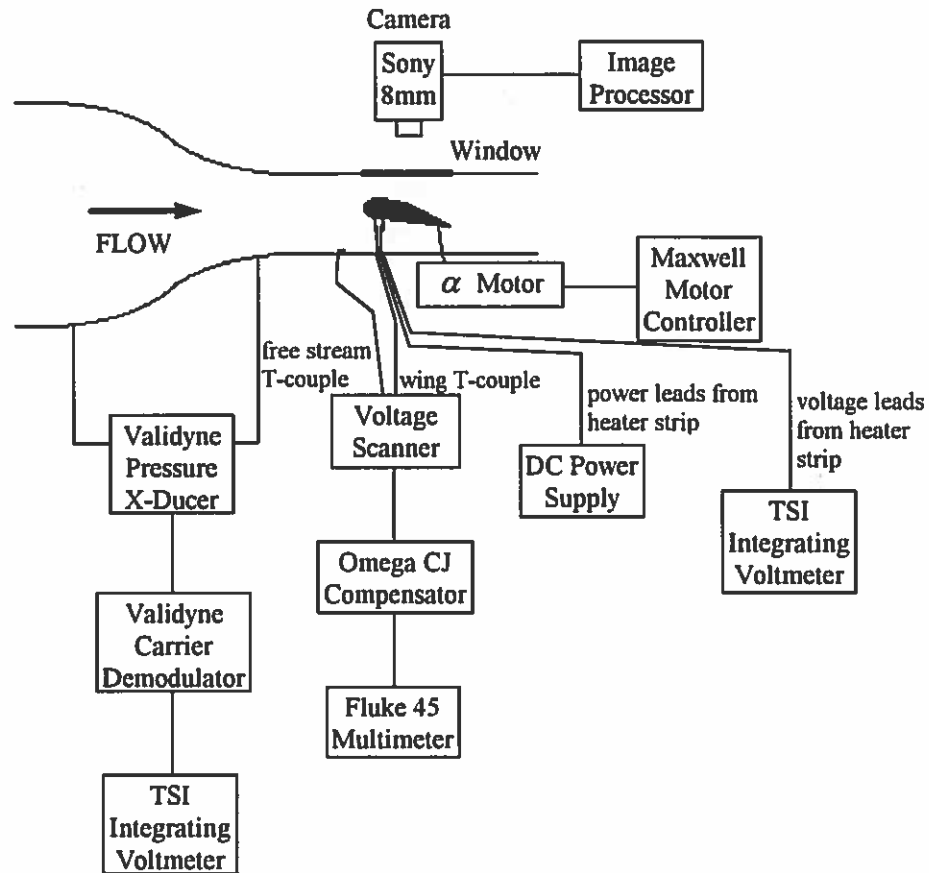


Figure 4.20: Schematic of ASWT Heat Transfer Experimentation Setup

4.2.10 ASWT Experimental Procedure

All experiments were conducted during the night to maximize the liquid crystal color contrast under the incandescent lighting system. Tests were conducted for a Reynolds number of 315,000. Angles of attack tested included 0, 5, and 10 degrees.

After setting the desired angle of attack, the velocity necessary to achieve a target Reynolds number of 315,000 was calculated based on the atmospheric conditions preceding a given experiment. From this velocity the required test section dynamic pressure was computed, and through the tunnel calibration the necessary pressure drop across the contraction section was determined. The wind tunnel was then run, increasing the flow speed until the required pressure drop was reached.

The DC power supply was turned on, and the voltage level was increased slowly until color first began to appear on the heater strip. At this point, the heat transfer was allowed

to reach steady state. A time of approximately 10 minutes was usually sufficient. Steady state was determined by watching the color pattern on the heater strip and by observing the model's internal thermocouple output voltage.

Once steady state was reached, the voltage applied across the heater strip was recorded along with the free stream and internal thermocouple output voltages. The incandescent lights were then illuminated. An image of the color pattern on the heater strip was then grabbed with the image processor. Approximately 15 seconds of video were then recorded with the camera, providing security in the event of a problem with the original image taken by the image processor. The lighting system was then turned off. Operating the lights in this manner minimized the effects of radiation to the heater strip from the lights (Wiedner, 1994).

The voltage across the heater strip was then increased slightly to allow the color bands to shift to a new area of the heater strip. Steady state was allowed to be reached, and the process described above was repeated for the new image. During a given experiment, a total of 10 to 15 images were usually necessary to ensure the entire heater strip surface had at one point been colored by the liquid crystals.

A FORTRAN code was written that directed the image processor to analyze the images taken during experimentation. For the colored locations on each image, the code computed the total heat flux generated by the heater strip (equation 4.4), the conduction losses into the wing (equation 4.5), and the radiation losses (equation 4.6). The convective heat transfer coefficient was then calculated via equation 4.3. The heater strip temperature (T_{wall} in the above equations) was determined from the colors of the liquid crystal patterns in the experimental images. The image processor was used to scan a vertical column of pixels on the horizontal heater strip in an image at a given chordwise station. Each pixel in the column was required to pass a hue and an intensity criterion. The acceptable hue range was determined from the liquid crystal calibration. The acceptable intensity range was discussed in Section 4.2.7. A lower limit was set on the total number of pixels in a column that must pass the hue and intensity criteria; if not enough pixels passed the entire column would be skipped. This limit ensured that a good average hue value would be obtained for each column. The hue values of the pixels in the

column passing both criteria were averaged, and this average hue was converted to a temperature through the liquid crystal calibration. The chordwise location of the column of pixels was recorded, thus providing the necessary information for a single h, x/c data point. The image processor then moved on to the next chordwise location scanning for pixels that passed both required criteria. This process was repeated for all images taken during the experiment, and a final compilation of the h, x/c points was made.

4.2.11 Problems Discovered and Knowledge Gained During ASWT Tests

Results of the initial heat transfer tests in the ASWT are presented in Figure 4.36 in Section 4.2.16 on the same graph as results for experimentation in the LSLTT. Only the zero degree angle of attack case is presented because problems encountered rendered other data taken in the ASWT very difficult to interpret. The intent of testing in the ASWT was not to interpret the h maps generated, but to determine any underlying problems that should be addressed before experimentation began in the LSLTT. The data generated in the LSLTT would be fully analyzed and interpreted (Sections 4.2.16 to 4.2.18).

Many problems did arise during this initial experimentation that reduced the accuracy of the heat transfer coefficients obtained. One of these problems involved the width of the heater strip. Edge effects on the color patterns reduced the region of the heater strip in which valuable data could be taken by about 50%. See Figure 4.21. Only the middle half of the strip provides a two-dimensional color band that may be used for determining average hue values at a given chordwise location. Because of this reduced region of valuable data, the lower limit on the total number of pixels in a given column that must pass the hue and intensity criteria had to be very low in order to obtain data at each chordwise station. Thus hue averages suffered because of these edge effects. This created scatter in the h maps and necessitated the use of an averaging technique. The data presented in Figure 4.36 of Section 4.2.16 have been averaged to achieve a smooth line.

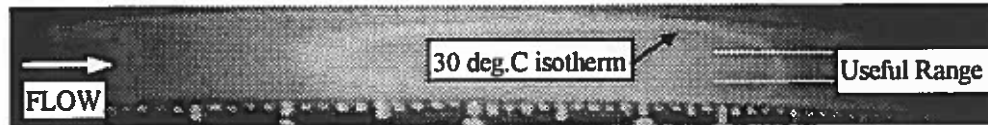


Figure 4.21: Edge Effects on the Heater Strip Color Pattern

Another problem involved the internal layout of the wing model as shown in Figure 4.22. The heater strip (located on the outside of the wing) had to pass over several internal features of the wing: the main aluminum spar, a composite spar support angle that held the main spar in position, the copper bus bars, a cutout area that was required to provide clearance for the angle of attack mount, and the trailing edge aluminum spar. All of these internal features affected the conduction losses from the heater strip. This situation would have to be remedied to provide more confidence in the experimentally determined h values.

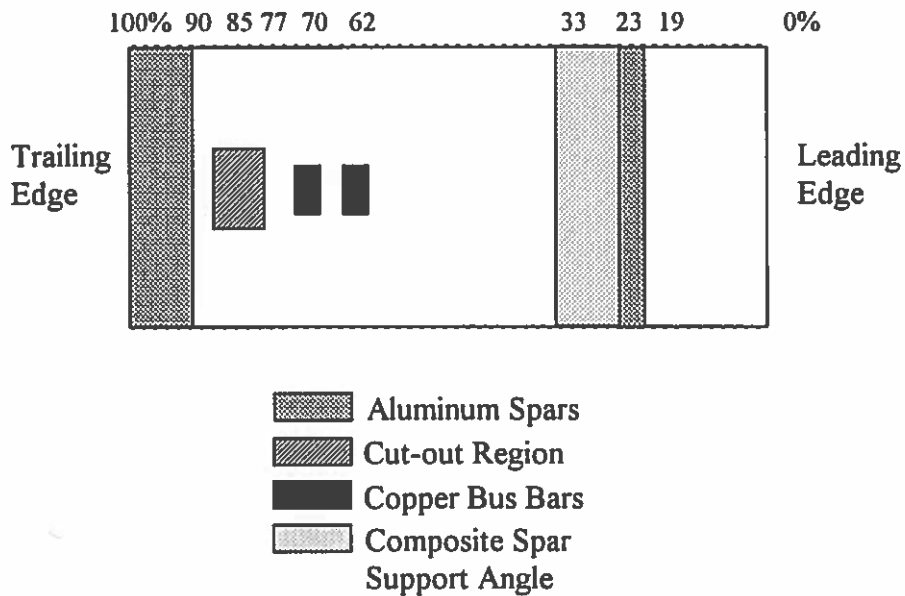


Figure 4.22: Sketch of Inside of Model for ASWT Tests

The internal thermocouple was also seen to be a problem in that it only provided an average temperature for the inside of the model. The conduction loss term would again suffer because of this shortcoming.

In addition to these problems, the lighting was not deemed to be satisfactory. Much intensity was lost through the wind tunnel Plexiglas windows. This was seen to be a possible problem in that if the intensity of the colors on the heater strip dropped too low, the color image CCD sensor would not provide an accurate hue value (Kim, 1991).

All of these problems had to be addressed before testing could begin in the LSLTT. The following section discusses the modifications made to the model and the solutions to the problems discovered during heat transfer experimentation in the ASWT.

4.2.12 Modifications to the Model Prior to LSLTT Heat Transfer Experimentation

4.2.12.1 Fabrication of the Wing Extensions

For the experimentation in the LSLTT, it was decided to conduct two-dimensional tests to eliminate the effects of tip vortices and to provide better support to the model at high angles of attack where buffeting occurred in the ASWT three-dimensional tests. To meet this testing requirement, a set of wing extensions had to be constructed since the wingspan of 31 inches was less than the LSLTT test section center height of approximately 40 inches. This fabrication is now discussed in detail.

Not only did the extensions have to increase the wingspan by over 10 inches, but they also needed to allow easy attachment of the wing to a horizontal rotary indexing table below the test section and a $\frac{3}{4}$ inch rotary bearing above the test section. The indexing table would allow the wing angle of attack to be adjusted.

The mounting piece that was designed to connect the lower wing extension to the indexing table is shown in Figure 4.23. It was built by machining a solid aluminum bar and tapping a piece of $\frac{1}{4}$ inch thick steel sheet.

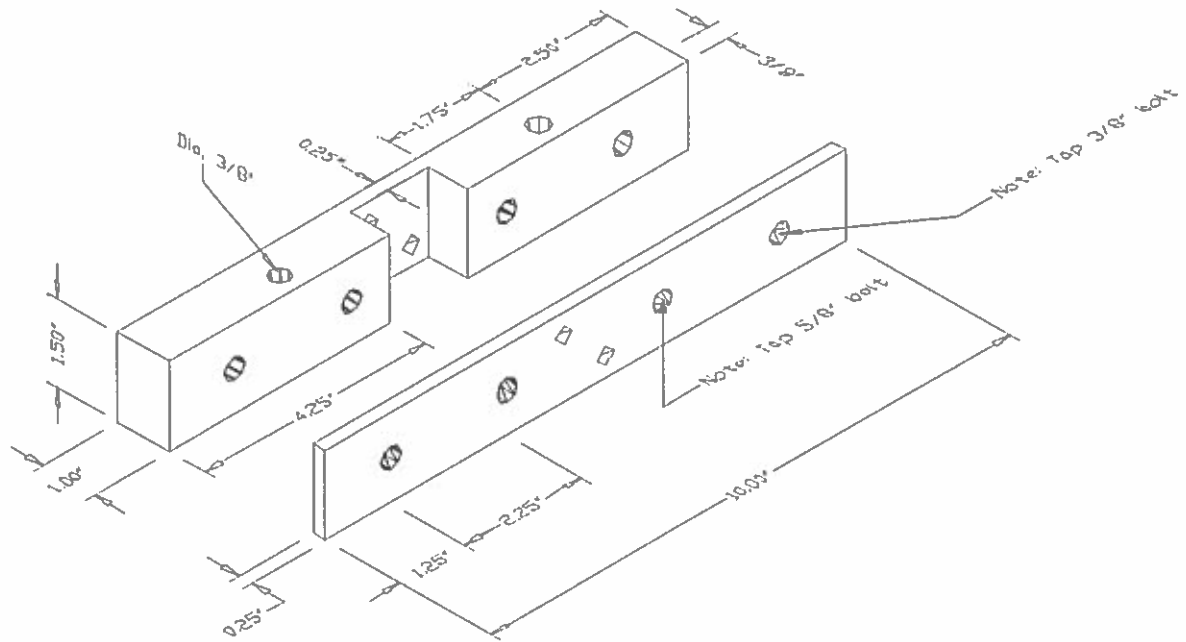


Figure 4.23: Rectangular Indexing Table Mount

The wing extensions were designed to increase the overall span of the model to 44 inches. This length allows slightly over one inch to protrude both above and below the test section ceiling and floor boards when the model is installed in the LSLTT. Drawings of the extensions are shown in Figure 4.24a and 4.24b. The bottom extension was constructed from a solid aluminum bar $18\frac{1}{4}$ inches long with a $1\frac{1}{2} \times \frac{3}{4}$ inch cross section. These cross section dimensions were calculated from a simple beam bending and twisting analysis using the maximum predicted aerodynamic loads. The top extension utilized an 18 inch long aluminum bar with the same cross section as the bar of the bottom extension. However, in addition to the aluminum bar, the top extension was built with a $\frac{3}{4}$ inch diameter rod protruding from the aluminum bar. This rod allowed an easy interface with the rotary bearing on the top of the wind tunnel. Figure 4.25 shows the model with extensions mounted in the LSLTT.

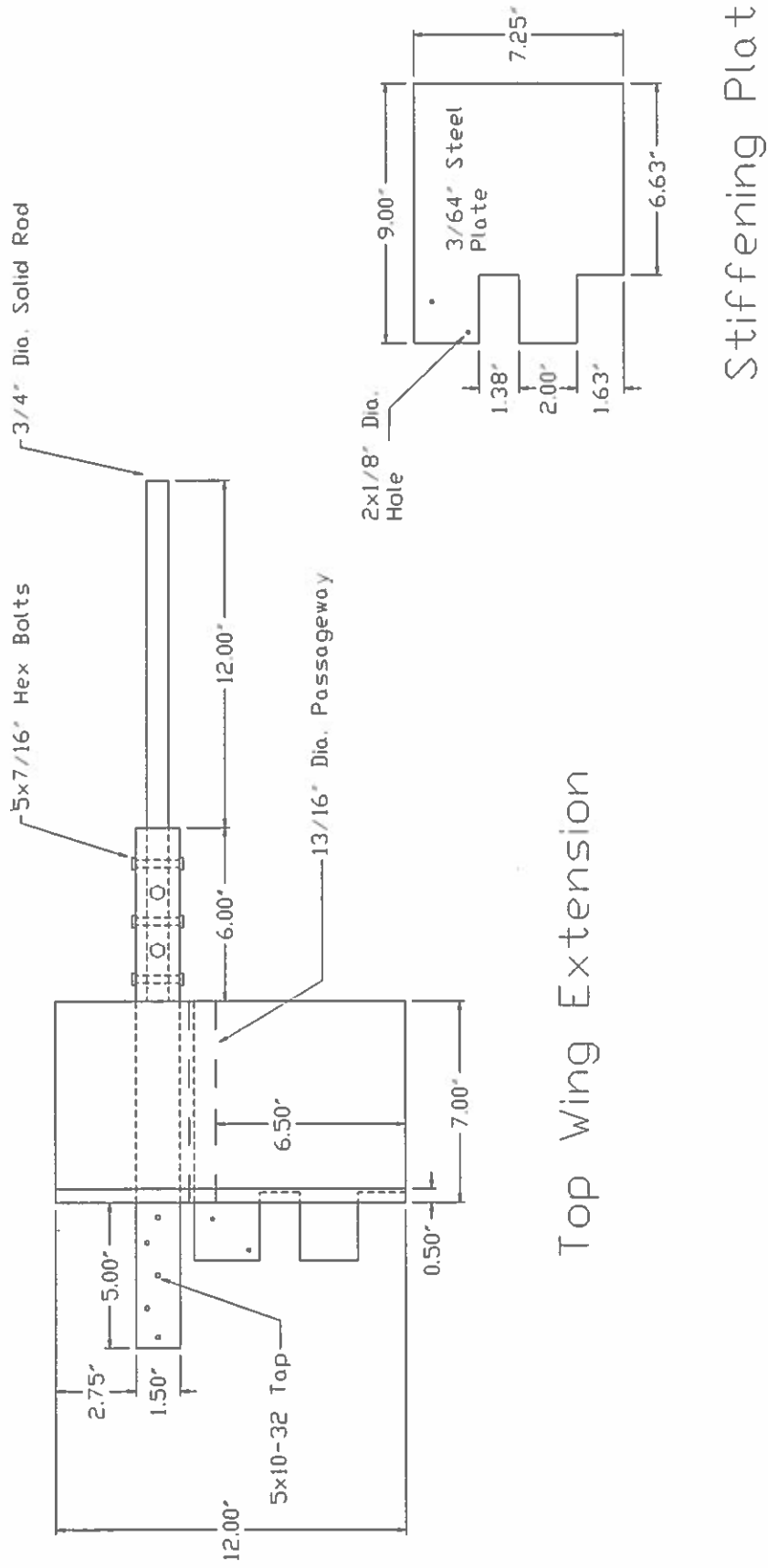


Figure 4.24a: Top Wing Extension (lower surface view)

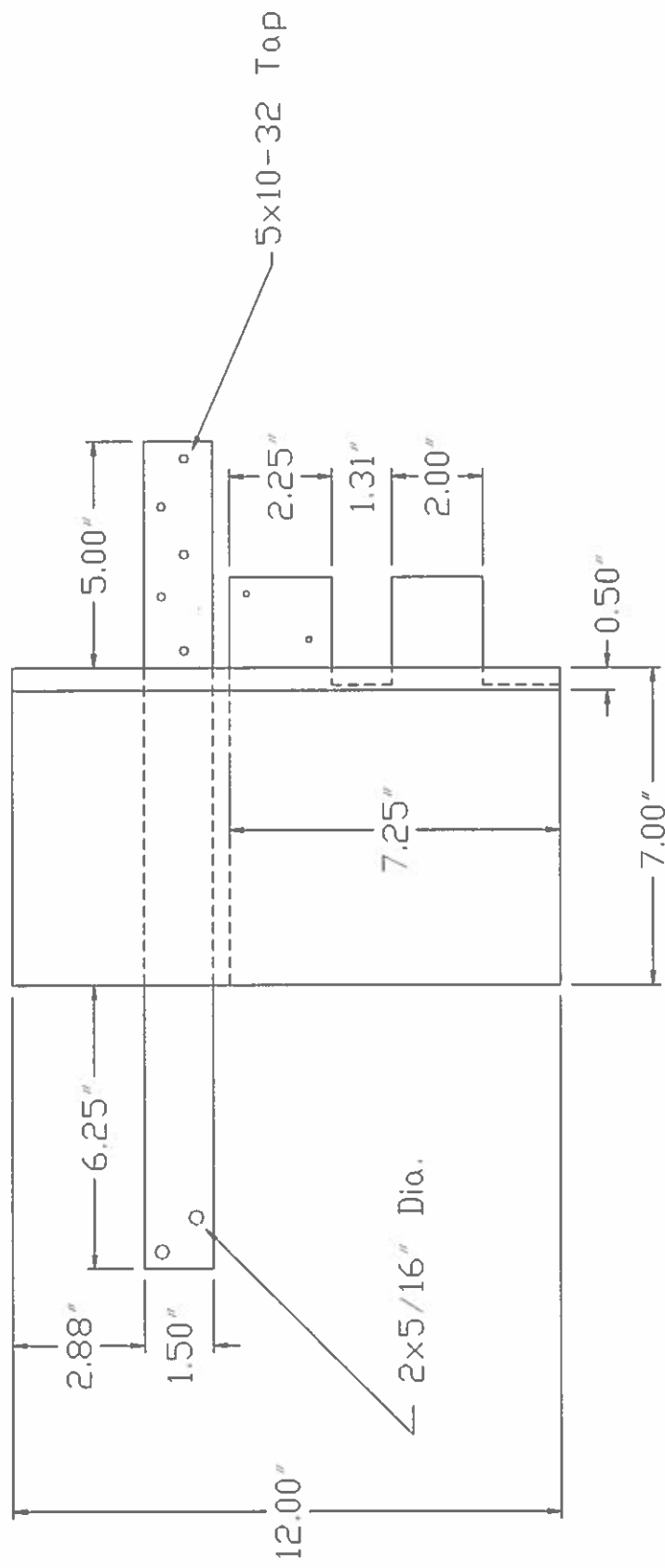


Figure 4.24b: Bottom Wing Extension (lower surface view)

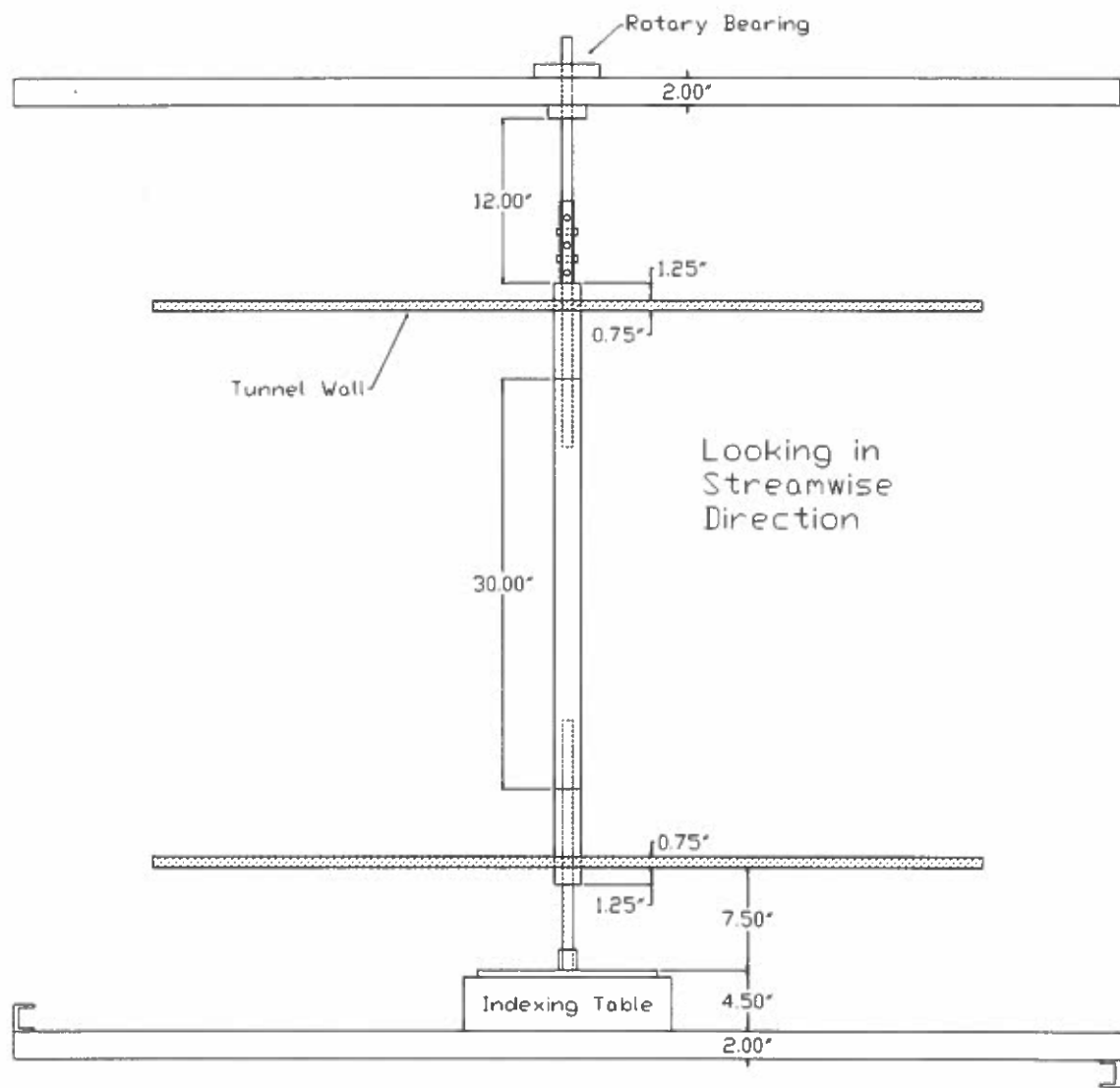
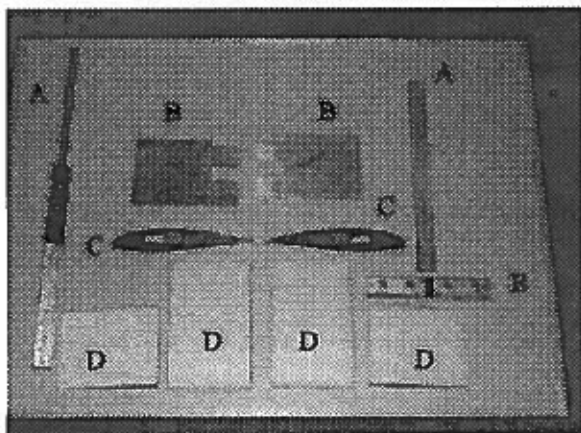


Figure 4.25: Model with Extensions Mounted in LSLTT
(NOTE: Vertical LSLTT components not drawn.)

A series of photographs is now presented to clarify the design and fabrication of the wing extensions. Figure 4.26 shows all the pieces that were built to construct the extensions.



- A. Load-carrying beam pieces
- B. Steel sheet stiffening pieces
- C. Wooden SM701 airfoil pieces
- D. Foam extension pieces
- E. Rotary indexing table mount

Figure 4.26: Wing Extension Pieces Before Assembly

To ensure precise alignment when attaching the aluminum beam pieces (A) to the main wing spar at both wing tips of the model, a small 10 mW helium-neon laser made by Hughes Aircraft Company was used. A small piece of Formica was cut so that it rode along the aluminum beams. The laser beam was first aligned with the leading edge of the wing. The laser was then traversed until it hit a vertical line on the Formica piece. By sliding the Formica along the length of the beam, adjustments could be made such that the beam was precisely aligned. Both extension beam pieces were aligned in this manner. See Figures 4.27a and 4.27b.

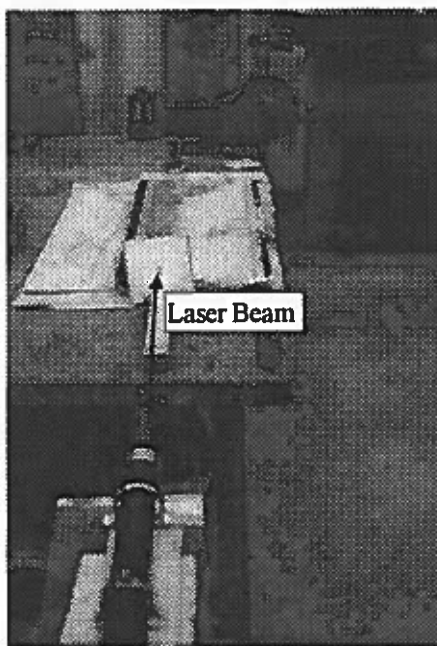


Figure 4.27a: Aligning Load-Carrying Beams

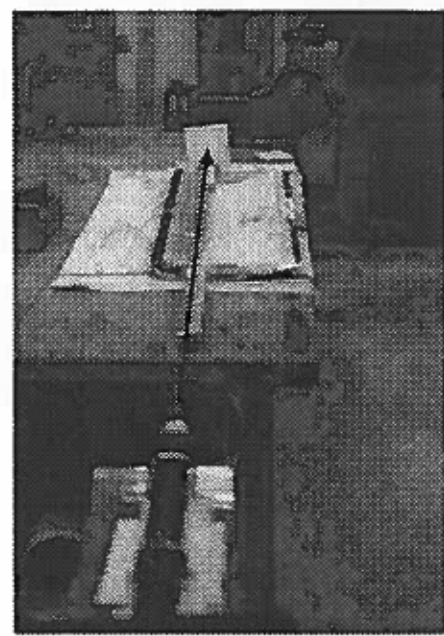


Figure 4.27b: Aligning Load-Carrying Beams (cont.)

After this alignment was completed, the assembly of the extensions could continue. The assembly of the bottom extension will be discussed. The top extension was assembled in the same manner.

The stiffening piece (B) was inserted through the slot in the wooden SM701 airfoil piece (C). See Figure 4.28a. The trailing edge has been molded from Evercoat Professional body filler (bondo). This provides more durability than using foam for the thin trailing edge.

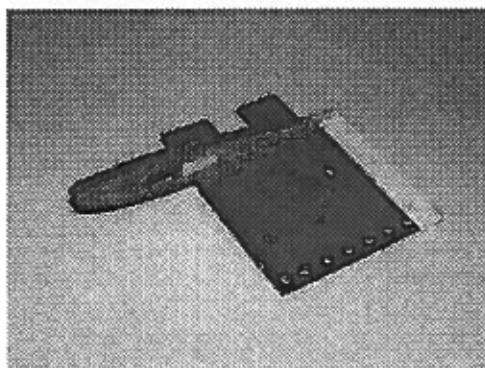


Figure 4.28a: Beginning Wing Extension Assembly

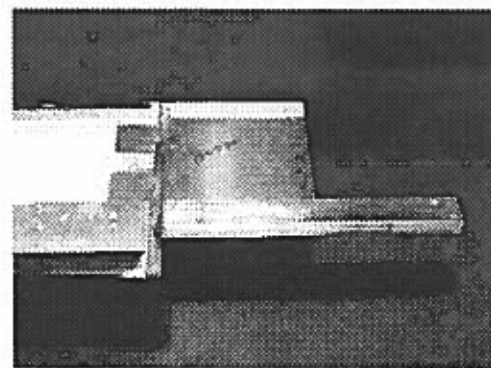


Figure 4.28b: Mating Extension to Wing

The load-carrying beam was then inserted through the wooden SM701 airfoil piece, and the entire assembly was attached to the main wing spar at the appropriate tip of the wing. See Figure 4.28b. Once the pieces were checked for proper positioning, Devcon 5 minute epoxy was applied to attach the stiffening piece (B) to the wooden airfoil piece (C).

A foam extension piece (D) was then glued to the stiffening piece (B) with the epoxy as seen in Figure 4.28c. The foam extension pieces had been cut from blocks of Owens Corning Foamular 150 insulating foam. Formica SM701 airfoil templates were first glued on either side of the foam blocks. A taut wire was then heated by passing a current through it, and the wire was used to slice the desired shapes out of the foam. Finishing was completed with 100 and 400 grit sandpaper to achieve fairly smooth surfaces.

A second foam extension piece was then glued to the assembly to complete the airfoil shape. Bondo was applied to seal remaining gaps. This can be seen in Figure 4.28d. Upon final sanding, the extension appeared as in Figure 4.28e.

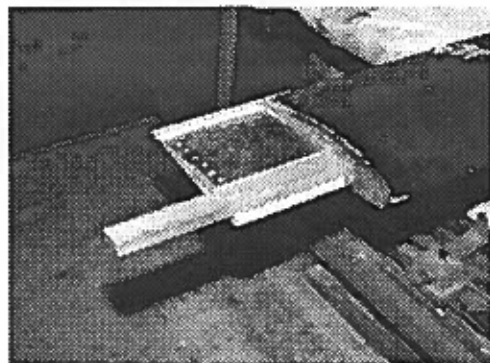


Figure 4.28c: Attachment of First Foam Piece

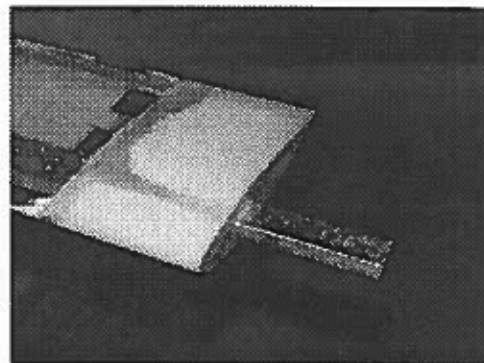


Figure 4.28d: Attachment of Final Foam Piece

A means had to be devised to pass internal wires out of the wing through one of the extensions. A 13/16 inch inner diameter metal pipe was used to form a passageway through the left wing tip extension. The pipe was heated with a propane torch and pressed into the extension immediately behind and parallel to the load carrying beam. The high temperature of the pipe allowed it to melt easily through the foam extension piece forming a passageway for the internal wires.

Both extensions can be seen attached to the model in Figure 4.28f. This picture was taken before the model received a final coat of black paint. The wing extensions were later covered with Top Flight Monokote (a heat-shrink plastic covering) to provide a smooth surface. Problems were encountered in this final step. The heat from the Hobbico custom sealing iron that was used to apply the plastic Monokote covering caused slight bumps to form in the foam of the extension piece. Thus, the final finished extensions were not entirely smooth. This was not seen to be a major problem, however, since the extensions were located far from the center span region of the model where the heat transfer measurements would be taken. The extensions could be improved by re-sanding and applying a layer of E-glass epoxy fiberglass instead of the Monokote plastic covering.

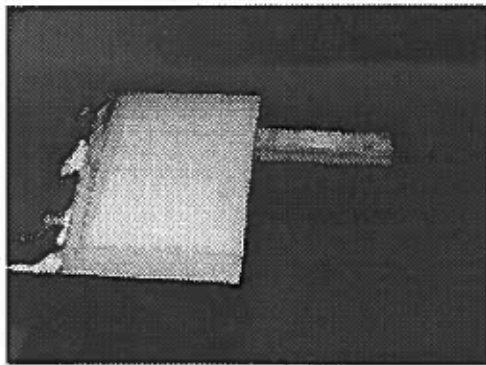


Figure 4.28e: Extension After Sanding



Figure 4.28f: Completed Extensions Before Covering

4.2.12.2 Model Changes Due to Knowledge Gained from ASWT Tests

To address the problem of edge effects on the heater strip color patterns, it was decided to increase the width of the heater strip from one inch to three inches. This would create a much larger region along the center of the strip in which the color bands would be two-dimensional. As a result of this change, a better average hue value would be attainable, and the scatter encountered in the ASWT h maps should be diminished.

The problem of the internal geometry of the wing as seen in Figure 4.22 of Section 4.2.11 was remedied by shifting the entire heater strip from the midspan by 4½ inches. Oil flow visualization had shown that the flow would still be two-dimensional in this new location, and by shifting the heater strip the cutout region near the trailing edge could be avoided. In addition, the composite spar support angle was cut away from the new location of the heater strip, and the new forward bus bar was built so that it did not interfere with the upper surface of the wing. Thus the heater strip only had to pass over the main aluminum spar, the aft bus bar, and trailing edge aluminum spar. The problems with the composite spar support angle, the forward bus bar, and the cutout region, totaling approximately 22% of the chord, were eliminated.

An internal array of eight thermocouples was installed along the inside of the upper surface to eliminate the uncertainty of only using one thermocouple. Internal temperatures at chordwise locations would be determined by linearly interpolating between the nearest thermocouples.

The problem with lighting was addressed by increasing the power of the bulbs from 200 Watts to 500 Watts. The lights were placed on variable ac (variac) power supplies so that the best light intensity could be achieved.

A final improvement was made for the experimentation in the LSLTT. A FORTRAN data acquisition code was written to sample the necessary voltages during the testing. A DAS20 board manufactured by MetraByte Corporation was used to digitize the analog voltage signals. This FORTRAN code is listed in Appendix C as the program getdata.for.

4.2.13 LSLTT Setup for Heat Transfer Experimentation

Before the model could be installed in the test section, the eight thermocouples comprising the internal thermocouple array as well as a thermocouple to be used to measure free stream temperature had to be calibrated. These nine thermocouples were connected to a mechanical voltage scanner. The single set of leads coming from the voltage scanner was connected to a MEPTS-9000B main unit to provide signal conditioning and amplification of the thermocouple output voltages. The conditioned output of the thermocouple signal was then sent to channel 2 of the DAS20 interface. A hot water bath was prepared in a one gallon insulating thermos. The nine thermocouples were placed in the bath along with a certified (NIST) thermometer against which the thermocouples would be calibrated. Calibration corrections for the thermometer were supplied by Brooklyn Thermometer Company, Incorporated. The water was stirred to achieve a good equilibrium temperature, and each thermocouple output voltage was sampled by the DAS20 board by rotating the dial of the voltage scanner. Cold water was added to the thermos to lower the temperature between calibration points. The calibration slopes for the nine thermocouples are seen in Figure 4.29.

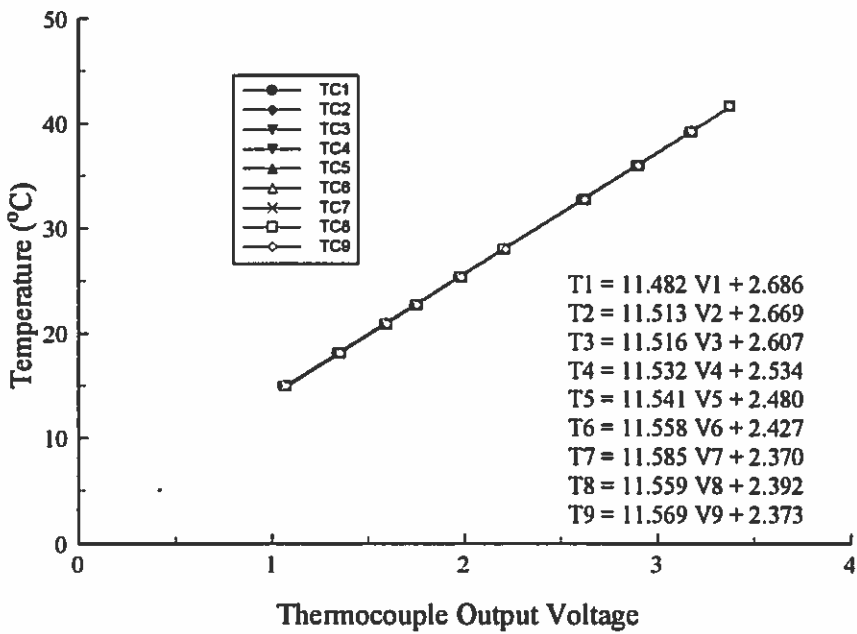


Figure 4.29: Calibration of the Nine Thermocouples

The tunnel was then calibrated in the same manner as discussed in Section 4.2.9 for the ASWT. A ± 10 inch H_2O and a ± 1 psi differential pressure transducer purchased from Techkor Instrumentation were used in this calibration process to record the pressure drop across the contraction section and the test section dynamic pressure, respectively. The pressure transducers were connected to a MEPTS-9000A main unit that provided signal conditioning and amplification. A Meriam Instrument hand pump was used to calibrate the pressure transducers against a Meriam Instrument manometer. The output voltage of the pressure transducer connected across the tunnel contraction was fed into the DAS20 interface on channel 0. This interface fed directly into the DAS20 A/D board inside a Compaq Deskpro 386s personal computer.

The model was mounted vertically in the center of the test section. Beneath the test section, the model was secured to a rotary indexing table which allowed angle of attack to be changed. Figure 4.30 shows the rotary indexing table with the wing mounted. Above the test section, a rotary bearing held the wing in place as shown in Figure 4.31. Mortite

Weatherstrip and Caulking Cord was used to seal any gaps between the model and the rotating wooden templates that interfaced with the test section.

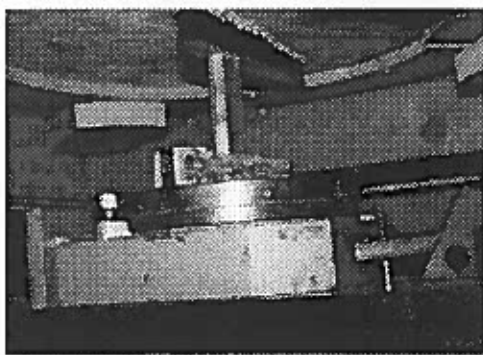


Figure 4.30: Model Mounted to
Rotary Indexing Table

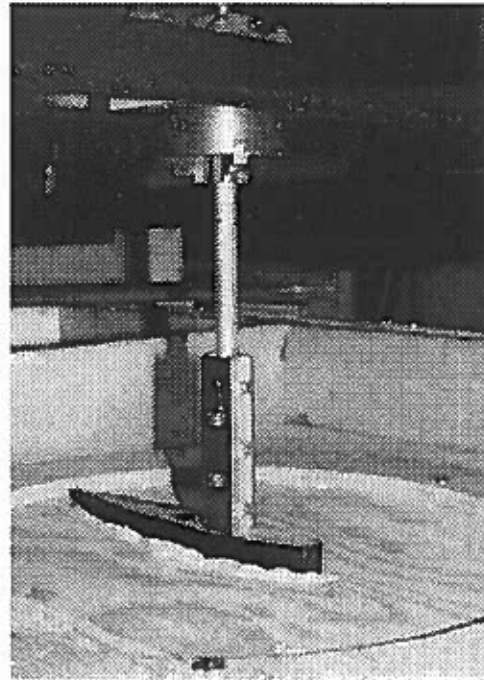


Figure 4.31: Rotary Bearing Mount
Above Test Section

A Hewlett Packard 6261B DC power supply was used to apply a voltage to the heater strip through a set of leads attached to the bus bars inside the model. A second set of leads wired to the heater strip was fed into channel 1 of the DAS20 interface to allow the applied bus-to-bus voltage to be recorded.

A Sony 8mm video camera mounted on a tripod viewed the heater strip on the upper surface of the model through the side windows of the test section. The heater strip was horizontal in the camera viewfield. The camera video output was connected to the Data Translation image processor inside a 286 personal computer. Two 500 Watt incandescent

light bulbs in reflectors were positioned to provide illumination for the liquid crystal coated heater strip.

Figure 4.32 shows the model mounted in the test section, and Figure 4.33 summarizes the experimental setup for the LSLTT heat transfer tests.

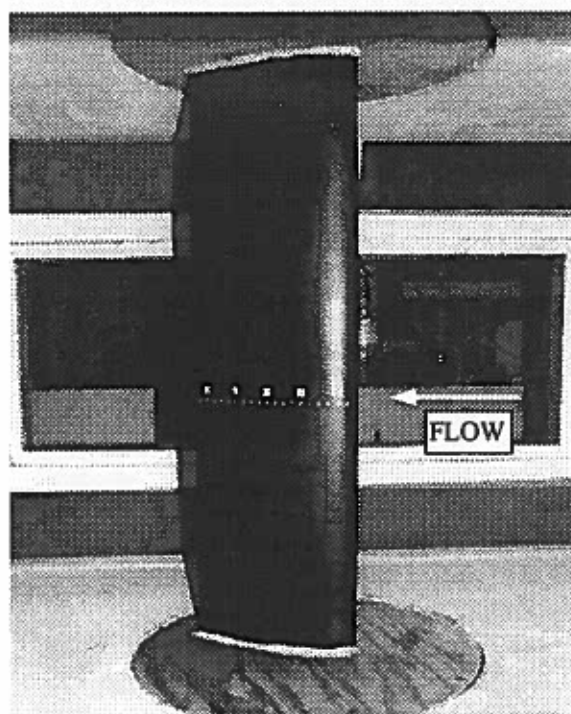


Figure 4.32: Model Mounted in LSLTT Test Section (view of upper surface)

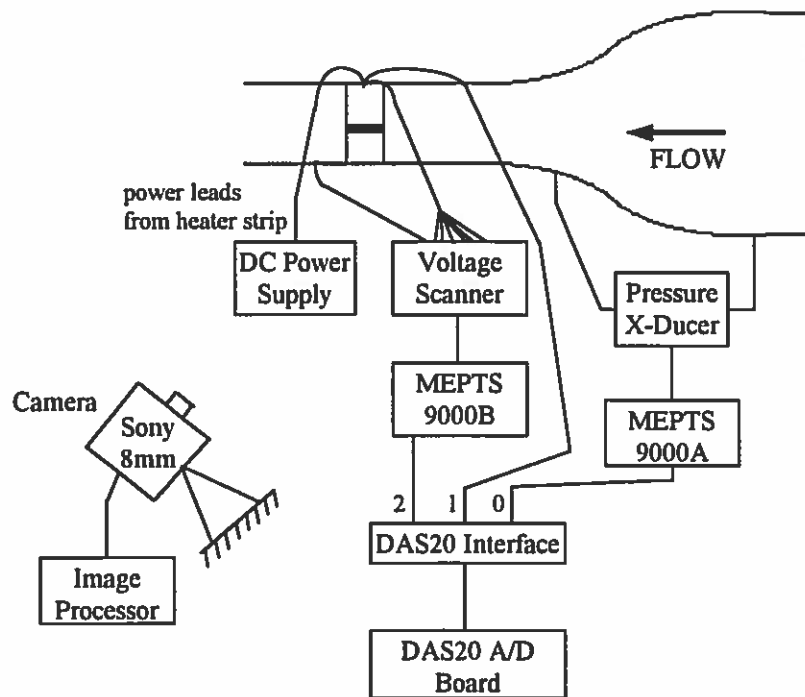


Figure 4.33: Schematic of LSLTT Heat Transfer Experimentation Setup

4.2.14 Calibration of the Liquid Crystals

Before heat transfer tests could be conducted, the liquid crystal layer sprayed onto the heater strip first had to be calibrated. This was done by first affixing a K-type cement-on thermocouple (with a response time of 3 to 5 ms) to a scrap piece of the wing material which was found to be a good insulator. The surface of this calibration piece of wing material was then spray painted black with the same paint that was used on the wing. Using the same slurry that was applied to the wing model's heater strip, thermochromic liquid crystals were then sprayed onto the black calibration piece using an airbrush.

The calibration piece was next placed in the wind tunnel test section in the same location as the wing model's heater strip. Two 500 Watt incandescent lights were set up to illuminate the test section. The power of the lights was adjusted with the variac unit until a uniform lighting was present. The intensity of the illumination was checked with the image processor. A video camera was positioned to record the color response of the calibration piece along with a voltmeter readout of the thermocouple voltage in the same field of view.

It is important to mention now that ideally the position of the lights should remain constant for both the liquid crystal calibration and the actual heat transfer experiments. For the current experimentation, however, it was necessary to slightly shift the lighting between tests. This was necessary since many different angles of attack were studied, and it was not practical to calibrate the liquid crystals for every different configuration. Had the lighting not been shifted, there would have existed regions of shadow at certain chordwise locations of the airfoil for the different angles of attack. While this slight shifting of the lights was not ideal, it was not expected to greatly affect the measurements. In fact, Kim found that the intensity of a pixel analyzed by the image processor did not greatly affect the measured hue value, the parameter to which the temperature is directly related. In performing a series of experiments in which he varied the intensity of the illumination of a liquid crystal coated surface, Kim discovered that the liquid crystal hue versus temperature linear slope calibration did not shift by more than ± 0.1 °C along the temperature axis. He summarized, "It was concluded that by significantly changing the intensity of illuminating light, the local hue values did not vary in a strong manner" (Kim, 1991).

The calibration piece was next heated through the event temperature range of the liquid crystals by using a Proheat heat gun. The wind tunnel windows were sealed just as would be the case when the airfoil is exposed to flow. The cooling of the calibration piece back down through the liquid crystal color event temperature range was videotaped. This transient process occurred in approximately 15-25 seconds. Had a better insulating material been used for the calibration piece, this time perhaps could have been increased.

Using the image processor, video images of this cooling process were captured one at a time. The pixel overlaying the thermocouple sensor location was analyzed for hue information. The instantaneous thermocouple voltage was converted to a temperature value through the calibration slope of the thermocouple. This process was repeated for many frames of the video, and a hue versus temperature calibration graph was constructed as shown in Figure 4.34.

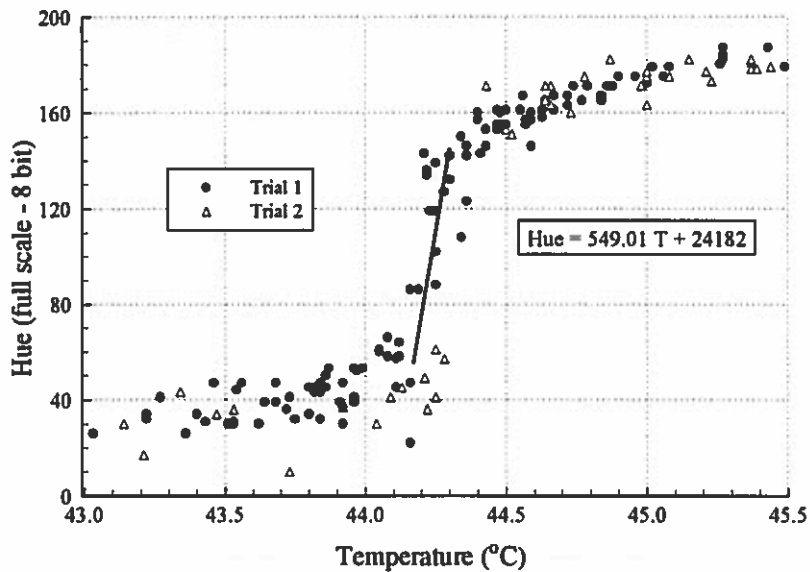


Figure 4.34: Liquid Crystal Calibration Graph

A useful linear range exists for this particular liquid crystal mixture between hue values of 55 and 145. A line was drawn through this range, and its slope found to be 549 per °C. The data are also seen to be repeatable from this graph. The scatter in the hue values is due to the noise level inherent in commercially available CCD sensors (Mauldin, 1996). From the experimental scatter, the uncertainty in the calculation of a temperature value from a hue value in the linear range may be estimated as ± 0.15 °C. However, factoring in the uncertainty in the thermocouple measurement (estimated as ± 0.1 °C), the overall uncertainty in the liquid crystal calibration is ± 0.25 °C for a given hue value falling in the linear range.

To perform a thorough liquid crystal calibration, Kim recommends that a plot of hue versus intensity also be constructed (Kim, 1991). He regards this as a useful tool in setting up the lighting for a successful heat transfer experiment. Kim explains that color image sensors do not provide accurate hue values if the local intensity drops below a value of approximately 50. Also if the local intensity exceeds 200, the accuracy of the hue values determined by the image processor suffers due to the saturation of the CCD sensor.

Thus a hue versus intensity plot should be included in the calibration of liquid crystals to examine whether these intensity boundaries are exceeded. If the local intensity values drop below 50 or climb above 200, the lighting should be adjusted and the calibration repeated. Ideally, Kim suggests intensity levels between 100 and 150 (Kim, 1991).

Such a plot was made for the current liquid crystal calibration as seen in Figure 4.35. The intensity values are not in violation of Kim's recommendation for a good liquid crystal calibration. For the most part, they fall into Kim's ideal range of 100 to 150.

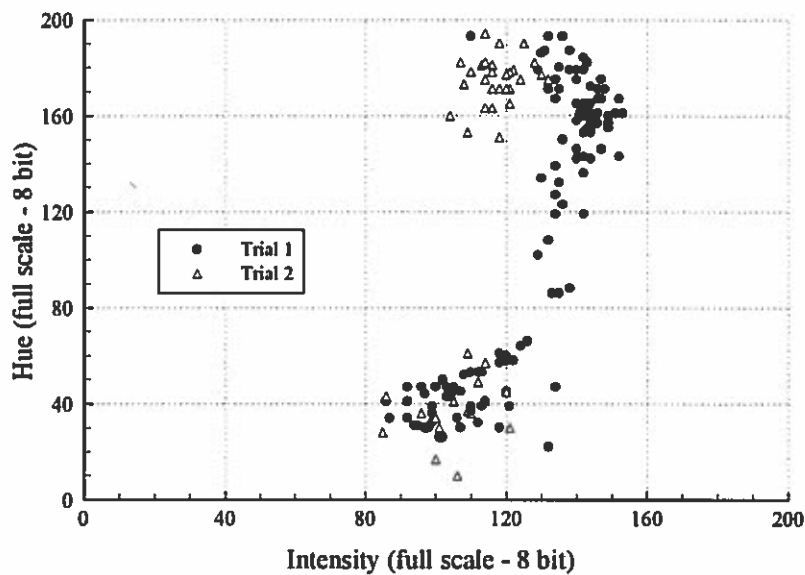


Figure 4.35: Hue Versus Intensity Check for Liquid Crystal Calibration

4.2.15 LSLTT Experimental Procedure

Tests were conducted for Reynolds numbers of 315,000 and 750,000. Angles of attack tested included 0, 5, 10, 15, 18, and 20°. The experimental procedure followed that used during the ASWT tests (Section 4.2.10) with a few differences. Computerized data acquisition was used for the LSLTT tests, and instead of recording the output of a single internal thermocouple, the array of eight thermocouples was monitored. The FORTRAN code used to analyze the images taken during experimentation and to calculate the

convective heat transfer coefficients may be found in Appendix C. It is named apbwng.for.

4.2.16 LSLTT Heat Transfer Results

Figures 4.36 to 4.44 contain the heat transfer results of the LSLTT tests. In addition to heat transfer information, each graph contains the corresponding oil flow visualization results as previously presented in Table 4.1 of Section 4.1.4. Easy comparisons can now be made between the heat transfer method and the oil flow visualization results.

The first area to be discussed is the validity of the experimental approach. The theoretical heat transfer distributions (discussed in Chapter 3.0) are included in Figures 4.36 to 4.41. These figures cover angles of attack of 0, 5, and 10°. No predictions were made for the cases of $\alpha = 15, 18$, or 20° . Two reasons exist for not making predictions at those angles of attack. First, the six predictions that were made adequately verified the experimental procedure as can be seen in Figures 4.36 to 4.41. In general, good agreement exists between the predicted h distributions and the experimentally determined h distributions. It should be mentioned that fluctuations in a small region near the stagnation point existed for the predicted h distributions (not shown on the graphs). These sudden variations were most likely caused by the rapid initial development of the boundary layer and the finite grid size in the x direction and in the y direction (normal to the airfoil surface). The influence of initial disturbances on the results presented for the rest of the airfoil is reported to be minimal (Crawford and Kays, 1975).

The predicted h distributions are also seen to mark the location of the laminar separation point fairly well. The parabolic nature of the boundary layer equations causes STAN5, the boundary layer code employed, to stop calculations when a reverse flow region is first predicted.

The second reason for not making h predictions for angles of attack of 15°, 18°, and 20° is because at higher angles of attack, gross separation exists on the airfoil. The potential flow solution will suffer greatly at those higher angles of attack since the panel code used for the inviscid calculations can not take separation into account. This poor potential flow solution will lead to errors in the predicted h distributions. Since the main

purpose of making theoretical predictions was to verify the experimental method (which had been accomplished at the lower angles of attack), no effort was made to obtain accurate h predictions at the higher angles of attack.

Figures 4.36 and 4.37 also contain flat plate laminar and turbulent heat transfer distributions under the appropriate test conditions. The predictions were made using the Reynolds analogy relating convective heat transfer to skin friction, equation 4.8. The skin friction coefficients were calculated using the Blasius solution for the laminar case (equation 4.9) and an empirical equation suggested by McLaughlin (Neumann and Hayes, 1986) for the turbulent case (equation 4.10).

$$St = \frac{h}{\rho U_s c_p} = \frac{C_f}{2 \Pr^{2/3}} \quad (4.8)$$

$$C_f = \frac{0.664}{\sqrt{\text{Re}_x}} \quad \text{laminar flow} \quad (4.9)$$

$$C_f = \frac{0.0592}{\text{Re}_x^{1/5}} \quad \text{turbulent flow} \quad (4.10)$$

These flat plate predictions further verify the experimental method employed by predicting the measured h data range with reasonable success. A more accurate differential boundary layer prediction method (STAN5) produces very good agreement with the h data from the low turbulence wind tunnel environment of the LSLTT.

ASWT data shown in Figure 4.36 can be taken as a higher free stream turbulence version of the experiment performed in the LSLTT. The trends in the h distributions are very similar for both turbulence intensity levels, but the higher turbulence intensity in the ASWT leads to higher values of measured convective heat transfer coefficient. It is evident from the data of Figure 4.36 that the free stream turbulence intensity level has a large effect on the measured heat transfer data. Definitive conclusions regarding free stream turbulence intensity effects can not be made because, in addition to the different T_u levels in the ASWT and the LSLTT, there are also different solid and wake blockage effects occurring in the two tunnels (see results of oil flow visualization in Section 4.1.3).

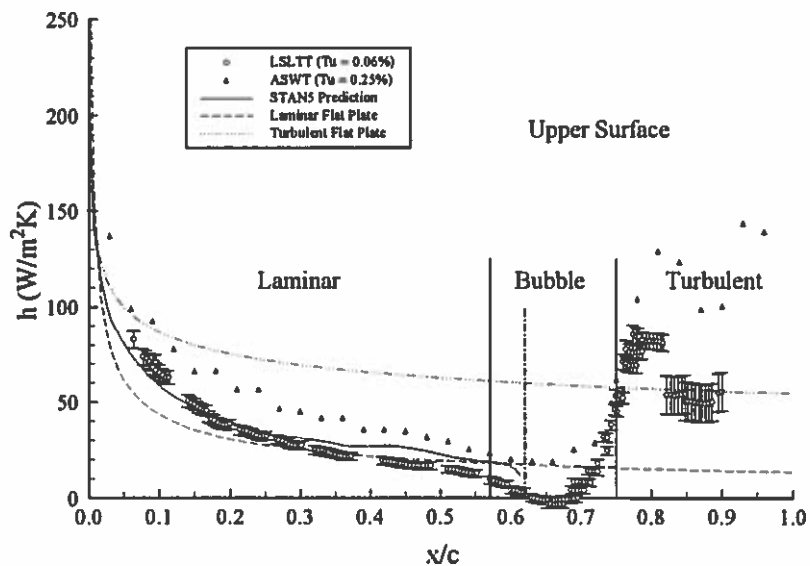


Figure 4.36: h Map for $\alpha = 0^\circ$, $Re = 315,000$

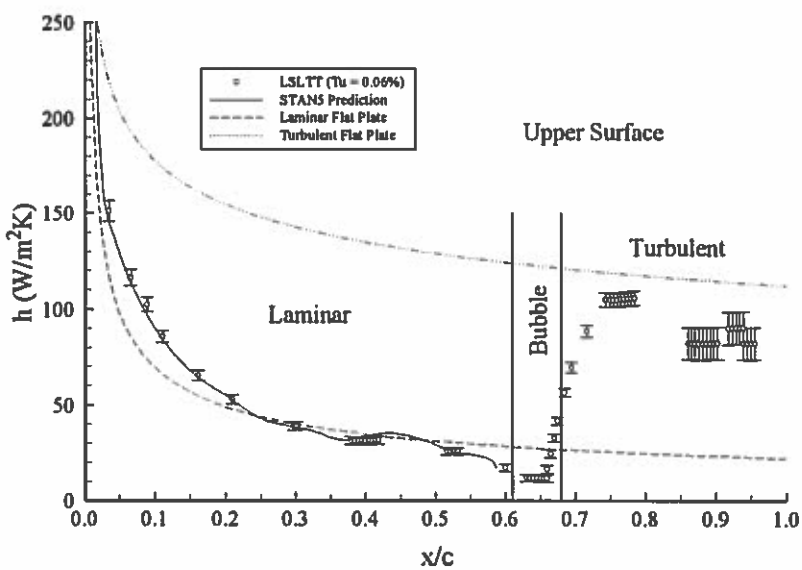


Figure 4.37: h Map for $\alpha = 0^\circ$, $Re = 750,000$

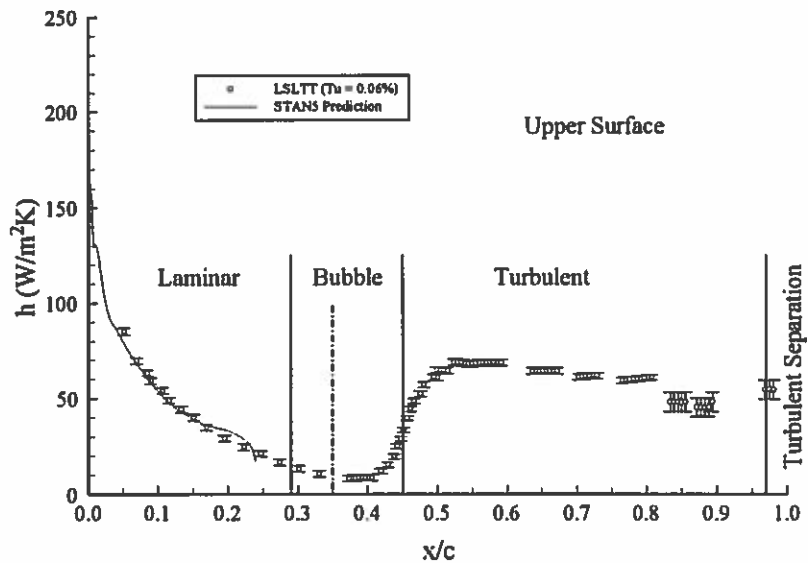


Figure 4.38: h Map for $\alpha = 5^\circ$, $Re = 315,000$

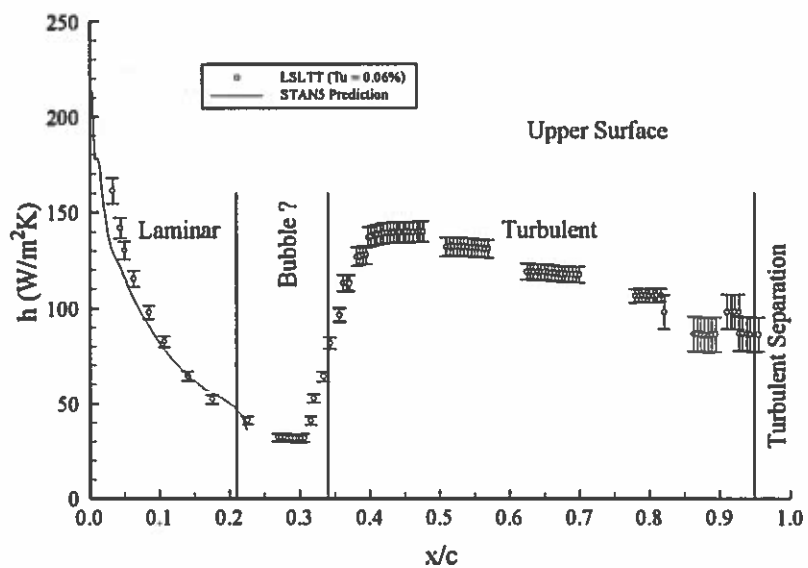


Figure 4.39: h Map for $\alpha = 5^\circ$, $Re = 750,000$

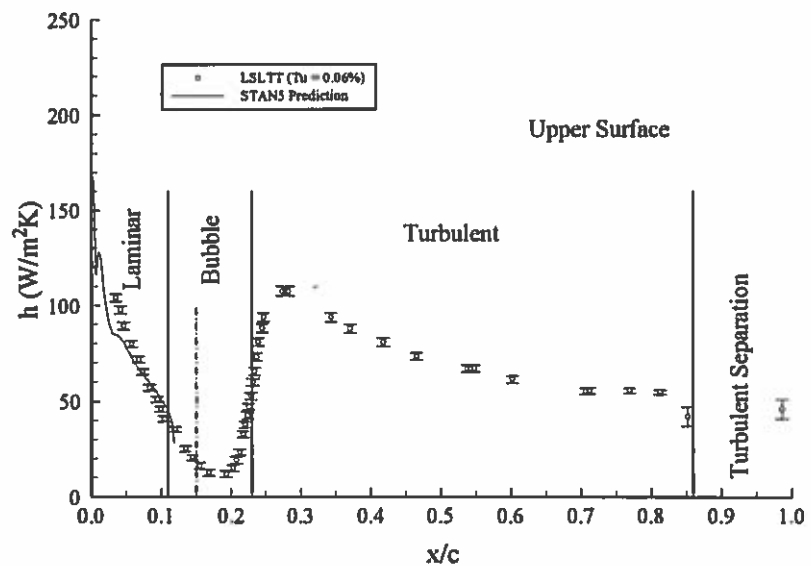


Figure 4.40: h Map for $\alpha = 10^\circ$, $Re = 315,000$

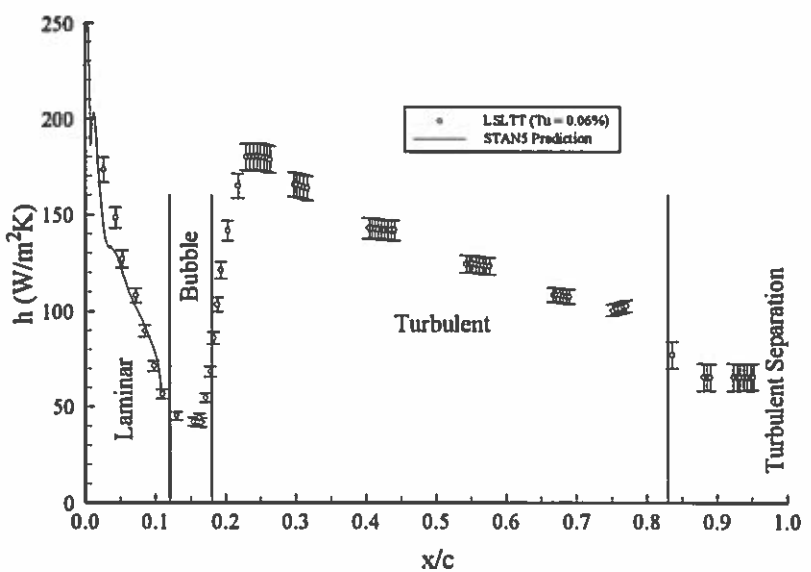


Figure 4.41: h Map for $\alpha = 10^\circ$, $Re = 750,000$

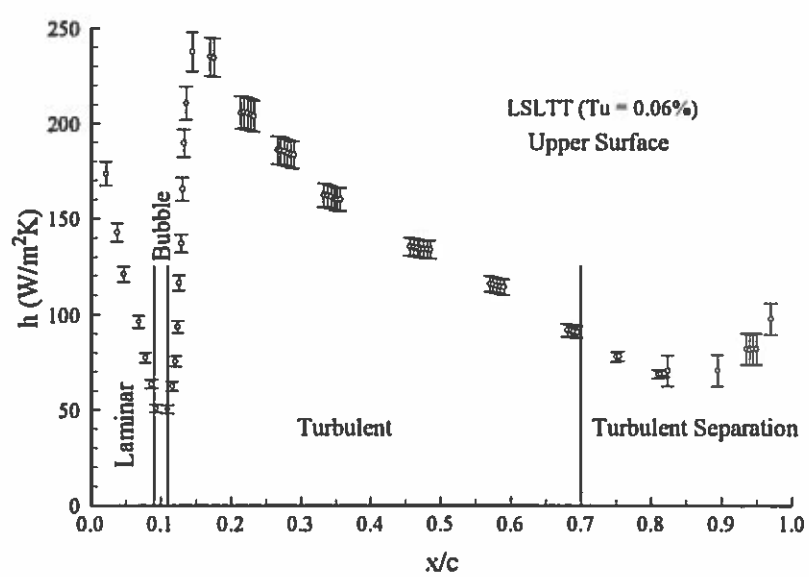


Figure 4.42: h Map for $\alpha = 15^\circ$, $Re = 750,000$

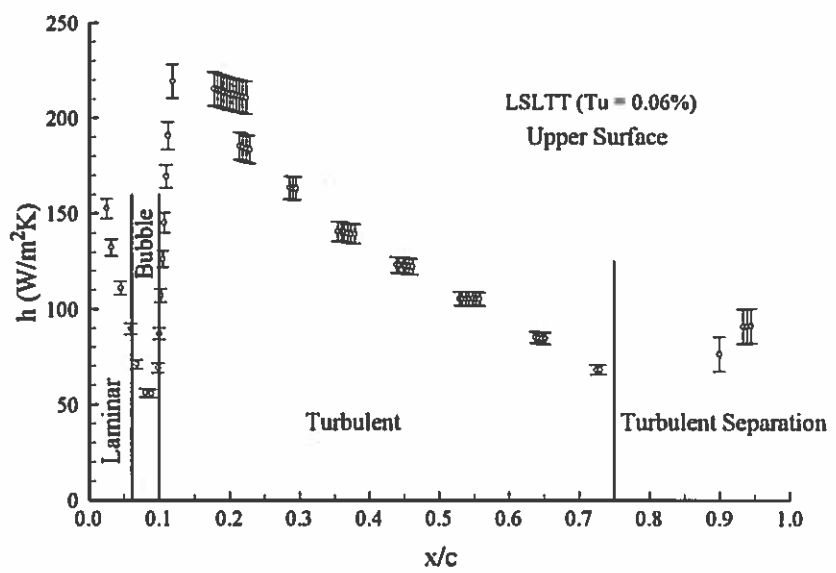


Figure 4.43: h Map for $\alpha = 18^\circ$, $Re = 750,000$

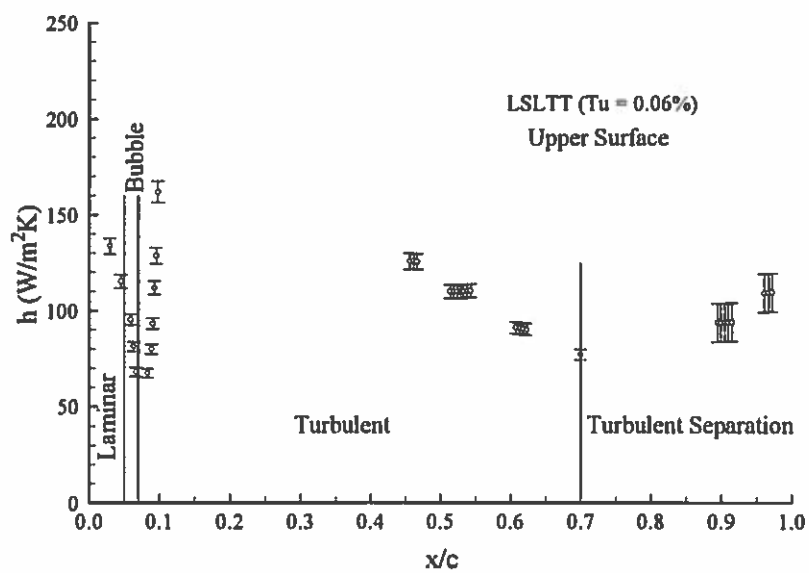


Figure 4.44: h Map for $\alpha = 20^\circ$, $Re = 750,000$

(NOTE: Image processor malfunctioned during test resulting in incomplete data.)

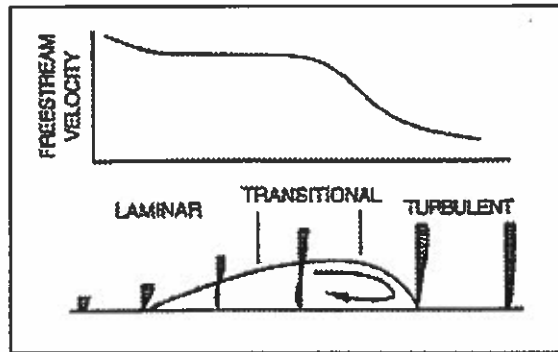
The main reason for performing the heat transfer experiments was to determine if the h maps could provide a good quantitative description of different flow regions existing on the airfoil. This topic will now be explored.

Examining Figures 4.36 to 4.44, it is seen that the laminar regions are marked on the h maps by a decaying trend. This trend is a result of the developing thermal boundary layer. The turbulent regions are also seen to display a decaying trend in the h distribution for the same reason as mentioned for the laminar boundary layer. The laminar and turbulent regions are seen to be well marked by the heat transfer method. Results concerning the separated regions are more unclear.

Regarding laminar separation bubbles, the heat transfer method does not do a good job in revealing the onset of separation. Only in Figure 4.36 does a somewhat noticeable change in the h distribution occur at the laminar separation point. The h distribution reveals no indication of laminar separation for any of the other experimental cases as seen in Figures 4.37 to 4.44.

This general failure of the heat transfer method to indicate laminar separation can possibly be explained by examining the nature of the forward portion of the laminar separation bubble and the laminar flow leading up to it. In general, the momentum of the fluid particles in the laminar flow approaching the separation bubble is being overcome by viscous and adverse pressure effects. By the time laminar separation occurs, the laminar boundary layer has been drained of most of its momentum. Laminar separation then does not bring about a drastic change to the near wall flow properties.

Now, looking into the laminar separation bubble, Malkiel and Mayle found that the forward portion of a laminar separation bubble is a constant pressure region which grows rather slowly (Malkiel and Mayle, 1996). As can be seen in Figure 4.45, a nearly constant free stream velocity exists over the forward portion of a laminar separation bubble. Because of this relatively unchanging velocity and the extreme thinness of the laminar separation region at the bubble's onset, the heat transfer characteristics would not be expected to radically alter at the beginning of the bubble. The data of Figures 4.37 to 4.44 reflect this hypothesis.



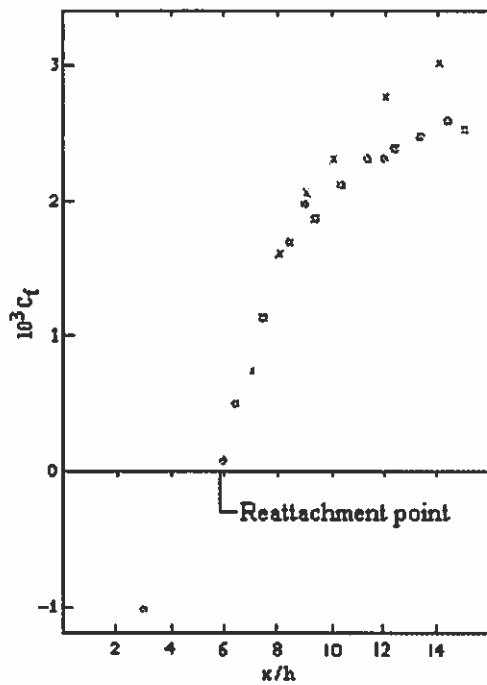
Source: Malkiel and Mayle, 1996

Figure 4.45: Velocity Distribution over a Separation Bubble

The flow reattachment at the end of the laminar separation bubble as marked by the oil flow visualization method is seen to occur in the region of the h distribution that exhibits the largest heat transfer coefficient gradient. This is especially obvious in Figures 4.36 to 4.41 in which large laminar separation bubbles exist. The local maximum heat transfer coefficient is seen to exist slightly downstream of the reattachment location. Rivir et al. (1994) found a similar result when examining a turbulent reattaching flow on a flat plate. Flow separation in their case was induced by an adverse pressure gradient created by deflection of the wind tunnel wall. They report, "The heat transfer rate increased rapidly approaching reattachment with a peak occurring slightly downstream of the mean reattachment point" (Rivir et al., 1994).

It appears that after reattachment, the newly formed turbulent boundary layer must adjust to the presence of the wall before taking on the characteristics of a typical turbulent boundary layer. As a possible explanation for this observed heat transfer coefficient trend, the reattachment region of flow that separated on a backward-facing step is examined. Bradshaw and Wong studied such a flow (Bradshaw and Wong, 1972). At reattachment, they report, the shear layer splits. Part of the flow is deflected upstream into the recirculating flow region, while the outer region of the shear layer forms the attached boundary layer. This newly formed boundary layer retains characteristics of the shear layer until the altered boundary condition (i.e., the presence of the wall) propagates

through it. Thus in the flow region immediately after reattachment, the boundary layer relaxes back to the expected “law of the wall” turbulent velocity profile. In this relaxation region, the intermittency of the boundary layer changes from a typical shear layer value to a typical turbulent boundary layer value of one. In addition, in this relaxation region the mixing length scales change from values typical of shear layers to varying linearly with distance from the wall as is expected in a turbulent boundary layer. Finally, in the relaxation region the wall skin friction coefficient continues to increase as was shown by Yoo and Baik (1992) and by Chandrsuda and Bradshaw (1981). Looking at reattaching flow on a flat plate, Castro and Epik (1996) found a similar trend for the skin friction coefficient immediately after reattachment. Figure 4.46 shows this C_f trend in the reattachment region of flow over a backward-facing step.



Source: Chandrsuda and Bradshaw, 1981

Figure 4.46: C_f Trend After Flow Reattachment

For the current work, the convective heat transfer coefficient is seen to follow the same trend in the reattachment region as the skin friction coefficient was shown to follow by

past experimenters. These similar trends are expected when the Reynolds analogy relating h to C_f is recalled.

A final interpretation regarding laminar separation bubbles and convective heat transfer coefficients comes from examining Figures 4.36, 4.38, and 4.40. In Section 4.1.3 it was mentioned that fluorescent oil surface flow visualization seemed to indicate a division of the laminar separation bubble into two regions. Figures 4.36, 4.38, and 4.40 contain an estimate of the extent of these two regions of the laminar separation bubble. The position of the bubble is marked by solid vertical lines, and the border between the forward stagnant region and the aft circulation region of the bubble is shown with a dash-dot vertical line. These three experimental cases were the only instances in which the oil flow visualization photographs clearly revealed these two distinct regions of the laminar separation bubble. It appears from these three figures that the minimum in convective heat transfer coefficient lies slightly after the boundary between the forward stagnant region and the aft circulation region of the laminar separation bubble. It is apparently in the aft circulation region of the laminar separation bubble that the convective heat transfer coefficient begins its increase to a turbulent level. Figure 4.47 is a qualitative representation of this apparent phenomenon.

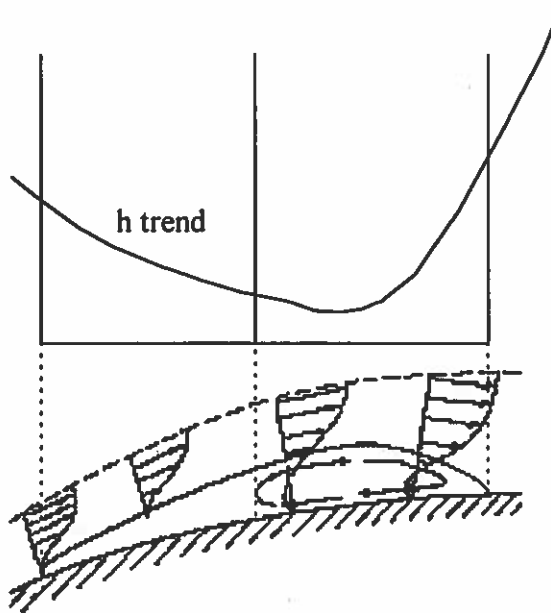


Figure 4.47: Convective Heat Transfer in a Separation Bubble

As has been discussed, the onset of laminar separation is not clearly revealed by the heat transfer method. However, Figures 4.36 to 4.44 clearly show that the separation bubble and the minimum heat transfer region are always coincident. The location of turbulent separation is also ambiguous from the heat transfer distributions. Figures 4.38 to 4.44 contain regions of turbulent separating flow. Figures 4.38 and 4.39 do not have sufficient h data in the turbulent separated region to make discussion meaningful. Therefore, the discussion will be restricted to Figures 4.40 to 4.44.

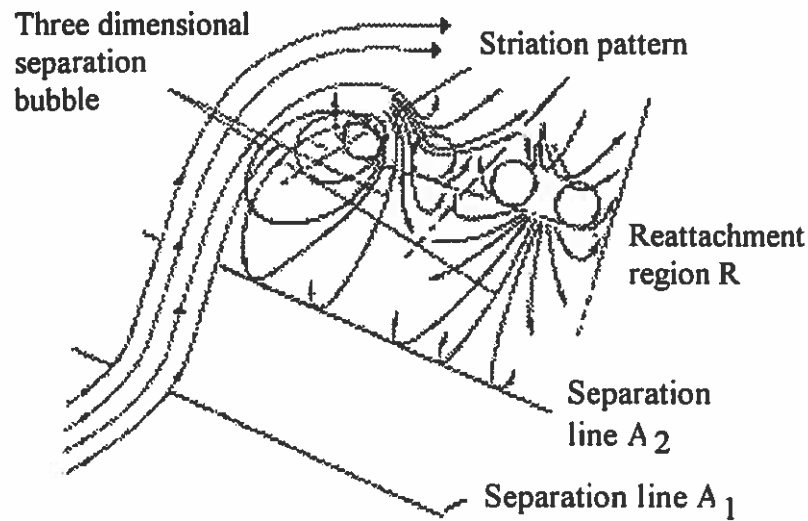
In Figures 4.40 and 4.41, the convective heat transfer coefficient appears fairly constant in the turbulent separated region. These two figures are for $\alpha = 10^\circ$, which for the Reynolds numbers considered is prior to stall. A different trend in h occurs after stall as can be seen in Figures 4.42 to 4.44 which are for $\alpha = 15^\circ$ (very near the stall angle), $\alpha = 18^\circ$, and $\alpha = 20^\circ$. A minimum in the h distribution exists in the turbulent separated region of those figures, and the convective heat transfer is being enhanced near the trailing edge. An explanation for this heat transfer enhancement will be offered in Section 5.1.6 which discusses results of qualitative shear stress experiments.

The location of the onset of turbulent separation is not clear from the heat transfer method. One possible explanation may lie in the nature of the turbulent separation. No distinct turbulent separation point really exists; turbulent separation is a very unsteady phenomenon. This was observed during the heat transfer tests by noticing "dancing" color patterns of the liquid crystals in the turbulent separated flow regions. The heat transfer method, however, was a steady state approach. Only a snapshot of this "dancing" color region at the turbulent separation location was taken and analyzed. Thus the time dependency of the separation location was lost, and the averaged h trend was found not to reveal the turbulent separation location.

Turbulent separation is also a three-dimensional phenomenon. The "dancing" separation region on the heater strip is not usually a two-dimensional line. It will be skewed at some angle (see, for instance, Figure 4.6c). However, the heat transfer coefficients were calculated based on two-dimensional columns of hue values on the strip. Thus a two-dimensional method was used on a three-dimensional flow phenomenon, yielding ambiguity in the turbulent separation location.

Now that the ability of the heat transfer method to provide flow region information has been explored by comparison to conventional oil flow visualization results, a few side topics will be explored. The first of these topics involves the formation of parallel, longitudinal vortices in the laminar separation bubble. Secondly, a comparison of the stagnation point region heat transfer results at a zero degree angle of attack will be made to theoretical cylinder-in-crossflow heat transfer predictions. Finally, a word of caution will be given regarding the heat transfer method employed.

Henckels, Kreins, and Maurer observed longitudinal vortices in the reattachment region of a laminar separation bubble on a flat plate in hypersonic flow (Henckels et al., 1992). The laminar separation was caused by the pressure gradient due to an oblique impinging shock wave. They explained that the concave curvature of the boundary layer in the reattachment region coupled with the instabilities of the laminar shear layer gave birth to these vortices. A qualitative sketch of these reattachment vortices, known as Görtler vortices, is given in Figure 4.48.



Source: Henckels et al., 1992

Figure 4.48: Schematic Interpretation of Streamwise Vortices at Reattachment

At a lower speed more relevant to the current experiments that were conducted, Jørgensen et al. detected small parallel vortices in the transition region on an A310 swept wing model with a constant chord (Jørgensen et al., 1992). Malkiel and Mayle describe counterrotating streamwise vortices forming in a laminar free shear layer (Malkiel and Mayle, 1996). These examples have been given because it is believed that the same phenomenon was observed during the present heat transfer experiments. Figure 4.49 shows a liquid crystal image taken during experimentation at $\alpha = 0^\circ$ and $Re = 750,000$. The indications of laminar separation and flow reattachment are taken from oil flow visualization results. Notice the diamond spanwise pattern on the heater strip at the flow reattachment location. A row of spanwise vortices would produce such a pattern of alternating hot and cold spots. Note that the color pattern from 90% to 100% chord is being affected by the trailing edge aluminum spar. However, the hot and cold spots are near 75% to 85%, locations where the internal features of the model do not interfere with the liquid crystal color patterns created by the flow.

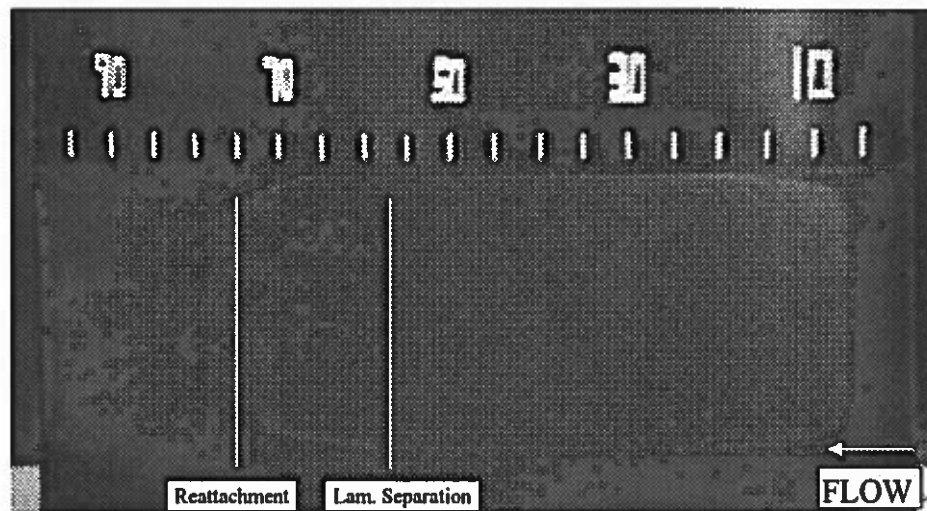


Figure 4.49: Evidence of Longitudinal Vortices at Reattachment

A second side topic is now explored. Computer codes often use cylinder-in-crossflow heat transfer values for the leading edge region of airfoils and turbine blades (Poinsatte and Van Fossen, 1990). An equivalent diameter for the airfoil's leading edge is first

determined, and then Frössling's analytical cylinder-in-crossflow solution (Frössling, 1958) is used to compute the heat transfer coefficients. For the cases of $\alpha = 0^\circ$ at $Re = 315,000$ and $750,000$, such analytical calculations were made. An equivalent leading edge diameter of 0.45 inches was found by inscribing a circle in the leading edge of the 12 inch chord SM701 airfoil. Results for the lower Reynolds number case are shown in Figure 4.50. The higher Reynolds number results are not shown because they exhibit similar characteristics to the results of Figure 4.50.

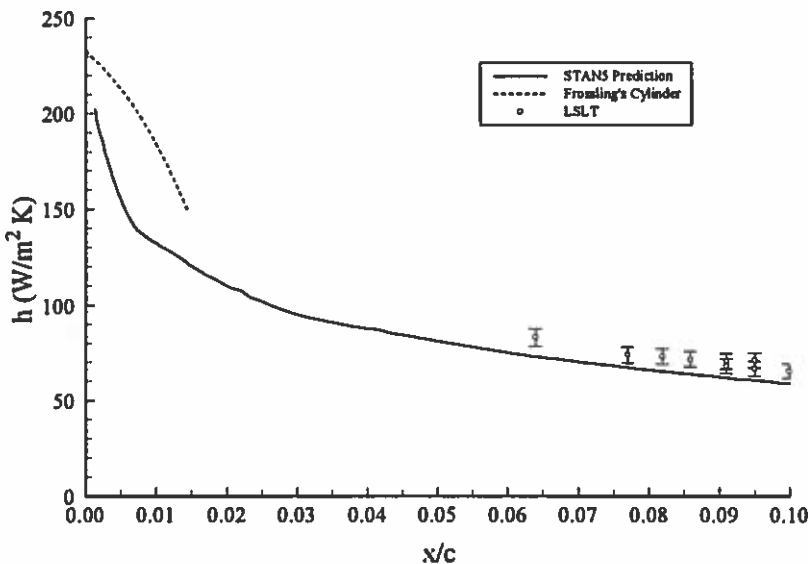


Figure 4.50: Comparison of Heat Transfer Results to Cylinder-in-Crossflow Predictions

As can be seen, experimental values are not available at the location where the analytical cylinder solution gives results. The STANS prediction, however, does provide comparison to the cylinder solution. In general, the cylinder-in-crossflow results over-predict the STANS results. Since the STANS prediction agrees fairly well with the experimental values where they are available, it is assumed that the cylinder-in-crossflow solution would over-predict experimentally determined h values as well very near the stagnation point. Poinsatte and Van Fossen found a similar over-prediction to occur for results on a NACA 0012 airfoil (Poinsatte and Van Fossen, 1990). From this discussion

the importance of experimentally determined heat transfer data is seen. The accuracy of the cylinder-in-crossflow analytical method is in question, and the analytical method only gives somewhat reasonable values very near the stagnation point.

A word of caution is now offered regarding the steady state heat transfer experiments performed. The experimenter must take great care in attaching the heater strip to the model being tested. Edges of the strip should "blend into" the model so as not to disturb the flow. Tests were conducted for the present study that included angles of attack of 15, 18, and 20° for $Re = 315,000$. However, no meaningful results could be obtained because the heater strip had a noticeable effect on the flow over it for those experimental conditions. This effect is seen in Figure 4.51 for $\alpha = 18^\circ$.

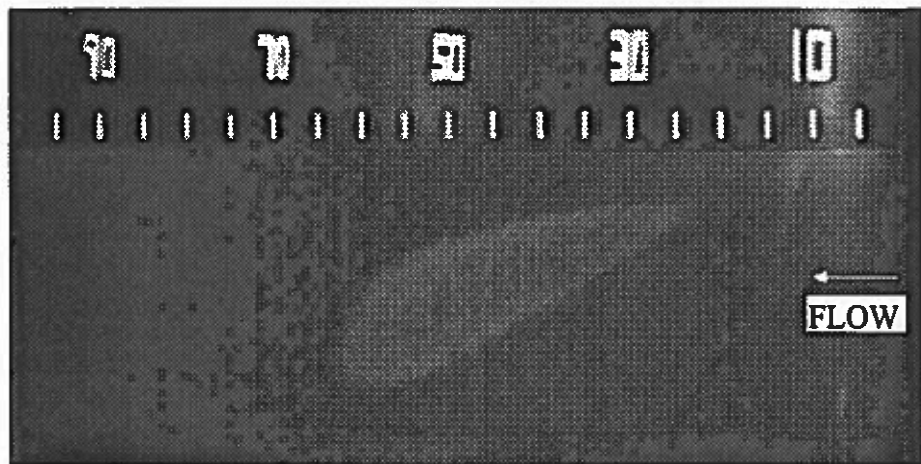


Figure 4.51: Heater Strip Negative Affect on Flow

A triangular color pattern has replaced the expected two-dimensional color pattern on the heater strip. The strip upper edge near the leading edge of the wing at about 5-10% chord seems to be causing a strong vortical structure that is greatly cooling the strip at a skewed angle. Referring back to Figure 4.5b of Section 4.1.3, the oil flow visualization picture hinted at this negative strip effect.

4.2.17 Conclusions from LSLTT Heat Transfer Measurements

Several conclusions may now be drawn regarding the success of the heat transfer method in revealing the various viscous flow regions on the SM701 airfoil. It was found that the heat transfer method predicts regions of laminar and turbulent flow fairly well as a decaying trend in the h distribution. The location of the laminar separation bubble as marked by the heat transfer method was consistent with the location as marked by the conventional oil flow visualization method; however, the beginning of the bubble (laminar separation) was not clearly marked by the heat transfer method as a distinct line. In addition, the turbulent separation location was also ambiguous when examining the heat transfer method.

The reattachment of the laminar separation bubble was shown by the heat transfer method to occur with the initially reattached boundary layer in a redeveloping state. It appears that after reattachment, the newly formed boundary layer requires a distance on the order of 5% chord to adjust to the presence of the wall and to take on the characteristics of a typical turbulent boundary layer. In this redeveloping region, the convective heat transfer coefficient continues to increase. This increase was clearly visualized by the liquid crystal method.

The conventional oil flow visualization method is much simpler to implement than the heat transfer method and requires much less time to execute. In addition, the oil flow visualization method marks the various viscous flow regions on the airfoil surface better than the heat transfer approach. The heat transfer method was of value, however, in that it verified the results of the oil flow visualization method and was shown, by comparison to numerical predictions, to provide accurate experimental airfoil heat transfer data. These data can serve as a benchmark solution for the development of better viscous flow and heat transfer prediction codes. The heat transfer method also gave insight into detailed flow structures that the oil flow visualization could not provide. These details include revealing a redeveloping boundary layer region immediately after flow reattachment and showing the presence of what is thought to be Görtler vortices.

4.2.18 LSLTT Heat Transfer Error Analysis

An estimate of the error in the heat transfer calculations was made using the Kline and McClintock method (Kline and McClintock, 1953). Using their approach, the uncertainty in the experimental values of h can be expressed as

$$\delta_h = \pm \sqrt{\left(\frac{\partial h}{\partial q''_{\text{TOTAL GENERATED}}} \delta_{q''_{\text{TOTAL GENERATED}}} \right)^2 + \left(\frac{\partial h}{\partial q''_{\text{COND}}} \delta_{q''_{\text{COND}}} \right)^2 + \left(\frac{\partial h}{\partial q''_{\text{RAD}}} \delta_{q''_{\text{RAD}}} \right)^2 + \left(\frac{\partial h}{\partial (T_{\text{wall}} - T_{\infty})} \delta_{(T_{\text{wall}} - T_{\infty})} \right)^2} \quad (4.9)$$

The uncertainty terms under the radical are found in an analogous manner by examining equations 4.4 to 4.6 of Section 4.2.3.2. The partial derivative terms come from differentiating equation 4.3 of the same section.

Using this uncertainty analysis method, estimates must be made of the uncertainties in the fundamental measurements such as length, voltage, and resistance. Table 4.3 contains the estimates used for this study.

Table 4.3: Estimates of Uncertainties in Measured Quantities

Symbol	Description	Uncertainty Estimate
$R_{\text{heater strip}}$	heater strip resistance	0.001 Ω
L	heater strip length	1/32 inch
W	heater strip width	1/32 inch
t_{wall}	wing wall thickness	0.015 inch
k_{wall}	thermal conductivity of model material	0.02 W/mK
ϵ	emissivity of black paint	0.02
T_{wall}	heater strip local temperature	0.25 $^{\circ}\text{C}$
T_{∞}	free stream temperature	0.2 $^{\circ}\text{C}$
T_2	model internal temperature	0.2 $^{\circ}\text{C}$
$V_{\text{heater strip}}$	heater strip voltage	0.001 V ($V < 3.25$) 0.010 V ($V \geq 3.25$)

Uncertainty in the convective heat transfer coefficient was calculated for every h, x/c experimental point during the execution of the data reduction program apbwng for listed in Appendix C. The uncertainty bars are seen in Figures 4.36 to 4.44 of Section 4.2.16. It should be mentioned that the uncertainty in the h measurements for chord locations of 82-100% was determined differently than for the rest of the chord locations. This was necessary since the internal array of eight thermocouples could not be positioned aft of 82% chord because of the internal geometry of the model. Specifically, the trailing edge spar and the aft bus bar occupied that internal region of the model. Since no internal temperature information was available in the 82-100% chord range, it was not possible to accurately determine the conduction losses in that region.

Conduction losses in the 82-100% region were estimated as an average percent of the total heat flux generated in that region based on the average percent conduction losses for chord locations 0-82%. Because of this additional uncertainty in the conduction losses for the 82-100% region, the total percent uncertainty in h in that region of the airfoil was estimated as twice the average percent uncertainty in h values for the region 0-82%. Therefore the error bars are larger for that region of the airfoil as seen in Figures 4.36 to 4.44 of Section 4.2.16.

Due to the large amount of data taken, it was not possible to examine all of the uncertainty results in detail. However, the case of $\alpha = 0^\circ$ at $Re = 315,000$ will be briefly mentioned.

The uncertainty in h for points located inside the laminar separation bubble (57-76% chord) is caused mainly by the uncertainty in the conduction loss term. In this region, the total heat flux is distributed as follows: ~65% conduction loss, ~20% radiation loss, and ~15% convection. The uncertainty in the conduction loss term is ~10%, while the uncertainties in the radiation loss term and the total heat flux generated term are ~4% and ~1%, respectively. This large uncertainty in the conduction loss term coupled with the fact that most of the heat generated is lost through conduction leads to large uncertainties in h values on the order of 30%.

In regions of high convective heat transfer, however, the story is different. Examining, for instance, the laminar flow region near the 15% chord location, the following values

were calculated. The total heat flux generated was divided as follows: ~20% conduction loss, ~10% radiation loss, and ~70% convection. The uncertainty in the conduction loss term, the radiation loss term, and the total heat flux generated term is ~10%, ~5%, and ~1%, respectively. The percent uncertainty in the conduction loss term is of the same order of magnitude as in the region of the laminar separation bubble, but since the conduction losses are now a much smaller percent of the total heat flux generated, the uncertainty in h falls to approximately 6%.

These calculated uncertainty values are summarized in Table 4.4. Wiedner's results for endwall heat transfer in a 90° turning duct are presented for comparison (Wiedner, 1994). He also performed steady state heat transfer measurements using liquid crystal thermography.

Table 4.4: Summary of Heat Transfer Uncertainty Analysis

	Location of Error Analysis		
	Laminar Separation Bubble	Laminar Region at 15% Chord	Wiedner Endwall of 90° Turning Duct
% Conduction Loss	~65	~20	~8
% Radiation Loss	~20	~10	~10
% Convection	~15	~70	~82
% u_{COND}	~10	~10	~8
% u_{RAD}	~4	~5	~3
% $u_{TOTAL GENERATED}$	~1	~1	~1
% u_h	~30	~6	~4

5 EXAMINATION OF POST-STALL FLOW INSTABILITIES

Now that the flow regions on the SM701 airfoil have been well established via oil flow visualization and convective heat transfer studies, work can proceed in the direction of active control of the gross separation region on the airfoil at various high angles of attack. Before success can be possible in active control of a complex flowfield, that flowfield must be well understood. This chapter, after presenting several background sections on flow instability and separation control, will discuss experiments aimed at uncovering the flow instability characteristics caused by the SM701 airfoil at high angle of attack. Both qualitative shear stress tests and quantitative single sensor hot-wire anemometry tests are used in this investigation. Due to the tight schedule of the LSLTT and the open schedule of the ASWT, tests were performed in the latter tunnel. Tests were conducted at a Reynolds number of 315,000 unless otherwise indicated.

5.0.1 Fluid Instability

The area of fluid dynamics involving flow instability has evolved in a different manner than other branches of the field. In particular, it has evolved “backwards” to what has been the norm. As early as 1895, Osborne Reynolds supposed that laminar velocity profiles, being solutions to the fluid dynamic equations of motion, always represent a possible type of flow but become unstable above a definite limit and change into a turbulent pattern (Schlichting, 1968). In the early years of the twentieth century, the Orr-Sommerfeld equation governing the growth of linear disturbances in a laminar boundary layer was derived. The Orr-Sommerfeld equation was simplified by examining its high-Reynolds-number (inviscid) form, known as the Rayleigh equation. In 1929, examining laminar flow over a flat plate (the Blasius profile), Tollmien adequately accounted for viscosity effects by first solving the Rayleigh equation and then using its solutions to help solve the Orr-Sommerfeld equation. Tollmien was able to calculate a neutral stability curve and from it a critical Reynolds number value for the Blasius profile at which small disturbances would first begin to grow. In 1933, Schlichting first studied the interior of the Blasius profile neutral stability curve, revealing details on the amplification of

disturbances of different wavelengths. These initial disturbances that appear in a laminar boundary layer have been termed Tollmien-Schlichting waves in honor of these two past researchers.

Linear stability theory thus allowed the prediction of dominant disturbances in laminar boundary layers. However, even in the late 1930's the prevailing view was that stability theory had little connection with boundary layer transition (Rice and Zaman, 1987). Not until Schubauer and Skramstad in 1947 revealed growing two-dimensional waves prior to transition in a flat plate boundary layer in their landmark experiment did stability theory become accepted as accurately modeling the linear processes leading to transition. (In actuality, their work was performed in 1943 but was kept confidential due to the involvement of the United States in World War II). This evolution of theory followed by experimental verification was opposite to the normal progression of experimental observation spawning a governing theory.

Many researchers have studied the two-dimensional Tollmien-Schlichting (T-S) waves that are now known to lead to transition. Experiments have been performed in which artificial T-S waves are introduced into a laminar boundary layer and are subsequently canceled by out-of-phase forcing at a downstream location. One such experiment was performed by Liepmann, Brown, and Nosenchuck who used heater strips on a flat plate (Liepmann, Brown, and Nosenchuck, 1982). The heater strips were powered by a source at certain frequencies. Partial cancellation was achieved when the downstream heater strip was driven out of phase of the upstream heater strip which was producing the original disturbances.

Flow instabilities do not only appear in attached boundary layers. For a laminar separated boundary layer, there exist instabilities that will amplify leading to transition to turbulence. A turbulent mixing layer will then exist which is dominated by large-scale coherent vortical structures (Brown and Roshko, 1974). These initial instabilities (termed Kelvin-Helmholtz instabilities) can be predicted with the Rayleigh equation which is the inviscid form of the more general Orr-Sommerfeld equation governing the linear stability of parallel flows.

Turbulent separated boundary layers also form mixing layers that contain dominant large-scale coherent vortical structures. In 1974 Winant and Browand showed that the growth of turbulent mixing layers is controlled by a pairing of the coherent vortical structures (Winant and Browand, 1974). It is believed today that this pairing phenomenon holds the key to actively controlling a turbulent mixing layer. The next section presents many reasons as to why it is desired to control the turbulent mixing layer, or in other words why it is desired to control flow separation.

5.0.2 Importance of Separation Control

The performance of air, land, and sea vehicles is dependent on their interaction with the fluid surrounding them. Separated flow regions are not usually desired and adversely influence the efficiency of the vehicle. Separation affects the performance of turbomachinery, diffusers, inlets, and other systems involving fluid flow. It is usually desired to postpone separation so that form drag is reduced, stall is delayed, lift is enhanced, and pressure recovery is improved (Gad-el-Hak and Bushnell, 1991).

Separation control will lead to more efficient propellers and windmills, more efficient inlets and diffusers, increased $c_{l_{max}}$ of airfoils, improved axial flow compressors, reduced engine noise, shorter runways and reduced approach speeds, supermaneuverability, better stall control, and lower drag on automobiles, ships, and aircraft (Gad-el-Hak and Bushnell, 1991). If flow separation control can provide a 5% increase in landing $C_{L_{max}}$, Butter estimates a 25% increase in payload would be realized (Butter, 1984). Muirhead and Saltzman estimate that 50 million barrels of oil per year could be saved if flow separation control on tractor-trailer trucks would become practical (Muirhead and Saltzman, 1979).

5.0.3 Approaches To Separation Control

Separation occurs when the motion of fluid particles is retarded by viscous effects and adverse pressure gradient effects such that the surface streamline can no longer follow the curvature of the surface. The main goal of separation control is thus to add momentum back to the near-wall region by transferring kinetic energy from the energy-rich free stream region. Two different approaches can be taken to provide separation control:

interaction with the attached boundary layer prior to separation or interaction with the separated shear layer.

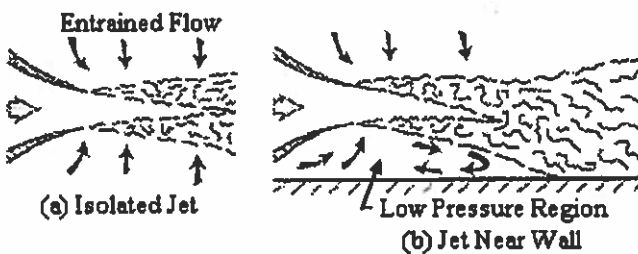
Many methods have been used to interact with the boundary layer before it separates. Gad-el-Hak and Bushnell provide many valuable references on this subject (Gad-el-Hak and Bushnell, 1991). Transpiration has been used to make the boundary layer fuller, thus prolonging the attached flow region. In addition, surface heating or cooling has been used to add momentum to the near-wall region. By cooling the wall (in gas), the viscosity of the gas in the boundary layer is lowered and its density is raised; this leads to a fuller boundary layer profile (Liepmann, Brown, and Nosenchuck, 1982).

Embedded cylinders and conveyor belts have also been used to energize the boundary layer flow. Trip strips (at low Re) and vortex generators (at high Re) are also used to energize the boundary layer, delaying separation. A main problem with these methods of separation control is that they utilize intrusive devices that have associated drag penalties. Energy consumption, weight, volume, reliability, and cost are also factors that must be examined when looking at separation control.

The second approach that can be taken to provide separation control is enhancement of the mixing rate of the separated shear layer. Acoustic drivers, oscillating flaps and wires, dynamic blowing, and oscillatory surface heating are among the methods that have been tried to excite the instabilities of the separated shear layer. Gad-el-Hak and Bushnell emphasize that this mixing rate enhancement of the separated shear layer can provide separation control for both laminar and turbulent separating boundary layers. They report, "For initially laminar flows, the zeroth order influence of dynamic forcing is to both trip transition and enhance the eddy dynamics of the low-Reynolds-number shear layer" (Gad-el-Hak and Bushnell, 1991). They also report, "What is obvious from the initially turbulent, dynamic-input separation control research thus far is that, once again, the method works" (Gad-el-Hak and Bushnell, 1991).

Rice and Abbott offer an explanation as to why this dynamic forcing of the separated shear layer provides separation control (Rice and Abbott, 1990). They explain that by enhancing the natural instabilities of the flow through use of small aerodynamic disturbances, the growth of the large-scale coherent structures which dominate the mixing

process in the shear layer will be enhanced. This enhancement of the large-scale coherent structures can lead to flow reattachment. Rice and Abbott explain this idea using the concept of the Coanda effect. Figure 5.1a shows an isolated jet. Entrainment occurs due to the free mixing layer, and fluid is drawn in from the ambient field on both sides to replace that which has become entrained by the jet. When the jet is placed near a wall, however, the situation changes. See Figure 5.1b. Entrainment is retarded near the wall since fluid can not be readily replaced due to the obstruction caused by the wall. A low static pressure region develops between the wall and the jet. This resulting pressure gradient forces the jet towards the wall.



Source: Rice and Abbott, 1990

Figure 5.1(a) and (b): The Coanda Effect (Surface Located Near a Jet)

The idea of separation control through enhancement of the mixing rate of the separated shear layer on an airfoil can then be explained using an analogy to the jet example. Refer to Figure 5.2. By applying excitation to the separated shear layer, the natural eddy formation and pairing process can be enhanced. By creating larger and more-coherent eddies in the separated shear layer, more entrainment will occur than would be the case for the unforced separated shear layer. Due to the presence of the surface of the airfoil, entrainment will be inhibited between the separated shear layer and the airfoil surface. A low static pressure region will develop, pulling the separated shear layer towards the airfoil surface. The separated region will be reduced. It can now be seen why separation control involving dynamic forcing of the separated shear layer is viewed as a mixing enhancement problem.

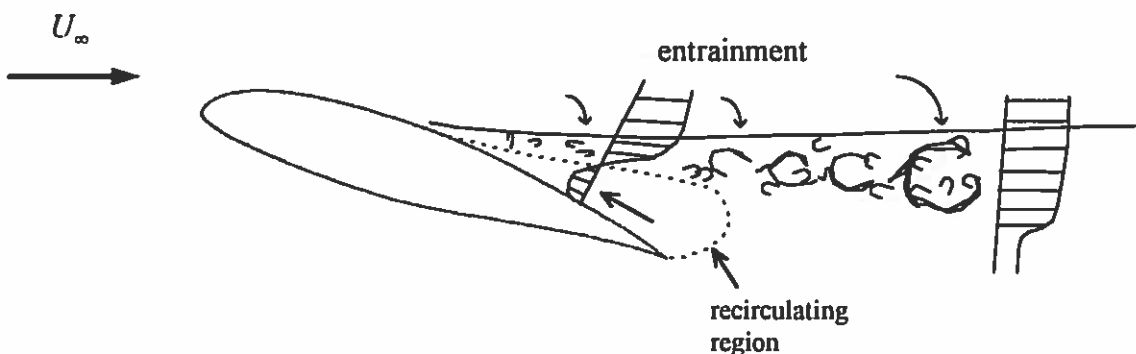


Figure 5.2: Airfoil Flow Separation

Figure 5.3 summarizes the two main approaches to separation control that have just been discussed. The following section discusses past work in the active control of separated shear layers.

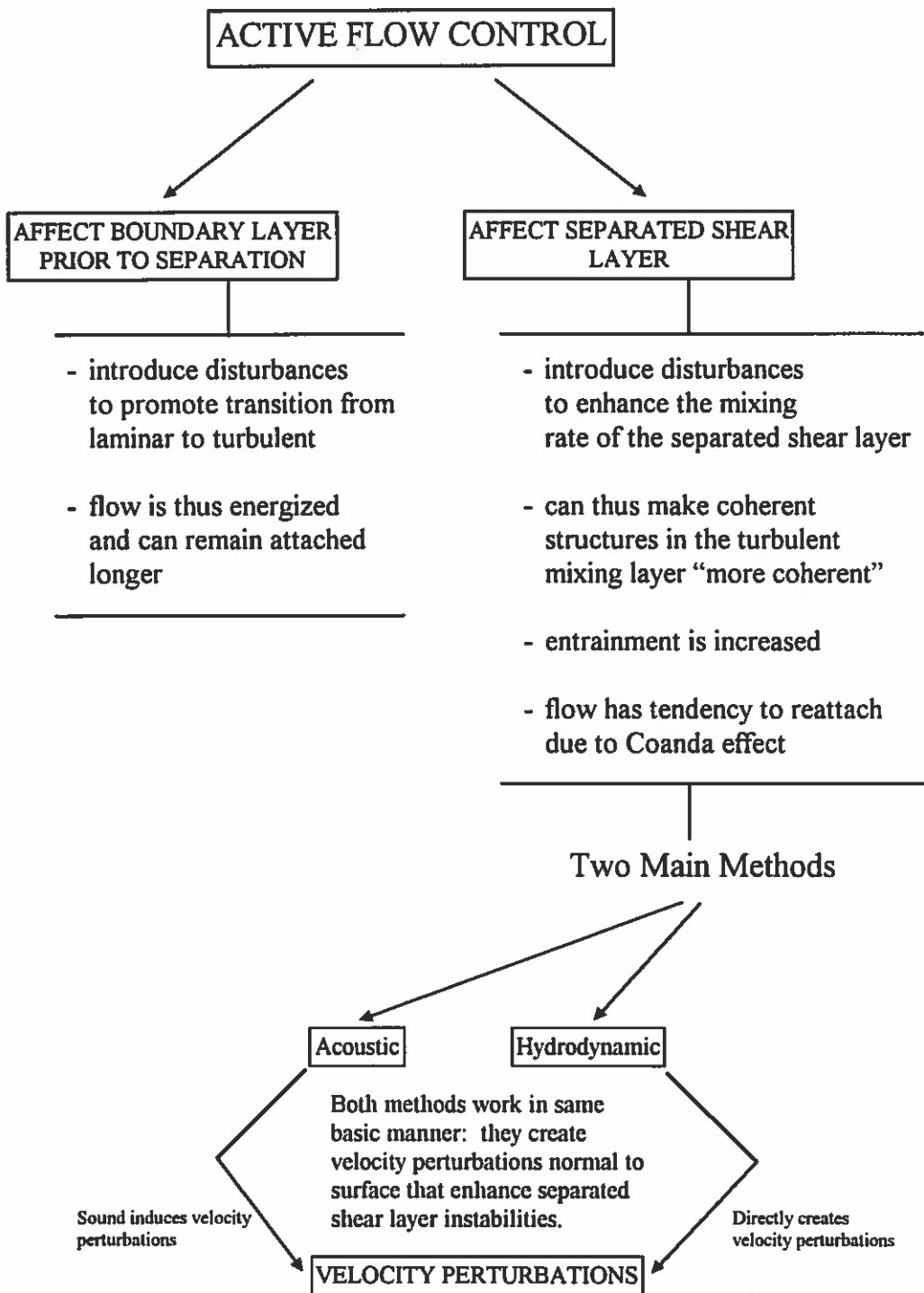
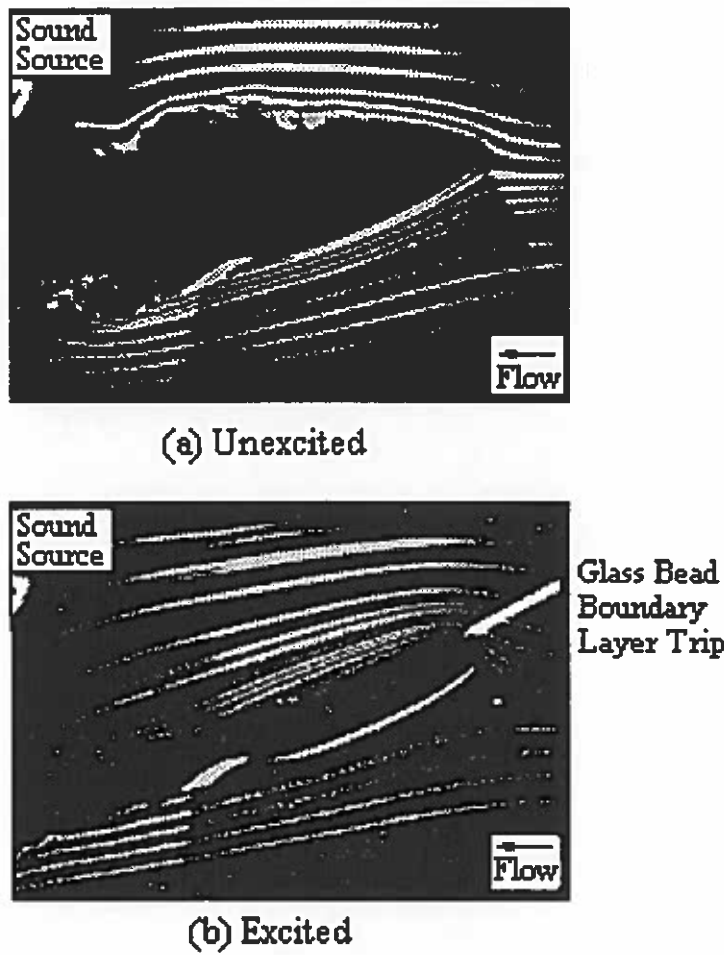


Figure 5.3: Summary of the Two Main Separation Control Approaches

5.0.4 Past Work in Control of Separated Shear Layers

This section will describe some of the past work performed in the area of active control of separated shear layers. Gad-el-Hak and Bushnell provide an extensive list of references regarding flow separation (Gad-el-Hak and Bushnell, 1991).

In 1983 Ahuja, Whipkey, and Jones successfully demonstrated that sound at the “right” frequency and sufficient amplitude could postpone the turbulent separation on an airfoil in both the pre-stall and post-stall regimes (Ahuja et al., 1983). An often-reproduced flow visualization photograph taken from their work is shown in Figure 5.4. Similar research was performed by Ahuja and Burrin in 1984 (Ahuja and Burrin, 1984).



Source: Ahuja et al., 1983

Figure 5.4: Flow Reattachment Caused by Sound

Acoustic excitation was also used by Zaman, Bar-Sever, and Mangalam in 1987 (Zaman et al., 1987). They tested an LRN-(1)-1007 airfoil at Reynolds numbers varying between 40,000 and 140,000. An acoustic driver provided sound through a hole in the test section floor. Appropriate excitation was able to eliminate laminar separation at the low Reynolds numbers tested. Just prior to stall at $\alpha = 15^\circ$, a modified Strouhal number of approximately 0.02 was measured based on the airfoil "shedding frequency," or in more precise words based on the frequency of the dominant flow instability created by the airfoil under the conditions at which it was tested. The modified Strouhal number is defined as

$$St_{\sin \alpha} = \frac{f_s c}{U_\infty} \sin \alpha \quad (5.1)$$

with f_s being the measured shedding frequency (dominant instability frequency), c the wing chord, U_∞ the free stream velocity, and α the angle of attack. This value of 0.02 is an order of magnitude lower than most other researchers have found for tests with other airfoils at high angle of attack and for bluff bodies. Follow-up work by Zaman and McKinzie in 1988 again found this low value of 0.02 prior to stall. During deep stall ($\alpha = 18^\circ$ and $\alpha = 20^\circ$), the usual "bluff body" shedding value of 0.2 was measured. Zaman and McKinzie concluded that the unusually low value of 0.02 prior to stall was caused by periodic formation and breakdown of a large separation bubble (Zaman and McKinzie, 1988).

Zaman and McKinzie also experimented with acoustic excitation in 1989 (Zaman and McKinzie, 1989). They studied the laminar separation at $\alpha = 6^\circ$ for an LRN-(1)-1007 airfoil and a Wortmann FX 63-137 airfoil. The LRN-(1)-1007 is a trailing edge stall type airfoil, while the Wortmann FX 63-137 is a leading edge stall type airfoil. Zaman and McKinzie were able to reduce the laminar separation on the upper surface. For this low α case, tests were conducted at Reynolds numbers between 25,000 and 100,000. The most effective excitation frequency varied as $U_\infty^{3/2}$ and was found to obey

$$\frac{St}{Re^{1/2}} = 0.02 \text{ to } 0.03 \quad (5.2)$$

with

$$St = \frac{f_{excitation} c}{U_\infty}.$$

At NASA Lewis Research Center, Zaman and Rice studied four different airfoils at small α and low Reynolds numbers. They found that acoustic excitation at about $\frac{f_{excitation} V}{U_\infty^2} = 10^{-5}$ was effective in removing laminar separation.

Huang, Maestrello, and Bryant used the technique of internal acoustic excitation to study the effect of sound on a separated shear layer (Huang et al., 1987). Sound was emitted through a spanwise 0.08 cm gap at $x/c = 15\%$ on the upper surface of a symmetric airfoil at a Reynolds number of 35,000. The angle of attack was 20° . At $f_{excitation} = 2f_s$, the separated region was drastically reduced. For $\alpha = 20^\circ$ the shedding frequency (dominant instability frequency) was 50 Hz, and the modified Strouhal number was 0.19. Excitation was applied at 115 dB, and an increase in lift, a reduction in drag, and a delay in stall were observed. Smoke flow visualization showed that separation over the upper surface of the airfoil is dominated by large-scale vortices shed periodically from the separation point. These vortices trigger large-scale circulatory motion in the wake of the airfoil and depend on the mean flow speed.

Huang, Bryant, and Maestrello also examined the effect of internal acoustic excitation on trailing edge separation (Huang et al., 1988). A symmetric airfoil with an 18% thickness ratio was tested at a Reynolds number of 35,000 with $\alpha = 0^\circ$. Sound emitted through a 0.08 cm slot near the trailing edge was seen to lessen the separated region by exciting large-scale structures in the separated shear layer. The optimum forcing frequency equaled the shedding frequency, and it was concluded that forcing was more effective when applied slightly before separation rather than after.

Hsiao, Liu, and Shyu also examined how the location of the localized internal acoustic excitation slot affected the ability of the sound to enhance a separated shear layer (Hsiao et al., 1989). They tested a NACA 63₃-018 airfoil for $6,300 < Re < 500,000$. A sound

pressure level (SPL) of 95 dB was maintained, and one millimeter wide slots at 1.25%, 6.25%, and 13.75% chord were used to emit the sound. Leading edge separation for α up to 24° was examined. It was found that excitation frequency and location were the most important control parameters. Excitation level was not as important. The best location for local acoustic excitation seemed to be slightly after the separation point. The most effective forcing frequency corresponded to a modified Strouhal number of two, an order of magnitude higher than the shedding frequency based modified Strouhal number. Hsiao et al. reasoned that the excitation “locks-in” to the shear layer instability frequency which is approximately one order of magnitude larger than the shedding frequency. Lift was increased and drag was decreased.

Hsiao, Shyu, and Chang returned to work on the NACA 63₃-018 airfoil in 1994 (Hsiao et al., 1994). They examined the effect of internal acoustic excitation through a 0.8 mm wide slot at 1.25% chord on the stalling performance at high post-stalled angles of attack ($\alpha > 24^\circ$). At $Re = 310,000$, leading edge separation existed. The modified Strouhal number was found to agree well with Roshko’s bluff body universal value of 0.17 to 0.19 (Roshko, 1954) for $24^\circ < \alpha < 35^\circ$. Hsiao et al. reached several conclusions regarding high α post-stall separation control. They concluded that at high α , the effectiveness of forcing diminishes, and flow may not become reattached when forced. However, even though the flow may not reattach, the base pressure over the upper surface would still decrease leading to an increase in lift and drag. Also, the effective range of excitation frequencies narrows for higher α with the center of the range being the shedding frequency. It was believed that the “enhancement of vortex shedding instability is the dominant mechanism in flow control” (Hsiao et al., 1994). Also concluded was that “...periodic perturbations possess the ability to synchronize the frequency of, and increase the strength of, vortices shed from the airfoil...” (Hsiao et al., 1994).

Besides acoustic excitation, other methods for separation control have been examined. Bar-Sever used an oscillating 0.1 mm tungsten wire 1.5 mm upstream and parallel to an LRN-(1)-1010 airfoil to excite the laminar separating leading edge shear layer (Bar-Sever, 1989). The Reynolds number of the test was 150,000, and $c_{l_{max}}$ was increased from 1.43 to 1.60 with α_{stall} going from 11° to 20° .

Gharib and Williams-Stuber used stainless steel heater strips on a symmetric NACA 63A008 airfoil in a study of the flow instabilities in the wake (Gharib and Williams-Stuber, 1989). They used linear stability analysis to examine the effect of the mean velocity profile on the development of the instabilities in the wake. They found that a receptivity range existed for the forcing frequency in which disturbances could produce a decrease in the airfoil's drag. For forcing frequencies outside of the receptivity range, little effect was seen on the instabilities in the wake. The mean velocity profile was found to adapt to become more receptive to the frequency of the forced disturbance.

Cui et al. used an oscillating leading edge flap on a 2D sharp leading edge wedge (Cui et al., 1992). They tested at a Reynolds number of approximately 800,000 with α up to 27.5° and were able to increase c_l through the use of the control flap.

One final experiment will be discussed as it relates to the research of this thesis. Kobayakawa, Kondo, and Suzuki used polyvinylidene fluoride (PVDF) piezoelectric film to provide a normal surface oscillation on a NACA 0012 airfoil. The film was attached to the upper surface covering the entire span from zero to 50% chord. A Reynolds number of 100,000 was studied. Leading edge stall existed under the test conditions. A 6% increase in $c_{l_{max}}$ was obtained at a control frequency of 50 Hz. The researchers reported that this increase in $c_{l_{max}}$ was caused by the laminar flow being forced into transition by the normal surface vibrations which were on average $11 \mu\text{m}$ in amplitude. The flow was thus energized and remained attached longer, providing additional lift. Although this mechanism of separation control is not involved with perturbing the separated shear layer (as all other examples in this section are), this idea of using a piezoelectric film to create flow disturbances is of interest.

5.0.5 Keys to Controlling the Separated Shear Layer

As can be seen, much work has been done in an effort to provide separation control by dynamically forcing the separated shear layer. Both laminar and turbulent separating boundary layers have been examined. The effect of forcing location, forcing level, and forcing frequency have been studied. Among the methods of forcing that have been

examined include external acoustic excitation, internal acoustic excitation, vibrating wires, oscillatory flaps, and periodic blowing.

Through all of this work, no clear results have yet been realized tying the enhancement of the mixing rate of separated shear layers on different bodies together. Some researchers obtain different results as to the most effective excitation frequency and forcing location. Other researchers are in agreement on those topics. It is clear that much more work must be done before active control by dynamic forcing of the separated shear layer becomes practical. The remainder of this section will describe some of the more-agreed-upon ideas involving active control of separated shear layers.

The forcing frequency is generally found to be the most important factor. Forcing at the natural shedding frequency or subharmonics of it has been found to be effective by many researchers. Ho and Huang found that the subharmonic of a vortex must amplify before that vortex will pair (Ho and Huang, 1982).

Forcing location is also important. Most researchers have found the best forcing location to be immediately upstream of separation. The entire instability growth phenomenon due to forcing is believed to take place in the separated shear flow region and not in the upstream boundary layer. This was documented by Rice and Zaman in 1987 and by Zaman and McKinzie in 1989.

It is also believed that small transverse velocity fluctuations are the triggering mechanism to control the separated shear layer. Zaman, Bar-Sever, and Mangalam used external acoustic excitation to affect the flow over a low Reynolds number airfoil, but they observed tunnel acoustic resonance effects. They believe that acoustic standing waves in the tunnel were inducing transverse velocity fluctuations near the airfoil. They concluded that, "alternative methods specifically inducing cross-stream velocity perturbations may be more viable in the excitation of the flows under consideration" (Zaman et al., 1987). Supporting this idea is the work of Hsiao, Liu, and Shyu. They examined the effect of the location of a slot emitting sound on the enhanced mixing rate of a separated shear layer. The location was found to be very important. They concluded that the "...nature of local excitation control is due to hydrodynamical disturbances rather than acoustics. If it were acoustics, the forcing should not be sensitive to the location. The reason is because the

length scale of the acoustic wave is much longer than the length scale of the models" (Hsiao et al., 1989).

5.1 Qualitative Shear Stress Measurements

It was decided to begin the initial flow instability experimentation by making simple qualitative shear stress measurements along the chord of the SM701 airfoil using McCroskey type shear stress gauges (hot film sensors). These gauges employ two similar thin metallic elements arranged in a V-configuration on a plastic film backing. This V-configuration makes the gauges directionally sensitive. Gauges typically have areas of only a few square millimeters and can be used to measure instantaneous wall shear stress, operating analogously to a conventional constant-temperature hot-wire anemometer. For the present experiments, a qualitative study was made following the work of Pucher and Göhl (1987). Their work is described in Section 5.1.2. Only one leg of the shear stress gauge was used since, as will be discussed in the next section, determining flow direction was not a goal of the current work.

5.1.1 Objectives of Qualitative Shear Stress Experimentation

Two objectives exist for performing this study. The main objective is to learn whether dominant flow instability frequencies can be detected and measured by surface shear stress gauges positioned downstream of separation on the airfoil's surface. These dominant frequencies, associated with the coherent structures in the separated shear region, are believed by many researchers to be the key frequencies in active control excitation as has been discussed in Sections 5.0.3 to 5.0.5. If surface gauges can detect and measure the dominant flow frequencies which exist away from the surface, future research will be simplified in that hot-wire probes would not need to be positioned in the flow to record the dominant instability frequencies (the standard practice). It is a much simpler task to set up a shear gauge system than it is to set up a hot-wire system.

The second objective of the qualitative shear stress measurements is to provide yet additional support for the results of the oil flow visualization and heat transfer experiments. Specifically, the flow region immediately after flow reattachment (the end of

the laminar separation bubble) will be examined. After reattachment, it was found that the convective heat transfer coefficient continues to increase as the boundary layer relaxes to a characteristic turbulent boundary layer (see Section 4.2.16). If this is indeed the case, then the shear stress gauge should yield a mean voltage signal that continues to increase after flow reattachment. This increase in the mean voltage signal is predicted since the mean voltage signal is, in addition to a measure of the mean surface skin friction, a measure of the convective heat transfer at the surface of the wing. When the shear stress gauge is located in a region of high convective heat transfer, the electronic bridge compensates to keep the gauge at a constant temperature by increasing the voltage applied to the gauge. Thus the qualitative shear stress method can also be interpreted as a qualitative heat transfer method.

It should be noted that the original finding regarding increasing convective heat transfer coefficient after flow reattachment was made in the LSLTT; any corroborative findings here would be further substantiated since current tests are in the ASWT where the wing mounting system, free stream turbulence intensity level, and blockage effects differ from the LSLTT.

5.1.2 Past Work with Shear Stress Gauges

Pucher and Göhl used shear stress gauges in a qualitative manner to examine boundary layer separation on a NACA 0018 airfoil (Pucher and Göhl, 1987). Their gauges were made of $0.3 \mu\text{m}$ nickel film vapor-deposited onto a polyimide foil. By examining the mean and rms fluctuation voltages from the gauge, Pucher and Göhl compared different flow regions on their airfoil. In their own words, "... the d-c voltage share E corresponds to the time-averaged heat transfer, whereas the a-c voltage share e describes the fluctuating part of the heat transfer" (Pucher and Göhl, 1987). In their terminology, e is the rms fluctuation voltage value.

Flittie and Covert performed quantitative shear stress measurements with a gauge of their own design on a NACA 0012 airfoil (Flittie and Covert, 1992). Their gauge utilized a 10% Rhodium-90% Platinum wire instead of a film as the sensing element. The sensing wire was positioned over a 0.001 inch deep by 0.002 inch wide cavity etched into the

gauge surface to minimize conduction effects that would reduce the dynamic response of the sensor. Flittie and Covert describe the calibration procedure for shear stress gauges very well. Martin examined wall shear stress values in a vertical annular two-phase flow (Martin, 1984). Baldwin et al. used a shear stress gauge made from a 0.125 mm wide platinum film strip covered with a 2.0 μm thick quartz coating to study wall shear stress inside an artificial heart ventricle (Baldwin et al., 1987).

5.1.3 Setup for Qualitative Shear Stress Measurements

Tests were conducted in the ASWT. A schematic of the experimental setup given as Figure 5.5 is now discussed. A DISA Type 55M01 main unit was used with a McCroskey type shear stress gauge to obtain a qualitative indication of mean and fluctuating shear stress on the surface of the SM701 airfoil. The mean voltage value obtained from the shear stress gauge gives an indication of the mean shear stress. Likewise, the rms value of the fluctuating voltages gives an indication of the rms value of the fluctuating shear stress. The fluctuating voltages can also be analyzed for frequency content.

An overheat ratio of 1.2 was used, and the frequency response of the gauge was ten to 15 kHz. The DISA 55M01 has two identical outputs, both of which were used. Data were sampled with a DASH-16 A/D 12-bit data acquisition board manufactured by MetraByte Corporation. The DASH-16 was installed in a 486 DX personal computer. To maximize the DASH-16 sampling resolution of the shear stress gauge voltage fluctuations about the mean voltage, the instantaneous signal from one of the DISA outputs was first sent through a Krohn-Hite model 3550 filter where the DC offset was removed and the signal low-pass filtered for anti-aliasing purposes. The signal out of the filter was then just the fluctuation component of the instantaneous signal. These fluctuations were amplified with a Techkor Instrumentation amplifier and were fed into channel one of the DASH-16 A/D board. Figure 5.6 shows the DISA 55M01 main unit along with the filter and the amplifier.

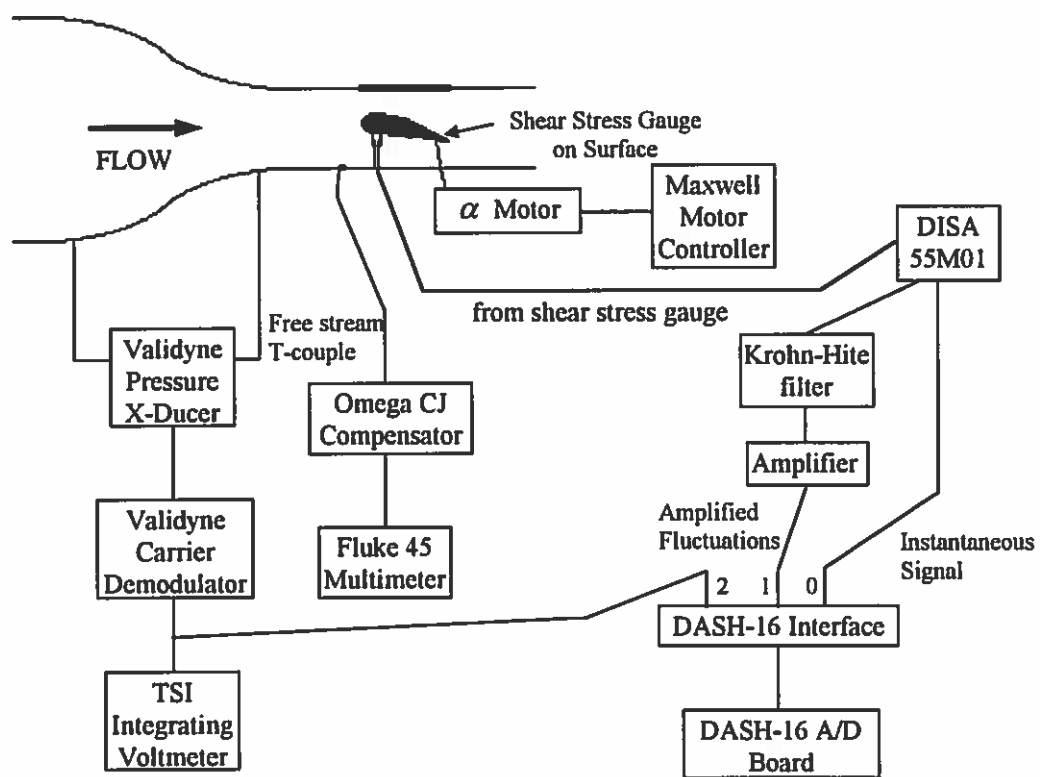


Figure 5.5: Schematic of Setup for Qualitative Shear Stress Measurements

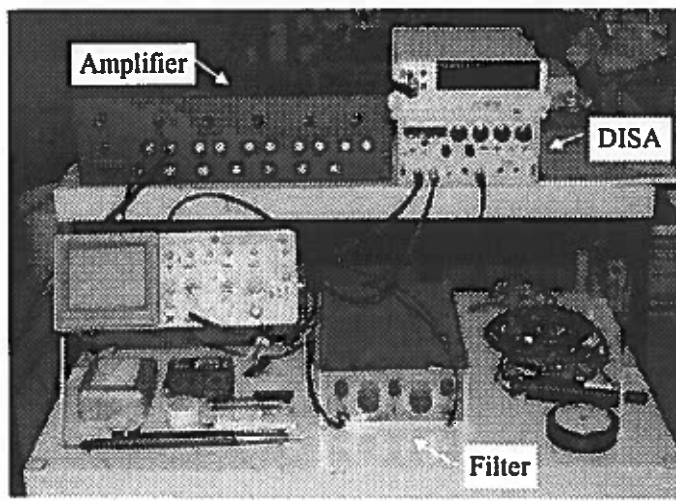


Figure 5.6: The DISA 55M01, Krohn-Hite Filter, and Techkor Amplifier

The second instantaneous signal output from the DISA 55M01 was fed directly into the DASH-16 board. The instantaneous signal recorded was used to obtain a mean voltage value of the shear stress gauge output. The amplified fluctuation voltage signal recorded through another channel at high resolution was used to obtain an rms voltage value.

A Validyne differential pressure transducer (0.125 psi rating) along with a Validyne Model CD15 Carrier Demodulator was used to measure the static pressure drop across the wind tunnel contraction section. The output from the demodulator was sent to channel two of the DASH-16 board to be sampled. From this static pressure drop, the test section dynamic pressure could be found as described in Section 4.2.9.

A K-type thermocouple was used to measure the free stream temperature. The thermocouple was attached to the tunnel wall immediately upstream of the leading edge of the model. An Omega-CJ cold junction compensator was used to electronically provide a zero °C reference point for the thermocouple. The output voltage from the thermocouple was viewed on a Fluke 45 Dual Display multimeter.

A Maxwell Electronics Inc. x-y stepping motor controller was used to drive the angle of attack adjust motor. The motor controller was operated manually to set the angle of attack for a given test with the help of a Mitutoyo Pro 360 digital protractor. This process was described in Section 4.2.9.

5.1.4 Description of Data Acquisition and Data Reduction Codes

The FORTRAN codes used for the shear stress experimentation are very similar to the codes that are described in Section 5.2.3 that were used in the hot-wire experimentation. The reader is referred to that section for details on the data acquisition and data reduction process. The codes used for the qualitative shear stress experiments differ from those used for the quantitative hot-wire experiments in Section 5.2 by the omission of a calibration for the qualitative shear stress tests and the omission of commands to drive the traverse that was used in the hot-wire tests.

5.1.5 Procedure for Qualitative Shear Stress Measurements

Tests were conducted at $Re = 315,000$ and were performed for angles of attack of 0, 5, 10, 15, 18, 20, 22, and 25° . The angle of attack was set to the desired value. A single McCroskey type shear stress gauge was attached to the SM701 model at a given chordwise station using 3M Scotch brand double-sided tape. This allowed testing to be performed at that chordwise position, and then the single gauge could be moved to a new position along the chord. The single gauge was always attached at the midspan.

The tunnel was brought up to speed to achieve a Reynolds number of 315,000. The data acquisition software, described in Section 5.1.4, then directed the computer to record the instantaneous output from the shear stress gauge. Sampling was performed at 2048 Hz for 25.5 seconds. The DC offset of the instantaneous shear gauge output signal was removed, and the signal was low-pass filtered at 820 Hz and amplified before being sent to channel one of the DASH-16 board to be sampled as fluctuation values. Typical amplification factors were ten to 30 dB. Several tests were conducted with a sampling rate of 20.48 kHz, but the resulting power spectra showed no significant energy content above a few hundred Hertz; hence it was decided to reduce the sampling rate to 2048 Hz which allowed a longer sampling time and increased frequency resolution in the fluctuation spectra.

After the data acquisition was completed for a given chordwise shear stress gauge location, the tunnel was shut off, and the single gauge was moved to a new location along the chord. The procedure was then repeated for this new chordwise position, as well as subsequent chordwise locations from the leading edge to the trailing edge. Testing then progressed to the other angles of attack. The test matrix is shown in Table 5.1. Because of the moving of the gauge for each chordwise measurement location, sometimes the sensing element would crack or an attachment wire would become unsoldered. In the course of all the testing, a total of about six or eight McCroskey gauges was used due to gauge breakage.

Table 5.1: Test Matrix for Qualitative Shear Stress Experimentation

α (deg)	Chordwise Location of Shear Stress Gauge (%)																		
	5	10	15	20	25	30	35	40	45	50	55	60	65	70	75	80	85	90	95
0						X				X		X	X	X	X	X			X
5		X		X		X	X	X	X			X		X		X			X
10	X	X	X	X	X		X			X		X		X		X	X	X	X
15	X	X	X	X		X		X		X	X	X	X	X		X		X	
18	X	X	X	X		X		X		X		X		X		X		X	
20	X	X	X	X		X		X		X		X		X		X		X	
22	X	X	X	X		X		X		X		X		X		X		X	
25	X	X	X	X		X		X		X		X		X		X		X	

5.1.6 Qualitative Shear Stress Results

Figures 5.7 to 5.11 and 5.18 to 5.21 contain results of the qualitative shear stress tests. Both the mean and rms fluctuation voltage values are presented in the figures. The mean voltages are presented as a fractional change from the offset mean voltage, E_o , that is acquired with no flow. This was done since the offset mean voltage would change slightly every time the shear stress gauge was moved to a new chordwise location. Also presented on the graphs are the results of fluorescent oil flow visualization taken from Table 4.1 of Section 4.1.4.

For $\alpha = 0^\circ$ Figure 5.7 shows that the mean voltage parameter, as expected, follows a similar trend to the convective heat transfer results presented in Section 4.2.16: a decreasing trend in the laminar flow region followed by an increasing trend in the transitional region of the separation bubble. The rms voltage data also show these flow regions very distinctly. The rms voltage value is an order of magnitude greater in the turbulent region than in the laminar region. As in the heat transfer study, the onset of laminar separation at the beginning of the separation bubble is not revealed by examining the qualitative shear stress results directly. In addition, both the mean and fluctuation voltage data continue to increase in value after the flow reattachment at the end of the

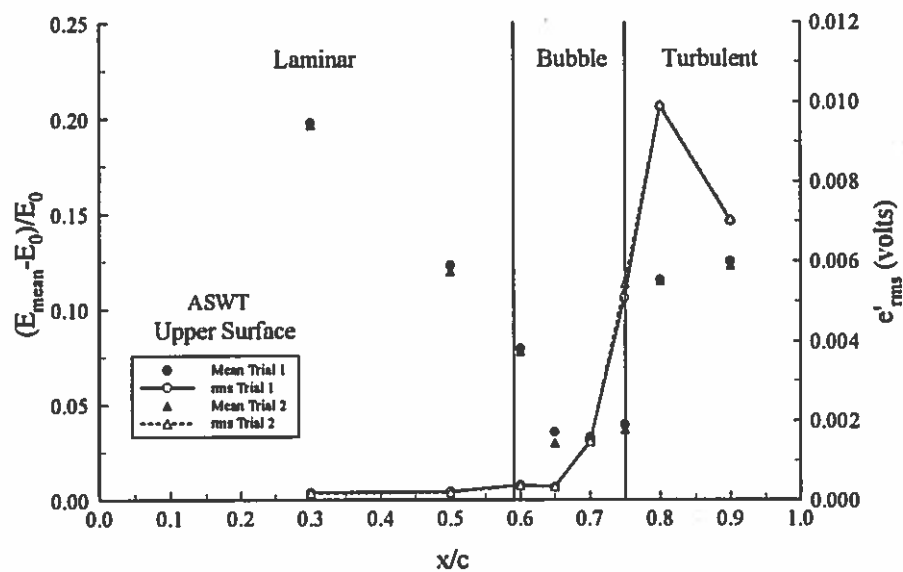


Figure 5.7: $\alpha = 0^\circ$, $Re = 315,000$

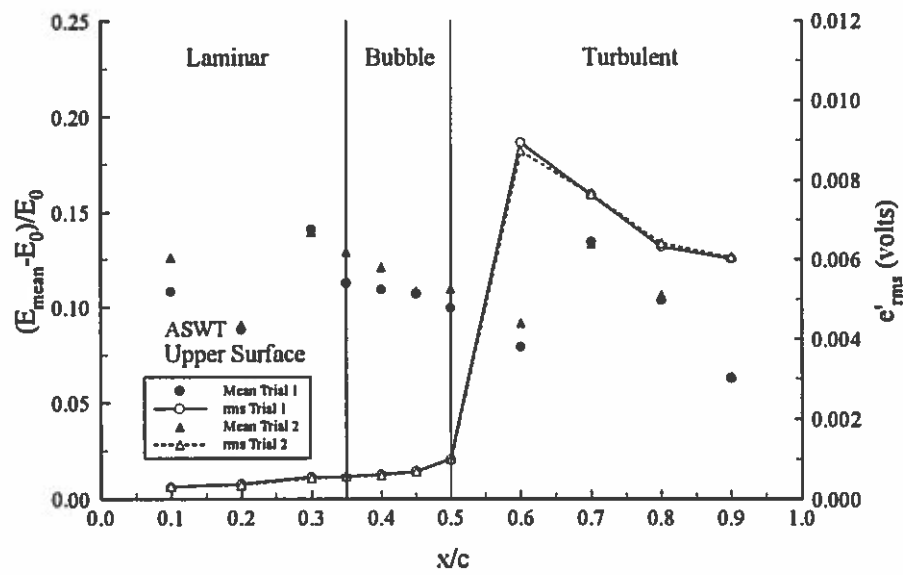


Figure 5.8: $\alpha = 5^\circ$, $Re = 315,000$

separation bubble. This is in agreement with the trend found in the convective heat transfer coefficient distributions and corroborates that the reattached boundary layer requires a distance to relax into a characteristic turbulent boundary layer.

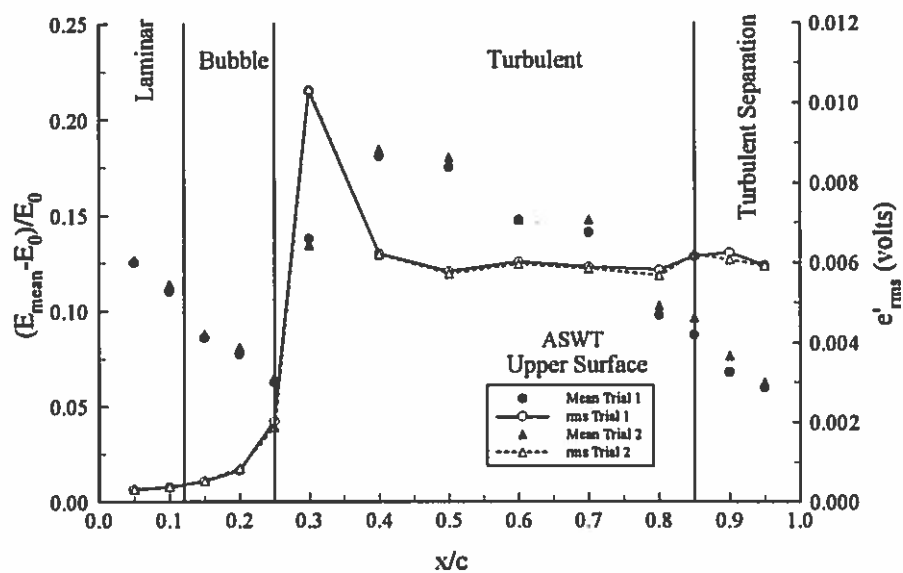
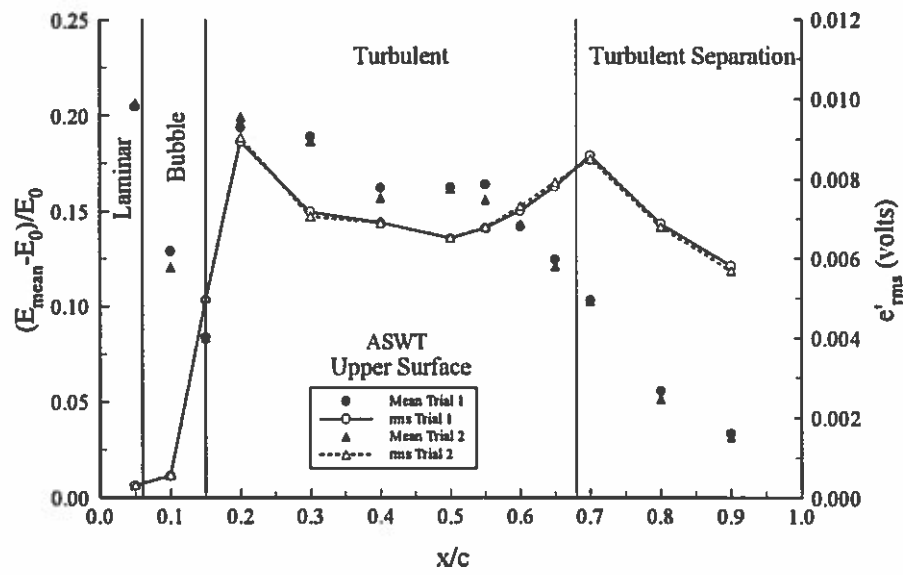
For $\alpha = 5^\circ$ the results of Figure 5.8 are rather confusing. The expected decaying trend of the mean voltage data in the laminar region is not seen. Also, the magnitude of the mean voltage data in the separation bubble is greater than that of the mean data in the laminar region. When examining the rms data, it appears that the location of reattachment as shown by the oil flow visualization is premature of the actual reattachment location. These discrepancies may be explained by reexamining the oil flow visualization results for $\alpha = 5^\circ$. Recall that the oil flow visualization results for $Re = 315,000$ (Figure 4.2a) were somewhat ambiguous as to the location of the separation bubble. If the oil flow visualization indication of the end of the bubble were shifted 5 to 10% aft, the qualitative shear stress voltage patterns would make more sense. It could easily be the case that the oil flow visualization photo (Figure 4.2a) was incorrectly interpreted due to its vagueness thus causing poor results now during comparison to the qualitative shear stress data.

The mean voltage values in the laminar region are more difficult to explain. It is possible that the shear stress gauge was damaged by moving it along the chord during experimentation (for this angle of attack, the gauge was first tested at 90% chord and then moved forward). By the time the gauge was located at 20% chord, it may have been faulty, thus yielding voltage values that do not follow the expected trends seen in the other angle of attack cases.

Figure 5.9 gives results for $\alpha = 10^\circ$. The mean voltage data follow trends as previously discussed for $\alpha = 0^\circ$. A decreasing trend is also seen in the mean voltage data in the turbulent region with a slightly more rapid decrease in the separated region. The rms data show a maximum slightly after the end of the separation bubble followed by a relatively constant trend throughout the turbulent region. It appears that at the location of turbulent separation, the rms value increases slightly.

Figure 5.10 displays results for $\alpha = 15^\circ$. The trends in the mean voltage points are the same as for Figure 5.9. The rms data show a local maximum slightly after flow reattachment at the end of the separation bubble. Another local maximum exists very near

the turbulent separation location. The angle of attack for this case is very near α_{stall} . The large rms maximum near turbulent separation is an indication of the eminency of stall.

Figure 5.9: $\alpha = 10^\circ$, $\text{Re} = 315,000$ Figure 5.10: $\alpha = 15^\circ$, $\text{Re} = 315,000$

Frequency spectra were computed based on the voltage fluctuation signal for chordwise locations of 70% and 90% at $\alpha = 15^\circ$. No dominant spectral component surfaced. As will be seen in Section 5.2.6, hot-wire measurements for $\alpha = 15^\circ$ also did not reveal a dominant spectral component. It appears that for $\alpha = 15^\circ$, which is very near the maximum of the lift curve slope of the SM701 airfoil at the Reynolds number tested, no dominant spectral component (shedding frequency) has yet developed.

As the angle of attack is increased into the stall region of the SM701 airfoil, the mean and rms voltage distributions change. See Figure 5.11. At $\alpha = 18^\circ$ this figure shows a leveling off of the mean voltage data near the turbulent separation location. This flat trend gives an indication of relatively low convective heat transfer from the shear stress gauge, and thus predominantly conduction heat transfer into the wing skin material.

The rms data are also fairly constant at the turbulent separation location, increasing both upstream and downstream of separation. This rms trend differs from the rms trend at $\alpha = 10^\circ$ and $\alpha = 15^\circ$ (pre-stall angles) where a local maximum occurred at the turbulent separation point. As will be seen in Section 5.2.6, hot-wire measurements revealed that a distinct dominant spectral component of the flow has evolved along the airfoil at $\alpha = 18^\circ$ and is prominent in the wake. The airfoil at $\alpha = 18^\circ$ is creating dominant instabilities in both the upper and lower half (mean shear regions) of the wake.

The value of e'_{rms} is an indication of the turbulent fluctuation level near the airfoil's surface, and the rms voltage increase near the trailing edge may be explained by examining the nature of the dominant flow instabilities being created under stalled conditions. These dominant instabilities are large coherent vortical structures that are convected downstream in the turbulent free shear layers. The pairing of these structures causes the free shear layers to grow. Figure 5.12 from Ewald et al. shows these coherent structures being shed from the separation point on an airfoil's upper surface. Figures 5.13 and 5.14 present results of computational flowfield simulations performed on the SM701 airfoil. A fluid dynamics prediction program, FIDAP 7.50, was used to solve the time-averaged continuity and momentum equations (Uzol, 1997). A $k - \varepsilon$ turbulence model was

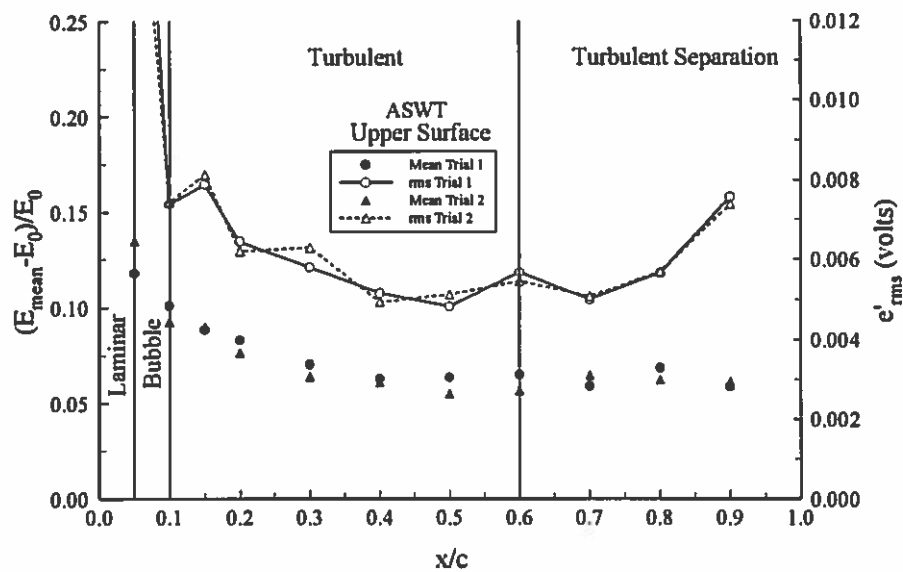
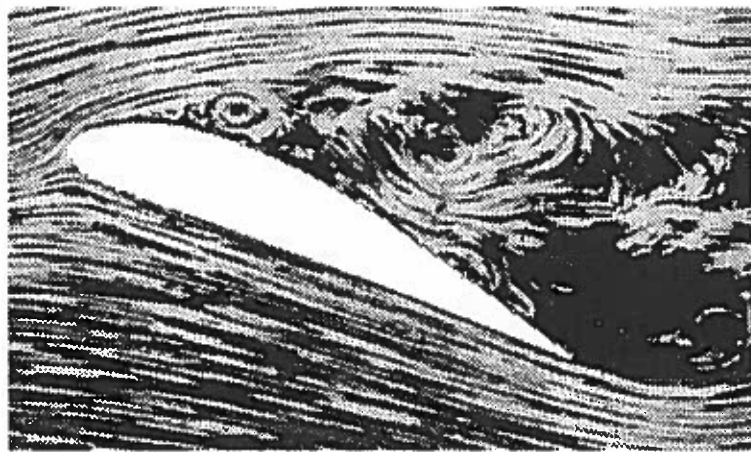


Figure 5.11: $\alpha = 18^\circ$, $Re = 315,000$



Source: Ewald et al., 1936

Figure 5.12: Coherent Vortical Structures in Separated Shear Layer

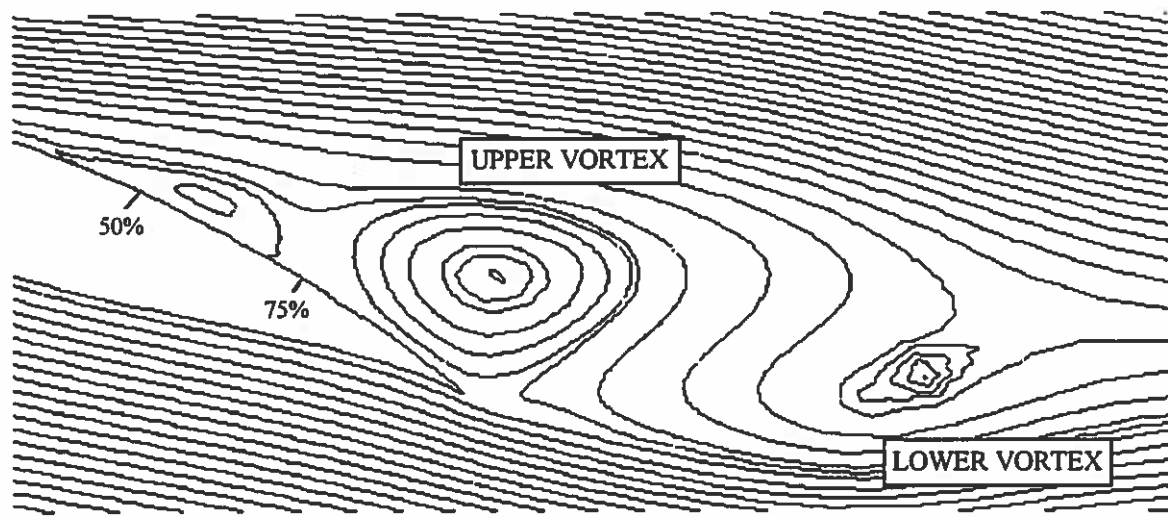


Figure 5.13: Separated Flow Region Streamlines, $\alpha = 20^\circ$, $Re = 315,000$ (from FIDAP)

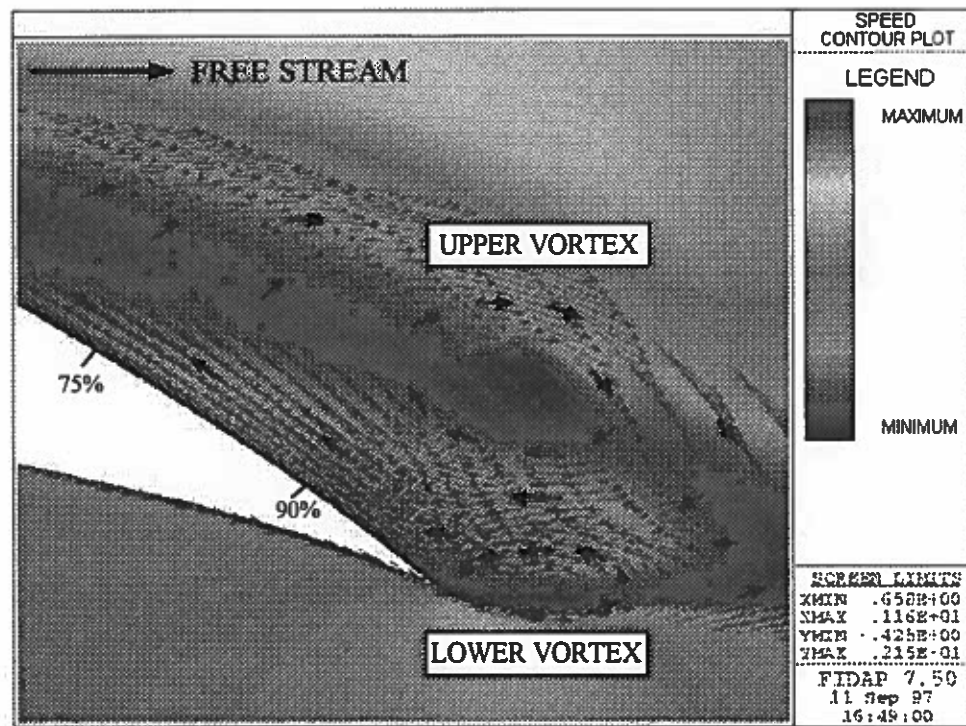


Figure 5.14: Separated Flow Region Velocity Vectors, $\alpha = 20^\circ$, $Re = 315,000$

utilized. A coherent structure is seen being formed near the separation point in Figure 5.13. Two other coherent vortical structures are also seen. One such flow structure is seen above the airfoil's trailing edge. The other coherent structure, which originated at the trailing edge, is seen convected downstream near the right-hand-side of the figure. In Figure 5.14, two coherent vortical structures can be seen near the trailing edge of the airfoil. The upper vortex is rotating clockwise while the lower vortex is rotating counterclockwise. Between these two coherent vortical structures, fluid is being sent upstream towards the airfoil's trailing edge creating an "impinging jet" phenomenon on the airfoil surface. The fluid flowing upstream between these coherent vortical structures is seen by the color contours of Figure 5.14 to have a greater speed than the fluid moving downstream on either side of this "impinging jet" phenomenon. This greater speed leads to locally increased turbulence levels and heat transfer rates on the airfoil surface near the trailing edge.

Figure 5.15 shows the prediction of turbulent kinetic energy along the airfoil's upper surface. As can be seen, an increase in turbulent kinetic energy near the trailing edge is predicted. Experimentation supports this prediction by revealing an increase in e_{rms} near the trailing edge when the airfoil is stalled and coherent vortical structures are being shed. Also, the convective heat transfer is enhanced at the trailing edge on the upper surface by this "impinging jet" phenomenon created by the shedding coherent vortical structures. This convective heat transfer enhancement was seen in the LSLTT under stalled conditions (Figures 4.42 to 4.44 of Section 4.2.16). The preliminary ASWT heat transfer experimentation (Sections 4.2.8 to 4.2.11) also indicated this trailing edge heat transfer enhancement when the airfoil was stalled. Figure 5.16 is presented to verify this claim.

To experimentally corroborate the computational results presented in Figures 5.13 and 5.14, smoke flow visualization was performed on the SM701 airfoil at $\alpha = 20^\circ$. The Reynolds number was approximately 20,000. A LaserIonics Argon ion four Watt laser was used to create a 2D light sheet by using a laser sheet fiber coupler. The laser was operated at a power level of approximately one Watt. A Rosco Omega-XT fog machine was used to provide the smoke. Figure 5.17 shows results of the smoke flow

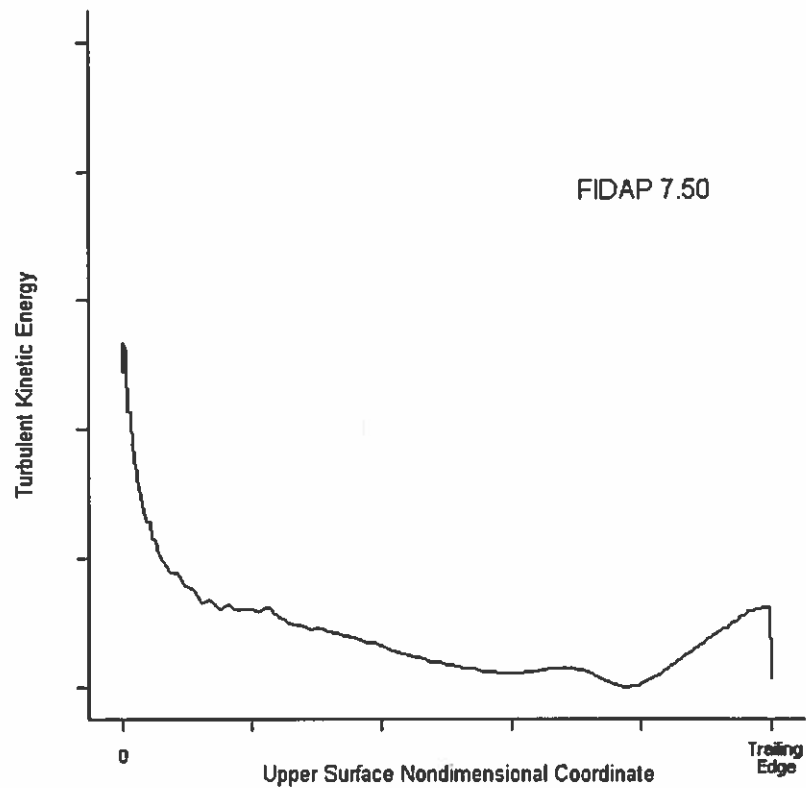


Figure 5.15: Turbulent Kinetic Energy Along Airfoil Surface, $\alpha = 20^\circ$, $Re = 315,000$

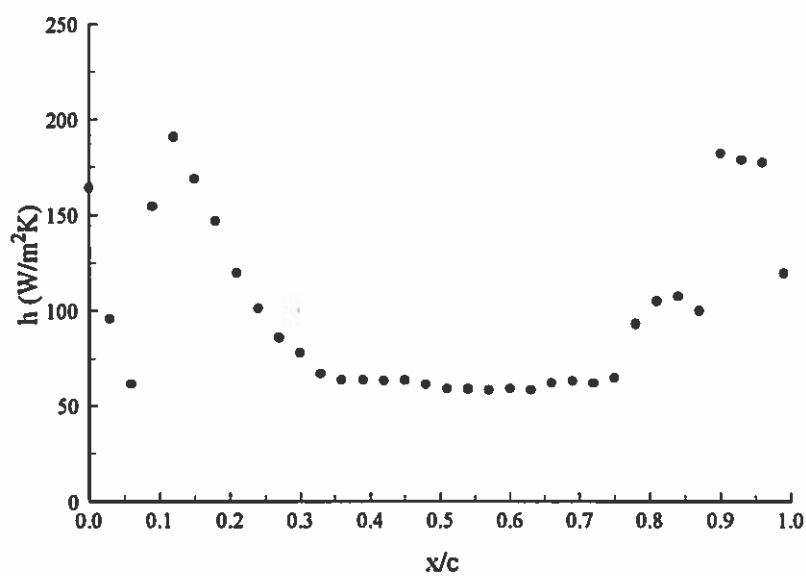
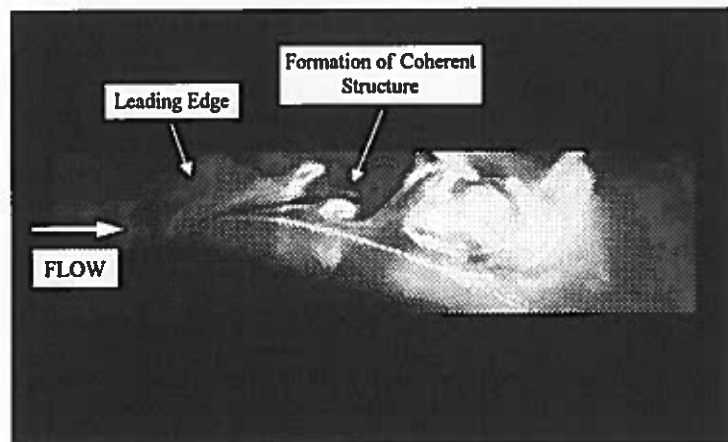
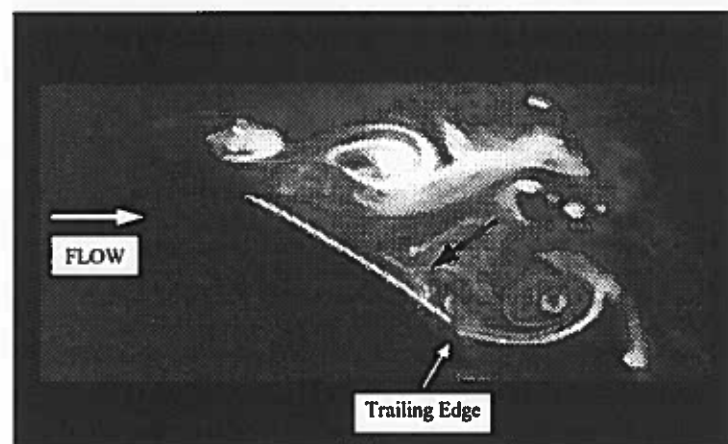


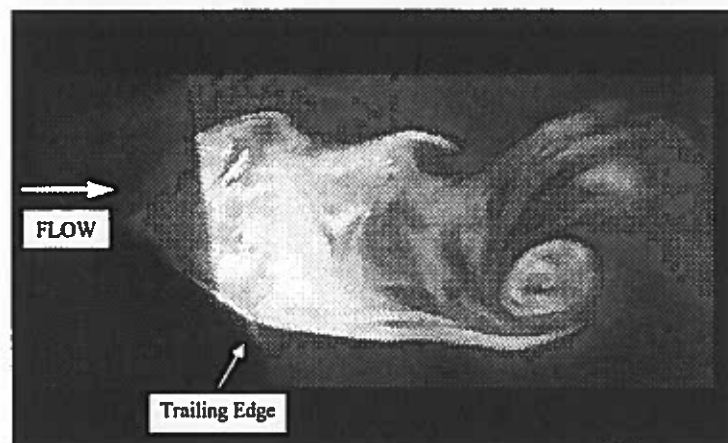
Figure 5.16: Enhanced Trailing Edge Heat Transfer (ASWT, $\alpha = 20^\circ$, $Re = 315,000$)



(a) Separation and Coherent Vortical Structure Creation



(b) Coherent Vortical Structures



(c) Coherent Vortical Structures in Wake

Figure 5.17: Visualization of Coherent Vortical Structures, $\alpha = 20^\circ$, $Re \approx 20,000$

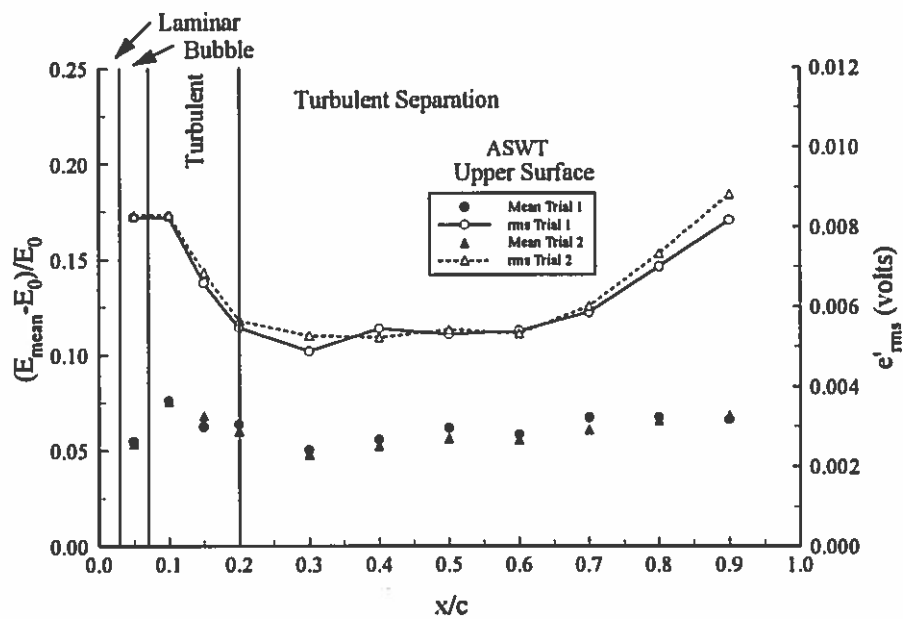
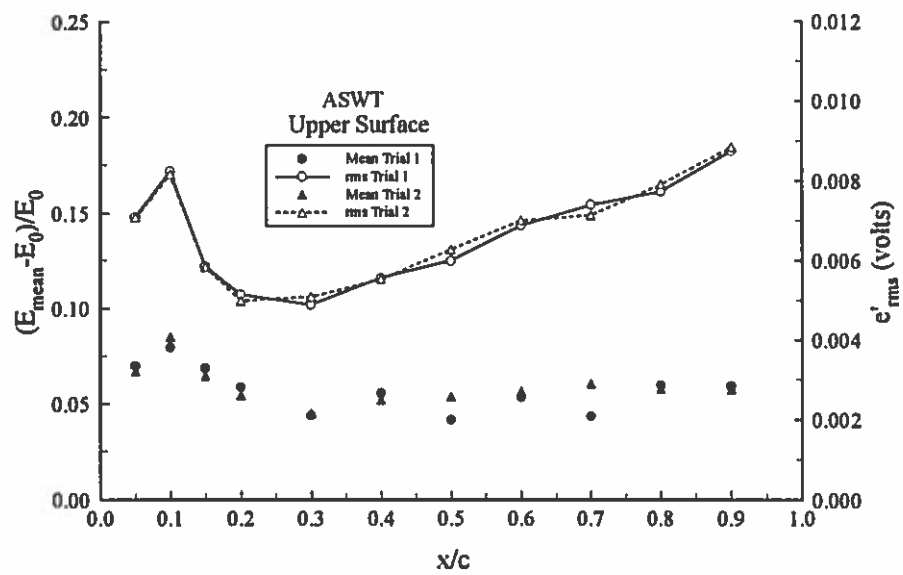
visualization. In Figure 5.17a the boundary layer separation is observed, and a coherent vortical structure is seen to be formed shortly after separation. Figure 5.17b shows coherent vortical structures that emanate from both the upper surface separation point and the trailing edge separation. This figure offers good qualitative agreement with the FIDAP flowfield predictions shown in Figures 5.13 and 5.14. Figure 5.17c shows the coherent vortical structures in the wake of the airfoil.

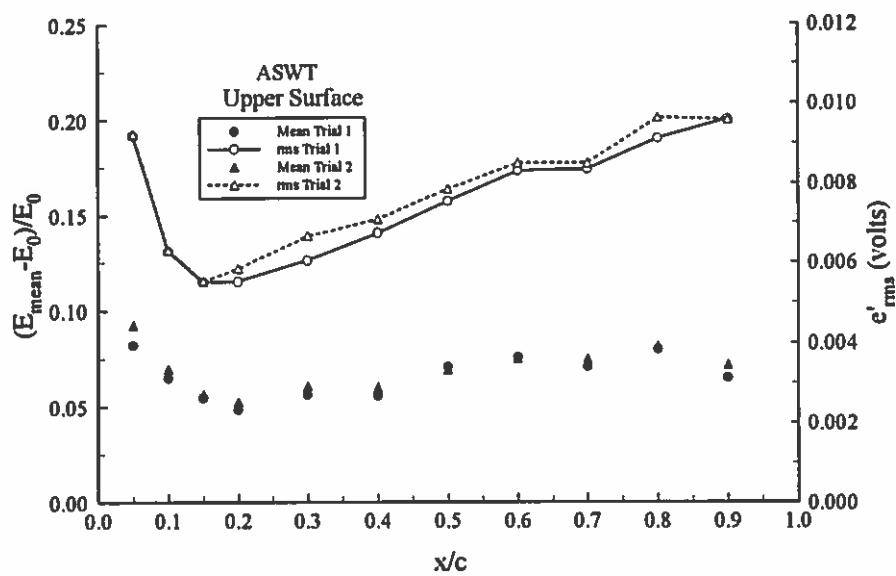
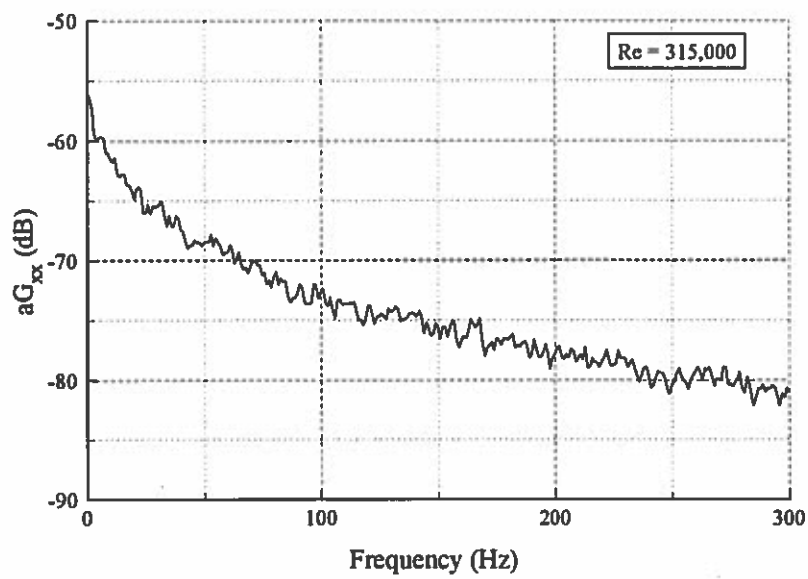
From this discussion, it is emphasized that a significant change has occurred in the flow physics from $\alpha = 15^\circ$ to $\alpha = 18^\circ$ and other post-stall angles of attack. Although the hot-wire experimentation reveals the existence of a dominant spectral component at $\alpha = 18^\circ$ (as will be seen), spectra computed from the voltage fluctuation signal of the shear stress gauge at chordwise locations of 70% and 90% showed no such indication of a dominant shedding frequency at that angle of attack.

Figures 5.18 to 5.20 were made for $\alpha = 20^\circ$, 22° , and 25° , respectively. Results are similar to the 18° case. The mean voltage signals are fairly constant in the turbulent separated regions indicating low convective heat transfer. The rms data seem to be near a minimum at turbulent separation and increase near the trailing edge. As has been discussed, it is believed that this increase in turbulent fluctuation level near the trailing edge is caused by an "impinging jet" phenomenon created by the coherent vortical structures being shed downstream under stalled conditions.

No oil flow visualization was performed for the $\alpha = 22^\circ$ and $\alpha = 25^\circ$ cases since they were added to the test matrix after the oil flow visualization was performed. However, following the trends noted for $\alpha = 18^\circ$ and $\alpha = 20^\circ$, the location of turbulent separation may be surmised. For Figure 5.19, at $\alpha = 22^\circ$ the leveling off of the mean data and minimum in the rms data occur near 20 to 25% chord; this is a good estimate of the turbulent separation location. For Figure 5.20, at $\alpha = 25^\circ$ the same reasoning would place turbulent separation at approximately 15 to 20% chord.

Spectra of the voltage fluctuations were computed for $\alpha = 20^\circ$, 22° , and 25° at various chordwise locations within the turbulent separated flow region. In no instance did the spectra reveal any dominant component corresponding to a dominant flow instability frequency. As a representative example, see Figure 5.21.

Figure 5.18: $\alpha = 20^\circ$, $Re = 315,000$ Figure 5.19: $\alpha = 22^\circ$, $Re = 315,000$

Figure 5.20: $\alpha = 25^\circ$, $Re = 315,000$ Figure 5.21: $\alpha = 20^\circ$, $x/c = 70\%$

5.1.7 Conclusions from Qualitative Shear Stress Measurements

The qualitative shear stress experiments have served to verify the laminar separation bubble reattachment region trend seen with the liquid crystal thermography tests. After reattachment, the convective heat transfer coefficient continues to increase as the newly-formed boundary layer relaxes from a mixing layer state to a turbulent boundary layer state (see Section 4.2.16 for a full explanation). The mean and rms voltage data were found to follow this same increasing trend after flow reattachment. This trend in the shear stress gauge voltage output, it should be noted, was seen in a facility (ASWT) different than that in which the heat transfer tests were conducted (LSLTT). This phenomenon thus was not caused somehow by the LSLTT wind tunnel. The ASWT has a higher free stream turbulence intensity, a smaller cross-section leading to increased blockage effects, and a different model mounting scheme than the LSLTT in which the heat transfer tests were performed.

The rms voltage data were found to vary by an order of magnitude in the laminar and turbulent regions. However, no obvious distinction in rms voltage occurs between laminar and laminar separation regions or between turbulent and turbulent separation regions.

The chordwise trends in both the mean and the rms voltage data radically change when the airfoil angle of attack enters the stalled regime. The mean voltages are nearly constant in the turbulent separation regions indicating low convective heat transfer and predominantly conduction heat transfer into the airfoil substrate. The rms voltage data are near minimum at turbulent separation, with an increasing trend throughout the separation region. It is believed that this increasing trend in e'_{rms} towards the trailing edge is tied to the generation of large scale coherent vortical structures that appear after the airfoil is stalled.

The qualitative shear stress tests proved a failure in revealing any dominant spectral components of the flow instabilities (shedding frequencies) at high angle of attack. Either no dominant flow instabilities exist at the conditions at which tests were conducted, or the dominant instabilities only exist in a confined region away from the airfoil surface or in the wake thus making the shear gauges blind to their presence. Hot-wire tests will prove the latter case to be true.

5.2 Hot-Wire Flowfield Measurements

Because of the failure of the qualitative shear stress tests to provide dominant flow instability information, efforts were turned to hot-wire anemometry experimentation. This section describes experiments in which velocity profiles along the chord of the airfoil and wake surveys were conducted and analyzed for dominant frequency content under different sets of experimental conditions.

5.2.1 Objectives of Hot-Wire Flowfield Experimentation

Several objectives are laid out for a hot-wire anemometry study of the SM701 airfoil flowfield. The first objective is to experimentally measure the dominant instability (shedding) frequency created by the airfoil at high angle of attack and to determine how that frequency scales with the experimental conditions. This shedding frequency has escaped the shear stress gauges discussed in Section 5.1. A second objective is to determine the best location at which to measure the shedding frequency; to explore this subject traversing measurements are made at various chordwise stations as well as at two longitudinal wake positions. By examining several chordwise stations, it is hoped to track the development of the shedding vortices and subsequent pairing and strengthening. The wake positions are examined with the hope that similar shedding frequency results will be found in the wake that are found in the profiles on the airfoil itself. It is much easier to perform a wake traverse than it is to perform a profile traverse normal to the chord of an airfoil. If both locations yield similar results, then future testing can be done in the wake where experimentation is easier.

5.2.2 Experimental Setup for Hot-Wire Flowfield Measurements

Tests were conducted in the ASWT at $Re = 315,000$. The finite aspect ratio 2.58 model that was used in the ASWT heat transfer experiments was modified slightly by making foam wing tip extensions. The model tested for the hot-wire experiments was thus two-dimensional. The model was mounted as described in Section 4.2.9 for the heat transfer measurements. A gap of about $\frac{1}{2}$ inch had to be left at both wing tips so that the angle of attack could be adjusted in the circular cross-section ASWT. Angles of attack

studied included 15°, 18°, 20°, 22°, and 25°. In order to seal the $\frac{1}{2}$ inch gaps between the wing tips and the rounded tunnel walls, foam weather stripping was attached to the wing tips. A schematic of the experimental setup is given as Figure 5.22 and will now be discussed.

A DISA Type 55M01 single sensor hot-wire system was used to measure mean and fluctuating velocities in the flowfield. The DISA 55M01 has two identical outputs, both of which were used. Data were sampled with a DASH-16 A/D 12-bit data acquisition board manufactured by MetraByte Corporation. The DASH-16 was installed in a 486 DX personal computer. To maximize the resolution of the measured velocity fluctuations, the instantaneous voltage signal from one of the DISA outputs was filtered and amplified before being sampled by the DASH-16 board. The filter was a Krohn-Hite model 3550 that was used to remove the DC voltage offset of the instantaneous hot-wire signal and to low pass the hot-wire signal for anti-aliasing purposes. The signal out of the filter was then just the fluctuation component of the instantaneous signal. These fluctuations were amplified with a Techkor Instrumentation Amplifier and fed into channel one of the DASH-16 A/D board.

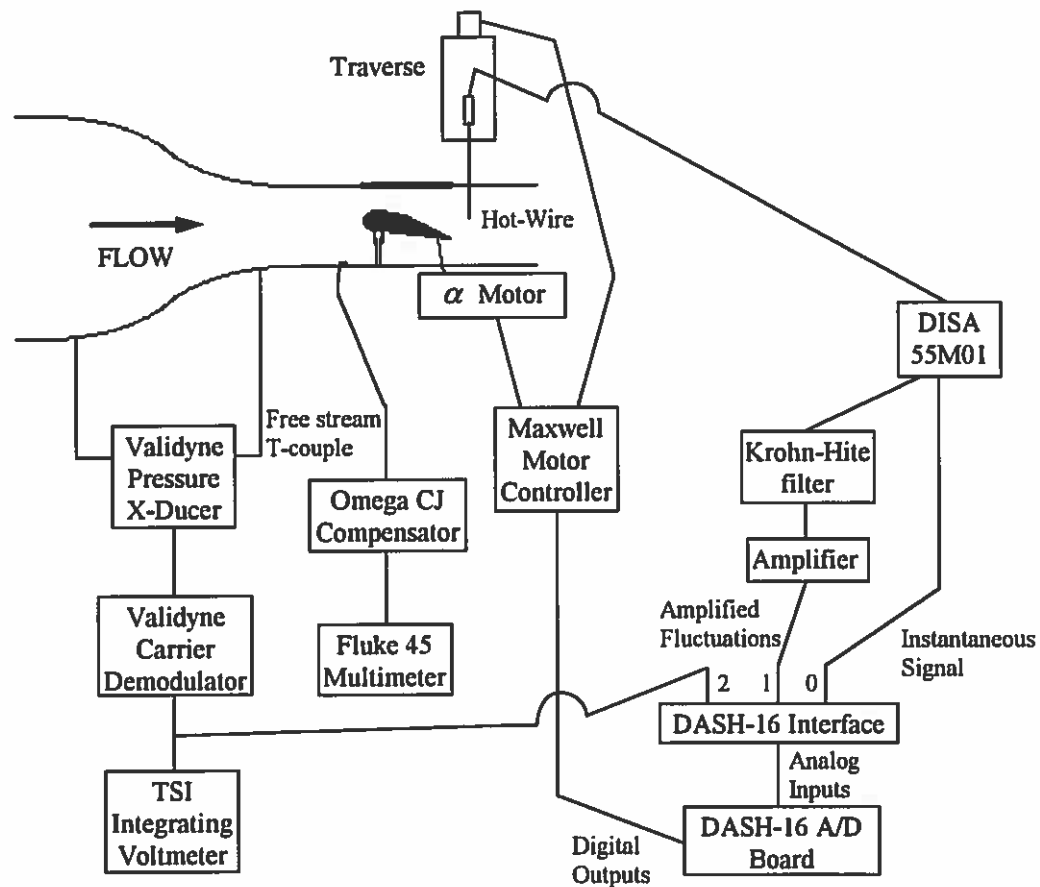


Figure 5.22: Schematic of Setup for Flowfield Measurements

The second instantaneous signal output from the DISA 55M01 was fed directly into channel zero of the DASH-16 board. Channel zero was then used to obtain mean voltage values from the hot-wire output while channel one was used to obtain amplified fluctuation voltage values at a high resolution. The instantaneous signal was found by adding the mean and fluctuation values.

The test section dynamic pressure and free stream temperature were measured as is discussed in Section 5.1.3 for the qualitative shear stress tests. A Maxwell Electronics Inc. x-y stepping motor controller was used to drive the motor of a UniSlide traverse as well as the angle of attack adjustment motor. The unidirectional traverse has a 14 inch range of motion and was made by Velmex, Inc. The angle of attack motor was operated manually to set the angle of attack for a given test with the help of a Mitutoyo Pro 360

digital protractor. This process was described in Section 4.2.9. The traverse motor, on the other hand, was computer-controlled. The DASH-16 digital outputs were used to send $\pm 5V$ pulses to the Maxwell stepping motor controller which in turn stepped the traverse motor one step for each pulse received. Using this control method, very accurate positioning of the hot-wire sensor could be achieved. The traverse was calibrated, and it was found that each step moved the hot-wire sensor 2.56×10^{-5} meters. The calibration is shown in Figure 5.23.

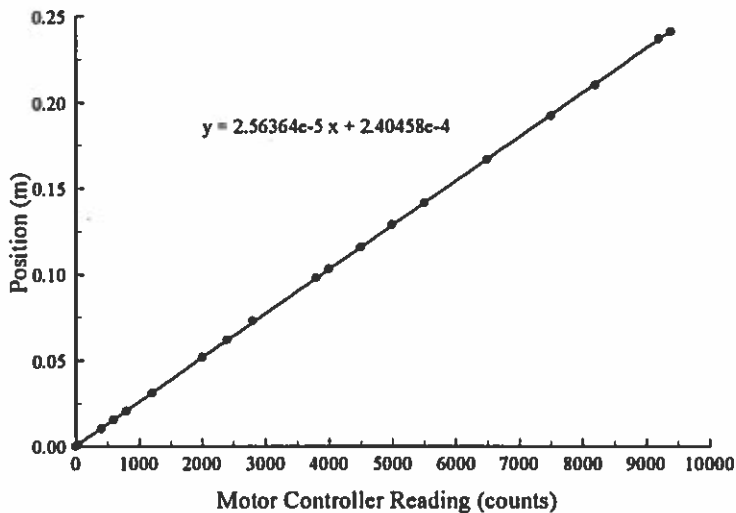


Figure 5.23: Traverse Calibration

Before tests could begin, the hot-wire had to first be calibrated. An overheat ratio of 1.8 was used for the hot-wire. The frequency response of the hot-wire was typically 35 to 40 kHz. A pitot-static probe provided the reference velocity against which the hot-wire output voltage was calibrated. A Validyne differential pressure transducer along with a Validyne Model CD15 Carrier Demodulator was used to record the pitot-static probe's measured pressure difference (the dynamic pressure). A small laminar air jet was used for the calibration. Figure 5.24 shows the hot-wire sensor positioned near the pitot-static probe at the jet outlet. Care was taken to keep the hot-wire sensor at least one pitot-static

probe diameter from the pitot-static probe, thus limiting interference effects that may occur between the two velocity measuring devices.

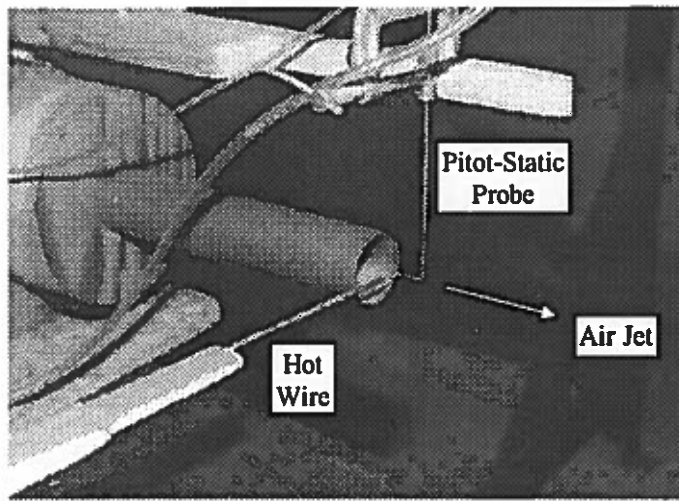


Figure 5.24: Calibration of Hot-Wire Against Pitot-Static Probe

A fourth-order polynomial curve was fit through the velocity versus volts data of the hot-wire calibration. The calibration was repeated every day that tests were conducted due to ambient temperature changes. Calibration results are shown in Figure 5.25. Notice that the calibration curves agree well. Some of the calibration curves from other test days did not agree as well with the curves shown in Figure 5.25; hence, it is important to calibrate each day that tests will be performed.

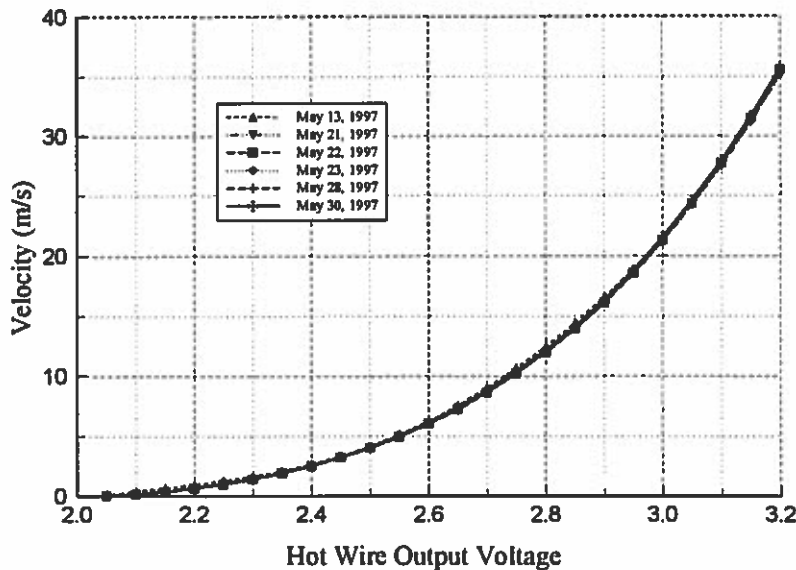


Figure 5.25: Hot-Wire Calibration Polynomial and Its Repeatability

5.2.3 Description of Data Acquisition and Data Reduction Codes

Several FORTRAN codes were written to integrate the experimental equipment components into a functioning system capable of hot-wire flowfield measurements. This section will briefly describe these codes. The only codes not written for this research were the programs that allowed real-time data from the hot-wire to be streamed to the computer for storage. These programs, named mkfile, streamer, and unpack, were developed by MetraByte Corporation.

Because of the need to run a commercially available code to stream the hot-wire data to the computer, other codes written to operate the experimental system had to be run through use of a batch file. A sample batch file (sample.bat) is given in Appendix D, followed by listings of the original codes to be discussed. This simple example batch file first executes a code named zeroes.exe. This code instructs the DASH-16 to read the initial offset voltage values from the instruments. Ambient conditions are inputted by the user.

The batch file then calls another batch file named hotwire.bat, listed in Appendix D after the main batch file sample.bat. The name after the “call hotwire” command is the name which will be used for the output files when data are taken at a given traverse location. The number after this name is the desired number of traverse steps that will be taken after data are recorded for the present traverse location.

Hotwire.bat first executes a code named waitgain.exe. This very simple code merely causes a delay that allows the wind tunnel to be brought up to speed and the hot-wire amplification gain to be set for the fluctuation signal. By setting the gain here, the fluctuation signal can be amplified to best fill the DASH-16 A/D voltage range. Next, hotwire.bat executes mkfile, a MetraByte Corporation code that creates a data file into which hot-wire data will be streamed. The data file is created on a virtual disk in the computer’s RAM. For this example, the data file is named hwdata.bin. Next, a DOS application, speedisk, is run to ensure that the region into which data are to be streamed is contiguous. This is a requirement of the streamer code.

Streamer.exe is then run. This causes the DASH-16 to sample channels zero and one and write the data to the virtual disk into the file hwdata.bin. Sampling rate and channel information are contained in a batch file named stream.bat.

After the hot-wire data have been collected, hotwire.bat runs a code named pitothot.exe. This code directs the DASH-16 to sample the contraction pressure transducer voltage and inputs from the user the thermocouple reading and the amplifier gain setting. A code to drive the hot-wire traverse is then executed (trav100.exe), moving the probe the desired number of steps as set in the main batch file sample.bat. The binary hwdata.bin file is then converted to an ascii file through use of a MetraByte Corporation program, unpack.exe.

At this point hotwire.bat is finished executing. The program control returns to the main batch file sample.bat. The user can simply repeatedly call hotwire.bat, specifying a new output file name and number of traverse steps for each line. The final time hot-wire sampling is desired, the line in the main batch file should be “call hotlast” instead of “call hotwire.” This “hotlast” batch file is identical to hotwire.bat except that it does not cause the traverse to be activated.

After taking data using the main batch file, the code hwreduce.exe is run to reduce the raw data and generate meaningful output data. After this data reduction code executes, the following files exist.

_____ .con → single file containing raw test condition voltage data for every traverse position

_____ .out → single file containing reduced data values for every traverse position including Re , Ma , ρ , U_∞ , T_∞ , and μ .

For each traverse position at which data were recorded, these files exist.

_____ .raw → contains raw counts for channels zero and one from hot-wire streaming

_____ .doc → contains hot-wire summary information such as sampling frequency, hot-wire position, and mean and rms hot-wire velocities

_____ .log → contains summary information about streamer execution

_____ .dad → contains single column of instantaneous fluctuation velocity values

_____ .fft → contains power spectrum information

5.2.4 Verification of Experimental Setup

It was decided that before beginning experimentation on the SM701 airfoil, the setup should first be verified as to be working properly. To accomplish this verification, three separate tests were performed. The first test involved putting a simple propeller between a jet of air and the hot-wire sensor as shown in Figure 5.26.

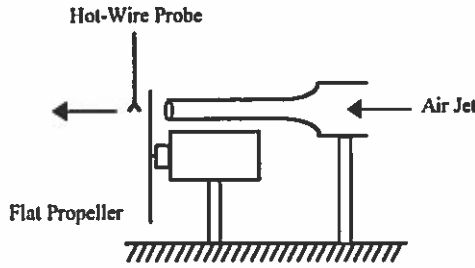


Figure 5.26: Simple Propeller Test for Hot-Wire Measurement System

The rotation rate of the propeller was recorded with an AMETEK Model 1726 Digital Tachometer. The hot-wire signal was recorded and then analyzed for frequency content using a FORTRAN FFT subroutine. The FORTRAN subroutine was taken from a numerical recipes book (Press et al., 1992). For several speeds of air flow and several propeller rotation rates, the frequency domain results consistently showed a distinct energy content peak at a frequency corresponding to the measured propeller rotation frequency.

The second verification test involved a 4.5 inch diameter circular cylinder mounted in the ASWT test section with the axis of the cylinder perpendicular to the flow direction. The hot-wire system was used to record the unsteady velocity field in the wake of the cylinder. From the velocity fluctuation measurements, the shedding frequency was obtained using the FORTRAN FFT subroutine. Based on the free stream velocity, a Strouhal number was calculated that agreed with the accepted value for cylinder shedding of $St \approx 0.2$.

The third test involved feeding a sine wave with a DC offset created by a function generator into the experimental setup. The sine wave had a known amplitude, DC offset, and frequency. The sine wave was correctly sampled by the experimental system, and the FFT power spectrum revealed the known frequency of the wave. From these three checks of the hot-wire system, confidence was gained that the components were functioning properly. Experimentation on the SM701 airfoil could begin.

5.2.5 Procedure for Hot-Wire Flowfield Measurements

The angle of attack was set to the desired value. Angles of attack tested included 15°, 18°, 20°, 22°, and 25°. The traverse mount was then adjusted such that the hot-wire probe traveled normal to the chordline at the desired chordwise location or perpendicular to the free stream direction when studying the wake. The hot-wire sensor was positioned approximately one millimeter off of the model surface for the chordwise profile measurements.

The tunnel was brought up to speed to give a Reynolds number of 315,000. The data acquisition software described in Section 5.2.3 then directed the sampling of the instantaneous hot-wire output voltage and the movement of the hot-wire sensor to the next traverse location. Several tests were done with sampling at 20.48 kHz, but the resulting power spectra revealed no significant energy content above a few hundred Hertz. It was decided to reduce the sampling rate to 2048 Hz to increase the resolution on the FFT frequency axis. The sampling time was 25.5 seconds. The low-pass filter seen in Figure 5.22 was set at 820 Hz for anti-aliasing purposes. Typical amplification factors of the fluctuation voltages were ten to 30 dB.

After sampling was completed at all points in the traverse sweep, the tunnel was shut off and the traverse repositioned to allow experimentation at a new location. The test matrix is shown in Table 5.2.

Table 5.2: Test Matrix for Hot-Wire Experimentation

α (deg)	Chordwise Location of Hot-Wire Profile Sweep (%)					Wake Position of Sweep	
	25	50	70	80	90	0.25c	0.75c
15			X	X	X	X	X
18							X
20	X	X	X			X	X
22							X
25							X

5.2.6 Hot-Wire Flowfield Measurements Results

Results of the hot-wire anemometry experimentation are now presented. Discussion will begin for $\alpha = 15^\circ$ and proceed through higher angles of attack. Figure 5.27 depicts the locations at which measurements were made for $\alpha = 15^\circ$. Two velocity profiles were recorded at 80% and 90% chord, and a wake survey 75% chord behind the airfoil's trailing edge was examined. Velocity profiles were measured starting approximately one millimeter above the airfoil surface and proceeding upwards away from the surface in a normal direction. At the wake survey location the hot-wire probe was lowered as far as was physically possible, constrained by the length of the probe. This minimum position of the hot-wire probe was termed $y = 0$. The survey was taken by traversing the probe upwards through the wake.

Figures 5.28a and 5.29a give the measured streamwise mean and rms velocity profiles for 80% and 90% chord locations, respectively. The profiles are seen to be very repeatable. The mean profiles on the airfoil show no clear indication of flow separation and reversal. Thus the separation revealed in Figure 4.4a of Section 4.1.3 is confined to a region very near the airfoil surface that is no thicker than one or two millimeters. The rms profiles in Figures 5.28a and 5.29a show the typical maximum in the middle of the region of high mean shear. The order of magnitude of the maximum rms fluctuation level on the airfoil is 0.1 when nondimensionalized by U_∞ . The numbers at various data points on the rms profiles are simply point numbers with the numbering system beginning with the data point nearest to the wall. At all numbered points both the skewness and the power spectrum of the streamwise velocity fluctuations were calculated. The skewness profiles are given in Figures 5.28b and 5.29b with the mean velocity profiles repeated for ease of comparison. The skewness is seen to be positive between the wall and the location of maximum u'_{rms}/U_∞ . Above that peak u'_{rms}/U_∞ location, the skewness becomes negative until locations very near the free stream are reached. There, the skewness becomes very large due to the drastic decrease of u'_{rms} in the free stream to values near 0.008 when nondimensionalized by U_∞ (the skewness is calculated as $\overline{(u')^3}/\left(\overline{u'^2}\right)^{3/2}$).

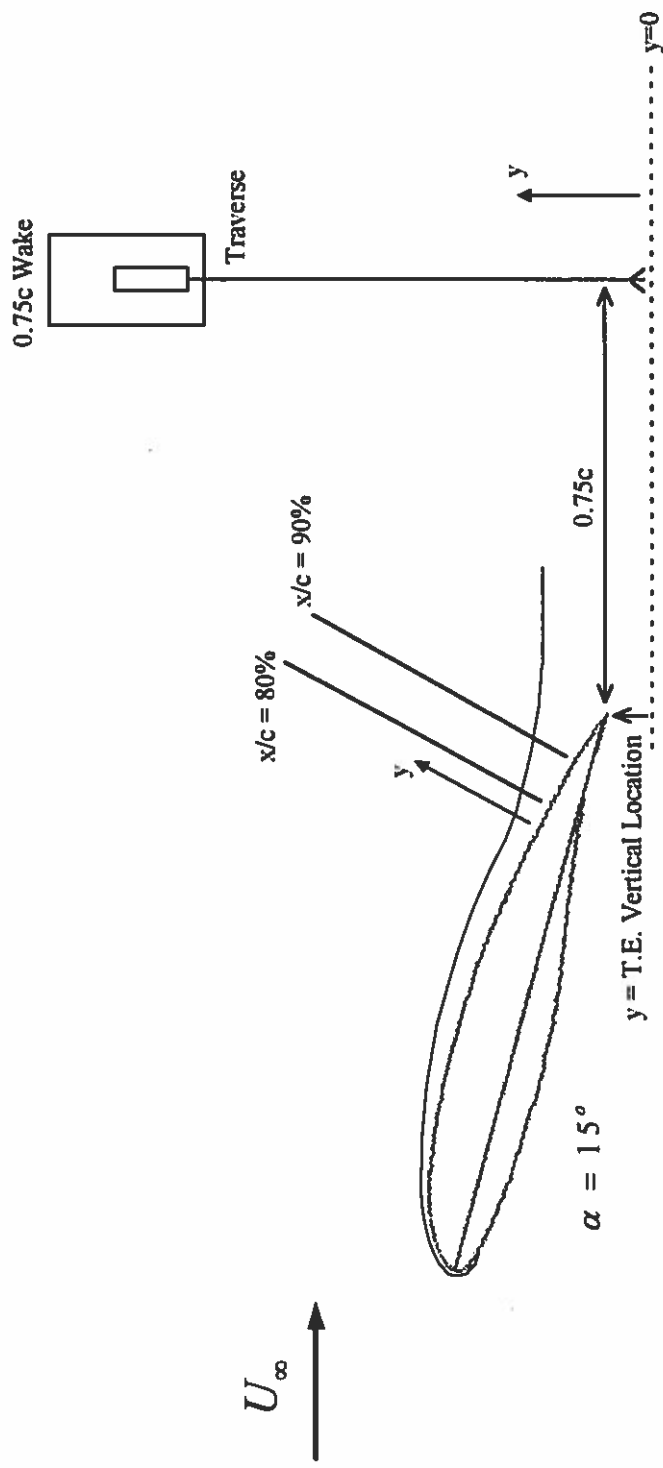
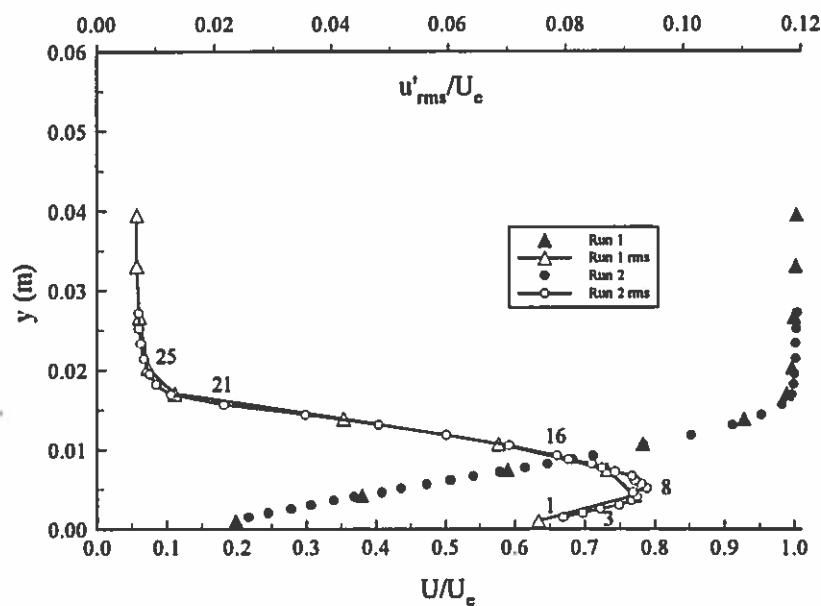
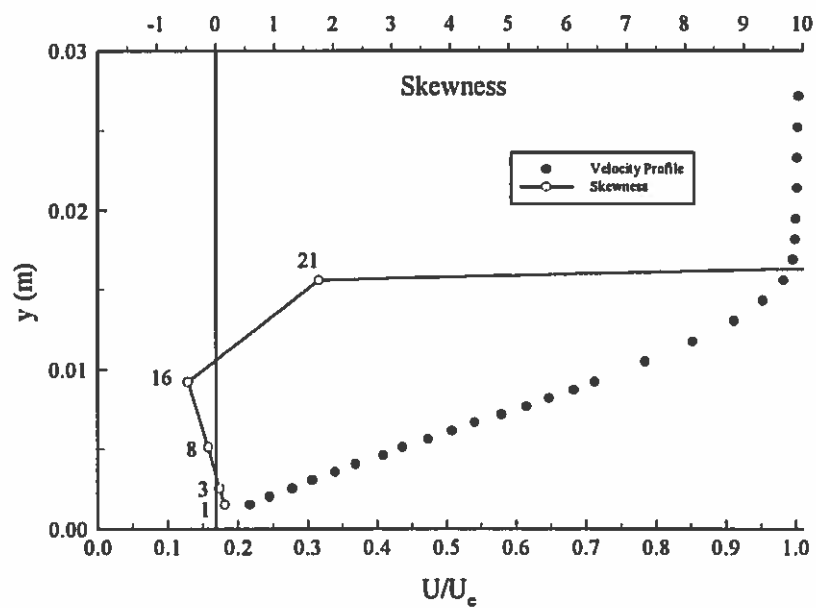


Figure 5.27: Velocity Profile and Wake Survey Locations for $\alpha = 15^\circ$

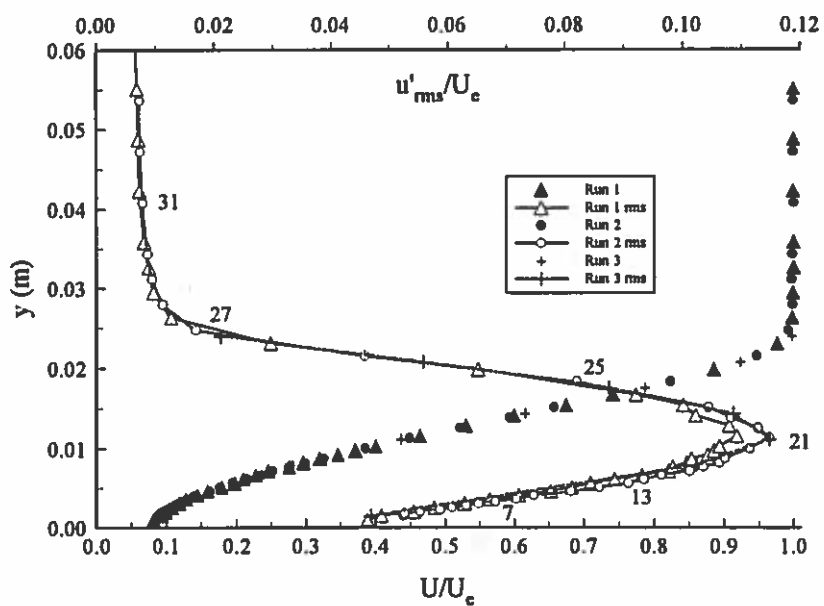


(a) Turbulence and Mean Velocity Profile

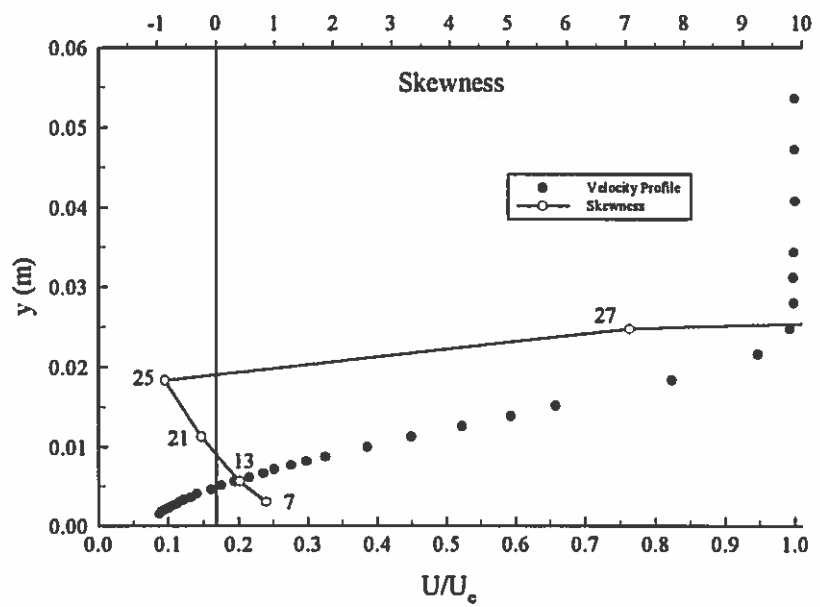


(b) Skewness Profile

Figure 5.28(a) and (b): $\alpha = 15^\circ$; $Re = 315,000$; $x/c = 80\%$



(a) Turbulence and Mean Velocity Profile



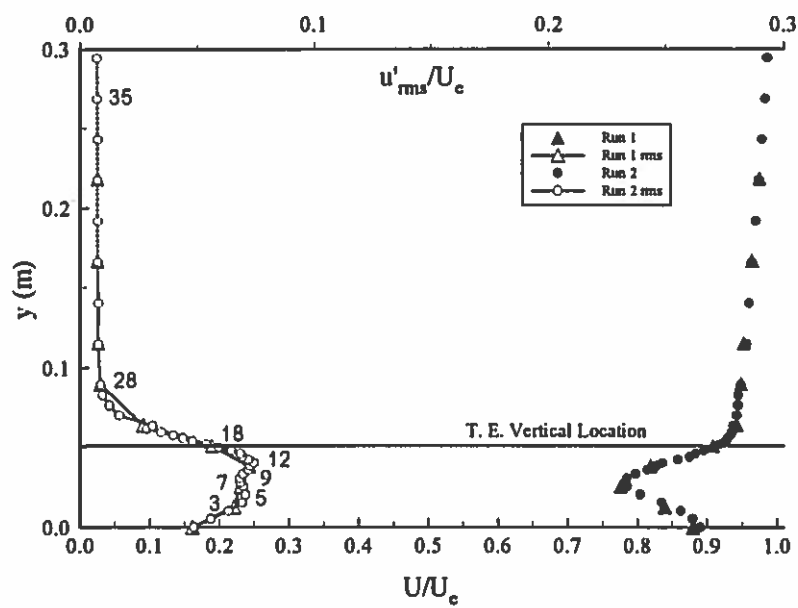
(b) Skewness Profile

Figure 5.29(a) and (b): $\alpha = 15^\circ$; $Re = 315,000$; $x/c = 90\%$

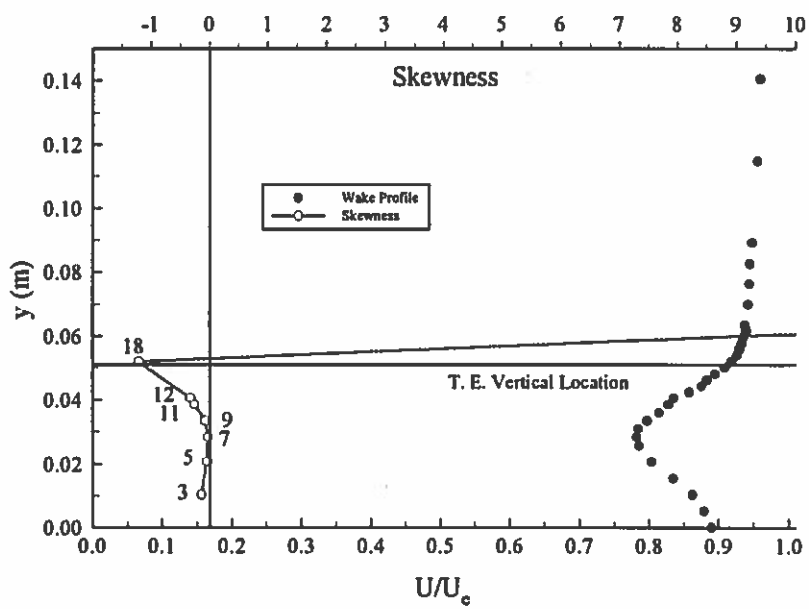
The wake survey for $\alpha = 15^\circ$ is given in Figure 5.30a. The wake is approximately six centimeters wide with only a 20% to 25% maximum wake velocity defect. The rms profile shows two slight peaks, one for each region of high mean shear on either side of the wake. Rms fluctuation levels range from near 0.08 at the maximum to 0.01 at the minimum when nondimensionalized by U_∞ . The maximum rms fluctuation level has thus decayed slightly from the value seen in the velocity profiles on the airfoil (Figures 5.28a and 5.29a). Skewness in the wake is seen to be negative, Figure 5.30b. The trailing edge vertical location is marked on the graph. Refer back to Figure 5.27 which depicts this location.

The spectra calculated for the various numbered locations in the velocity profiles on the airfoil and in the wake survey profile did not reveal any dominant instabilities. Only broadband turbulence was seen (these graphs are not shown). The thinness of the separated flow region on the airfoil along with the thin wake, small wake velocity defect, and broadband frequency spectra indicate that the airfoil at $\alpha = 15^\circ$ and $Re = 315,000$ is not severely stalled. In fact, the SM701 lift curve reaches a maximum very near $\alpha = 15^\circ$ for $Re = 315,000$. Thus it is clear that for this test configuration, the airfoil is just beginning to enter the stalled regime.

Figure 5.31 shows the location of the wake survey that was performed for $\alpha = 18^\circ$. The mean and rms velocity profiles are given in Figure 5.32a. The wake is much wider compared to the $\alpha = 15^\circ$ case at the 0.75c wake location (≈ 25 cm compared to ≈ 6 cm). Also the maximum velocity defect is much larger ($\approx 65\%$ compared to $\approx 25\%$). The rms fluctuation level nondimensionalized by U_∞ has also increased greatly, ranging from a maximum of about 0.25 to a minimum of about 0.04 (compared to 0.10 and 0.01 for $\alpha = 15^\circ$). The rms maximum in the lower portion of the wake occurs at the same vertical location as the airfoil's trailing edge. The skewness in Figure 5.32b is seen to be positive between the two rms maxima locations in the middle of the two high mean shear regions. The skewness is negative outside of this rms peak-to-peak region. Note that the skewness does not obtain extremely large values in the upper free stream as had occurred for $\alpha = 15^\circ$; this may be attributed to higher u'_{rms} values in the free stream at $\alpha = 18^\circ$.



(a) Turbulence and Mean Velocity Profile



(b) Skewness Profile

Figure 5.30(a) and (b): $\alpha = 15^\circ$; $Re = 315,000$; $0.75c$ Wake

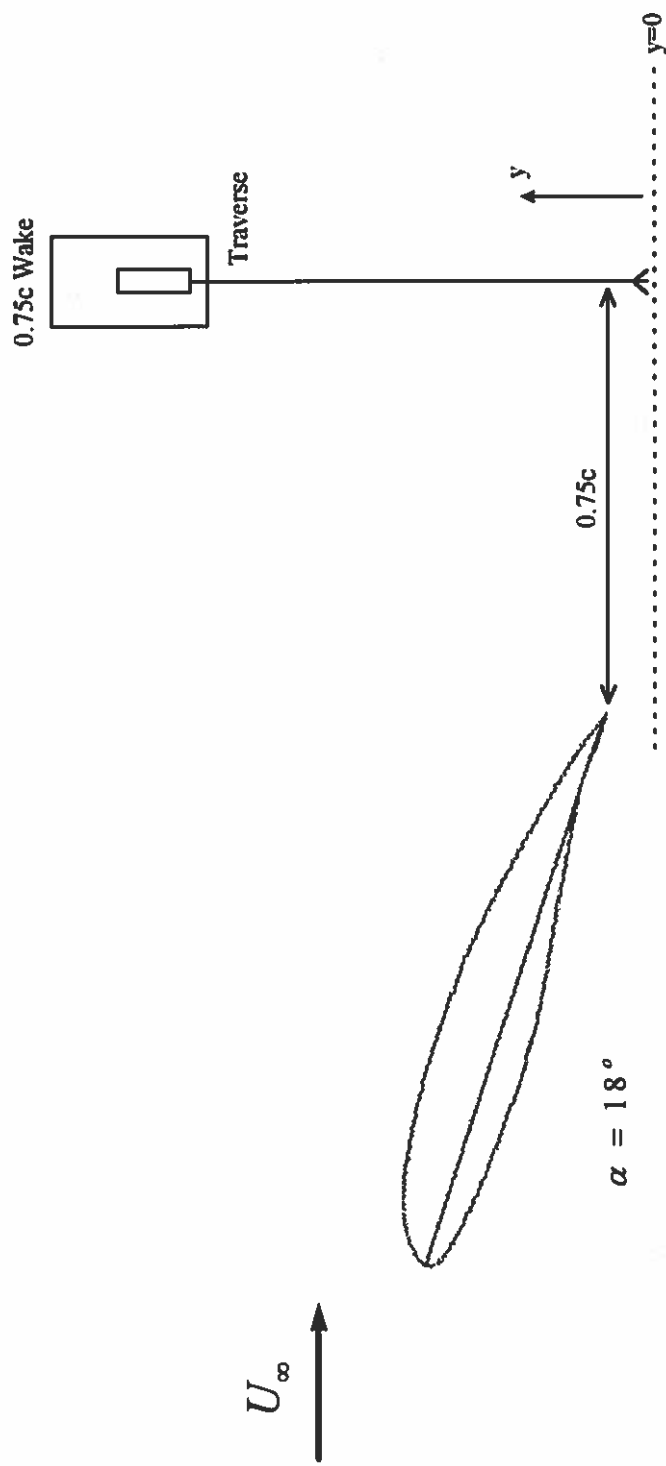
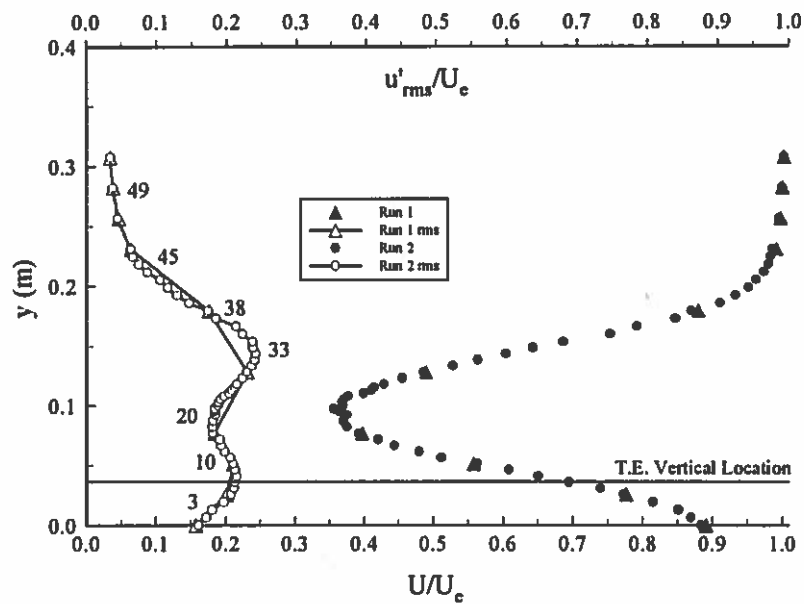
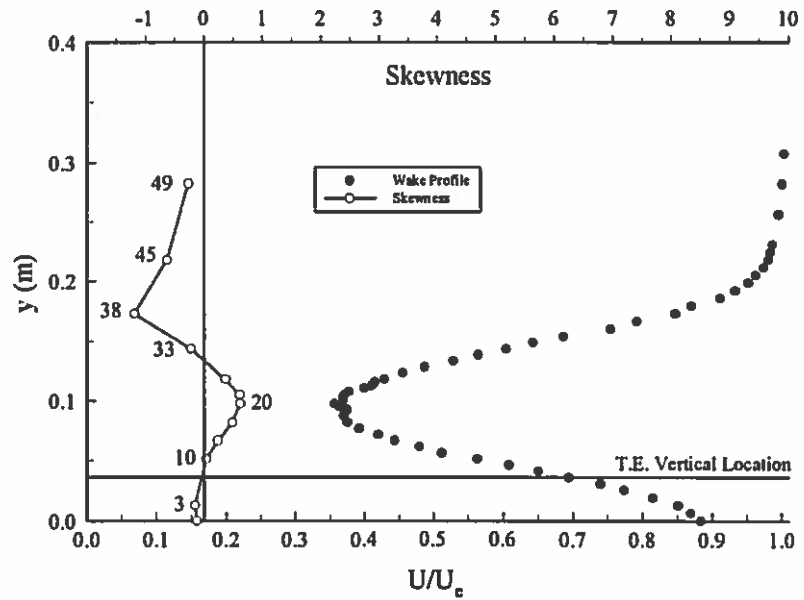


Figure 5.31: Wake Survey Location for $\alpha = 18^\circ$



(a) Turbulence and Mean Velocity Profile



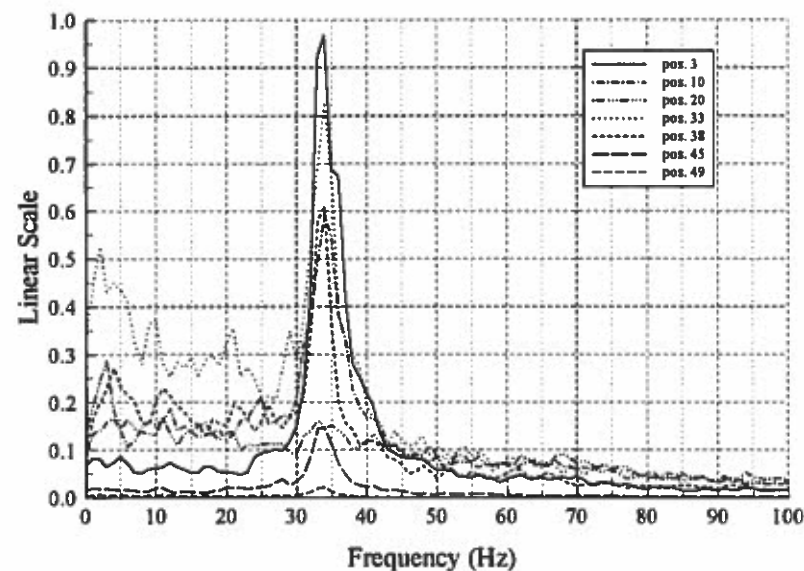
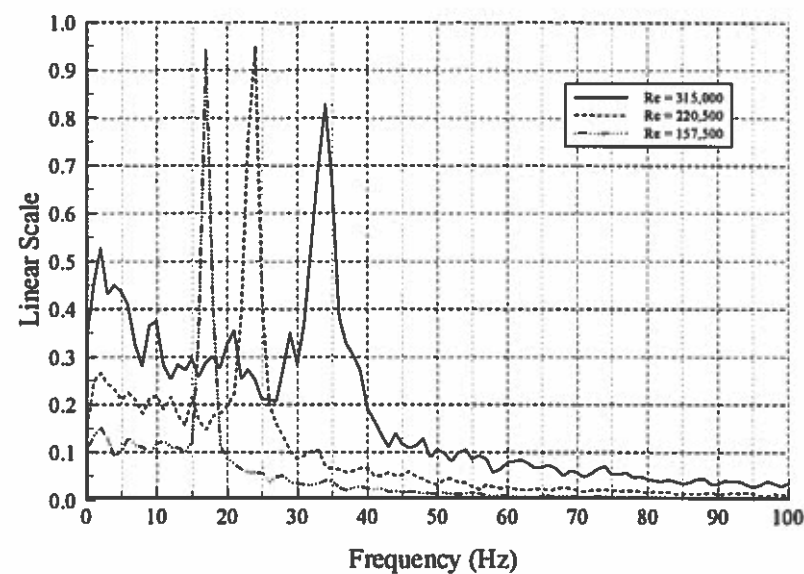
(b) Skewness Profile

Figure 5.32(a) and (b): $\alpha = 18^\circ$; $Re = 315,000$; $0.75c$ Wake

Figure 5.33a shows the spectra at the numbered locations in Figure 5.32a. It is obvious that a dominant flow structure exists at the $0.75c$ wake position for $\alpha = 18^\circ$. The frequency of this flow structure is approximately 34 Hz. From Figure 5.33a, the best hot-wire locations for measuring this dominant flow instability seem to be positions 3, 10, 33, and 38 which are located in the regions of high mean shear near the maximum u'_{rms} point on both sides of the wake. The instability is not seen well at positions 20, 45, or 49. Position 20 is at the maximum velocity defect location. Positions 45 and 49 are at the outer edge of the upper high mean shear region and in the free stream, respectively.

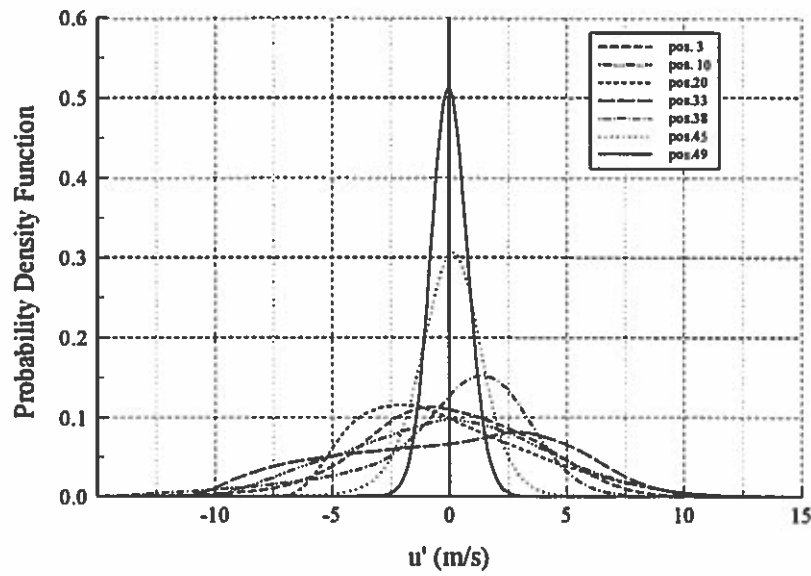
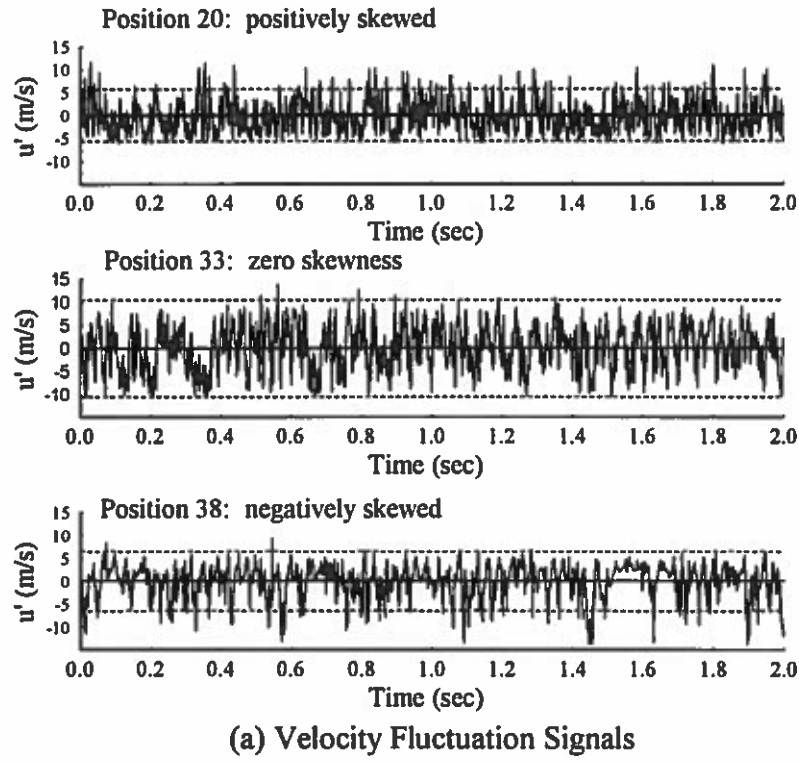
This dominant flow instability is seen to vary with U_∞ in Figure 5.33b. When the modified Strouhal number is calculated for each Reynolds number given in Figure 5.33b, a constant value of ≈ 0.20 is obtained.

Skewness has been discussed now for $\alpha = 15^\circ$ and $\alpha = 18^\circ$. Figure 5.34a shows typical velocity fluctuation signals for $\alpha = 18^\circ$. The upper signal is positively skewed, the middle signal has a skewness near zero, and the bottom signal is negatively skewed. (For example, positive skewness means that most of the time the signal is at relatively small negative values, but relatively large positive fluctuations do occur. No relatively large negative fluctuations exist). The fluctuation levels in Figure 5.34a are seen to be very large when compared to the mean velocity levels upon which they are imposed. For position 20 the mean velocity is near 7 m/s. For position 33 the mean velocity is near 12 m/s, and for position 38 the mean velocity is near 15 m/s. From the velocity fluctuation signals in Figure 5.34a, the flow is seen to fluctuate from its mean value to very near zero. Positive fluctuations are on the order of the mean velocity. It is thus seen that the flow is extremely unsteady, and the airfoil at $\alpha = 18^\circ$ is in the stalled regime. Figure 5.34b shows the probability density function computed for various wake points. The lines on this graph give a visual indication of the velocity fluctuation skewness at points in the wake survey. For instance, by examining the area under the curve for position 20, it is seen that at that position the velocity fluctuations are most likely to be in a negative velocity range. However, the curve for position 20 also shows that relatively large positive velocity fluctuations can occur but at a reduced probability.

(a) Power Spectrum ($Re = 315,000$)

(b) Free Stream Velocity Effects; Pos. 33

Figure 5.33(a) and (b): $\alpha = 18^\circ$; $0.75c$ Wake



(b) Probability Density Function

Figure 5.34(a) and (b): $\alpha = 18^\circ$; $Re = 315,000$; $0.75c$ Wake

Figure 5.35 shows the three velocity profile locations on the airfoil along with the two wake survey locations for $\alpha = 20^\circ$. The mean and rms velocity profiles are given in Figures 5.36a to 5.38a for chordwise locations of 25%, 50%, and 70%, respectively. It appears that a reverse flow region exists on the airfoil for these test conditions. The mean data seem to indicate the flow reversal near the surface by an increase in mean velocity near the wall. It is impossible to tell precisely, however, the thickness of the reverse flow region since the single sensor hot-wire is not directionally sensitive. Estimates of reverse flow region thickness are approximately one, three, and five centimeters for $x/c = 25\%$, 50%, and 70%, respectively.

Also of interest is the apparent shift of the nondimensional mean velocity data by about 0.13 on the abscissa, Figure 5.36a. The mean data do not show the mean velocity approaching zero as must occur near the boundary of the reverse flow region and the shear region. A sensitivity analysis was performed on the hot-wire calibration polynomial from which instantaneous velocity values are computed from the hot-wire output voltage. For calculated velocities below one meter per second, only a two percent uncertainty is expected. For calculated velocities above one meter per second, the uncertainty is less than a percent. The shift seen in the mean profiles in Figures 5.36a to 5.38a is on the order of $U/U_* \cong 0.15$ or $U \cong 2$ m/s on the average. This shift can not be caused by uncertainty in the velocity calculations alone. A possible explanation for this apparent shift can be found if hot-wire rectification is examined. A single sensor hot-wire can not detect a reversal of flow direction due to the symmetry of the sensing element. If a hot-wire sensor is put in a reversing flow, such as the flow region near the boundary between the reverse flow and the shear layer flow on a stalled airfoil, ambiguity in the velocity measurements will result. For instance, a given flow speed will be registered by the hot-wire as a certain voltage regardless of the direction of the flow. A sample of a hot-wire signal in such a reversing flow is shown in Figure 5.39.

The hot-wire output voltage displays a folding or rectification (shaded areas) when flow reversal occurs. This rectification causes the measured U_{mean} values to be too high

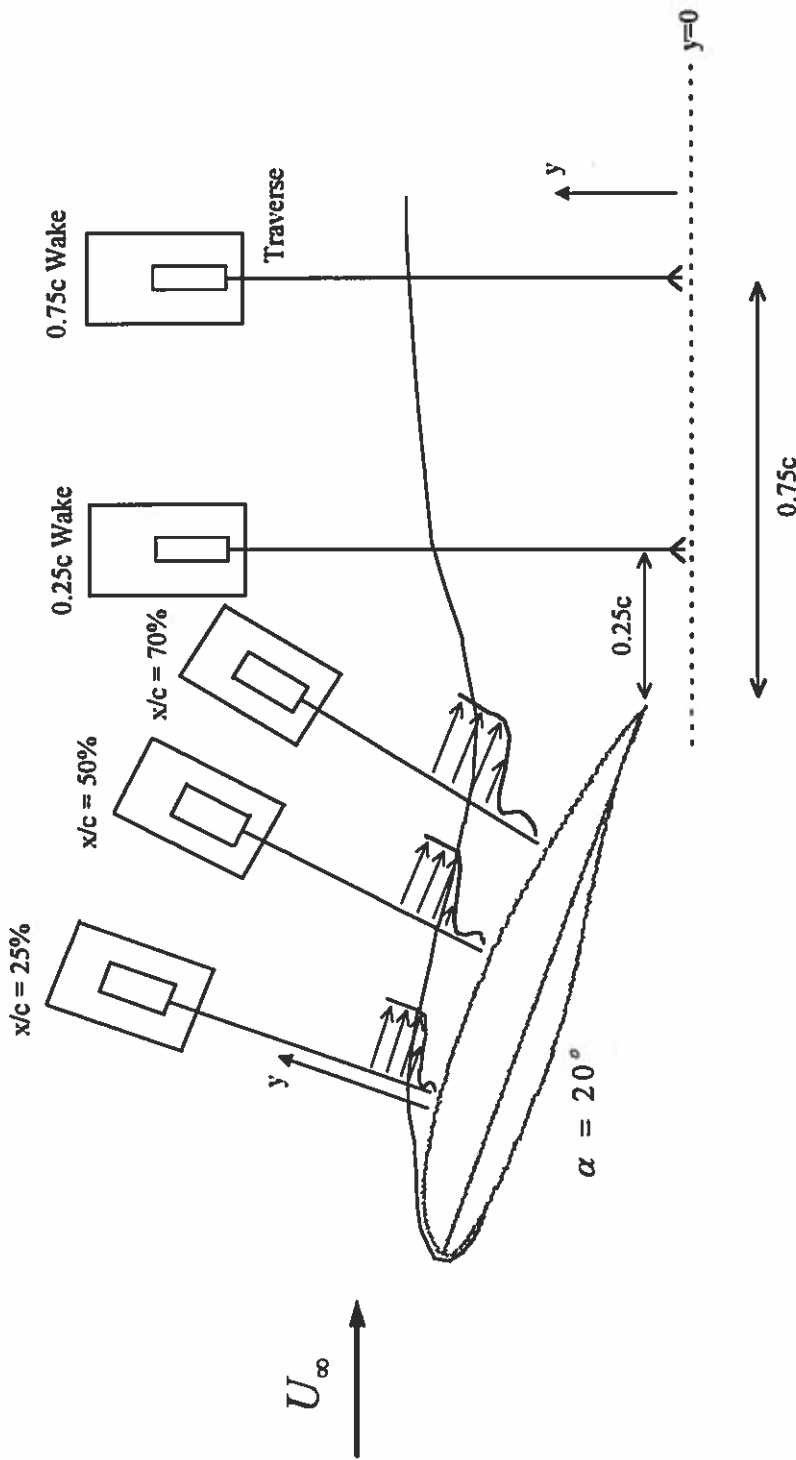
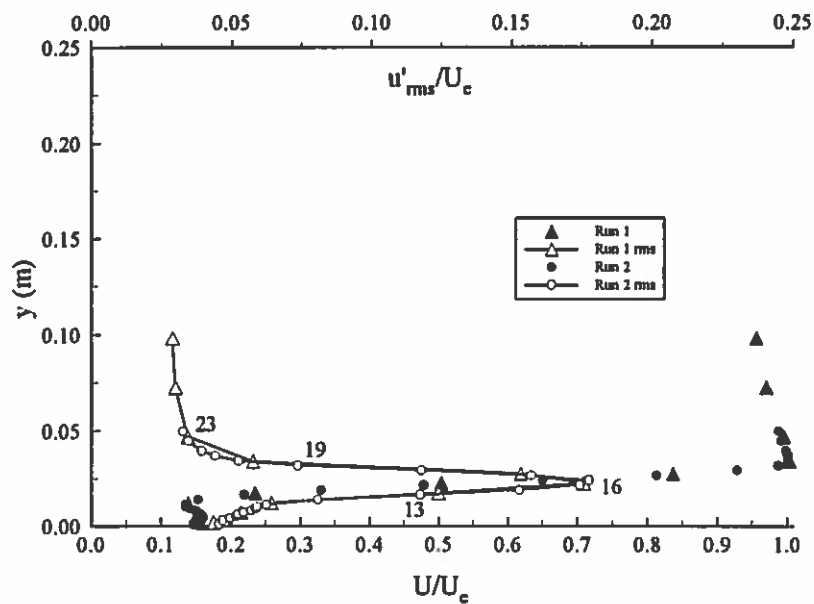
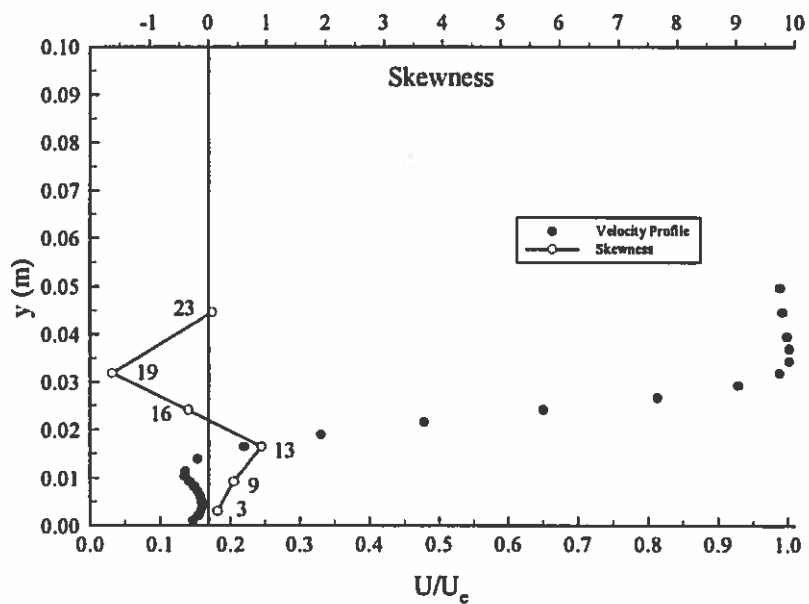


Figure 5.35: Velocity Profile and Wake Survey Locations for $\alpha = 20^\circ$

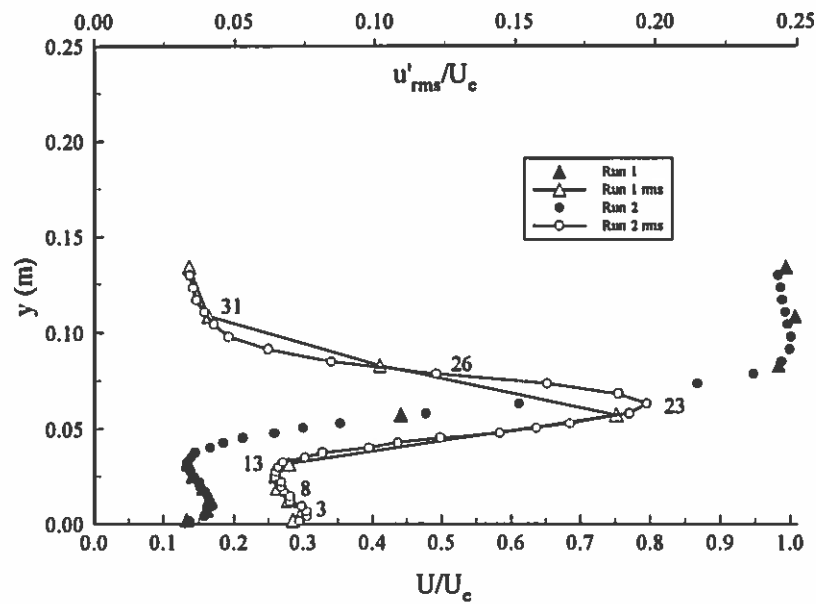


(a) Turbulence and Mean Velocity Profile

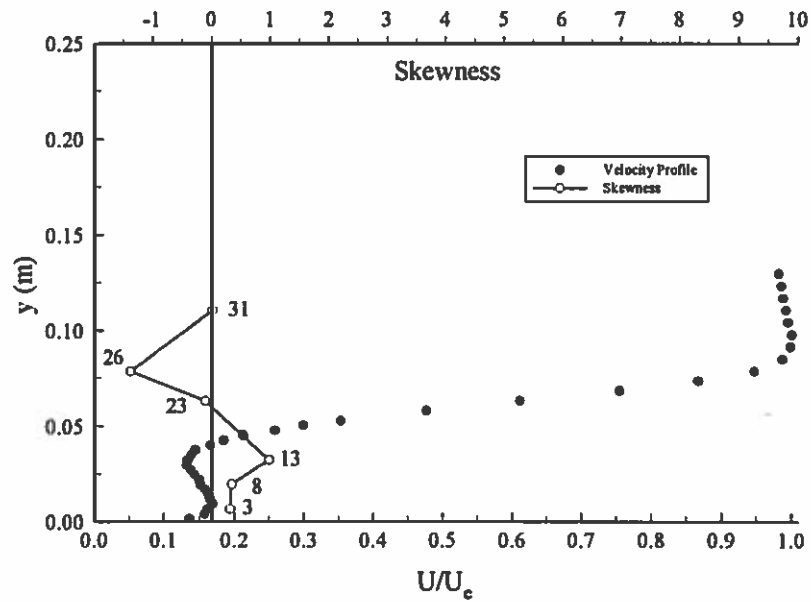


(b) Skewness Profile

Figure 5.36(a) and (b): $\alpha = 20^\circ$; $Re = 315,000$; $x/c = 25\%$

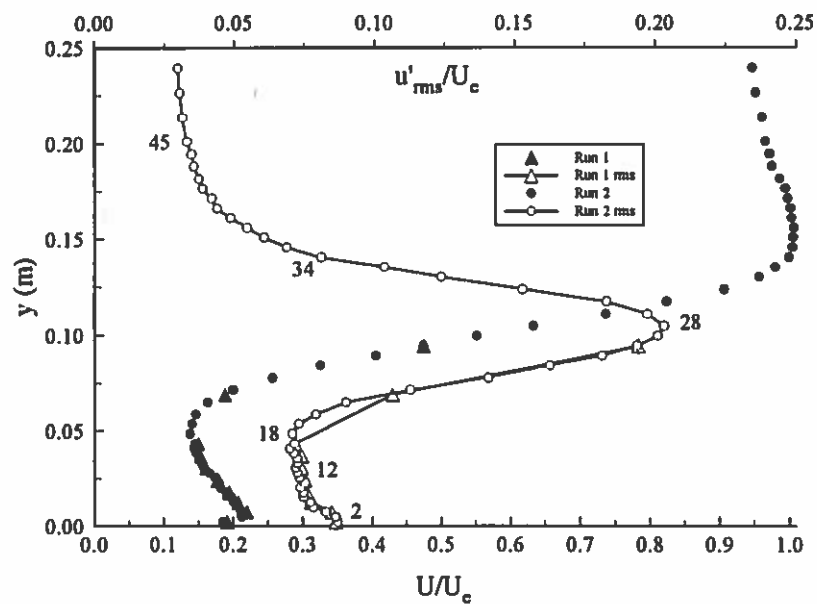


(a) Turbulence and Mean Velocity Profile

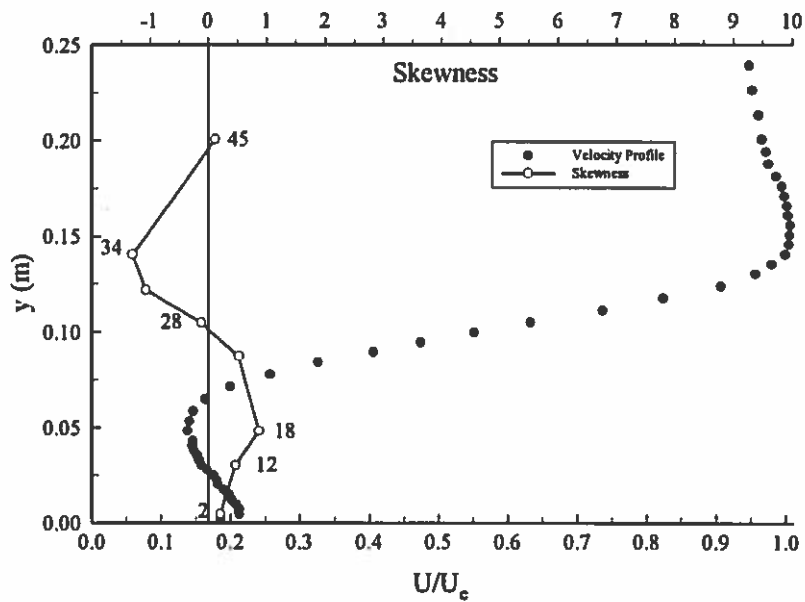


(b) Skewness Profile

Figure 5.37(a) and (b): $\alpha = 20^\circ$; $Re = 315,000$; $x/c = 50\%$

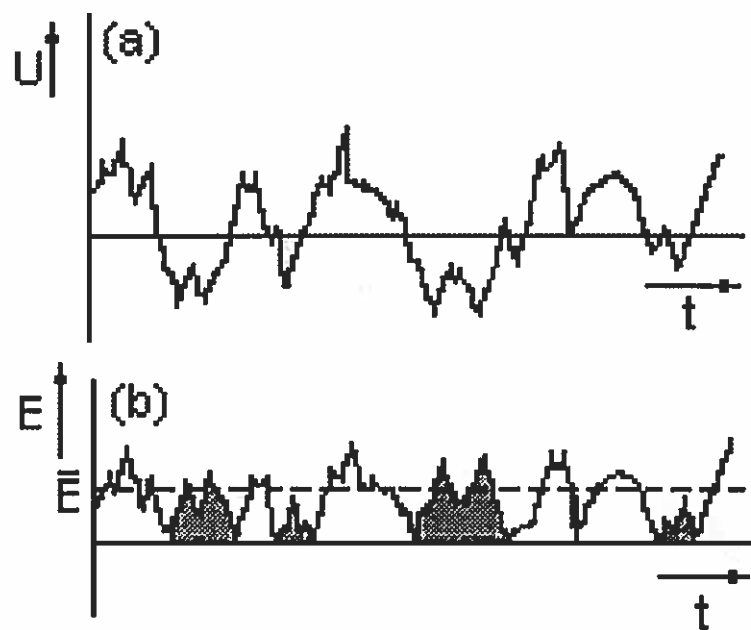


(a) Turbulence and Mean Velocity Profile



(b) Skewness Profile

Figure 5.38(a) and (b): $\alpha = 20^\circ$; $Re = 315,000$; $x/c = 70\%$



Source: Bruun, 1995

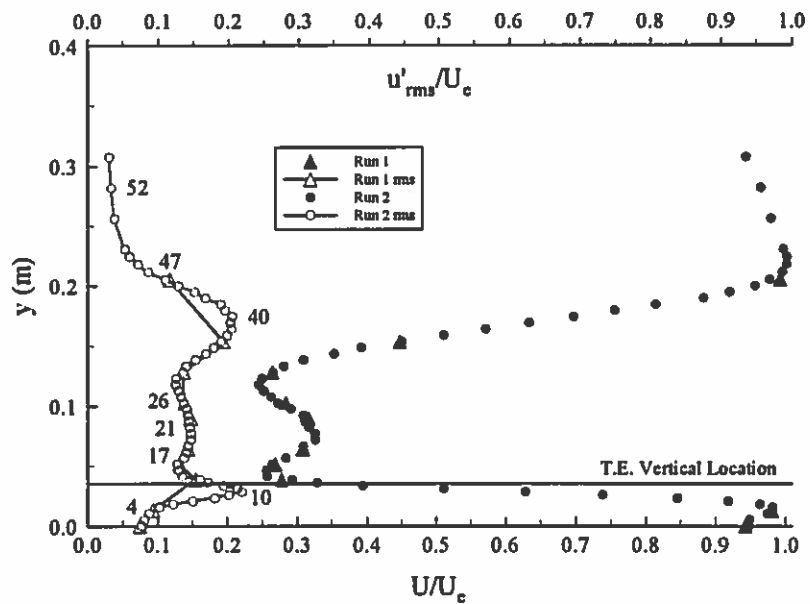
Figure 5.39: Hot-Wire Rectification in 1D Reversing Flowfield

and the measured $\overline{u'^2}$ values to be too low (Bruun, 1995). Thus, hot-wire rectification could be causing the mean data of Figures 5.36a to 5.38a to be too high near the boundary between the reverse flow region and the separated shear layer.

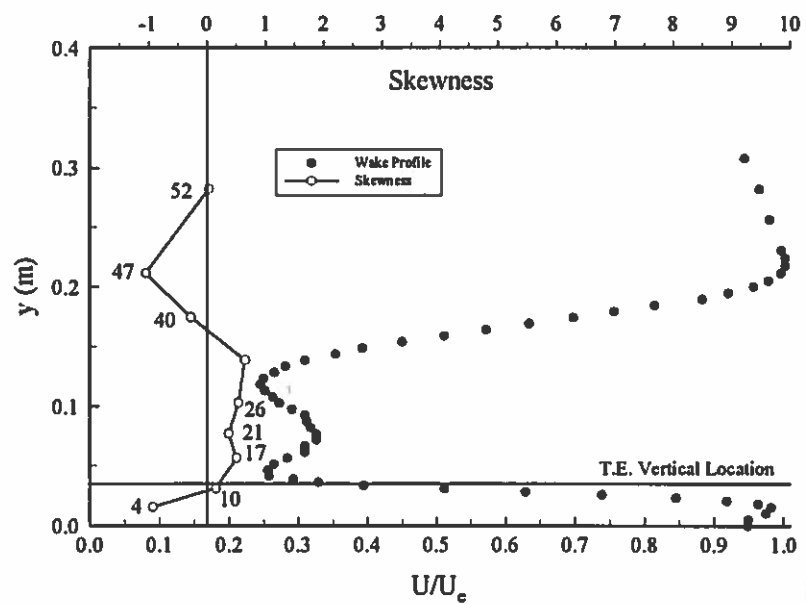
The skewness profiles for chordwise locations of 25%, 50%, and 70% are given as Figures 5.36b to 5.38b, respectively. For all three chordwise locations, the flow is positively skewed between the wall and the location of maximum u'_{rms}/U_e . Above that peak u'_{rms}/U_e location, the flow is negatively skewed.

Wake survey results are given in Figures 5.40 and 5.41. As was the case for $\alpha = 18^\circ$, a local u'_{rms}/U_e maximum occurs at the same vertical location as the airfoil's trailing edge. Rms levels are consistent with results for $\alpha = 18^\circ$. The velocity fluctuations are positively skewed between the two local u'_{rms}/U_e maxima and negatively skewed outside of this rms peak-to-peak region (Figures 5.40b and 5.41b).

Power spectra were calculated for the various numbered points given in Figures 5.36 to 5.41. Figure 5.42 shows the development of a dominant flow instability over the chord and into the wake at $\alpha = 20^\circ$. In Figure 5.42a, only a turbulent spectrum is seen with significant energy content dying out after ≈ 300 Hz when examining the spectrum at the maximum u'_{rms}/U_e location (the solid line in the figure). Figure 5.42b indicates no distinct change at $x/c = 50\%$ from $x/c = 25\%$. By 70% chord, a very slight indication of a dominant instability frequency begins to appear at position 45 located in the free stream (see Figure 5.42c). A subharmonic is also noticed. By the 0.25c wake location, the instability has amplified to be very noticeable. Figure 5.42d shows the instability to be approximately 33 Hz. Spectra at points 4, 10, 40, and 47 provide the strongest indication of the instability. These points are located in the regions of high mean shear between the maximum u'_{rms}/U_e location and the free stream (refer back to Figure 5.40a). It appears that the lower half of the wake (positions 4 and 10) provides a slightly stronger indication of the dominant instability frequency than the upper half of the wake (positions 40 and 47). Position 26, located in the maximum velocity defect region of the wake, does not provide a clear indication of a dominant instability frequency.

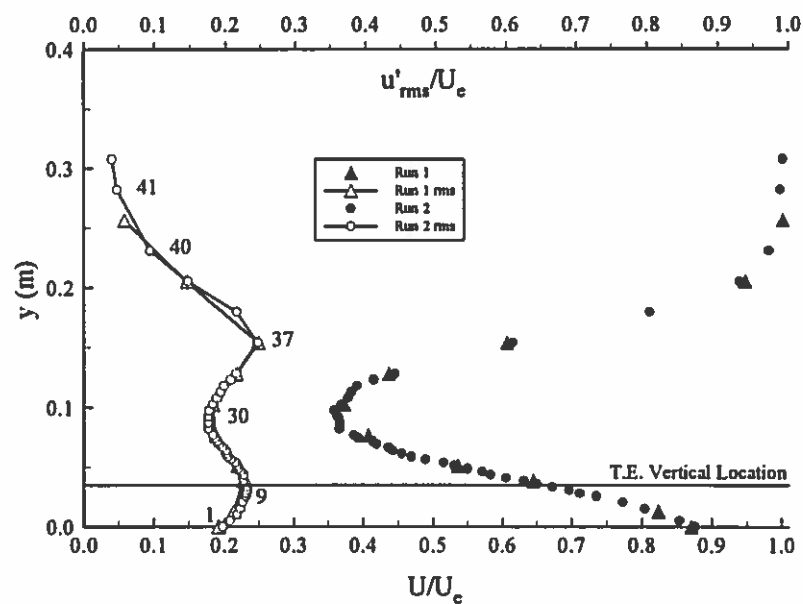


(a) Turbulence and Mean Velocity Profile

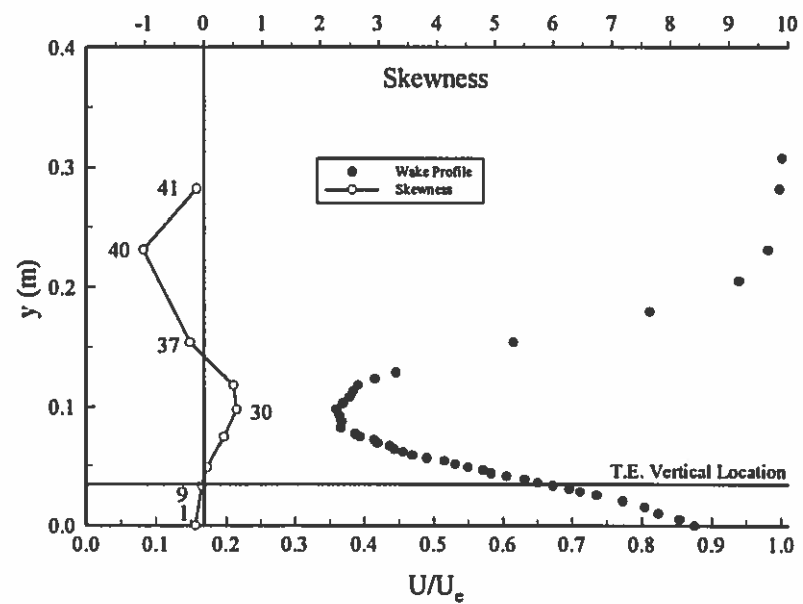


(b) Skewness Profile

Figure 5.40(a) and (b): $\alpha = 20^\circ$; $Re = 315,000$; $0.25c$ Wake



(a) Turbulence and Mean Velocity Profile



(b) Skewness Profile

Figure 5.41(a) and (b): $\alpha = 20^\circ$; $Re = 315,000$; $0.75c$ Wake

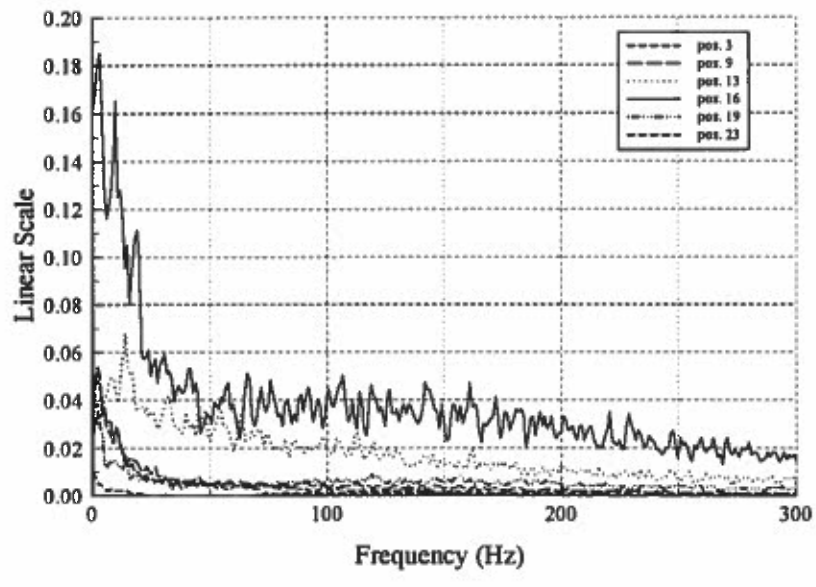
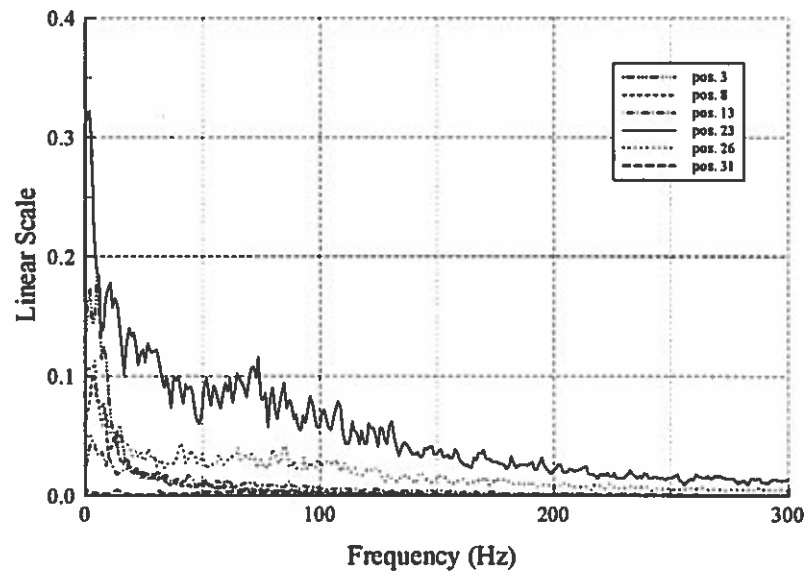
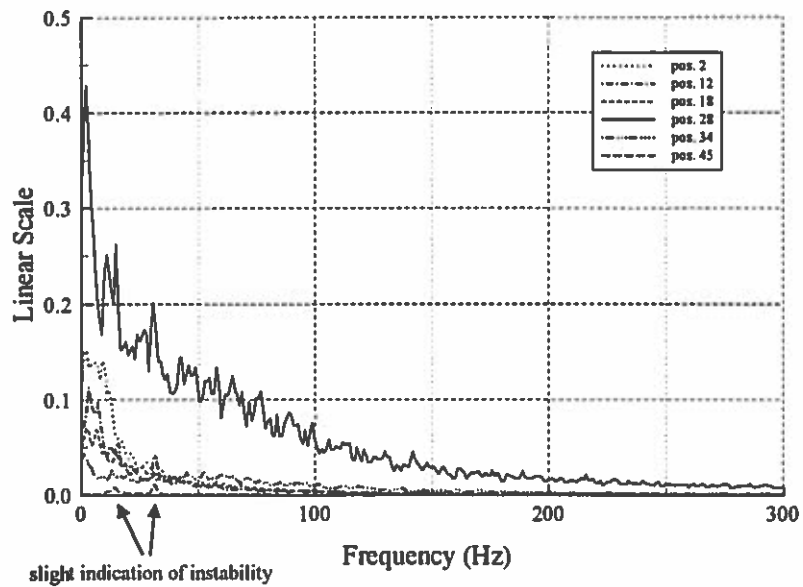
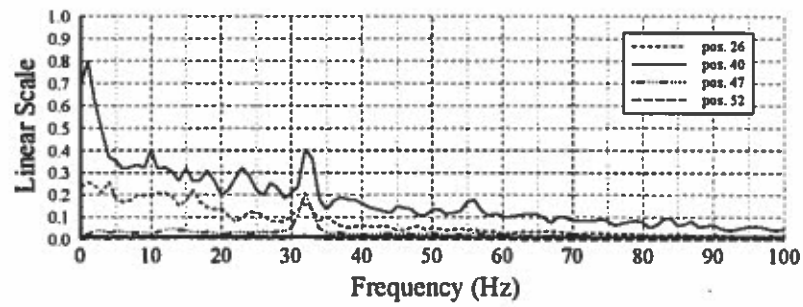
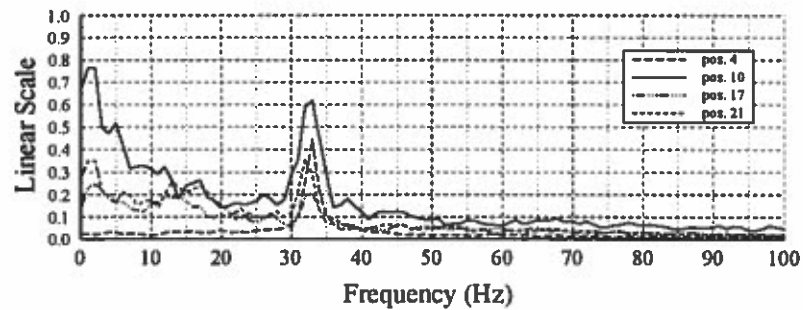
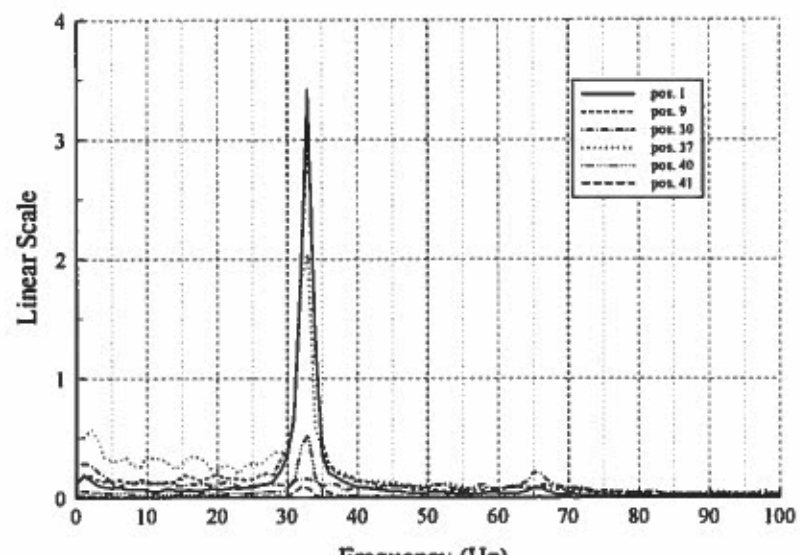
(a) Power Spectrum ($x/c = 25\%$)(b) Power Spectrum ($x/c = 50\%$)

Figure 5.42(a) and (b): $\alpha = 20^\circ$; $Re = 315,000$

(c) Power Spectrum ($x/c = 70\%$)(d) Power Spectrum ($0.25c$ Wake)Figure 5.42(c) and (d): $\alpha = 20^\circ$; $Re = 315,000$



(e) Power Spectrum (0.75c Wake)

Figure 5.42(e): $\alpha = 20^\circ$; $Re = 315,000$

Figure 5.42e contains spectra for the 0.75c wake location. At this location a dominant instability frequency of 33 Hz is clearly seen along with its first harmonic. Locations 1, 9, 37, and 40 most clearly indicate the dominant instability. These points are located in the high mean shear regions on both sides of the wake between the maximum u'_{rms}/U_e location and the free stream. The positions in the lower half of the wake (1 and 9) give the best indication. Position 30, located in the maximum velocity defect region, does not reveal the dominant instability frequency but does give an indication of its first harmonic.

Figure 5.43 depicts the wake survey location for $\alpha = 22^\circ$. The mean and rms velocity profiles are given in Figure 5.44a. Skewness is presented in Figure 5.44b. Trends are consistent with wake results for $\alpha = 18^\circ$ and $\alpha = 20^\circ$. The lower rms maximum occurs at the same vertical position as the airfoil trailing edge. Rms maxima are on the order of 0.25 when nondimensionalized by U_e . The velocity fluctuations are positively skewed in the maximum velocity defect region located between the two local rms maxima. Outside of this rms peak-to-peak region, the skewness is negative. A dominant instability frequency of about 30 Hz surfaced when velocity fluctuation spectra were examined at the numbered positions indicated in Figure 5.44a. The dominant instability was best indicated at points 3, 8, and 35 which lie in the regions of maximum mean shear near the u'_{rms}/U_e maximum locations. The frequency peaks of the spectra are actually the strongest at positions 3 and 8 in the lower half of the wake. The dominant instability frequency is also seen at points 29 and 45 to a lesser extent than for the previously discussed wake points. Positions 29 and 45 lie near the maximum velocity defect location and near the free stream, respectively, of the upper half of the wake. Position 17 at the maximum velocity defect location gives no indication of a dominant instability but does indicate a frequency of approximately 59 Hz, a harmonic of the dominant 30 Hz instability frequency.

Figure 5.45 shows the wake survey location for $\alpha = 25^\circ$. Mean and rms velocity profiles are given in Figure 5.46a with skewness results in Figure 5.46b. Again, trends are consistent with the other stalled angle of attack cases. A maximum in the rms profile occurs at the same vertical location as the airfoil trailing edge. The velocity fluctuations

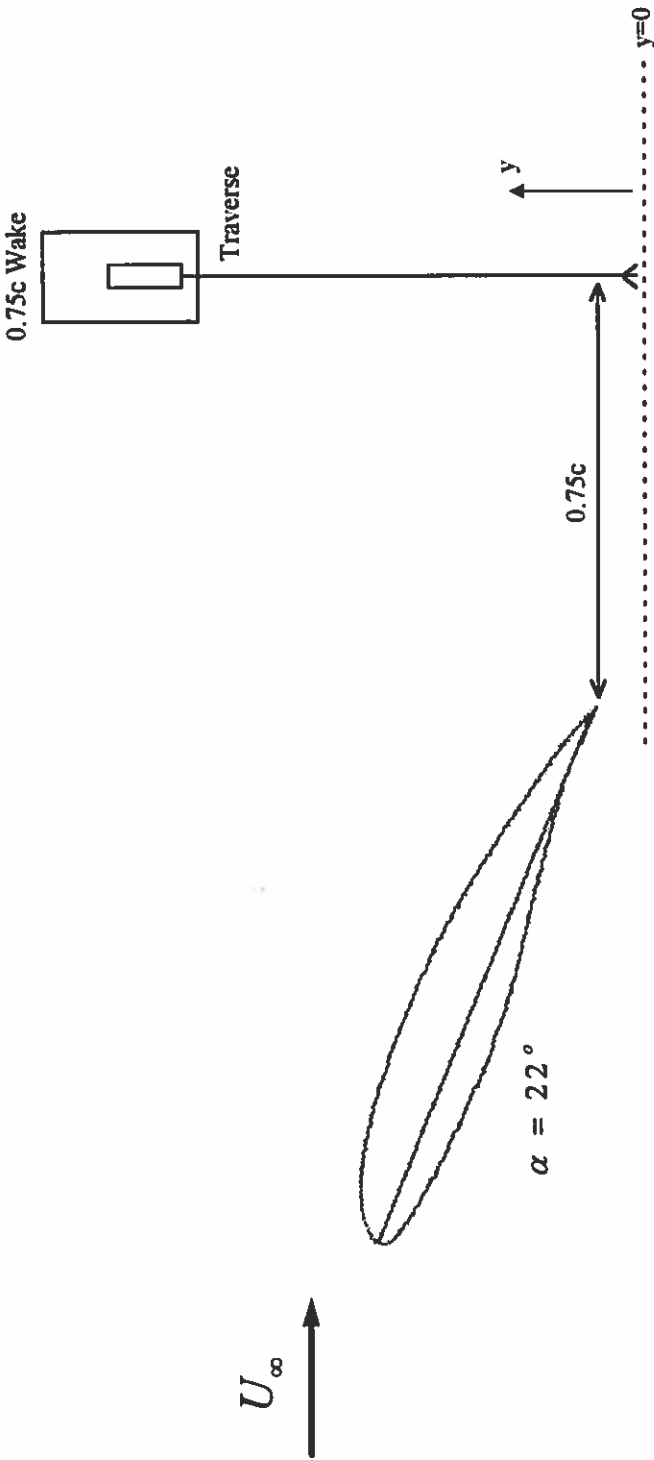
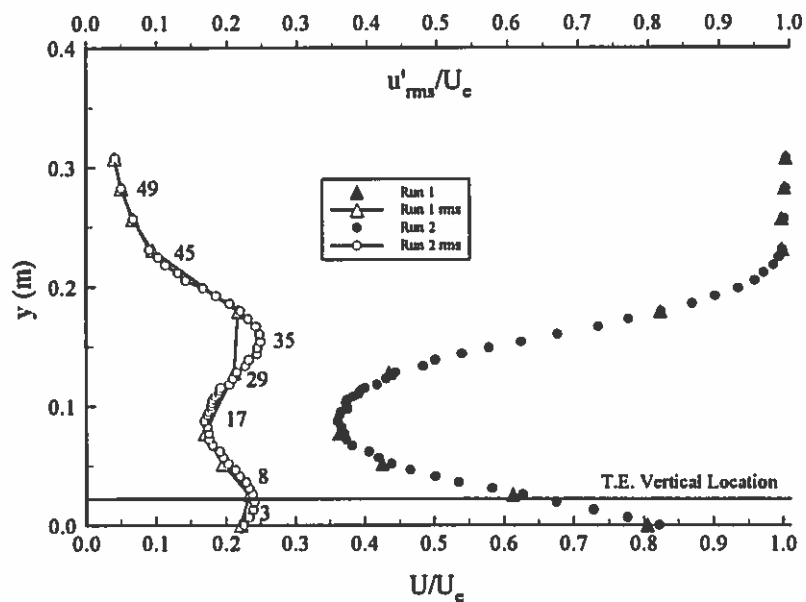
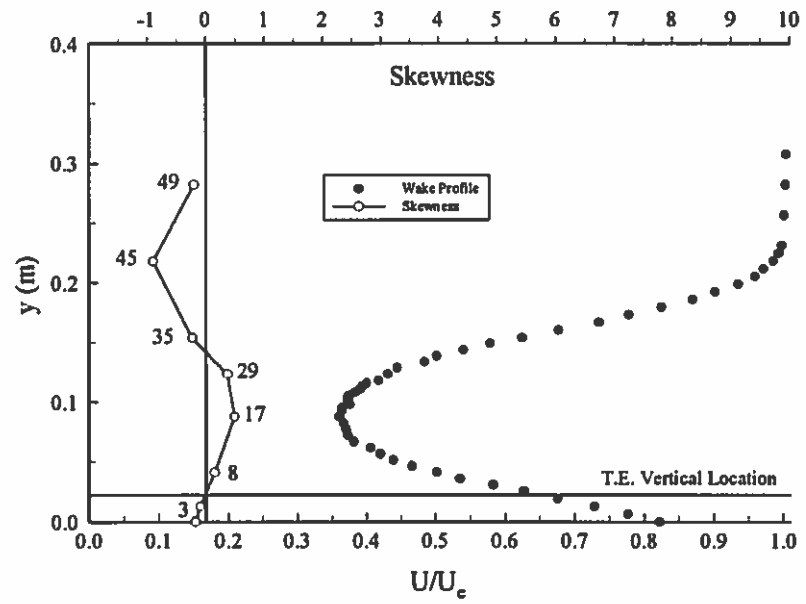


Figure 5.43: Wake Survey Location for $\alpha = 22^\circ$



(a) Turbulence and Mean Velocity Profile



(b) Skewness Profile

Figure 5.44(a) and (b): $\alpha = 22^\circ$; $Re = 315,000$; $0.75c$ Wake

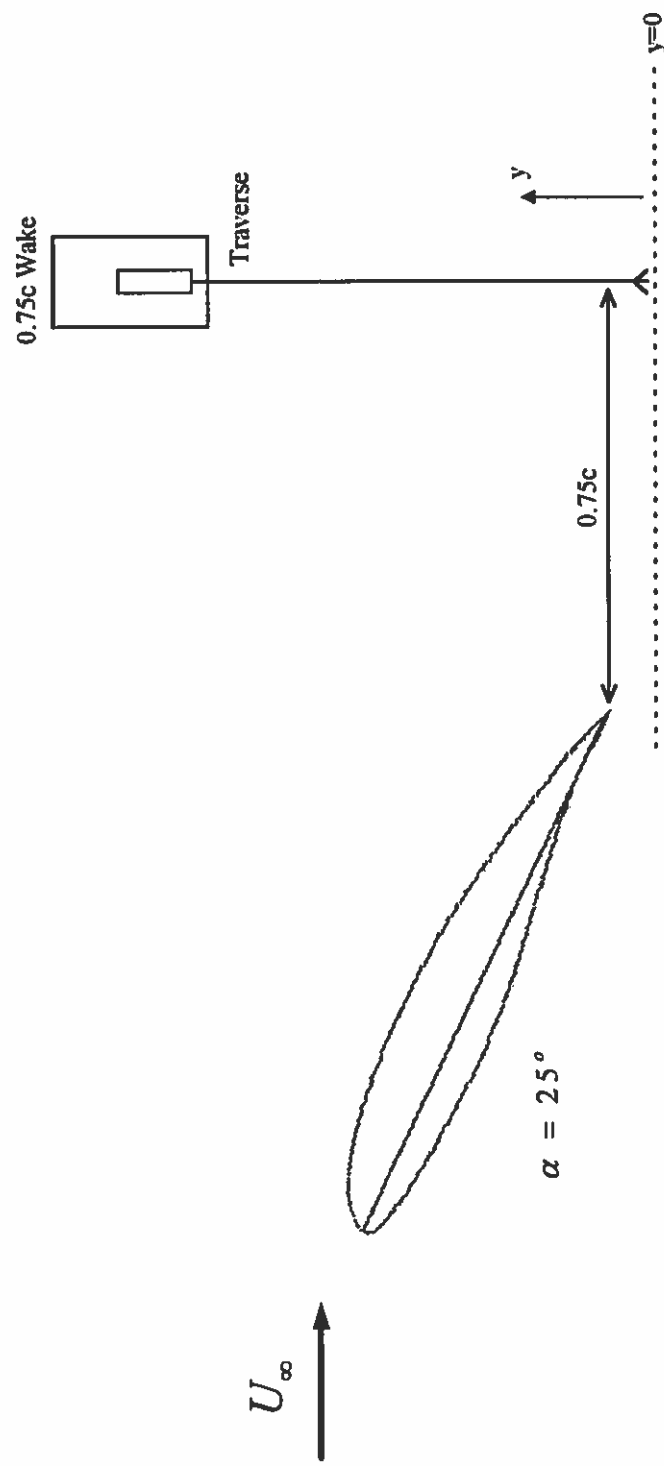
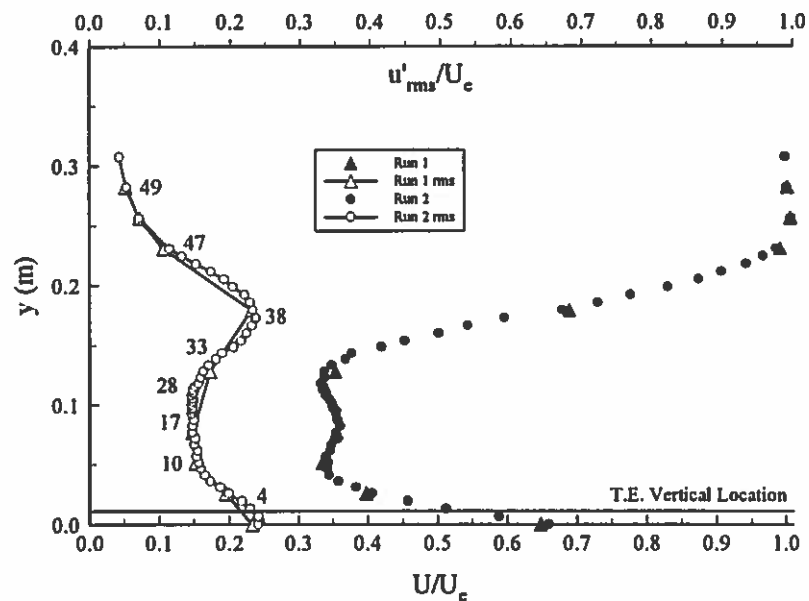
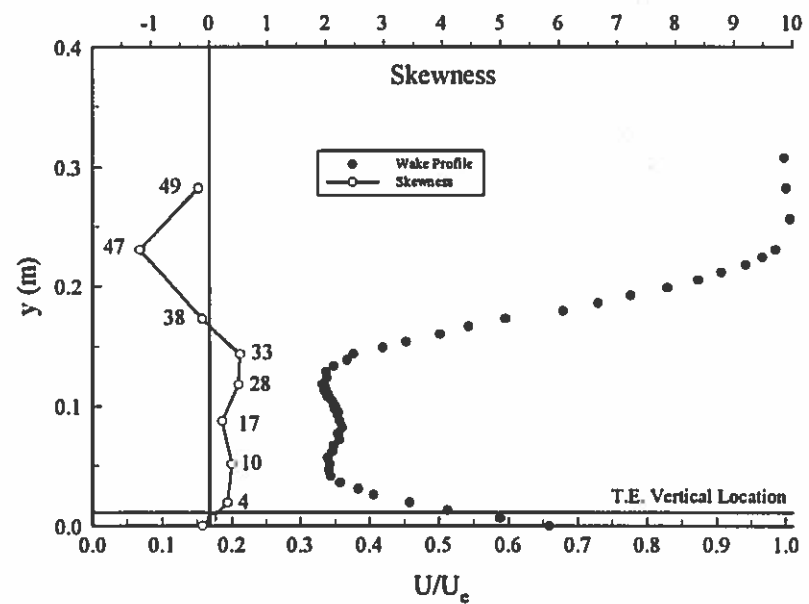


Figure 5.45: Wake Survey Location for $\alpha = 25^\circ$



(a) Turbulence and Mean Velocity Profile



(b) Skewness Profile

Figure 5.46(a) and (b): $\alpha = 25^\circ$; $Re = 315,000$; $0.75c$ Wake

are positively skewed between the rms maxima in the two wake high mean shear regions; outside of these regions the velocity fluctuations are negatively skewed. A dominant instability frequency of 27 Hz is best observed when the frequency spectra is computed at points 4 and 38 in the high mean shear regions, with the position in the lower half of the wake yielding the tallest spectral peak. The dominant instability is also seen as smaller spectral peaks at points 10, 33, and 47 which are near the maximum mean velocity defect and the free stream. In the center of the mean velocity defect region, points 17 and 28 yield no indication of a dominant flow instability.

Consistent for all tests in the post-stalled regime, the skewness of the velocity fluctuations in the wake profiles was positive between the two u'_{rms}/U_e local maxima that exist in the regions of high mean shear on both sides of the wake. The skewness was negative outside of that peak-to-peak u'_{rms}/U_e region. For the pre-stalled angle tested ($\alpha = 15^\circ$), the skewness was negative throughout the wake (Figure 5.30b). This change in skewness profile trend is a result of the large-scale coherent vortical structures being formed under stalled conditions. Recall that two counter-rotating coherent vortices are being produced when the airfoil is stalled: one coherent vortex rotating clockwise emanates from the separation point on the upper surface while a second coherent vortex rotating counterclockwise emanates from the trailing edge (refer back to Figure 5.14). At both edges of the wake where the shear layer meets the free stream, the x-direction velocity component of the coherent vortices caused by their rotation is in the free stream direction. Between the points of maximum u'_{rms}/U_e in the mean shear regions, the two counter-rotating coherent vortices have an x-direction velocity component caused by their rotation in a direction opposite the free stream flow. These two different velocity directions due to the rotation of the coherent vortical structures create skewed fluctuation velocity signals throughout the wake. It is not completely understood at this time why the velocity skewness in the wake is positive between the u'_{rms}/U_e maximum points and negative outside of those rms maxima instead of being vice-versa. For the current study the skewness results are used to help verify the existence of counter-rotating vortical

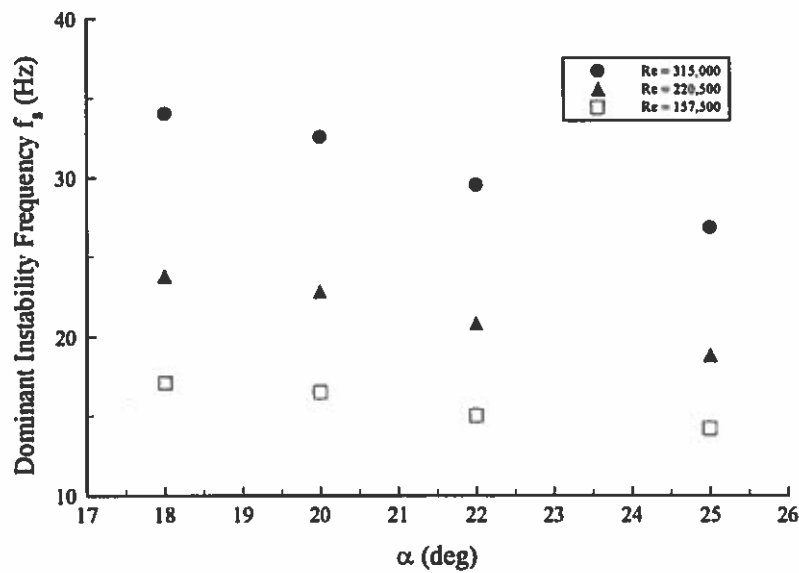


Figure 5.47: Dominant Instability Frequency as Function of Alpha

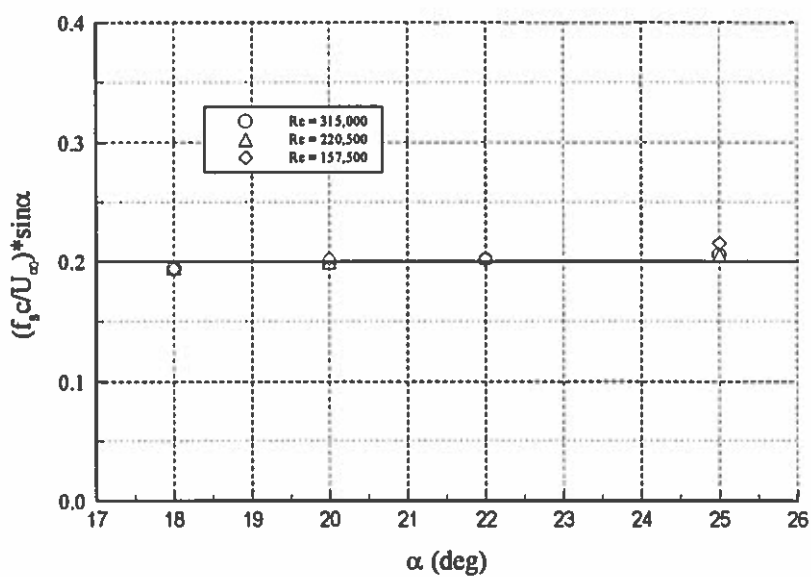


Figure 5.48: Modified Strouhal Number as Function of Alpha

structures in the turbulent shear layers of the wake, the dominant frequency of these flow structures having been found through examination of velocity fluctuation spectra.

Measured dominant flow instability frequencies for various angles of attack are presented in Figure 5.47 for three different Reynolds numbers. As expected, for a given Reynolds number the dominant instability frequency decreases with increasing angle of attack. For a given angle of attack, the dominant instability frequency increases with Reynolds number. When the dominant instability frequency is nondimensionalized as a modified Strouhal number, $St_{\sin \alpha} = \frac{f_s c}{U_\infty} \sin \alpha$, a constant value of approximately 0.20 is obtained for all test cases. This constant trend is seen in Figure 5.48. Free stream velocity values have been corrected for solid and wake blockage. Results from other experimenters are presented with the current findings in Table 5.3. An analogy can perhaps be made for these results to the vortex shedding phenomenon from a cylinder in crossflow, the Strouhal number of which is also approximately 0.20 for a wide range of Reynolds numbers. The length scale used in the cylinder Strouhal calculation is the diameter, the cross-stream length of the free stream that is obstructed by the cylinder. The length scale used in the stalled airfoil Strouhal calculation is $c \cdot \sin \alpha$, the cross-stream length of the free stream that is obstructed by the airfoil. It is interesting that different low-speed airfoils at different stalled angles of attack and different Reynolds numbers all create dominant coherent vortical structures at frequencies that can be nondimensionalized (using as the length scale the cross-stream obstructed length of the free stream) to give the same result as for vortex shedding from a cylinder in crossflow.

Table 5.3: $St_{\sin \alpha}$ Results for Various High-Angle-of-Attack Airfoil Experiments

Experimenter	Airfoil Tested	Re	$St_{\sin \alpha}$	α
Huang et al., 1987	18% thick symmetric airfoil	35,000	0.19	20°
Zaman and McKinzie, 1988	LRN-(1)-1007	40,000 < Re < 140,000	0.2	18°, 20°
Hsiao et al., 1989	NACA 63 ₃ -018	6,300 < Re < 500,000	≈ 0.2	24°
Hsiao et al., 1994	NACA 63 ₃ -018	310,000	0.17 - 0.19	24° < α < 35°
Current Work	SM701	315,000	0.20	18°, 20°, 22°, 25°

5.2.7 Conclusions from Hot-Wire Flowfield Measurements

Several conclusions may now be drawn as a result of the hot-wire experimentation. The mean velocity profiles were found to be very repeatable for all tests performed (both pre-stall and post-stall). The mean profiles were difficult to interpret in regions where flow reversal created the possibility of hot-wire rectification. A directionally sensitive probe would have to be used to clarify these regions of the mean velocity profiles.

The rms profiles of the streamwise velocity fluctuations revealed, as expected, a maximum fluctuation level peak in the region of high shear of the mean velocity and wake profiles. The rms peak in the lower half of the wake consistently occurred directly downstream from the airfoil's trailing edge when the airfoil was stalled. Maximum rms levels in the wake of the airfoil were of order 0.10 when nondimensionalized by U_∞ for the pre-stalled angle of attack tested ($\alpha = 15^\circ$) and of order 0.25 for the post-stalled angles of attack tested ($\alpha = 18^\circ, 20^\circ, 22^\circ$, and 25°).

Velocity skewness profiles had distinct characteristics for pre-stalled and post-stalled tests. A profile with all negative values was measured for the pre-stalled angle of attack test. After stall, the skewness pattern changed. The skewness was positive in the wake between the two rms fluctuation peaks and negative outside of that peak-to-peak region. This skewness pattern is related to the post-stalled formation of counter-rotating coherent vortical structures that dominate the mixing in the turbulent free shear layers. With flow over the airfoil from left to right as seen in Figure 5.14, a clockwise vortical structure

forms due to the upper surface separation and a counterclockwise vortical structure forms due to the trailing edge separation.

The frequencies of these coherent vortical structures originating during stall from the upper surface separation and the trailing edge separation were found to be the same. This dominant frequency scales with the free stream velocity such that the modified Strouhal number equals 0.20 for all angles of attack and all Reynolds numbers tested in the stalled regime. This result is consistent with the work of other researchers as seen in Table 5.3.

The best streamwise position at which to measure the dominant frequency of the coherent vortical structures was found to be in the wake 75% chord downstream from the airfoil's trailing edge (the farthest downstream location that was studied). A dominant instability was not seen in velocity profiles on the airfoil. A dominant flow instability frequency surfaced, however, at the first wake survey location (25% chord behind the trailing edge) which grew more coherent as the wake developed.

Within a wake survey profile, the dominant instability was most clearly measured between the free stream and the peak u'_{rms}/U_∞ , location that occurred in the middle of the mean shear regions on both sides of the wake. These regions are where the entrainment of the free stream is occurring. A dominant instability was not seen in the wake's maximum velocity defect region. Consistent for all tests at stalled angle of attack, this region of no dominant instability frequency was between the two peak u'_{rms}/U_∞ locations in the regions of high mean shear which exist on both sides of the wake. This "quiet" region in the middle of the wake indicates that the coherent vortical structures are confined to the turbulent separated shear layers. Figure 5.49 summarizes some of these conclusions.

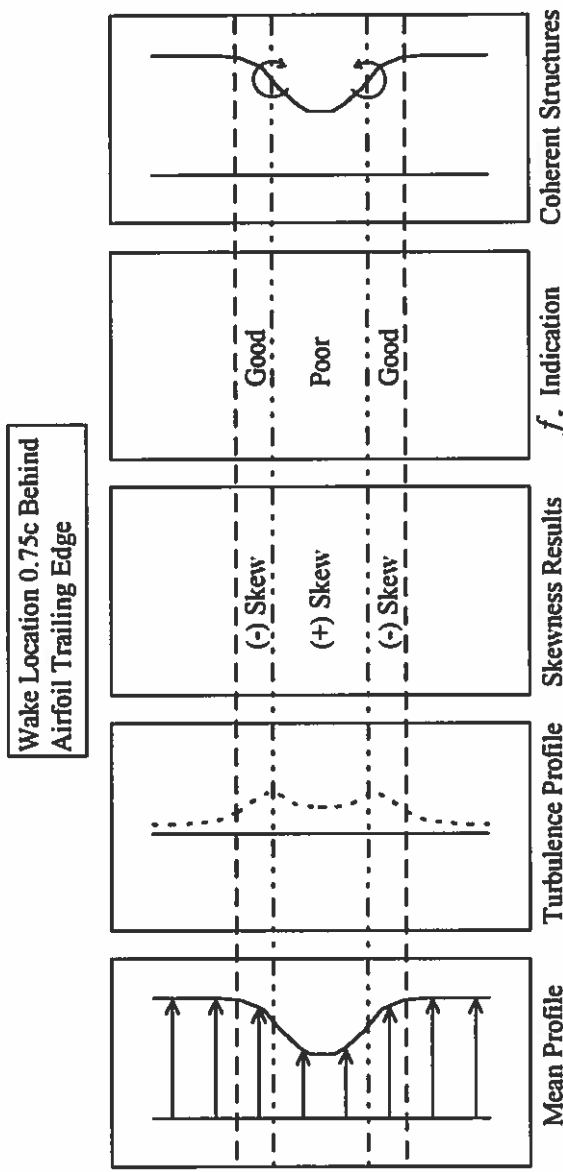


Figure 5.49: Summary of Important Hot-Wire Experimentation Conclusions

6 SIMPLE ACTIVE CONTROL TEST USING PIEZOELECTRIC FOIL

Now that the physics of the separated flow region of the SM701 airfoil is better understood, an effort can be made to control the separation. This section describes a brief examination of the effectiveness of piezoelectric polyvinylidene fluoride (PVDF) film as an active control actuator. Section 5.0.4 contained a description of experiments (Kobayakawa et al., 1992) using such piezoelectric film on an airfoil's surface to promote early transition; the flow thus was energized and remained attached longer. Whitehead et al. used a compressible dielectric electrostatic film transducer to also promote early transition by small surface vibrations on a Clark-Y and a NACA 64₁-412 airfoil (Whitehead et al., 1996). The angle of stall was increased slightly. For the current work, a piezoelectric film was examined as an active control actuator that would enhance the mixing rate of the separated shear layer. Advantages of using a piezoelectric film as an actuator include the relatively non-intrusive nature of the very thin film on an airfoil's surface as well as the absence of sliding parts in a piezoelectric film actuator. While results of this very brief study are by no means conclusive, they do reveal difficulties in using piezoelectric films as a means to control a separated shear layer.

6.1 Background on Piezoelectric Materials

Piezoelectricity, meaning "pressure electricity," is "the capability of certain crystalline materials to change their dimensions when subjected to an electrical field or, conversely, to produce electrical signals when mechanically deformed" (Chatigny, 1984). Pierre and Jacques Curie first observed the piezoelectric phenomenon in natural quartz crystals. Piezoelectric films, as their name implies, also exhibit piezoelectric properties. PVDF film manufactured by AMP, Incorporated was used in this study. The manufacturing process begins with a melt extrusion of PVDF resin pellets into sheet form. The sheet is then stretched to approximately 1/5 of its extruded thickness causing chain packing of the molecules into parallel crystal planes. This state of the material is called the "beta phase." The beta phase polymer is then exposed to very high electric fields to align the crystallites

relative to the poling field. Finally, electrodes are applied to the piezo film surfaces (AMP Incorporated, 1993).

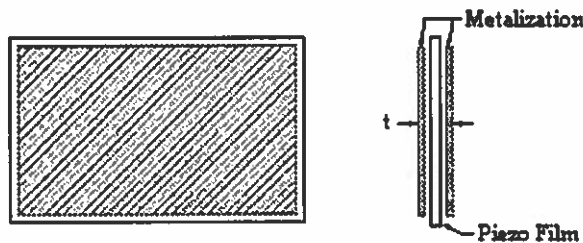
When the piezo film is deformed, a change in the surface charge density of the material occurs due to the piezoelectric effect. The electrodes collect the charge so that a voltage appears between the electrodes.

When voltage is applied to the piezo film, the film extends or contracts along the axis of stretching during its fabrication. The film increases in length and width while decreasing in thickness or decreases in length and width while increasing in thickness.

PVDF film is very thin (order of μm), flexible, inert, and can withstand several thousand volts before breaking down. It has been used in pressure switches, acoustic transducers, high-fidelity tweeters, roadway counters, sports timers, and novelty items, to name a few applications.

6.2 The Experiment

A 28 μm thick PVDF film with dimensions of 5 x 7.5 inches was attached to the leading edge of the SM701 model in the ASWT. A sketch of the piezoelectric film is given in Figure 6.1. The film had sputtered nickel copper alloy conductive surfaces and was attached at the midspan using Grafix 2 Sided Adhesive Double Tack tape as shown in Figure 6.2. With this attachment method, the film would operate primarily in its thickness mode.



Source: AMP Incorporated, 1993

Figure 6.1: Piezoelectric Film

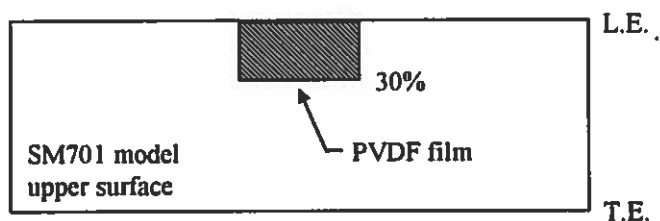


Figure 6.2: Attachment Location of PVDF Film Element on Model Upper Surface

The film wrapped around the leading edge to the lower surface of the model where 32 gauge wire was attached to both of the nickel copper coated surfaces. Circuit Works conductive epoxy was used to attach the wires to the film. The wires were run out of the test section of the ASWT and were connected to the output of a Hewlett Packard 3310B function generator. The output of the function generator was also sent to a Tektronix 2230 100MHz digital storage oscilloscope so that the generated signal could be viewed and its frequency set accurately. The function generator and the oscilloscope can be seen in Figure 6.3. For all control tests, a 30 Volt peak-to-peak (30 V p-p) square wave was used as the excitation signal. The rest of the experimental setup mirrored the setup as described in Section 5.2.2 for the hot-wire flowfield measurements. The angle of attack was set to 20°, and a Reynolds number of 315,000 was studied.

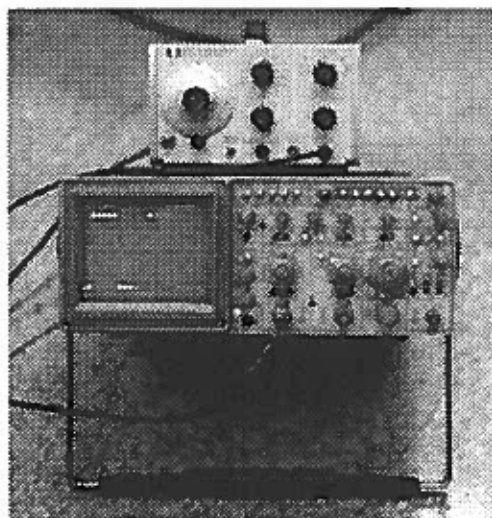


Figure 6.3: The Function Generator with Digital Oscilloscope

The hot-wire sensor was positioned at point 37 (see Figure 5.41a of Section 5.2.6) in the wake 0.75c from the model's trailing edge. Under natural conditions, a modified Strouhal number of 0.20 (based on the dominant flow instability frequency) was measured at that hot-wire location during the original hot-wire study. With the PVDF element in place on the model, the measured frequency of the dominant vortical structures being shed from the airfoil was approximately 28 Hz which led to a modified Strouhal number of 0.17. It appears that the mere presence of the film element on the model may be having an effect on the flow. The PVDF film was then excited at frequencies of 14, 28, 56, 280, 560, and 2800 Hz. These values were chosen based on others' past work in active control of separated shear layers. The mean and rms fluctuation velocities as measured by the hot-wire sensor at its fixed location did not noticeably change under these different excitation frequencies. In addition, the power spectra of the velocity fluctuations under these different control frequencies did not vary noticeably. In short, no noticeable effect was observed at the single sensor hot-wire position in the wake when the PVDF foil element was oscillated.

A possible explanation as to why no effect was observed when control was applied is offered. From Sections 5.0.3 to 5.0.5 discussing active control of separated shear layers on airfoils, it is evident that two main methods can be successful in controlling a separated shear layer. The first method is by using acoustic waves to generate induced normal velocity fluctuations at the airfoil surface near the separation point. Acoustic tunnel resonance usually plays a role in this form of active control. The second method of controlling the separated shear layer is by providing a hydrodynamic disturbance, i.e. by directly introducing normal velocity fluctuations at the airfoil surface near the separation location. It is believed that neither of these methods (acoustically induced or directly introduced velocity fluctuations) are realistic options with the piezoelectric film as tested for this work.

Tests were performed to determine the sound pressure level (SPL) of the PVDF control element on the model surface. A Larson-Davis ½ inch condenser microphone was positioned 0.125 inch above the film in the test section of the ASWT. See Figure 6.4. The microphone was connected to a Larson-Davis 2200C Preamp/P.S., and the output

signal was sent to a Hewlett Packard 35660A Dynamic Signal Analyzer. The microphone had been calibrated with a Larson-Davis pistonphone producing a 250 Hz tone at 114.0 dB SPL prior to installation into the test section.

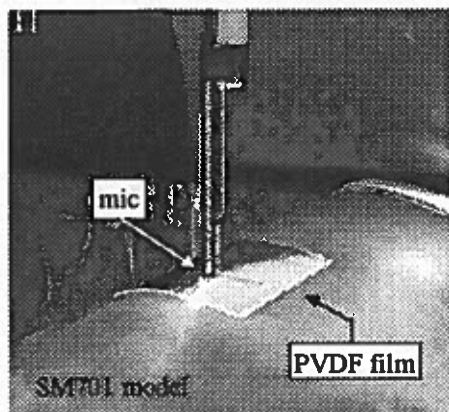


Figure 6.4: The Microphone Above the PVDF Element

The control element was excited at 30 Hz. The spectrum analyzer could not detect any difference from the background room noise. The PVDF element was then excited at 250 Hz. The spectrum analyzer revealed energy peaks at approximately 1250 Hz, 1750 Hz, 2750 Hz, and at other higher harmonics. No noticeable energy peak was seen at the applied excitation frequency of 250 Hz. The element, due to its physical composition and geometry, is preferring to vibrate at the higher harmonics. The measured SPL was approximately 52 dB at the 1750 Hz energy peak.

The element was then excited at 2000 Hz with the spectrum analyzer showing a peak at 2000 Hz. The SPL at the 2000 Hz peak was approximately 62 dB. This value was 42 dB above the background noise at 2000 Hz. The element thus seems to be responding much better to a high frequency input signal; however, to realize effective active control of the separated shear layer it is believed that the excitation frequency needs to be on the order of 30 Hz corresponding to the dominant natural flow instability frequency.

Hsiao et al. created a table comparing sound pressure levels for various successful acoustic active control experiments (Hsiao et al., 1989). Their table reveals that the SPL for the six experiments they referenced varied from 95 to 156 dB. It is now reiterated that

the PVDF element tested for the current work produced a SPL level on the order of 50 to 60 dB. It seems likely that this level is not sufficient to create the acoustically induced velocity fluctuations necessary to control the separated shear layer. It must be mentioned that while the SPL measurements for the current work were made in the near field of the PVDF film, it is not known whether the information presented by Hsiao et al. was measured in the near or in the far field of the given acoustic source.

The PVDF element can also act as a hydrodynamic disturbance source in that its vibration caused by the applied square wave electrical signal can directly create velocity fluctuations. However, based on deformation formulas provided by AMP Incorporated, the expected normal oscillation of the PVDF element (thickness mode) caused by the 30 V p-p square wave is around 0.001 μm . This extremely small deformation is not expected to produce velocity fluctuations that are capable of interacting with the separated shear layer. Whitehead et al. present a similar view stating, "...none of the commercially available thin film transducers are capable of efficiently introducing substantial motion into the boundary layer air flow" (Whitehead et al., 1996). Chang et al. used maximum velocity fluctuations on the order of 10 m/s (induced by sound through a slot in a NACA 63₃-018 airfoil) to achieve flow reattachment (Chang et al., 1992). Their SPL level was roughly 120 dB. It is not expected that the piezoelectric foil as tested can produce either the velocity fluctuation level or the SPL that Chang et al. achieved.

Recapping, from the brief experimentation performed, the piezoelectric film element does not seem practical as an active control actuator for exciting a separated shear layer. The PVDF film does not seem to be generating an adequate SPL based on other experimenters' work to acoustically induce the necessary normal velocity perturbations. Also, the PVDF element does not appear to vibrate normal to the airfoil surface with large enough amplitude to directly introduce the required velocity perturbations. PVDF films may possibly be used to promote early transition and thus delay separation; however, after separation occurs it does not seem that PVDF film actuators can be readily used to enhance the mixing in the separated shear layer thus causing flow reattachment to occur.

7 CONCLUSIONS

As a result of this study of the separated flow characteristics of the SM701 airfoil at high angle of attack and low Reynolds number, much insight has been gained into the nature of the coherent structures that dominate the separated flow region. Now that these dominant flow structures are better understood for a wide range of operating conditions (Reynolds numbers and angles of attack), future work can begin on actively enhancing these natural structures in an attempt to reduce the separated flow region.

The heat transfer study that was performed showed consistent results with a conventional fluorescent oil flow visualization study. By using both oil flow visualization and a heat transfer study, the viscous flow regions existing on the airfoil at various Reynolds numbers and angles of attack were revealed. The heat transfer method complemented the oil flow visualization method in revealing flow structures not captured by the qualitative oil flow visualization method. These details of the viscous flow at the airfoil's surface include a flow relaxation region when the laminar separation bubble reattaches and the presence of Görtler vortices in that reattachment region. In addition, the heat transfer method revealed an increasing heat transfer trend in the turbulent separated regions when the airfoil was stalled. This enhanced heat transfer near the trailing edge in the turbulent separated region when the airfoil was stalled is believed to be caused by the counter-rotating coherent vortical structures that are shed from the airfoil. Entrained free stream fluid is sent upstream and impinges near the trailing edge, thus causing enhanced heat transfer.

The qualitative shear stress study that was undertaken gave results consistent with the heat transfer study. The flow relaxation region after the reattachment of the laminar separation bubble was seen with the shear stress gauges. In addition, the level of turbulent fluctuations near the airfoil's surface was seen to increase near the trailing edge in the separated flow region when the airfoil was stalled. This increased turbulent fluctuation level is tied to the increased convective heat transfer, both being caused presumably by the shedding of the coherent vortical structures as described in the previous paragraph. The qualitative shear stress tests were not able to reveal the presence of any dominant coherent

structures in the separated flow region. These dominant structures exist in the turbulent separated shear layers while the shear stress gauges were located on the airfoil's surface. The flow recirculating region existing between the dominant coherent structures of the separated shear layer and the shear stress gauges on the airfoil's surface effectively made the flow structures invisible to the shear stress gauges.

Hot-wire anemometry tests revealed dominant frequencies of coherent vortical structures in the separated shear layers when the airfoil was stalled. These dominant frequencies scaled with the free stream velocity such that the modified Strouhal number for all Reynolds numbers and post-stall angles of attack tested was approximately 0.20. The dominant coherent structures were best detected in the wake after they had a chance to develop over the airfoil. In a given wake profile, the dominant structures were best sensed with the hot-wire in the region between the free stream and the point of maximum streamwise rms velocity fluctuation level in the middle of the shear layer on both sides of the wake. Skewness of the velocity fluctuations in the wake was also examined and confirmed the existence of these dominant flow structures.

Enough information is now known on the post-stall flow behavior of the SM701 airfoil to begin a detailed active flow control study. A preliminary study using PVDF films as control actuators revealed difficulties involving SPL and vibration displacement levels of the films. Despite the current difficulties, active control has been shown by past experimenters to be an attainable goal in fluid mechanics. Various methods have been employed, working with both laminar separating and turbulent separating flow regions. The challenge that lies ahead is to take active control out of the laboratory and make it practical in real-world applications.

8 SUGGESTIONS FOR FUTURE WORK

Suggestions regarding future experimentation in the areas explored for this thesis are given in this section. These suggestions come from the work that has been done and should help future experimentation go more smoothly. It is recommended that all future work be done in the LSLTT only. The flow about the 12 inch chord airfoil tested was greatly influenced by the tunnel walls for tests in the ASWT. A 12 inch chord model is too large to test in the ASWT.

Liquid Crystal Thermography

- Use a heater strip width of 2.5 inches. This reduced width will cause the heater strip resistance to raise, thus lowering the overall uncertainty in h slightly. The two-dimensional color band width on the heater strip during experimentation should still be acceptable with this decreased heater strip width.
- Build a new liquid crystal calibration piece out of Plexiglas. The current calibration piece is made out of the wing material composite. Plexiglas has a more isotropic composition and less irregularities than the wing material. Using Plexiglas should yield longer transients during calibration and thus more accurate calibrations.
- Use a model with more uniform wall thickness and built out of a uniform material. Knowing t_{wall} and k_{wall} more accurately will lower the uncertainty in h .

Qualitative Shear Stress Tests

- Use both legs of the McCroskey sensor so that flow directionality can be sensed. Reverse flow regions could then be better documented.

Hot-Wire Flowfield Measurements

- Redesign the traverse mount to eliminate vibration tendency. (Wooden reinforcement pieces were used to temporarily solve the problem for the current work).

- Perform the hot-wire tests that were done in the ASWT in the LSLTT to re-determine the modified Strouhal number for vortex shedding from the SM701 model at high angle of attack. The results from the LSLTT should be more accurate than the results obtained in the ASWT due to less tunnel blockage effects in the LSLTT.
- Use two hot-wire sensors for measurements. One should be located in a region of positive velocity fluctuation skewness, and the second hot-wire should be located in a region of negative velocity fluctuation skewness. Coherence measurements can give more insight into the vortex shedding phenomenon.

Active Control

using PVDF

- Use films with silver ink conductive surfaces rather than nickel copper. The silver ink conductive surfaces can take high voltages and repeated use without deterioration. The nickel copper conductive surfaces are more brittle and crack with high voltages and repeated use leading to lesser film displacements.
- Operate the film in its elongation mode (where deformations take place in the film plane) instead of in its thickness mode. The thickness mode is more suited for ultrasonic applications. The maximum transmission occurs at $\frac{1}{2}$ wavelength resonance in the thickness mode, which for 28 μm film is approximately 40 MHz. A film over 1 mm thick would be required to bring this value down to the low MHz range. In the elongation mode, lower frequencies and larger displacements can be achieved (on the order of 10's of μm). However, to operate in elongation mode, the entire film could not be secured to the wing surface as was done in the thickness mode application (perhaps only 2 edges). Wind blowing over the film would then tend to shake and flutter the loose film leading to the possibility of tearing.
- Use larger square wave amplitude to increase the film's displacements and SPL.

- Use films with larger surface area on the model to interact with a larger region of the flow.

general suggestions

- Recommend putting aside PVDF foil for now and examining control methods that directly introduce velocity perturbations (as opposed to acoustic methods in which sound induces velocity perturbations).
- Synthetic jets offer an interesting control possibility. A synthetic jet is a push-pull, cavity-generated jet. The net mass flow from the cavity is zero. Thus for synthetic jets no additional fluid needs to be pumped, eliminating the need for tubing systems. A synthetic jet is depicted in Figure 8.1.

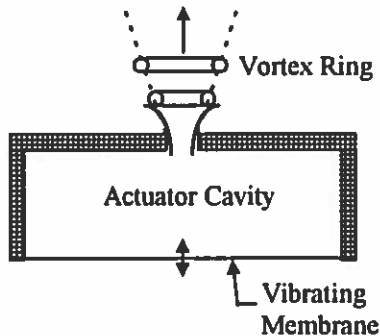


Figure 8.1: Synthetic Jet Actuator

- Recommend pressure tapping the model and using c_l , c_d , and C_p distribution, along with hot-wire information to determine the effect of any applied active control. The hot-wire can be attached to the wake survey pitot probe traverse since hot-wire tests showed that the shedding frequency is seen stronger in the wake than in velocity profiles along the chord of the airfoil.
- Recommend that a system using direct introduction of velocity perturbations is first made to work. Then, experiments should be performed that examine what velocity

perturbation levels are required to provide control under different experimental conditions. Once insight into the necessary magnitude of the forcing level for effective control is obtained, the feasibility of using PVDF films to create velocity fluctuations will be better seen.

APPENDIX A: ASWT Turbulence Intensity Information

This appendix contains turbulence intensity information for the ASWT.

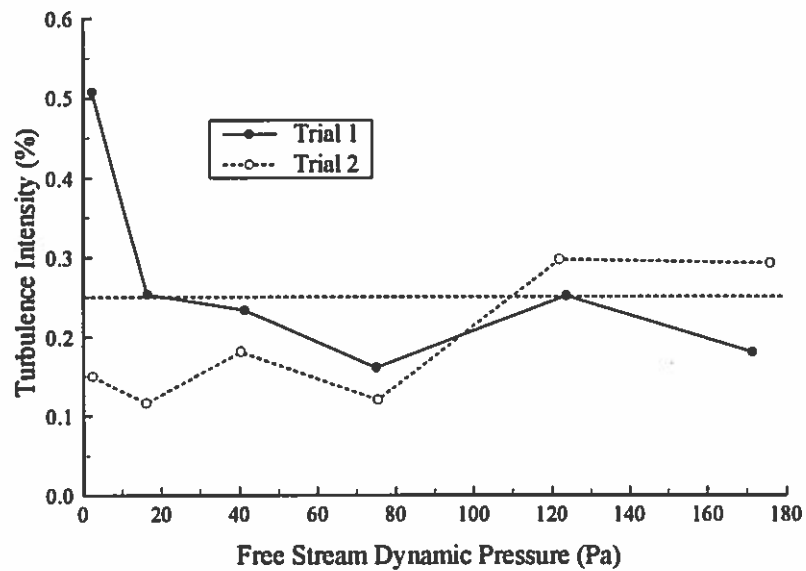


Figure A.1: ASWT Turbulence Intensity Level

APPENDIX B: Numerical Predictions Input Information

This appendix contains input information used in the prediction of the convective heat transfer coefficients on the SM701 airfoil. The tables in this appendix are discussed in Chapter 3.0.

Table B.1: Inputs for panel.f for Angle of Attack = 0 degrees

Code Asks For	Answer Given
General output file?	out0.out
Cp output file?	outcp0.out
x,y output file?	outxy0.out
Type of analysis?	(0) Analysis of a given shape
Type of object?	(5) Arbitrary airfoil
Angle of attack?	0.0
Mach number?	0.0
Number of desired panels?	43
clustering?	0.8
Input file with x/c, y/c airfoil coordinates?	sm701.dat
Include blowing or suction?	(0) No

Table B.2: STAN5 Input File - SM701 Airfoil; $\alpha = 0^\circ$; Re=315000

RUN 015	AOA = 0 degrees	ReAVG = 310601	TITLE LINE
1	1	1	39 = # POINTS IN STARTING PROFILE (EXCLUDES Y=0 PT)
0.000835	0.319148	2.0	# # # DELTAX RETRAN 0.05 ENFRA 0.0
0	1		NOTE: VARY DELTAX, RETRAN, ENFRA TO TRY TO OBTAIN BETTER RESULTS
99492.1	1.174	0.0000183	39 = # POINTS ALONG BOUNDARY AT WHICH $U_e(s)$ IS SPECIFIED
39	1		
0.000835	1.0		
0.002581	1.0		
0.004579	1.0		
0.006990	1.0		
0.009964	1.0		
0.013642	1.0		
0.018131	1.0		
0.023525	1.0		THIS COLUMN OF NUMBERS BEFORE THE 1.0'S CONTAINS THE s-LOCATIONS OF THE $U_e(s)$ BOUNDARY CONDITIONS
0.029905	1.0		
0.037319	1.0		
0.045785	1.0		
0.055297	1.0		
0.065821	1.0		
0.077296	1.0		
0.089636	1.0		
0.102735	1.0		
0.116466	1.0		
0.130685	1.0		
0.145237	1.0		
0.159959	1.0		
0.174681	1.0		
0.189232	1.0		
0.203451	1.0		
0.217183	1.0		
0.230282	1.0		
0.242623	1.0		
0.254098	1.0		
0.264623	1.0		
0.274136	1.0		
0.282606	1.0		
0.290024	1.0		
0.296412	1.0		
0.301816	1.0		
0.306309	1.0		
0.309988	1.0		
0.312968	1.0		
0.315387	1.0		
0.317393	1.0		
0.319148	1.0		
0.322907	0.0	304665.8	FIRST COLUMN IS $U_e(s)$ FROM PANEL CODE; THIRD COLUMN IS $C_p \cdot T_{wall}$
5.285353	0.0	304665.8	
9.075281	0.0	304665.8	
11.882699	0.0	304665.8	
14.710274	0.0	304665.8	
16.978252	0.0	304665.8	

18.514802 0.0	304665.8
19.937199 0.0	304665.8
20.980344 0.0	304665.8
21.647628 0.0	304665.8
21.958311 0.0	304665.8
22.041322 0.0	304665.8
22.000875 0.0	304665.8
21.895056 0.0	304665.8
21.636130 0.0	304665.8
21.437016 0.0	304665.8
21.293046 0.0	304665.8
21.089755 0.0	304665.8
21.061069 0.0	304665.8
20.951147 0.0	304665.8
20.683146 0.0	304665.8
20.421249 0.0	304665.8
20.109851 0.0	304665.8
19.613651 0.0	304665.8
19.113549 0.0	304665.8
18.745883 0.0	304665.8
18.374198 0.0	304665.8
18.066007 0.0	304665.8
17.773847 0.0	304665.8
17.496313 0.0	304665.8
17.162097 0.0	304665.8
16.728523 0.0	304665.8
16.166471 0.0	304665.8
15.475848 0.0	304665.8
14.998527 0.0	304665.8
14.690658 0.0	304665.8
14.340861 0.0	304665.8
13.977651 0.0	304665.8
12.515596 0.0	304665.8
0.0000000 0.0000000 304665.8	FIRST COLUMN IS y LOCATION IN BOUNDARY LAYER STARTING PROFILE
0.0000261 0.0433922 304458.3	SECOND COLUMN IS U(y) PROFILE
0.0000522 0.0826964 304250.8	THIRD COLUMN IS STAGNATION ENTHALPY LINEAR PROFILE
0.0000782 0.1180063 304043.4	
0.0001043 0.1494606 303835.9	
0.0001304 0.1772403 303628.5	
0.0001565 0.2015616 303421.0	
0.0001826 0.2226668 303213.6	
0.0002087 0.2408142 303006.1	
0.0002347 0.2562685 302798.7	
0.0002608 0.2693042 302591.2	
0.0002869 0.2801926 302383.8	
0.0003130 0.2891920 302176.3	
0.0003391 0.2965575 301968.9	
0.0003652 0.3025184 301761.4	
0.0003912 0.3072942 301554.0	
0.0004173 0.3110754 301346.5	
0.0004434 0.3140333 301139.1	
0.0004695 0.3163259 300931.6	
0.0004956 0.3180793 300724.2	
0.0005217 0.3194032 300516.7	
0.0005477 0.3203945 300309.3	
0.0005738 0.3211275 300101.8	
0.0005999 0.3216603 299894.4	
0.0006260 0.3220413 299686.9	
0.0006521 0.3223158 299479.5	

0.0006781 0.3225063 299272.0
0.0007042 0.3226387 299064.6
0.0007303 0.3227291 298857.1
0.0007564 0.3227905 298649.7
0.0007825 0.3228325 298442.2
0.0008086 0.3228583 298234.8
0.0008346 0.3228777 298027.3
0.0008607 0.3228874 297819.9
0.0008868 0.3228938 297612.4
0.0009129 0.3229003 297405.0
0.0009390 0.3229035 297197.5
0.0009651 0.3229035 296990.1
0.0009911 0.3229035 296782.6
0.0010172 0.3229070 296575.2
0.41 0.085 0.01 0.22 0.38 1.0 0.0
25.0
4000.0 0.86
1.0 1.0
1 21 2

**MAKE SURE LAST U(y) VALUE
MATCHES FIRST U_s(s) VALUE**

APPENDIX C: Heat Transfer Codes

This appendix contains the FORTRAN codes that were used for data acquisition and data reduction throughout the LSLTT heat transfer experiments. The codes are well-commented.

Data Acquisition Code getdata.for

```

program getdata
*****
* This program is the Data Acquisition code for my liquid crystal      *
* work at APB. It samples the venturi voltage, the inconel            *
* voltage, and the 9 thermocouple voltages. The code is                 *
* completely menu driven, so just run it and it will be self-        *
* explanatory.                                                       *
*                                                               *
* Last Modified on : 11-17-96 by Todd Klaput                         *
*                                                               *
*****
integer*2 sch,fch,nsapch,irange(8),totsamp,nch,i,ans,switch,iter
integer basadr,intlev,dmalev,rcode,buffer,alloc,flag
integer*2 param(10),imode,das20
real frepch,b(8),xslope,vslope,v(8),patm,vvent0,vinc0,vincon
real vt1,vt2,vt3,vt4,vt5,vt6,vt7,vt8,vtinf,tinf,vvent,vinc
real mu,rho,q,vel,re,chord,qdtot,l,w,ainc,rinc,retarg,event
real vtinf0,vt10,vt20,vt30,vt40,vt50,vt60,vt70,vt80,temp
real tslop1,tslop2,tslop3,tslop4,tslop5,tslop6,tslop7,tslop8
real tslop9,incslp,vinact0,tavg,crytem
character*1 yesno
character*3 runno
character*40 des
character*15 date
character*10 fname,fname1,fname2
character*6 imgnam
character*8 imgcnt

*** tunnel calibration slopes
* units -> Pa/volt
  xslope=95.2519527
* units -> Pa/Pa
  vslope=2.77778
* units -> Actual Volts (voltmeter)/DAS20 Sensed Volts
  incslp=0.9999637
* units -> deg.C/volt
  tslop1=11.4819661
  tslop2=11.5132545
  tslop3=11.5158382
  tslop4=11.5320815
  tslop5=11.5411361
  tslop6=11.5582363

```

```

tslop7=11.5853887
tslop8=11.5590531
tslop9=11.5687180

*** DAS20 settings
* basadr=base address, intlev=interrupt level, dmalev=DMA level
basadr=#300
intlev=2
dmalev=1

*** properties of the Inconel strip in SI units
l=0.3984625
w=0.0762
rinc=0.2643
c rinc = 0.2479
chord=0.3048

switch=0
flag=0
iter=0
ainc=l*w

*** read in board calibration information
open(unit=8,file='board.dat',status='old')
  read(8,*) sch,nch,nsapch
  read(8,*) freqch
  read(8,*) irange(1),irange(2),irange(3)
  read(8,*) irange(4),irange(5),irange(6)
  read(8,*) irange(7)
  read(8,*) b(1),b(2),b(3)
  read(8,*) b(4),b(5),b(6)
  read(8,*) b(7)
close(unit=8)

*** total number of samples = #channels * #samples per channel
totsamp=nch*nsapch
if(totsamp.gt.32760)then
  print*, 'Total # of samples must not exceed 32760'
  print*, 'i.e. # of channels * # of samples per channel'
  print*, 'must be less than 32760'
endif

sch=sch+nch-1

*** user inputs run information
print*, 'Enter 3 digit run number'
read(0,'(a3)') runno
print*
print*, 'Enter run description'
read(0,'(a40)') des
print*
print*, 'Enter test date'
read(0,'(a15)') date
print*

```

```

print*, 'Enter output file name without extension (max 6 letters)'
read(0,'(a6)') fname
print*
print*, 'Enter crystal temperature (30, 45)'
read*,crytem

fname1(1:6)=fname(1:6)
fname1(7:10)=' .raw'
fname2(1:6)=fname(1:6)
fname2(7:10)=' .out'
print*
print*, 'Enter ambient Temperature (deg.F)'
read*,temper
* convert deg.F to deg.C
temper=(5.0/9.0)*(temper-32.)

*** DAS20 channel information
print*
print*
print*
print*, 'CHANNEL 0 -----> VENTURI CONTRACTION PRESSURE XDUCER'
print*, 'CHANNEL 1 -----> INCONEL VOLTAGE'
print*, 'CHANNEL 2 -----> ALL THERMOCOUPLES'
print*
print*, 'Enter Actual Inconel Voltage reading with POWER OFF'
read*,vinact0

*** open output files
open(unit=9,file=fname1,status='new')
open(unit=10,file=fname2,status='new')

*** write header information to data files
write(9,*) 'Run Number: ',runno
write(9,*) 'Date : ',date
write(9,*) des
write(10,*) 'Run Number: ',runno
write(10,*) 'Date : ',date
write(10,*) des

*** initialize DAS20: Mode 0
imode=0
param(1)=basadr
param(2)=intlev
param(3)=dmalev

rcode=das20(imode,param)
if(rcode.ne.0)print*,imode,rcode

buffer=alloc(32766)

*** take zeroes
1 print*
print*
print*, 'Ready to take zeroes? (y or n)'


```

```

read(0,'(a1)') yesno
if(yesno.eq.'y'.or.yesno.eq.'Y')then
    vvent0=0.0
    vinc0=0.0
    print*
    print*
    pause'Set thermocouple to Tinside1 and press <enter>'
    call vmean(v,sch,fch,nch,nsapch,frepch,iter,freact,irange,b)
    vvent0=vvent0+v(1)
    vinc0=vinc0+v(2)
    vt10=v(3)
    print*
    pause'Set thermocouple to Tinside2 and press <enter>'
    call vmean(v,sch,fch,nch,nsapch,frepch,iter,freact,irange,b)
    vvent0=vvent0+v(1)
    vinc0=vinc0+v(2)
    vt20=v(3)
    print*
    pause'Set thermocouple to Tinside3 and press <enter>'
    call vmean(v,sch,fch,nch,nsapch,frepch,iter,freact,irange,b)
    vvent0=vvent0+v(1)
    vinc0=vinc0+v(2)
    vt30=v(3)
    print*
    pause'Set thermocouple to Tinside4 and press <enter>'
    call vmean(v,sch,fch,nch,nsapch,frepch,iter,freact,irange,b)
    vvent0=vvent0+v(1)
    vinc0=vinc0+v(2)
    vt40=v(3)
    print*
    pause'Set thermocouple to Tinside5 and press <enter>'
    call vmean(v,sch,fch,nch,nsapch,frepch,iter,freact,irange,b)
    vvent0=vvent0+v(1)
    vinc0=vinc0+v(2)
    vt50=v(3)
    print*
    pause'Set thermocouple to Tinside6 and press <enter>'
    call vmean(v,sch,fch,nch,nsapch,frepch,iter,freact,irange,b)
    vvent0=vvent0+v(1)
    vinc0=vinc0+v(2)
    vt60=v(3)
    print*
    pause'Set thermocouple to Tinside7 and press <enter>'
    call vmean(v,sch,fch,nch,nsapch,frepch,iter,freact,irange,b)
    vvent0=vvent0+v(1)
    vinc0=vinc0+v(2)
    vt70=v(3)
    print*
    pause'Set thermocouple to Tinside8 and press <enter>'
    call vmean(v,sch,fch,nch,nsapch,frepch,iter,freact,irange,b)
    vvent0=vvent0+v(1)
    vinc0=vinc0+v(2)
    vt80=v(3)
    print*

```

```

pause'Set thermocouple to Tinf and press <enter>'
call vmean(v,sch,fch,nch,nsapch,frepch,iter,freact,irange,b)
vvent0=vvent0+v(1)
vinc0=vinc0+v(2)
vtinf0=v(3)
print*

vvent0=vvent0/9.0
vinc0=vinc0/9.0
else
  goto 1
endif

*** set up menu
2  do 5 i=1,6
    print*
5  continue

print*,           MENU'
print*
print*
print*, 'Please enter...'
print*
print*
print*, '      1  to calculate target Venturi voltage'
print*, '      2  to enter a new value for Patm'
print*, '      3  to take data'
print*
print*
print*, '      90  to quit'
print*
print*
print*
print*
print*
print*
if(switch.eq.1)print*, 'Current value of Patm = ',patm/3386.3881578
$9,' inHg'
print*
read*,ans

if(ans.eq.90)then

*** user chooses to quit
goto 1000

elseif(ans.eq.1)then

*** user chooses to calculate target Venturi voltage
if(switch.eq.0)then
  print*, 'Enter value of atmospheric pressure (inHg)'
  read*,patm
* convert inHg to Pascal
  patm=patm*3386.38815789

```

```

        switch=1
    endif
    print*,'Is thermocouple for freestream temperature Tinf on chan
$nel 2 now? (y or n)'
    read(0,'(a1)') yesno
    if(yesno.eq.'y'.or.yesno.eq.'Y')then
        call vmean(v,sch,fch,nch,nsapch,frepch,iter,freact,irange,b)
        vtinf=v(3)
        tinf=temper+(vtinf-vtinf0)*tslop9
    * convert temperature from degrees Celsius to degrees Kelvin
        tinf=tinf+273.15
        tavg=(tinf+(crytem+273.15))/2.0
    else
        goto 2
    endif
    print*
    print*
    print*,'Enter desired Reynolds number'
    read*,retarg
    event=((2.99958065442e-10)*retarg**2*tavg**4)/(chord**2*patm*(t
$avg+110.0)**2*xslope*vslope)
    print*
    print*
    write(0,20)'Target Venturi Voltage = ',event+vvent0
20    format(1x,a,f6.3)

    print*,vinact0+(event)*incslp
    print*
    print*
    pause'Press enter to continue'

    elseif(ans.eq.2)then
        *** user chooses to enter new value of Patm
        print*
        print*
        print*,'Enter value of atmospheric pressure (inHg)'
        read*,patm
    * convert inHg to Pascal
        patm=patm*3386.38815789
        switch=1

        elseif(ans.eq.3)then
        *** user chooses to take data

            if(switch.eq.0)then
                print*,'You must first tell me the atmospheric pressure'
                print*
                pause'Press <enter> to continue'
                goto 2
            endif
            vvent=0.0
            vinc=0.0
            print*

```

```

print*
pause'Set thermocouple to Tinside1 and press <enter>'
call vmean(v,sch,fch,nch,nsapch,frepch,iter,freact,irange,b)
vvent=vvent+v(1)
vinc=vinc+v(2)
vt1=v(3)
print*
pause'Set thermocouple to Tinside2 and press <enter>'
call vmean(v,sch,fch,nch,nsapch,frepch,iter,freact,irange,b)
vvent=vvent+v(1)
vinc=vinc+v(2)
vt2=v(3)
print*
pause'Set thermocouple to Tinside3 and press <enter>'
call vmean(v,sch,fch,nch,nsapch,frepch,iter,freact,irange,b)
vvent=vvent+v(1)
vinc=vinc+v(2)
vt3=v(3)
print*
pause'Set thermocouple to Tinside4 and press <enter>'
call vmean(v,sch,fch,nch,nsapch,frepch,iter,freact,irange,b)
vvent=vvent+v(1)
vinc=vinc+v(2)
vt4=v(3)
print*
pause'Set thermocouple to Tinside5 and press <enter>'
call vmean(v,sch,fch,nch,nsapch,frepch,iter,freact,irange,b)
vvent=vvent+v(1)
vinc=vinc+v(2)
vt5=v(3)
print*
pause'Set thermocouple to Tinside6 and press <enter>'
call vmean(v,sch,fch,nch,nsapch,frepch,iter,freact,irange,b)
vvent=vvent+v(1)
vinc=vinc+v(2)
vt6=v(3)
print*
pause'Set thermocouple to Tinside7 and press <enter>'
call vmean(v,sch,fch,nch,nsapch,frepch,iter,freact,irange,b)
vvent=vvent+v(1)
vinc=vinc+v(2)
vt7=v(3)
print*
pause'Set thermocouple to Tinside8 and press <enter>'
call vmean(v,sch,fch,nch,nsapch,frepch,iter,freact,irange,b)
vvent=vvent+v(1)
vinc=vinc+v(2)
vt8=v(3)
print*
pause'Set thermocouple to Tinf and press <enter>'
call vmean(v,sch,fch,nch,nsapch,frepch,iter,freact,irange,b)
vvent=vvent+v(1)
vinc=vinc+v(2)
vtinf=v(3)

```

```

print*
vvent=vvent/9.0
vinc=vinc/9.0

*** calculate temperatures in degrees Celsius
t1=temper+(vt1-vt10)*tslop1
t2=temper+(vt2-vt20)*tslop2
t3=temper+(vt3-vt30)*tslop3
t4=temper+(vt4-vt40)*tslop4
t5=temper+(vt5-vt50)*tslop5
t6=temper+(vt6-vt60)*tslop6
t7=temper+(vt7-vt70)*tslop7
t8=temper+(vt8-vt80)*tslop8
tinf=temper+(vtinf-vtinf0)*tslop9

*** convert temperatures from degrees Celsius to degrees Kelvin
t1=t1+273.15
t2=t2+273.15
t3=t3+273.15
t4=t4+273.15
t5=t5+273.15
t6=t6+273.15
t7=t7+273.15
t8=t8+273.15
tinf=tinf+273.15

*** calculate air viscosity using Sutherland's law
* temperature near strip assumed average of freestream
* and liquid crystal strip temperature
tavg=(tinf+(crytem+273.15))/2.0
mu=0.000018*(tavg/293.15)**1.5*(403.15)/(tavg+110.0)

*** calculate air density
rho=patm/(287.0*tinf)

*** calculate dynamic pressure and airspeed
q=(vvent-vvent0)*xslope*vslope
vel=sqrt(2.0*q/rho)

*** calculate Reynolds number
re=(rho*vel*chord)/mu
print*, 'rho = ', rho
print*, 'vel = ', vel
print*, 're = ', re

vincon=vinact0+(vinc-vinc0)*inclspl
print*
print*, 'vvent = ', vvent
print*, 'vincon = ', vincon
print*, 'vt1 = ', vt1
print*
print*, 'Do you wish to use these values?'
read(0,'(a1)') yesno
if(yesno.eq.'n'.or.yesno.eq.'N')goto2

```

```

print*
print*, 'Enter INCONEL voltage'
read*,vincon

*** calculate total heat flux generated per unit area
qdtot=(vincon**2)/(rinc*ainc)

*** input image name and counter number
print*
print*, 'Enter image name (6 characters)'
read(0,'(a6)') imgnam
print*
print*, 'Enter video counter (xx:xx:xx)'
read(0,'(a8)') imgcnt

*** write raw voltages and processed data to files
if(flag.eq.0)then
  write(9,45) 'Patm = ',patm
  write(9,*)
  write(10,45) 'Patm = ',patm
  write(10,*)
  flag=1
45      format(1x,a,f8.1)
endif

      write(9,50) imgnam,imgcnt,vvent-vvent0,vincon,vtinf-vtinf0,vtl-
$vt10,vt2-vt20,vt3-vt30,vt4-vt40,vt5-vt50,vt6-vt60,vt7-vt70,vt8-vt8
$0
      write(10,60) imgnam,imgcnt,re,vel,rho,qdtot,tinf,t1,t2,t3,t4,t5
$,t6,t7,t8
50  format(1x,a6,1x,a8,1x,f5.3,1x,f6.3,1x,9(f8.3,1x))
60  format(1x,a6,1x,a8,1x,f7.0,1x,f5.2,1x,f5.3,1x,f10.4,1x,9(f7.3,1x))

else
  print*
  print*, 'PLEASE CHOOSE A NUMBER BETWEEN 1 AND 3 (OR 90 TO QUIT)'
endif

goto 2

1000 close(unit=9)
      close(unit=10)

end

*****
SUBROUTINE VMEAN(V,SCH,FCH,NCH,NSAPCH,FREPCH,ITER,FREACT,
&IRANGE,b)
*
* Calculates the mean voltage sampled in each input channel
*
  INTEGER*2  ICOUNT(11000),IRANGE(8)
  INTEGER*2  NCH,SCH,FCH,IPRINT,NSAPCH

```

```

      REAL*4    IE,E,V,A(8),B(8)
*   COMMON    A(8),B(8)
*   DIMENSION IE(8),E(8),V(8)
*
*   IPRINT=0
*
* SAMPLE: external subroutine (MODE6VG.FOR)
* Use of Mode 6 for sampling

      CALL SAMPLE(SCH,FCH,NCH,NSAPCH,FREPCH,ICOUNT,IPRINT,ITER,
&FREACT,IRANGE)
*
* Scaling conversion when transferring bipolar data in unipolar mode
* Make sure this conversion is performed before the averaging loops.
      DO 10 I=1,11000
        IF (ICOUNT(I).GT.2047) THEN
          ICOUNT(I)=ICOUNT(I)-4096
        ENDIF
10    CONTINUE
*
* WRITE(0,*) (ICOUNT(I),I=1,NSAPCH*NCH)
      DO 20 J=1,NCH
        E(J)=0.0
        IE(J)=0.0
20    CONTINUE
*
* These loops average (running average) all sampled data (counts)
* in the 1-D array ICOUNT and categorize the averaged data by channels
* into a different 1-D array E(J).
*
      DO 40 I=1,NSAPCH
        INDEX=(I-1)*NCH
        DO 45 J=1,NCH
          IE(J)=ICOUNT(INDEX+J)
          E(J)=E(J)+REAL(IE(J)-E(J))/I
*
          IF (IE(J).EQ.0) THEN
*
            PRINT*,I,INDEX,J
*
            STOP
*
          ENDIF
45    CONTINUE
40    CONTINUE
*
*
      DO 60 I=1,NCH
* Conversion from counts to volts for the appropriate input range
*   V(I)=B(SCH+I)*E(I)
60    CONTINUE
*
300  FORMAT(//,9X,' No.',9X,' Ch.1',9X,' Ch.2')
320  FORMAT(4F15.5)
330  FORMAT(4I15)
      RETURN
      END

```

Data Reduction Code apbwing.for

```

$include:'c:\aurora\auerrs.for'
$include:'c:\aurora\audefs.for'
c
*****
* apbwing.for: This program was written to reduce data for the
* liquid crystal experiments on the SM701 airfoil done at APB
* in the LSLTT wind tunnel.
*
* By Robert T. Klaput      Last Modified ---> 1-8-97
*
* The program reads an input file called input.dat which
* contains the following information:
*
* Line 1 : Liquid Crystal Temperature (30 or 45)
* Line 2 : Starting Value of Hue, Band of Hue, Saturation
*           Threshold
* Line 3 : # of Intensities to reduce (nred)
* Line 4 : Intensity 1, Intensity 2, Intensity 3, ...
* Line 5 : output file name to contain h, x/c data for Intensity 1
*           (be sure to include extension)
* Line 6 : output file name to contain h, x/c data for Intensity 2
* Line 7 : "   "   "   "   "   Intensity 3
*
* Line nred : "   "   "   "   "   Intensity nred
* Line nred+1: atmospheric pressure in Pa
* Line nred+2: number of images that need to be column-corrected
* Line nred+3: image #, column correction value
*           "   "   "   "
*           "   "   "   "
*           "   "   "   "
* Line .   : number of images that need user-added h values
* Line .   : image#, col 1 to calc.h, col 2 to calc.h, col 3 to calc.h
*           "   "   "   "   "   "
*           "   "   "   "   "   "
*           "   "   "   "   "   "
* Line   : beginning screen row of reduction, ending row
* Line   : # of pixels required in a column to average
* Line   : total # of images
* Line   : Image names (total number equal to line nred+4)
* Line XX-XX : imgnam,imgcnt,re,vel,rho,qdtot,tinf,ttc(1),ttc(2),
*           ttc(3),ttc(4),ttc(5),ttc(6),ttc(7),ttc(8)
*           for each image. These values come from the data
*           acquisition code getdata.exe.
*****
integer*2 init,err,status,endd,buf0(1),buf1(1),buf2(1)
real avghue,tcryst,vinc,slope,intcpt,ratio
real qdtot,rho,re,xoc,ttc(8),thick(8),tinf
real p,qdconv,qdcond,qdrad,r,xoverc,avgrat,avgmu
real q,vel,chord,mu,twing,h,aa,bb,xoc(21)
real sigma,epsinc,epswal,k,tavg,tinsid,avgre,avgvel,avgrho

```

```

real tot(500),rad(500),tcr(500),tfinfin(500),xovc(500),cond(500)
real conv(500),hh(500),dhdv,dhdr,dhdl,dhdw,dhdk,dhdtw,dhde,dhdtc
real dhdtin,dhdtif,l,w,rstrip,eps,delw,delr,dell,uqdcnv,uqdrad
real delk,dele,deltw,delic,deltin,deltif,dely,uh,ut,uqdtot,uqdcod
real dtotdv,dtotdr,dtotdl,dtotdw,dcdk,dcdtc,dcdti,dcdtw
real drdde,drddtc,drddtf,blank
integer numxc,col(21),begrow,endrow,ni,i,ii,imgnum,imgcor(20)
integer npic,nred,int(20)j,cryitem,numrat,numcor,corval,addpt3(20)
integer*2 lb,mb,n,lr,nc,sat,count
integer addpt1(20),addpt2(20),numpts,colpt1,colpt2,colpt3
integer flag1,flag2,flag3,numest
character*16 print(20),printfil
character*16 imgfil,outfil,logfil,xfile
character*6 imgnam
character*8 imgcnt

```

- * hardcoded physical data
- * thermal conductivity of wing material in Watts/m/K
k=0.224
- * wing chord in meters (chord is 12 inches)
chord=0.3048
- * Inconel strip length in meters
l=0.3984625
- * Inconel strip width in meters
w=0.0762
- * Inconel strip resistance in ohms
rstrip=0.2643
- * Stefan-Boltzmann constant in Watts/m^2/K^4
sigma=5.67e-8
- * emissivity of the black paint on the Inconel strip
epsinc=0.94
eps=epsinc
- * emissivity of the beige tunnel walls with Plexiglas sections
epswal=0.94
- * Ideal Gas constant in SI units
r=287.0
- * uncertainty analysis values in SI units
dell=0.00079375
delw=0.00079375

- delk=0.02

- dele=0.02

- deltw=0.000381

- delr=0.001

- deltin=0.2
deltif=0.2

- * x/c locations and corresponding wing thicknesses (inches)
- * of the 8 thermocouple positions
xoetc(1)=0.02

```

xoclc(2)=0.10
xoclc(3)=0.175
xoclc(4)=0.26
xoclc(5)=0.40
xoclc(6)=0.545
xoclc(7)=0.70
xoclc(8)=0.82

thick(1)=0.405
thick(2)=0.414
thick(3)=0.410
thick(4)=0.413
thick(5)=0.377
thick(6)=0.412
thick(7)=0.387
thick(8)=0.382

* convert inches to meters
do 1 i=1,8
    thick(i)=thick(i)*0.0254
1  continue

* read column, x/c data table
numxc=21

xfile='colxoc.dat'

open(unit=10,file=xfile,status='old')
read(10,125) (col(i),xoc(i),i=1,numxc)
125 format(i3,f5.2)
close(unit=10)

* zero imgcor (image column correction array)
* zero addpts (array for user added h points)
do 2 i=1,20
    imgcor(i)=0
    addpt1(i)=0
    addpt2(i)=0
    addpt3(i)=0
2  continue

* read input file containing all necessary information for an entire run
open(unit=14,file='input.dat',status='old')
j=1
blank=0.0
3  print*
ratio=0.0
numrat=0
numest=0
avgre=0.0
avgvel=0.0
avgrho=0.0

read(14,*) crytem

```

```

if(crytem.eq.30)then
  deltc=0.2
elseif(crytem.eq.45)then
  deltc=0.15
else
  print*, 'Crystal Temperature must be either 30 or 45!'
endif

read(14,*) lb, mb, sat
read(14,*) nred
read(14,*) (int(i),i=1,nred)

do 4 i=1,nred
  read(14,'(a)') print(i)
4  continue

read(14,*) p
read(14,*) numcor
if(numcor.eq.0)goto6
do 5 i=1,numcor
  read(14,*) imgnum,corval
  imgcor(imgnum)=corval
5  continue
6  continue

read(14,*) numpts
if(numpts.eq.0)goto8
do 7 i=1,numpts
  read(14,*) imgnum, colpt1, colpt2, colpt3
  addpt1(imgnum)=colpt1
  addpt2(imgnum)=colpt2
  addpt3(imgnum)=colpt3
7  continue
8  continue

read(14,*) begrow, endrow
read(14,*) npic
read(14,*) ni

inten=int(j)
printfil=print(j)

* open print file which will contain all x/c, h data to facilitate plotting
open(unit=13,file=printfil,status='unknown')

* Output files will contain the following information
*   x/c h(W/m^2/K) Uh %Uh qdtot(W/m^2) Uqdtot qdconv U qdconv qdcond
*   Uqdcond qdrad Uqdrad (tcryst-tinf) U(tcryst-tinf) %CONV %COND %RAD
*   tcryst(K) tinsid(K) tinf(K) twing(m)
  write(13,135) 'xoc h Uh Percent_Uh qdtot Uqdtot qdconv Uqdconv qd
$cond Uqdcond qdrad Uqdrad tcry_minus_tinf U_tcry_minus_tinf Percen
$t_CONV Percent_COND Percent_RAD tcryst tinsid tinf twing'

```

```

* begin loop to reduce each image in turn
do 1000 ii=1,ni
flag1=0
flag2=0
flag3=0

*****
* Initialization and set-up
*****
* Initialize 2871 board to default settings
err=auerrm(1)
init=auinit()
status=ausmod(0)
status=audisp(1)

read(14,10) imgnam,imgcnt,re,vel,rho,qdtot,tinf,ttc(1),ttc(2),ttc(
$3),ttc(4),ttc(5),ttc(6),ttc(7),ttc(8),vinc
10 format(1x,a6,1x,a8,1x,f7.0,1x,f5.2,1x,f5.3,1x,f10.4,1x,9(f7.3,1x),
$f6.3)
if(vinc.lt.3.25)then
  delv=0.001
else
  delv=0.01
endif

avgre=avgre+re
avgvel=avgvel+vel
avgrho=avgrho+rho

imgfil(1:6)=imgnam
imgfil(7:10)='.'img'
open(unit=8,file=imgfil,status='old')

outfil(1:6)=imgnam
outfil(7:10)='.'out'
open(unit=11,file=outfil,status='unknown')

logfil(1:6)=imgnam
logfil(7:10)='.'log'
open(unit=12,file=logfil,status='unknown')

write(0,*)"Name of file containing column,x/c information must be
$called colxoc.dat"
write(0,*)
write(0,130)'Name of image file    : ',imgfil
write(0,130)'Name of output data file: ',outfil
write(0,130)'Name of log file     : ',logfil
write(0,130)'Name of print file   : ',printfil
130  format(1x,2a)

write(11,135) 'xoc h Uh Percent_Uh qdtot Uqdtot qdconv Uqdconv qd
$cond Uqdcond qdrad Uqdrad tcry_minus_tinf U_tcry_minus_tinf Perce
$t_CONV Percent_COND Percent_RAD tcrys tinsid tinf twing'
135  format(1x,a)

```

```

* print to screen so user can check for input errors
  write(0,*)
  write(0,*)
  write(0,150) 'Crystal Temperature (deg.C): ',crytem
  write(0,150) 'Starting value of Hue: ',lb
150  format(1x,a30,i3)
  write(0,150) 'Band of Hue: ',mb
  write(0,150) 'Intensity Threshold: ',inten
  write(0,150) 'Saturation Threshold: ',sat
  write(0,*)
155  format(1x,a25,f5.3)
  write(0,157) 'Atmospheric Pressure (Pa): ',p
157  format(1x,a25,f8.1)
  write(0,*)
  write(0,*)
  write(0,*)
  write(0,*)
  write(0,*)
  write(0,*)
  write(0,*)
  write(0,*)
  write(0,*)

status=aurest(0,0,0,imgfil,jet)

*****
*   GET HUE VALUES AND SAVE
*****
do 200 nc=510,2,-2
if(nc+imgcor(ii).gt.col(1).or.nc+imgcor(ii).lt.col(numxc))goto200
  avghue=0.0
  count=0
  do 100 nr=begrow,endrow,1

* read HSI
* and copy into next column to fix bad columns

  status=augitx(0,nc,1,buf0,buf1,buf2)
*   status=aupitx(0,nc+1,1,buf0,buf1,buf2)
* this line was to correct the hardware problem on psu image processor

* check local saturation value and discard if less than threshold value
  if(buf1(1).lt.sat) goto 100

* check local intensity value and discard if less than threshold value
  if(buf0(1).lt.inten) goto 100

* hue buffer filtering
* discard if hue is not in defined range
  if(buf2(1).lt.lb.or.buf2(1).gt.lb+mb) goto 100

* passes all criteria; keep point and count it
  count=count+1

```

```

avghue=avghue+real(buf2(1))

* now that the hue has been recorded, change the pixel on the image
* processor screen to a DARK COLOR so it can be seen
  buf0(1)=0
  buf1(1)=180
  buf2(1)=170

status=aupittx(0,nr,nc,1,buf0,buf1,buf2)

100      continue

c now it's done with one column; average the hue
if(count.le.npic-1)goto200

avghue=avghue/real(count)

* convert hue to temperature based on liquid crystal calibration
* this temperature will be in degrees Celsius
* Note that 2 calibrations are coded: 30 and 45 deg.C crystals

* from the hue vs temperature calibration in degrees Celsius
if(crytem.eq.30)then
  slope=122.52
  intcpt=-3535.5
elseif(crytem.eq.45)then
  slope=549.01
  intcpt=-24182.0
else
  print*,'Only 30 and 45 degree Celsius crystals are valid!!'
  goto 2000
endif

tcrys=(avghue-intcpt)/slope

* convert degrees Celsius to Kelvin
tcrys=tcrys+273.15

* find x/c location for the given column, nc
179  continue
  do 180 i=1,numxc-1
    if(nc+imgcor(ii).le.col(i).and.nc+imgcor(ii).gt.col(i+1))goto185
180  continue
185  continue
  aa=real(nc+imgcor(ii)-col(i))/real(col(i+1)-col(i))
  bb=xoc(i+1)-xoc(i)
  xoverc=aa*bb+xoc(i)

* find conduction losses
* x/c falls before the first TC location (0.02)
  if(xoverc.ge.0.0.and.xoverc.lt.xoctc(1))then
    tinsid=ttc(1)
    twing=thick(1)
    goto 195

```

```

        endif

* find internal temperature at x/c location by interpolating
* from thermocouple array
    do 190 i=1,7
        if(xoverc.ge.xoctlc(i).and.xoverc.lt.xoctlc(i+1))goto 191
190  continue
191  continue
    aa=(xoverc-xoctlc(i))/(xoctlc(i+1)-xoctlc(i))
    bb=ttc(i+1)-ttc(i)
    tinsid=aa*bb+ttc(i)

* then find wing thickness at x/c location
    do 192 i=1,7
        if(xoverc.ge.xoctlc(i).and.xoverc.lt.xoctlc(i+1))goto 193
192  continue
193  continue
    aa=(xoverc-xoctlc(i))/(xoctlc(i+1)-xoctlc(i))
    bb=thick(i+1)-thick(i)
    twing=aa*bb+thick(i)

195  continue

    qdcond=k*(tcryst-tinsid)/twing

* find radiation losses
    qdrad=sigma*(epsinc*tcryst**4-epswal*tinf**4)

    if(xoverc.le.xoctlc(8))then
        ratio=ratio+qdcond/qdtot
        numrat=numrat+1
        avgrat=ratio/real(numrat)
    endif

* Note that if x/c falls after the last TC location (0.82), then
* the conduction losses will be estimated as the average percentage
* conduction loss that occurred during the first 0.82 x/c of the chord.
* This is because the internal structure of the wing does not allow an
* easy calculation of the conduction losses.

    if(xoverc.gt.xoctlc(8).and.xoverc.le.1.0)then
        numest=numest+1
        tot(numest)=qdtot
        rad(numest)=qdrad
        tcr(numest)=tcryst
        tinf(numest)=tinf
        xovc(numest)=xoverc
        goto206
    endif

* find convective heat transfer coefficient, h (Watts/m^2/K)
    qdconv=qdtot-qdcond-qdrad
    h=qdconv/(tcryst-tinf)

```

* uncertainty in h calculation

```

dhdv=2.*vinc/(rstrip*I*w*(tcryst-tinf))
dhdr=-vinc**2/(rstrip**2*I*w*(tcryst-tinf))
dhdl=-vinc**2/(I**2*rstrip*w*(tcryst-tinf))
dhdw=-vinc**2/(w**2*rstrip*I*(tcryst-tinf))
dhdk=-(tcryst-tinsid)/(twing*(tcryst-tinf))
dhdtw=k*(tcryst-tinsid)/(twing**2*(tcryst-tinf))
dhde=-sigma*(tcryst**4-tinf**4)/(tcryst-tinf)
dhdtc=-vinc**2/(rstrip*I*w*(tcryst-tinf)**2)-k*(tinsid-tinf)/(twin
$g*(tcryst-tinf)**2)-4.*sigma*eps*tcryst**3/(tcryst-tinf)+sigma*eps
$*(tcryst**4-tinf**4)/(tcryst-tinf)**2
dhdtif=vinc**2/(rstrip*I*w*(tcryst-tinf)**2)-k*(tcryst-tinsid)/(tw
$ing*(tcryst-tinf)**2)+4.*sigma*eps*tinf**3/(tcryst-tinf)-sigma*eps
$*(tcryst**4-tinf**4)/(tcryst-tinf)**2
dhdtin=k/(twing*(tcryst-tinf))
uh=sqrt((dhdv*delv)**2+(dhdr*delr)**2+(dhdl*dell)**2+(dhdw*delw)**2
$2+(dhdk*delk)**2+(dhdtc*deltc)**2+(dhdtin*deltin)**2+(dhdtw*deltw)
$**2+(dhdtif*deltif)**2+(dhde*dele)**2)

```

* uncertainty in (Tcryst-Tinf) calculation-->h denominator

```
ut=sqrt(detc**2+deltif**2)
```

* uncertainty in qdot calculation (total heat flux generated)

```

dtotdv=2.*vinc/(rstrip*I*w)
dtotdr=-vinc**2/(rstrip**2*I*w)
dtotdl=-vinc**2/(rstrip*I**2*w)
dtotdw=-vinc**2/(rstrip*I*w**2)
uqdtot=sqrt((dtotdv*delv)**2+(dtotdr*delr)**2+(dtotdl*dell)**2+(dt
$otdw*delw)**2)

```

* uncertainty in qccond calculation (conductive heat flux)

```

dcddk=(tcryst-tinsid)/twing
dcddtc=k/twing
dcddti=-k/twing
dcddtw=-k*(tcryst-tinsid)/(twing**2)
uqcdcod=sqrt((dcddk*delk)**2+(dcddtc*deltc)**2+(dcddti*deltin)**2+(dc
$ddtw*deltw)**2)

```

* uncertainty in qdrad calculation (radiative heat flux)

```

drdde=sigma*(tcryst**4-tinf**4)
drddtc=4.*sigma*eps*tcryst**3
drddtf=-4.*sigma*eps*tinf**3
uqdrad=sqrt((drdde*dele)**2+(drddtc*deltc)**2+(drddtf*deltif)**2)

```

* uncertainty in qdconv calculation (convective heat flux)--> h numerator

```
uqdcnv=uqdtot+uqcdcod+uqdrad
```

* store x/c and h data along with all other data in a file

```

write(11,198) xoverc,h,uh,uh/h*100.,qdot,uqdtot,qdconv,uqdcnv,qdc
$ond,uqcdcod,qdrad,uqdrad,(tcryst-tinf),ut,qdconv/qdot*100.,qdcond/
$qdot*100.,qdrad/qdot*100.,tcryst,tinsid,tinf,twing

```

```

        write(0,199) xoverc,h,uh/h*100.
199  format(1x,f4.2,3x,f6.2,3x,f6.1)

        write(13,198) xoverc,h,uh,uh/h*100.,qdtot,uqdtot,qdconv,uqdcnv,qdc
$ond,uqdcod,qdrad,uqdrad,(tcryst-tinf),ut,qdconv/qdtot*100.,qdcond/
$qdtot*100.,qdrad/qdtot*100.,tcryst,tinsid,tinf,twing
206  continue

        if(flag1.eq.1.or.flag2.eq.1.or.flag3.eq.1)goto201
* continue onward to the next column

200  continue
201  continue

if(addpt1(ii).ne.0)then
  tcryst=44.23+273.15
  nc=addpt1(ii)
  addpt1(ii)=0
  flag1=1
  goto179
endif

if(addpt2(ii).ne.0)then
  tcryst=44.23+273.15
  nc=addpt2(ii)
  addpt2(ii)=0
  flag2=1
  goto179
endif

if(addpt3(ii).ne.0)then
  tcryst=44.23+273.15
  nc=addpt3(ii)
  addpt3(ii)=0
  flag3=1
  goto179
endif

* all columns done now
* write test information to log file
        write(12,150)'Crystal Temperature (deg.C): ',crytem
        write(12,150)'Starting value of Hue: ',lb
        write(12,150)'Band of Hue: ',mb
        write(12,150)'Intensity Threshold: ',inten
        write(12,150)'Saturation Threshold: ',sat
        write(12,*)
        write(12,157)'Atmospheric Pressure (Pa): ',p
        write(12,*)
        write(12,155)'Density (kg/m^3): ',rho
        write(12,160)'Wind Velocity(m/s): ',vel
        write(12,165)'Reynolds Number: ',re
        if(ii.eq.ni)then
          write(12,250)

```

```

        write(12,250)'Average Re (all images): ',avgre/real(ni)
        write(12,251)'Average Vel (all images): ',avgvel/real(ni)
        write(12,252)'Average Rho (all images): ',avgrho/real(ni)
        avgmu=(avgrho/real(ni))*(avgvel/real(ni))*chord/(avgre/real(ni))
        write(12,253)'Average Mu (all images): ',avgmu
    endif
250  format(1x,a,f7.0)
251  format(1x,a,f5.2)
252  format(1x,a,f5.3)
253  format(1x,a,f11.9)

endd=auend()
write(0,'(A10,I3)') 'ENDD = ',endd

close(unit=8)
close(unit=11)
close(unit=12)

* continue on to next image
1000  continue

* now write x/c,h data to print file for x/c > xoclc(8)
do 1500 i=1,numest
    cond(i)=avgrat*tot(i)
    conv(i)=tot(i)-cond(i)-rad(i)
    hh(i)=conv(i)/(tcr(i)-tfin(i))

    write(13,198) xovc(i),hh(i),blank,tot(i),blank,conv(i),blank,co
$nd(i),blank,rad(i),blank,(tcr(i)-tfin(i)),blank,conv(i)/tot(i)*1
$00.,cond(i)/tot(i)*100.,rad(i)/tot(i)*100.,tcr(i),blank,tfin(i),
$blank

1500  continue

close(unit=13)
rewind(unit=14)

j=j+1
if(j.eq.nred+1)goto2000
* continue on to next intensity criteria value
goto3

2000  close(unit=14)
* all images for all intensity criteria values now done

stop
end

```

APPENDIX D: Hot-Wire Anemometry Codes

This appendix contains the FORTRAN codes that were used for data acquisition and data reduction throughout the ASWT hot-wire anemometry experimentation. The codes are well-commented.

Sample Main Batch File sample.bat

```
zeroes
call hotwire e101f000 100
call hotwire e102f000 100
call hotlast e103f000
copy cond.out E1CON000.CON
```

hotwire.bat

```
waitgain
erase f:\hwdata.bin
mkfile f:\hwdata.bin/v 204
speedisk f:\
streamer /b=stream.bat
pitohot
trav%2
copy f:\hwdata.bin e:\todd\hw\aswt\sm701\hotwire\%1.bin
copy f:\hwdata.log e:\todd\hw\aswt\sm701\hotwire\%1.log
erase f:\hwdata.log
rem unpack f:\hwdata.bin,e:\todd\hw\aswt\sm701\hotwire\%1.raw,0-104448/b/das16
```

hotlast.bat

```
rem THIS BATCH FILE DOES NOT TRAVERSE THE PROBE!!! (USED FOR LAST POINT WHERE
rem NO TRAVERSE IS DESIRED)

waitgain
erase f:\hwdata.bin
mkfile f:\hwdata.bin/v 204
speedisk f:\
streamer /b=stream.bat
pitohot
copy f:\hwdata.bin e:\todd\hw\aswt\sm701\hotwire\%1.bin
copy f:\hwdata.log e:\todd\hw\aswt\sm701\hotwire\%1.log
erase f:\hwdata.log
unpack f:\hwdata.bin,e:\todd\hw\aswt\sm701\hotwire\%1.raw,0-104448/b/das16
```

Zeroes.for

```

program zeroes
*****
* This program acquires initial atmospheric pressure and temperature
* values as well as zeroes for : contraction pressure xducer, TC,
* Ptotalwake pressure xducer, and Pstatic wake pressure xducer.
*
* CHANNEL 2 ----> Contraction Pressure Transducer
* CHANNEL 3 ----> Thermocouple
* CHANNEL 4 ----> P total wake Pressure Transducer
* CHANNEL 5 ----> P static wake Pressure Transducer
*
*****
real patm,temper,fapp,vvent0,vtc0,clock,v(8),em(8),frepch
real vptw0,vpsw0
integer*2 basadr,dmalev,intlev,sch,fch,nch,nsapch,irange(8)
integer totsamp
character*40 date
character*1 ans
common a(8),b(8)
data basadr,dmalev,intlev,clock/816,3,5,1.0e6/

* set DASH-16 calibration constants for +/- 5V range
* note that a(3) is for channel 2; a(4) is for channel 3...
open(unit=7,file='board.dat',status='old')
    read(7,*) sch,fch,nsapch
    read(7,*) frepch
    read(7,*) irange(1),irange(2),irange(3)
    read(7,*) irange(4),irange(5),irange(6)
    read(7,*) irange(7),irange(8)
    do 3 i=1,8
        read(7,*) a(i), b(i)
3     continue
    close(unit=7)

* initialize DASH-16 board
call adinit(basadr,dmalev,intlev,rtnflg)

* set sampling information
itype = 0
nch = fch-sch+1

* Total number of samples = no. of channels x no. samples per channel
TOTSAMPA=NCH*NSAPCH
IF (TOTSAMPA .GT. 32760) THEN
    PRINT*, 'Total no. of samples must not exceed 32,760'
    PRINT*, 'i.e. No. of samples per channel x No. of channels'
    PRINT*, 'must be less than 32,760'
    stop
ENDIF

* user enters information

```

```

print*,'Please enter the DATE'
read(0,'(a40)') date
print*,'Please enter the APPLIED FREQUENCY (Hz)'
read*,fapp

c   print*,'Please enter ATMOSPHERIC PRESSURE (inHg)'
c   read*,patm
c* convert inHg to Pascals
c   patm=patm*3386.38815789

print*,'Please enter ATMOSPHERIC PRESSURE (mmHg)'
read*,patm
* convert mmHg to Pascals
patm=patm*133.322368421

print*,'Please enter Temperature (deg.F)'
read*,temper
* convert deg.F to Kelvin
temper=5.0/9.0*(temper-32.0)+273.15

5   print*
      print*

* record zeroes
print*,'Ready to sample zeroes? (y/n)'
read(0,'(a1)') ans
if(ans.eq.'y'.or.ans.eq.'Y')then
    call vmean(em,v,sch,fch,nch,nsapch,frepch,itype,iter)
    print*
    print*,'chan.0 zero = ',v(1)
    print*,'chan.1 zero = ',v(2)
    print*,'chan.2 zero = ',v(3)
    print*,'chan.3 zero = ',v(4)
    print*,'chan.4 zero = ',v(5)
    print*,'chan.5.zero = ',v(6)

    pause'Press <enter> to continue'
    vvent0=v(3)
    vtc0=v(4)
    vptw0=v(5)
    vpsw0=v(6)
else
    print*
    print*
    print*
    print*,'Well, when you are ready press y!'
    goto 5
endif

open(unit=8,file='cond.out',status='unknown')
write(8,*) date
write(8,*) patm
write(8,*) temper
write(8,*) fapp

```

```

write(8,*) vvent0
write(8,*) vtc0
write(8,*) vptw0
write(8,*) vpsw0
close(unit=8)

end

*-----
SUBROUTINE VMEAN(E,V,SCH,FCH,NCH,NSAPCH,FREPCH,ITYPE,ITER)

INTEGER*2 ICOUNT(10000)
INTEGER*2 NCH,SCH,FCH,NSAPCH
integer MODE
COMMON A(8),B(8)
DIMENSION IE(8),E(8),V(8)

DATA clock/1.e6/
mode=17

CALL SAMPLE(clock,SCH,FCH,NCH,NSAPCH,FREPCH,ICOUNT,ITYPE,mode,frea
$ct)

DO 20 J=1,NCH
20 E(J)=0.0

IPRINT=0
IF(IPRINT.EQ.1) WRITE(6,300)
DO 40 I=1,NSAPCH
    INDEX=(I-1)*NCH
    DO 45 J=1,NCH
        IE(J)=ICOUNT(INDEX+J)
45      E(J)=E(J)+REAL(IE(J)-E(J))/real(I)
        IF(IPRINT.EQ.1) WRITE(6,330) I,(IE(J),J=1,NCH)
40  CONTINUE

DO 50 J=1,NCH
50   V(J)=B(SCH+J)*E(J)+A(SCH+J)

300 FORMAT(//,9X,' No.',9X,' Ch.1',9X,' Ch.2')
320 FORMAT(4F15.5)
330 FORMAT(4I15)
      RETURN
END

```

Waitgain.for

```
program waitgain
    print*
    print*,'MAKE SURE TUNNEL IS UP TO SPEED'
    print*
    print*
    pause'Please SET GAIN then press <enter> to begin sampling'
    print*
end
```

Stream.bat

```
DAS16 LF=F:\HWDATA.LOG DR= F DF=HWDATA.BIN R= 4.096 FC= 0 LC= 1 STRT= INT CSRC=
INT BA= 330 DL= 3 CLK= 1
```

PitotHot.for

```

program pitothot
*****
* This program will read an input file containing data from previous
* traverse positions. It will then sample new information for the
* current traverse position. Then it will write all the traverse
* positions' data back to the original file. Finally it will traverse
* the probe to a new location.
*
* CHANNEL 2 ----> Contraction Pressure Transducer
* CHANNEL 3 ----> Thermocouple
* CHANNEL 4 ----> P total wake Pressure Transducer
* CHANNEL 5 ----> P static wake Pressure Transducer
*
*****
character*40 date
real patm,temp,rapp,vvent0,vtc0,v(8),em(8),frepch
real vvent(500),vtc(500),vptw0,vpsw0,vptw(500),vpsw(500),gain(500)
integer i,hwpos(500),motor(500),numpos,itype,totsamp,ans
integer*2 basadr,dmalev,intlev,sch,fch,nch,nsapch,irange(8),func
integer*4 flag
common a(8),b(8)

data basadr,dmalev,intlev,clock/816,3,5,1.0e6/

* read in data from previous traverse positions
open(unit=8,file='cond.out',status='old')
read(8,'(a40)') date
read(8,*) patm
read(8,*) temper
read(8,*) rapp
read(8,*) vvent0
read(8,*) vtc0
read(8,*) vptw0
read(8,*) vpsw0
do 10 i=1,500
  read(8,*,end=50) hwpos(i),motor(i),vvent(i),vtc(i),vptw(i),vpsw(i)
$,gain(i)
10  continue
50  if(i.eq.1)then
      numpos=i
    else
      numpos=i-1
    endif
  close(unit=8)

* set DASH-16 calibration constants for +/- 5V range
* note that a(3) is for channel 2; a(4) is for channel 3...
open(unit=7,file='board.dat',status='old')
read(7,*) sch,fch,nsapch
read(7,*) frepch
read(7,*) irange(1),irange(2),irange(3)

```

```

        read(7,*) irange(4),irange(5),irange(6)
        read(7,*) irange(7),irange(8)
        do 70 i=1,8
            read(7,*) a(i), b(i)
70      continue
            close(unit=7)

* initialize DASH-16 board
    call adinit(basadr,dmalev,intlev,rtnflg)

* set sampling information
    itype = 0
    nch = fch-sch+1

* Total number of samples = no. of channels x no. samples per channel
    TOTSAMP=NCH*NSAPCH
    IF (TOTSAMP .GT. 32760) THEN
        PRINT*, 'Total no. of samples must not exceed 32,760'
        PRINT*, 'i.e. No. of samples per channel x No. of channels'
        PRINT*, 'must be less than 32,760'
        stop
    ENDIF

* sample Venturi contraction, thermocouple, Ptotalwake, and Pstaticwake
* voltages for the current traverse position
    call vmean(em,v,sch,fch,nch,nsapch,frepch,itype,iter)
*2
* sample Venturi contraction, thermocouple, Ptotalwake, and Pstaticwake
* voltages for the current traverse position
    call vmean(em,v,sch,fch,nch,nsapch,frepch,itype,iter)
    vvent(numpos)=v(3)
    vtc(numpos)=v(4)
    vptw(numpos)=v(5)
    vpsw(numpos)=v(6)
    hwpos(numpos)=numpos

    if(numpos.eq.1)then
        motor(numpos)=0
    endif

    print*, 'Please enter thermocouple mV:'
    read*, vtc(numpos)
    v(4)=vtc(numpos)
    print*
        print*, 'chan.0 = ',v(1)
        print*, 'chan.1 = ',v(2)
        print*, 'chan.2 = ',v(3)
        print*, 'chan.3 = ',v(4)
        print*, 'chan.4 = ',v(5)
        print*, 'chan.5 = ',v(6)
    c      pause 'Press <enter> to continue'
*2
* write new cond.out output file including the new traverse position data
    open(unit=8,file='cond.out',status='old')

```

```

write(8,'(a40)') date
write(8,*) patm
write(8,*) temper
write(8,*) fapp
write(8,*) vvent0
write(8,*) vtc0
write(8,*) vptw0
write(8,*) vpsw0

80 print*
print*, 'Please enter GAIN'
print*
print*, ' 6 dB ----> 1.997174 gain'
print*, ' 10 dB ----> 3.159860 gain'
print*, ' 12 dB ----> 3.981072 gain'
print*, ' 16 dB ----> 6.309573 gain'
print*, ' 20 dB ----> 10.001598 gain'
print*, ' 26 dB ----> 19.952623 gain'
print*, ' 30 dB ----> 31.622777 gain'
print*, ' 34 dB ----> 50.118723 gain'
print*, ' 36 dB ----> 63.095734 gain'
print*, ' 40 dB ----> 100.000000 gain'
print*, ' 42 dB ----> 125.89254 gain'
print*, ' 46 dB ----> 199.52623 gain'
print*, ' 52 dB ----> 398.10717 gain'
print*
print*, '0 ----> USER INPUT GAIN VALUE'
print*
read*,ANS
c      ANS=10

if(ans.eq.6)then
    gain(numpos)=1.997174
elseif(ans.eq.10)then
    gain(numpos)=3.159860
elseif(ans.eq.12)then
    gain(numpos)=3.981072
elseif(ans.eq.16)then
    gain(numpos)=6.309573
elseif(ans.eq.20)then
    gain(numpos)=10.001598
elseif(ans.eq.26)then
    gain(numpos)=19.952623
elseif(ans.eq.30)then
    gain(numpos)=31.622777
elseif(ans.eq.34)then
    gain(numpos)=50.118723
elseif(ans.eq.36)then
    gain(numpos)=63.095734
elseif(ans.eq.40)then
    gain(numpos)=100.000000
elseif(ans.eq.42)then
    gain(numpos)=125.89254
elseif(ans.eq.46)then

```

```

        gain(numpos)=199.52623
elseif(ans.eq.52)then
        gain(numpos)=398.10717
elseif(ans.eq.0)then
        print*
        print*, 'Enter GAIN: '
        read*,gain(numpos)
else
        goto 80
endif
print*
do 100 i=1,numpos
        write(8,*) hwpos(i),motor(i),vvent(i),vtc(i),vptw(i),vpsw(i),ga
$in(i)
100 continue
close(unit=8)
end

*-----
SUBROUTINE VMEAN(E,V,SCH,FCH,NCH,NSAPCH,FREPCH,ITYPE,ITER)

INTEGER*2 ICOUNT(10000)
INTEGER*2 NCH,SCH,FCH,NSAPCH
integer MODE
COMMON A(8),B(8)
DIMENSION IE(8),E(8),V(8)

DATA clock/1.e6/
mode =17

CALL SAMPLE(clock,SCH,FCH,NCH,NSAPCH,FREPCH,ICOUNT,ITYPE,mode,frea
$ct)

DO 20 J=1,NCH
20 E(J)=0.0

IPRINT=0
IF(IPRINT.EQ.1) WRITE(6 ,300)
DO 40 I=1,NSAPCH
        INDEX=(I-1)*NCH
        DO 45 J=1,NCH
                IE(J)=ICOUNT(INDEX+J)
45        E(J)=E(J)+REAL(IE(J)-E(J))/real(I)
                IF(IPRINT.EQ.1) WRITE(6 ,330) I,(IE(J),J=1,NCH)
40    CONTINUE

        DO 50 J=1,NCH
50        V(J)=B(SCH+J)*E(J)+A(SCH+J)

300 FORMAT(//,9X,' No.',9X,' Ch.1',9X,' Ch.2')
320 FORMAT(4F15.5)
330 FORMAT(4I15)
        RETURN
END

```

Trav100.for

```

program trav100
*****
* This program will drive the traverse stepping motor by using the
* DASH-16 digital outputs.
*
*      param(1)=1  will drive motor one direction
*      param(1)=2  will drive motor in other direction
*
* DASH-16 output wiring to Maxwell Stepping Motor Controller (SMC-102A)
*      Box Parallel I/O port:
*      DASH-16 outputs ----> Maxwell Parallel I/O pin
*
*      +5V ----> pin 2 (+5V logic power)
*      OP1 ----> pin 7 (X single step +)
*      OP0 ----> pin 6 (X single step -)
*      GND ----> pin 8 (X motor enable)
*      GND ----> pin 1 (logic ground)
*
* Thus to step the motor, use mode 13 of the DASH-16 to send pulses
* to the digital outputs. The Maxwell box operates ACTIVE LOW, so
* first of all send voltage to both digital outputs OP0 and OP1. This
* will send +5V to both output channels.
*
*      OP3  OP2  OP1  OP0
*      0    0    1    1    ---> 2^1 + 2^0 = 3
*
*      param(1)=3
*      call fdasg(mode,param,flag)
* Now both output channels (0 and 1) will see +5 volts. To cause the motor
* to step, send a low signal to one of the channels. For instance, to cause
* the motor to step in the +X direction, we need to cause OP1 to go low.
*
*      OP3  OP2  OP1  OP0
*      0    0    0    1    ---> 2^0 = 1
*
*      param(1)=1
*      call fdasg(mode,param,flag)
* Now finish the step by bringing OP1 back up to high.
*
*      OP3  OP2  OP1  OP0
*      0    0    1    1    ---> 2^1 + 2^0 = 3
*
*      param(1)=3
*      call fdasg(mode,param,flag)
* This completes 1 step in the +X direction. Use a loop for many steps.
* Use delay loops inside the stepping loop to control motor speed.
*
* NOTE: The computer code must be linked to the library: dasg.lib
*****
integer*2 basadr,dmalev,intlev
integer*2 mode,param(16),flag

```

```

character*40 date
real patm,temper,fapp,vvent0,vtc0,vptw0,vpsw0
real vvent(500),vtc(500),vptw(500),vpsw(500),gain(500)
integer i,hwpos(500),motor(500),steps,numpos

parameter(steps=100)

data basadr,dmalev,intlev,clock/816,3,5,1.0e6/

*** initialize DASH-16 board
mode=0
param(1)=basadr
param(2)=intlev
param(3)=dmalev
call fdasg(mode,param,flag)

*** set mode to write to digital outputs of DASH-16
mode=13

*** send +5V to digital outputs 0 and 1 to establish "high" reference
param(1)=3
call fdasg(mode,param,flag)
if(flag.ne.0)then
  print*, 'FLAG = ',flag
  pause
endif

*****
*** index traverse ----- param(1)=1 will "shorten" entire setup
DO 105 I=1,steps
* setting param(1)=1 will cause digital output 0 to remain at +5V
* while causing digital output 1 to go to zero volts. Thus digital
* output 1 will be pulsed from high to low. This leads to a +X step.

param(1)=1
call fdasg(mode,param,flag)

IF (FLAG .NE. 0) THEN
  PRINT*, 'INDEXING ERROR HAS OCCURED'
  PRINT*, 'FLAG = ',FLAG
ENDIF

* internal delay loop controlling motor speed
do 50 j=1,4
  print*, 'Traversing probe ("shortening") ...'
50  continue

*****
*** setting param(1)=3 will cause both digital outputs 0 and 1 to see +5V
*** and thus complete the step

param(1)=3
call fdasg(mode,param,flag)

```

```

* internal delay loop controlling motor speed
do 60 j=1,4
   print*, "Traversing probe ("shortening") ..."
60   continue
105  CONTINUE
*****
* update COND file with motor counts for new position that was just moved to
* read in data from previous traverse positions
  open(unit=8,file='cond.out',status='old')
  read(8,'(a40)') date
  read(8,*) patm
  read(8,*) temper
  read(8,*) fapp
  read(8,*) vvent0
  read(8,*) vtc0
  read(8,*) vptw0
  read(8,*) vpsw0
  do 110 i=1,500
    read(8,*,end=150) hwpos(i),motor(i),vvent(i),vtc(i),vptw(i),vpsw(
$ i),gain(i)
110   continue
150   numpos=i
      close(unit=8)

  motor(numpos)=motor(numpos-1)+steps
  hwpos(numpos)=0
  vvent(numpos)=0.0
  vtc(numpos)=0.0
  vptw(numpos)=0.0
  vpsw(numpos)=0.0
  gain(numpos)=0.0

* write new cond.out output file including the new traverse position data
  open(unit=8,file='cond.out',status='old')
  write(8,'(a40)') date
  write(8,*) patm
  write(8,*) temper
  write(8,*) fapp
  write(8,*) vvent0
  write(8,*) vtc0
  write(8,*) vptw0
  write(8,*) vpsw0
  do 200 i=1,numpos
    write(8,*) hwpos(i),motor(i),vvent(i),vtc(i),vptw(i),vpsw(i),ga
$ in(i)
200   continue
      close(unit=8)
      print*, 'Start Delay Loop...'
      do 210 i=1,1500
c      print*
210   continue
      print*, 'End Delay Loop'
      end

```

Hwreduce.for

```

program hwreduce
*-----
*   * HWREDUCE.FOR : This program will take the raw data
*   * acquired during hot-wire experimentation
*   * and calculate mean and fluctuation
*   * velocities, as well as flow conditions.
*   * This program also will calculate Cd by
*   * an integration technique; a little work
*   * needs to be done for this to occur. (Cd not
*   * calculated for current experimentation).
*
*   * Note: The file containing the hot-wire calibration constants
*   * must be called 'hwcal.cal'
*
*   * When data were taken, the following channels were used.
*   * CHANNEL 0 --> MEAN FLOW
*   * CHANNEL 1 --> FLOW FLUCTUATIONS (AMPLIFIED)
*
*   * The following unit numbers are used in this code.
*
*   * UNIT 5 --> READING SAMPLING INFORMATION
*   * UNIT 7 --> READING TUNNEL AND BOARD CALIBRATION INFORMATION
*   * UNIT 8 --> READING TEST CONDITIONS FOR EACH TRAVERSE POSITION
*   * UNIT 10 --> READING IN DATA FILE CONTAINING RAW COUNT VALUES
*   * UNIT 11 --> READING HOT WIRE CALIBRATION FILE
*   * UNIT 14 --> READING K-TYPE THERMOCOUPLE CHART
*
*   * UNIT 2 --> WRITING FFT INFORMATION
*   * UNIT 3 --> WRITING DOC INFORMATION
*   * UNIT 9 --> WRITING CALCULATED VELOCITY, RE,...also Cd
*   * UNIT 12 --> WRITING HWLOC,UMEAN,UMEAN/Uinf,urms
*   * UNIT 13 --> WRITING VELOCITY FLUCTUATIONS FOR USE BY DaDiSP TO FFT
*
*   * UNIT 4 --> TEMPORARY FILE
*-----

```

\$LARGE

PARAMETER (M=2048,MH=M/2)

```

CHARACTER*30 fraw,ffft,fdoc,hwcal,fcond,fout,input,fad
character*40 date
character*3 freqap
character*2 tpchar
character*1 elem
REAL*8 X,XX,X2
REAL*8 pi
real aa,bb,vt(61)
integer tt(61)
double precision sum,sum2,avgvel,avolt,avel,avgvl,rmsvel
double precision gain(200),sum3,voltfl,avgvfl,a(8),b(8),c1(10)

```

```

real fapp,vvent(200),vtc(200),vptw(200),vpsw(200)
real vvent0,vtc0,patm,tinf,mu,temper,psloc,velloc
real tslope,rho,venslp,tunslp,velinf,re,chord,ti
real freqch,vptw0,vpsw0,offset,mach,reavg,maavg
real ptw(200),psw(200),psinf(200),cd,tol,qinf(200)
real deltw
double precision dw
integer i,j,jj,npts,countm,n1,n1pl,hwpos(200),tolpos,trapos
integer countf,k,numhw,hotpos(200),motor(200)

COMPLEX*16 FX(M),FX2(M)

DIMENSION FXX(M)
DIMENSION X(M),X2(M),WINDOW(M)
DIMENSION XX(MH)

HANWIN(J) = 0.5*(1.-COS(2.*PI*real(J-1)/real(M-1)))
pi = acos(-1.0)

chord=0.3048

*** user enters information
print*, 'Enter ELEMENT #'
read(0,'(a1)') elem
print*, 'Enter APPLIED FREQUENCY (3 digits)'
read(0,'(a3)') freqap

*** read control parameters
input='e//elem//inp//freqap//.inp'
open(unit=5,file=input,STATUS='OLD')
* note that npts is the total number of samples taken...later it
* is divided by 2 since I sampled 2 channels to obtain the number
* that I must loop to in order to read all raw data
read(5,*) k,freqch,npts
read(5,'(2a20)') hwcal

*** Read hot wire calibration file
open(unit=11,file=hwcal,status='old')
read(11,*) n1
n1pl=n1+1
read(11,*) (c1(j),j=1,n1pl)
close(unit=11)

*** Read K-Type Thermocouple Chart
open(unit=14,file='chartk.dat',status='old')
read(14,2) (tt(i),vt(i),i=1,61)
2 format(i2,f6.3)
close(unit=14)

*** read tunnel and board calibration information
* Note:
*   tunslp ---> Pa/Pa -----> TUNNEL DYNAMIC vs contraction drop
*   venslp ---> Pa/volt -----> Venturi PRESSURE TRANSDUCER slope
*   pslope ---> Pa/Pa -----> PSTATIC vs contraction drop

```

```

*
*           ??? or pstatic-patm vs contraction drop???
* ptwslp ---> Pa/volt -----> Ptotalwake PRESSURE TRANSDUCER slope
* pswslp ---> Pa/volt -----> Pstaticwake PRESSURE TRANSDUCER slope
* tslope ---> deg.K/volt ---> THERMOCOUPLE slope

      open(unit=7,file='calib.dat',status='old')
      read(7,*) tunslp, venslp, pslope
      read(7,*) ptwslp, pswslp, tslope
* read in wake traverse single step increment {meters per count}, distance
* between Pitot-Static probe and hotwire {meters}, and
* tolerance {xXXXXXXXX????????}
      read(7,*) dw, offset, tol
* read in board calibration constants
      do 3 i=1,8
          read(7,*) a(i), b(i)
3    continue
* Note: I don't need to read the IRANGE( ) values that tell the DAS20
* the individual channel gains since I'm not sampling in this code. I'm
* only doing data reduction.
* read in the traverse position values at which HW data were taken
      do 5 i=1,1000
          read(7,*,end=7) hotpos(i)
5    continue
7    numhw=i-1

*** read test conditions for each traverse position
fcond='e//elem//con//freqap//.con'
open(unit=8,file=fcond,status='old')
      read(8,'(a40)') date
      read(8,*) patm
      read(8,*) temper
      read(8,*) fapp
      read(8,*) vvent0
      read(8,*) vtc0
      read(8,*) vptw0
      read(8,*) vpsw0
      totpos=0
      do 10 j=1,200
          read(8,*,end=20) hwpos(j),motor(j),vvent(j),vtc(j),vptw(j),vpsw(j)
$),gain(j)
          totpos=totpos+1
10   continue
20   close(unit=8)

***** ANALYZE THE WAKE DEFICIT *****
*
* open output file that will contain calculated velocity, Re ... values
fout='e//elem//out//freqap//.out'
open(unit=9,file=fout,status='unknown')
write(9,*)trapos psloc velinf veloc ma re rho tinf mu ptw psw ps
$inf
reavg=0.0
maavg=0.0

```

```

*** begin loop over all traverse positions in wake
do 50 trapos=1,totpos

*** calculate tunnel velocity, Re, ... for current traverse position
* find temperature in Kelvin
c      tinf=temper+tslope*(vtc(trapos)-vtc0)
c      tinf=temper

* correct for gain on thermocouple (56 dB)
c      vtc(trapos)=vtc(trapos)/630.9573445
      do 30 i=1,60
          if(vtc(trapos).ge.vt(i).and.vtc(trapos).lt.vt(i+1))goto 35
30      continue
35      continue
          aa=(vtc(trapos)-vt(i))/(vt(i+1)-vt(i))
          bb=float(tt(i+1))-float(tt(i))
          tinf=aa*bb+float(tt(i))
c convert tinf from Celsius to Kelvin
          tinf=tinf+273.15

* find air viscosity in SI units using Sutherland's law
          mu=0.000018*(tinf/293.15)**1.5*(403.15)/(tinf+110.0)
* find air density in SI units
          rho=patm/(287.0*tinf)
* find dynamic pressure and airspeed in SI units
          qinfs(trapos)=(vvent(trapos)-vvent0)*venslp*tunslp
          velinf=sqrt(2.0*qinfs(trapos)/rho)
* find Reynolds number
          re=(rho*velinf*chord)/mu
* find Mach number
          mach=velinf/sqrt(1.4*287.0*tinf)
          print*, 'rho = ',rho,' kg/m^3'
          print*, 'vel inf = ',velinf,' m/s'
          print*, 'Re = ',re
          print*, 'Ma = ',mach
          print*
* find Ptotalwake
c      ptw(trapos)=(vptw(trapos)-vptw0)*ptwsdp + patm
* find Pstaticwake
c      psw(trapos)=(vpsw(trapos)-vpsw0)*pswsdp + patm
* find vlocal
c      velloc=sqrt(2.0*(ptw(trapos)-psw(trapos))/rho)
* find P static infinity
c      psinf(trapos)=(vvent(trapos)-vvent0)*venslp*pslope + patm
* find Pitot-Static probe location
c      psloc=real(trapos-1)*dw
          psloc=real(motor(trapos))*dw
*** write information for current traverse position to output file
      write(9,40) trapos,psloc,velinf,velloc,mach,re,rho,tinf,mu,ptw(tr
$apos),psw(trapos),psinf(trapos)
40      format(1x,i2,2x,f8.6,2x,2(f5.2,2x),f5.3,2x,f7.0,2x,f5.3,2x,f6.2
,$,2x,f9.8,3(2x,f8.1))

maavg=maavg+mach

```

```

reavg=reavg+re
50 continue

maavg=maavg/real(totpos)
reavg=reavg/real(totpos)

*** call subroutine to calculate Cd
cc this section to calculate Cd needs a little work

goto7777

* ??????
***** IS C (chord) IN INCHES? MY CHORD IN METERS.
*?????

!!!!!!!
c   MAKE SURE EVERYTHING IS DEFINED RIGHT. THE DELTW I THINK IS THE
c   DISTANCE BETWEEN EACH WAKE POINT WHICH FOR ME IS THE SINGLE STEP
c   DISTANCE, DW, TIMES THE # OF STEPS BETWEEN EACH WAKE POINT,
c   FOR EXAMPLE,40. MAYBE MAKE THIS A PARAMETER IN THE BEGINNING OF
c   THE CODE
!!!!!!!

deltw=dw*40.
call wake(ptw,psw,psinf,cd,qinf,tol,deltw,chord,totpos)

7777 continue

write(9,*)
write(9,*)
c   write(9,45)'Coefficient of Drag ---> Cd = ',cd
write(9,46)'Average Re -----> = ',reavg
write(9,47)'Average Mach -----> = ',maavg
45 format(1x,a,f8.6)
46 format(1x,a,f7.0)
47 format(1x,a,f5.3)
close(unit=9)

*****
***** ANALYZE THE FREQUENCY CONTENT *****
*
open(unit=12,file='eprofile.pro',status='unknown')
do 1000 i = 1,numhw
    trapos=hotpos(i)
    hwloc=real(motor(trapos))*dw-offset

    open(unit=4,file='temp.tem',status='unknown')
    write(4,48) trapos
48    format(i2)
    rewind(unit=4)
    read(4,'(a2)') tpchar
    close(unit=4)
    if(trapos.lt.10) tpchar(1:1)='0'

```

```

*** open data file containing raw counts from DAS board
fraw='e//elem//tpchar//f//freqap//.raw'
print*,fraw
open(unit=10,file=fraw,status='old')

*** find Umean and do FFT
* raw data file has 2 columns: mean flow counts, fluctuation flow counts
  print*, 'Calculating Mean Hot Wire Velocity...'
* Mean Velocity calculation & amplifier offset DC voltage calculation
  sum=0.0
  sum2=0.0
  avgvel=0.0
  avgvfl=0.0

  read(10,*)
  read(10,*)

  do 100 j = 1,npts/2
    read(10,*) countm, countf
    avolt=a(1)+b(1)*real(countm)
    avel=c1(1)
    do 90 jj=2,nlp1
      avel=avel+c1(jj)*avolt**(jj-1)
90      continue
      sum=sum+avel
      sum2=sum2+avolt
* calculate offset amplified voltage of fluctuation
  voltfl=a(2)+b(2)*real(countf)
  avgvfl=avgvfl+voltfl
100     continue
      avgvel=sum/real(npts/2)
      avgvl=sum2/real(npts/2)
      avgvfl=avgvfl/real(npts/2)

      print*, 'Mean velocity = ',avgvel,' m/s'
      print*
c      print*, 'Amplified Fluctuation DC offset = ',avgvfl,' volts'

*** Calculate Turbulence Intensity
* find fluctuation velocity value
  print*
  print*, 'Calculating TI...'
  rewind(unit=10)

  read(10,*)
  read(10,*)

  sum3=0.0
  rmsvel=0.0
  SUM4=0.0

  fdad='e//elem//tpchar//f//freqap//.dad'
  open(unit=13,file=fdad,status='unknown')
  do 170 j = 1,npts/2

```

```

      read(10,*) countm, countf
* find offset amplified voltage of fluctuation
      avolt=a(2)+b(2)*real(countf)
* correct for DC shift due to amplification of DC trickle through filter
      avolt=avolt-avgvfl
* reverse gain to obtain actual voltage of fluctuation
      avolt=avolt/gain(trapos)
* add fluctuation volts to average volt value
      avolt=avolt+avgvl
* find instantaneous velocity
      avel=c1(1)
      do 160 jj=2,n1p1
         avel=avel+c1(jj)*avolt**(jj-1)
160     continue
* find fluctuation velocity
      avel=avel-avgvel

      write(13,*) real(avel)
      sum3=sum3+avel*avel
      SUM4=SUM4+AVEL
170     continue
      rmsvel=sqrt(sum3/real(npts/2))
      PRINT*, 'AVERAGE OF U FLUCTUATIONS: ',SUM4/REAL(NPTS/2)
      close(unit=13)

* find temperature in Kelvin
c      tinf=temper+tslope*(vtc(trapos)-vtc0)
c      tinf=temper
* correct for gain on thermocouple (56 dB)
c      vtc(trapos)=vtc(trapos)/630.9573445
      do 180 j=1,60
         if(vtc(trapos).ge.vt(j).and.vtc(trapos).lt.vt(j+1))goto 185
180     continue
185     continue
      aa=(vtc(trapos)-vt(j))/(vt(j+1)-vt(j))
      bb=float(tt(j+1))-float(tt(j))
      tinf=aa*bb+float(tt(j))
c convert tinf from Celsius to Kelvin
      tinf=tinf+273.15
* find air density in SI units
      rho=patm/(287.0*tinf)
* find airspeed in SI units
      velinf=sqrt(2.0*qinfs(trapos)/rho)
* find Turbulence Intensity
      ti=rmsvel/velinf

      print*, 'TI = ',ti*100.,' percent'
      print*

      print*, 'rms Velocity = ',rmsvel
c      print*, 'average volts = ',avgvl
      write(12,190) hwloc,avgvel,avgvel/velinf,rmsvel,rmsvel/velinf
190     format(5(1x,f8.5))

```

```

*** PERFORM FFT
* calculate frequency bin
FOLD=FREPCH/2.
DELTAF=FREPCH/REAL(M)
DELTAT=1./FREPCH
NTOTAL=(K+1)*MH

* calculate window weighting factor
DO 200 J=1,M
  WINDOW(J)=HANWIN(J)
200  CONTINUE
  SUMW= 0.0
  DO 210 J=1,M
    SUMW=SUMW+WINDOW(J)**2
210  CONTINUE
  FACT=SUMW/REAL(M)
  DEN=real(K*M*M)*FACT

  rewind(unit=10)
  read(10,*)
  read(10,*)

* prepare output files
ffft='e'//elem//tpchar//f//freqap//'.fft'
open(unit=2,file=ffft,status='unknown')
fdoc='e'//elem//tpchar//f//freqap//'.doc'
open(unit=3,file=fdoc,status='unknown')

DO 220 J=1,M
  FXX(J)=(0.0,0.0)
220  CONTINUE
  WRITE(0,*) 'BEGIN FFT'
  IT=0
  DO 250 J=1,MH
    read(10,*) countm, countf
    IT=IT+1
* find offset amplified voltage of fluctuation
  avolt=a(2)+b(2)*real(countf)
* correct for DC shift due to amplification of DC trickle through filter
  avolt=avolt-avgvfl
* reverse gain to obtain actual voltage of fluctuation
  avolt=avolt/gain(trapos)
* add fluctuation volts to average volt value
  avolt=avolt+avgvl
* find instantaneous velocity
  avel=c1(1)
  do 260 jj=2,n1pl
    avel=avel+c1(jj)*avolt**(jj-1)
260  continue
* find fluctuation velocity
  avel=avel-avgvel
  XX(J)=avel
250  CONTINUE

```

```

AS=0.
KK=0
DO 300 IK=1,K
    DO 265 J=1,MH
        X(J)=XX(J)
265    CONTINUE
    DO 275 J=1,MH
        read(10,*) countm, countf
        IT=IT+1
* find offset amplified voltage of fluctuation
    avolt=a(2)+b(2)*real(countf)
* correct for DC shift due to amplification of DC trickle through filter
    avolt=avolt-avgvfl
* reverse gain to obtain actual voltage of fluctuation
    avolt=avolt/gain(trapos)
* add fluctuation volts to average volt value
    avolt=avolt+avgvl
* find instantaneous velocity
    avel=c1(1)
    do 270 jj=2,n1p1
        avel=avel+c1(jj)*avolt**(jj-1)
270    continue
* find fluctuation velocity
    avel=avel-avgvel
    XX(J)=avel
275    CONTINUE

c      WRITE(0,*) IK,IT
      DO 280 J=1,MH
          X(J+MH)=XX(J)
280    CONTINUE

*** Apply the window to the data
      DO 290 J=1,M
          X(J)=X(J)*WINDOW(J)
290    CONTINUE
      CALL TWOFFT(X,X2,FX,FX2,M)
      DO 295 J=1,M
          FXX(J)=FX(J)+CONJG(FX(J))*FX(J)
295    CONTINUE
300    CONTINUE

* write to DOC output file
      WRITE(3,330) FDOC
      WRITE(3,340) FREPCH,IT,K
      write(3,350) trapos,hwloc,avgvel,rmsvel,ti*100.

* write to FFT output file
      DO 320 J=1,MH
          GXX=2.0*FX(J)/DEN/DELTAf
          AGXX=10.0* ALOG10(CABS(GXX))
          F=(real(J-1))*DELTAf
          WRITE(2,310) F,AGXX,GXX
320    CONTINUE

```



```

*-----  

SUBROUTINE FOUR1(DATA,NN,ISIGN)  

* from Press et al., 1992  

REAL*8 WR,WI,WPR,WPI,WTEMP,THETA,data  

dimension data(*)  

N=2*NN  

J=1  

DO 11 I=1,N,2  

  IF(J.GT.I)THEN  

    TEMPR=DATA(J)  

    TEMPI=DATA(J+1)  

    DATA(J)=DATA(I)  

    DATA(J+1)=DATA(I+1)  

    DATA(I)=TEMPR  

    DATA(I+1)=TEMPI  

  ENDIF  

  M=N/2  

1   IF ((M.GE.2).AND.(J.GT.M)) THEN  

    J=J-M  

    M=M/2  

    GO TO 1  

  ENDIF  

  J=J+M  

11  CONTINUE  

  MMAX=2  

2   IF (N.GT.MMAX) THEN  

    ISTEP=2*MMAX  

    THETA=6.28318530717959D0/(ISIGN*MMAX)  

    WPR=-2.D0*DSIN(0.5D0*THETA)**2  

    WPI=DSIN(THETA)  

    WR=1.D0  

    WI=0.D0  

    DO 13 M=1,MMAX,2  

      DO 12 I=M,N,ISTEP  

        J=I+MMAX  

        TEMPR=SNGL(WR)*DATA(J)-SNGL(WI)*DATA(J+1)  

        TEMPI=SNGL(WR)*DATA(J+1)+SNGL(WI)*DATA(J)  

        DATA(J)=DATA(I)-TEMPR  

        DATA(J+1)=DATA(I+1)-TEMPI  

        DATA(I)=DATA(I)+TEMPR  

        DATA(I+1)=DATA(I+1)+TEMPI  

12   CONTINUE  

    WTEMP=WR  

    WR=WR*WPR-WI*WPI+WR  

    WI=WI*WPR+WTEMP*WPI+WI  

13   CONTINUE  

  MMAX=ISTEP  

  GO TO 2  

ENDIF  

RETURN  

END

```

BIBLIOGRAPHY

- Ahuja, K. K. and Burrin, R. H. "Control of Flow Separation by Sound." AIAA Paper 84-2298, Oct. 1984.
- Ahuja, K. K., Whipkey, R. R., and Jones, G. S. "Control of Turbulent Boundary Layer Flows by Sound." AIAA Paper 83-0726, 1983.
- Althaus, D. and Würz, W. "Wind Tunnel Tests of the SM701 Airfoil." Institut Für Aerodynamik Und Gasdynamik, Universität Stuttgart, Germany, Jun. 1991.
- AMP, Incorporated. *Piezo Film Sensors Technical Manual*. May, 1993.
- Anbar, M. "Clinical Applications of Computerized Thermography." In NASA, Washington, D. C. Noncontact Temperature Measurement (See N88-23895 17-29), 1988, pp. 405-414.
- Baldwin, J. T., Tarbell, J. M., Deutsch, S., and Geselowitz, D. B. "Wall Shear Stress Measurements Within an Artificial Heart Ventricle." *1987 IEEE Engineering in Medicine and Biology Ninth Annual Conference*, Vol. 3, 1987, pp. 1189-1191.
- Bar-Sever, A. "Separation Control on an Airfoil by Periodic Forcing." *AIAA Journal*, Vol. 27, Jun. 1989, pp. 820-821.
- Becker, H. A. and Massaro, T. A. "Vortex Evolution in a Round Jet." *J. Fluid Mechanics*, Vol. 31, 1968, pp. 435-448.
- Bejan, A. *Heat Transfer*. John Wiley & Sons, Inc., New York, 1993, pp. 624-629.
- Bellhouse, B. J. and Schultz, D. L. "Determination of Mean and Dynamic Skin Friction, Separation and Transition in Low-Speed Flow with a Thin-Film Heated Element." *J. Fluid Mechanics*, Vol. 24, part 2, 1966, pp. 379-400.
- Bosetti, C. *Experimental Investigation of the Effects of Windward Surface Devices on the Primary Vortices of an Aspect Ratio 1.0 Delta Wing*. Master's Thesis, The Pennsylvania State University, Department of Aerospace Engineering, 1995.
- Bradshaw, P. and Wong, F. Y. F. "The Reattachment and Relaxation of a Turbulent Shear Layer." *J. Fluid Mechanics*, Vol. 52, 1972, pp. 113-135.
- Brown, G. L. and Roshko, A. "On Density Effects and Large Structure in Turbulent Mixing Layers." *J. Fluid Mechanics*, Vol. 64, 1974, pp. 775-816.

- Brophy, C. M. *Turbulence Management and Flow Qualification of the Pennsylvania State University Low-Turbulence, Low-Speed, Closed-Circuit Wind Tunnel*. Master's Thesis, The Pennsylvania State University, Department of Aerospace Engineering, 1994.
- Bruun, H. H. Hot-Wire Anemometry, Principles and Signal Analysis. Oxford University Press, New York, 1995, pp. 234-235.
- Butter, D. J. "Recent Progress on Development and Understanding of High Lift Systems." In AGARD Conference on Improvement of Aerodynamic Performance through Boundary Layer Control and High Lift Systems, AGARD-CP-365, Brussels, Belgium, 1984, pp. 1-1 to 1-26.
- Camci, C. "Liquid Crystal Thermography." A book chapter published for the 1996 von Karman Institute Lecture series on *Temperature Measurements*, VKI-LS-1996-09, Brussels, Belgium, Apr. 1996.
- Camci, C. "Liquid Crystal Thermography on the Rotating Surfaces of Turbomachinery Systems." A book chapter in *Advanced Turbomachinery Design*, ed. Chunill Hah, published by Marcel Dekker Inc., New York, 10016.
- Camci, C. and Glezer, B. "Liquid Crystal Thermography on the Fluid Solid Interface of Rotating Systems." *J. Heat Transfer*, Vol. 119, No. 1, Feb. 1997, pp. 20-29.
- Camci, C., Hippensteele, S. A., and Poinsatte, P. E. "Evaluation of a Hue Capturing Based Transient Liquid Crystal Method for High Resolution Mapping of Convective Heat Transfer on Curved Surfaces." *J. Heat Transfer*, Vol. 115, No. 2, May 1993.
- Camci, C., Kim, K., and Hippensteele, S. A. "A New Hue Capturing Technique for the Quantitative Interpretation of Liquid Crystal Images Used in Convective Heat Transfer Studies." *J. Turbomachinery*, Vol. 114, No. 4, Oct. 1992, pp. 765-775.
- Carslaw, H. S. and Jaeger, J. C. *Conduction of Heat in Solids*. 2nd edition, Clarendon Press, Oxford, 1959.
- Castro, I. P. and Epik, E. "Boundary-Layer Relaxation After a Separated Region." *Experimental Thermal and Fluid Science*, Vol. 13, n. 4, Nov. 1996, pp. 338-348.
- Centolanza, L., Dunn, C., Papay, P., Park, D., Smith, R., and Thibodeau, T. "Composite Wind Tunnel Model Design." Senior project final report, The Pennsylvania State University, Department of Aerospace Engineering, May 1995.
- Chandrsuda, C. and Bradshaw, P. "Turbulent Structure of a Reattaching Mixing Layer." *J. Fluid Mechanics*, Vol. 110, 1981, pp. 171-194.

- Chang, R. C., Hsiao, F. B., and Shyu, R. N. "Forcing Level Effects of Internal Acoustic Excitation on the Improvement of Airfoil Performance." *J. Aircraft*, Vol. 29, No. 5, Sept.-Oct. 1992, pp. 823-829.
- Chatigny, V. J. "Piezo Film Yields Novel Transducers." *Electronics Week* 57 (17), Aug. 6, 1984, pp. 74-77.
- Coe, D. J., Allen, M. G., Smith, B. L., and Glezer, A. "Addressable Micromachined Jet Arrays." *The 8th International Conference on Solid-State Sensors and Actuators, and Eurosensors IX*, Stockholm, Sweden, Jun. 25-29, 1995.
- Coe, D. J., Allen, M. G., Trautman, M. A., and Glezer, A. "Micromachined Jets for Manipulation of Macro Flows." *Solid-State Sensor and Actuator Workshop*, Hilton Head, SC, Jun. 13-16, 1994.
- Cole, K. D. "Separation Detection with Stochastic Signals From Flush-Mounted Hot-Film Sensors." *Fluid Measurement and Instrumentation Forum*, Vol. 95, 1990, pp. 35-37.
- Cooper, T. E., Field, R. J., and Meyer, J. F. "Liquid Crystal Thermography and Its Application to the Study of Convective Heat Transfer." *J. Heat Transfer*, Aug. 1975, pp. 442-449.
- Crawford, M. E., and Kays, W. M. *STAN5 - A Program for Numerical Computation of Two Dimensional Internal/External Boundary Layer Flows*. Stanford University, Department of Mechanical Engineering, Thermosciences Division, Report HMT-23, Dec. 1975.
- Cui, E. J., Yu, X. T., Fu, G. M., Xu, C., Zhang, S. Y., and Zhou, M. D. "Separation Control and Lift Enhancement on Airfoil Using Unsteady Excitations." *ICAS Congress 18th Proceedings*, Vol. 2, Beijing, China, Sept. 20-25, 1992.
- Dagenhart, J. R. and Stack, J. P. "Boundary Layer Transition Detection Using Flush-Mounted Hot-Film Gages and Semiconductor Dynamic Pressure Transducers." AIAA Paper No. 82-0593, 1982.
- DISA Electronics. *Instruction Manual DISA 55M System with 55M10 CTA Standard Bridge*. DISA Information Department, Marina Del Rey, CA.
- Dwinnell, James H. *Principles of Aerodynamics*. 1st edition, McGraw-Hill Book Company, Inc., New York, 1949.
- Ewald, P. P., Pöschl, Th., and Prandtl, L. *The Physics of Solids and Fluids*. Blackie & Sons, Limited, 1936.

- Fergason, J. L. "Liquid Crystals," *Scientific American*, Vol. 211, No. 2, 1964, pp. 76-85.
- Flittie, K. J. and Covert, E. E. "Unsteady Turbulent Skin-Friction Measurement in an Adverse Pressure Gradient." *AIAA Journal*, Vol. 30, No. 11, Nov. 1992, pp. 2647-2652.
- Frössling, N. "Evaporation, Heat Transfer, and Velocity in Two Dimensional and Rotationally Symmetrical Laminar Boundary Layer Flow." NACA TM 1432, 1958.
- Gad-el-Hak, M. "Separation Control for Steady and Unsteady Flows." *Proc. Int. Symp. on Non-Steady Fluid Dynamics*, eds. J. A. Miller and D. P. Telionis, FED-Vol. 92, ASME, New York, 1990a, pp. 261-275.
- Gad-el-Hak, M. and Bushnell, D. "Status and Outlook of Flow Separation Control." AIAA-91-0037, 29th Aerospace Sciences Meeting, Reno, NV, Jan. 7-10, 1991.
- Gharib, M. and Williams-Stuber, K. "Experiments on the Forced Wake of an Airfoil." *J. Fluid Mechanics*, Vol. 208, 1989, pp. 225-255.
- Henckels, A., Kreins, A. F., and Maurer, F. "Development and Application of Infrared and Other Flow Visualization Techniques in a Hypersonic Wind Tunnel of DLR Cologne." *Wind Tunnels and Wind Tunnel Test Techniques; Proceedings of the Conference*, Southampton, United Kingdom, Sept. 14-17, 1992.
- Hippensteele, S. A. and Russell, L. M. "High-Resolution Liquid Crystal Heat-Transfer Measurements on the End Wall of a Turbine Passage With Variations in Reynolds Number." NASA TM 100827, 1988.
- Hippensteele, S. A., Russell, L. M., and Stepka, F. S. "Evaluation of a Method for Heat Transfer Measurements and Thermal Visualization Using a Composite of a Heater Element and Liquid Crystals." *J. Heat Transfer*, Vol. 105, Feb. 1983, pp. 184-189.
- Hippensteele, S. A., Russell, L. M., and Torres, F. J. "Local Heat-Transfer Measurements on a Large Scale-Model Turbine Blade Airfoil Using a Composite of a Heater Element and Liquid Crystals." NASA TM 86900, 1985.
- Hippensteele, S. A., Russell, L. M., and Torres, F. J. "Use of a Liquid-Crystal, Heater-Element Composite for Quantitative, High-Resolution Heat Transfer Coefficients on a Turbine Airfoil, Including Turbulence and Surface Roughness Effects." NASA TM 87355, May 1987.
- Ho, Chih-Ming, and Huang, Lein-Saing. "Subharmonics and Vortex Merging in Mixing Layers." *J. Fluid Mechanics*, Vol. 119, 1982, pp. 443-473.

- Houghton, E. L. and Carpenter, P. W. *Aerodynamics for Engineering Students*. 4th edition, Halsted Press, New York, 1993.
- Hsiao, Fei-Bin, Liu, Chin-Fung, and Shyu, Jong-Yaw. "Control of Wall-Separated Flow by Internal Acoustic Excitation." *AIAA Journal*, Vol. 28, No. 8, 1989, pp. 1440-1446.
- Hsiao, Fei-Bin, Shyu, Rong-Nan, and Chang, R. C. "High Angle-of-Attack Airfoil Performance Improvement by Internal Acoustic Excitation." *AIAA Journal*, Vol. 32, No. 3, Mar. 1994.
- Huang, L. S., Bryant, T. D., and Maestrello, L. "The Effect of Acoustic Forcing on Trailing Edge Separation and Near Wake Development of an Airfoil." AIAA Paper 88-3531, Jul. 1988.
- Huang, L. S., Maestrello, L., and Bryant, T. D. "Separation Control over an Airfoil at High Angles of Attack by Sound Emanating from the Surface." AIAA Paper No. 87-1261, 1987.
- Hussain, A. K. M. F. "Large-Scale Organized Motions in Jets and Shear Layers." *Recent Advances in Aerodynamics*, ed. Krothapalli Smith, Proceedings of an International Symposium held at Stanford University, Aug. 22-26, 1983, pp. 205-262.
- Incropera, F. P. and DeWitt, D. P. *Fundamentals of Heat & Mass Transfer*. 3rd edition, John Wiley & Sons, New York, 1990.
- Ireland, P. T. and Jones, T. V. "The Measurement of Local Heat Transfer Coefficients in Blade Cooling Geometries." *AGARD Heat Transfer and Cooling in Gas Turbines*, 8p (See N86-29823 21-07), 1985.
- Ireland, P. T. and Jones, T. V. "The Response Time of a Surface Thermometer Employing Encapsulated Thermochromic Liquid Crystals." *J. Phys. E: Sci. Instrm.*, Vol. 20, 1987.
- Jones, T. V. and Hippenssteel, S. A. "High-Resolution Heat-Transfer-Coefficient Maps Applicable to Compound-Curve Surfaces Using Liquid Crystals in a Transient Wind Tunnel." NASA TM 89855, Aug. 1988.
- Joslin, R. D., Nicolaides, R. A., Erlebacher, G., Hussaini, M. Y., Gunzburger, M. D. "Active Control of Boundary-Layer Instabilities: Use of Sensors and Spectral Controller." *AIAA Journal*, Vol. 33, No. 8, 1995, pp. 1521-1522.

- Jørgensen, L., Swoboda, M., and Nitsche, W. "Application of Piezo-Foil Sensors as a Means of Sensing Wall Pressure Fluctuations in Wind Tunnel Tests." *Wind Tunnels and Wind Tunnel Test Techniques; Proceedings of the Conference*, Southampton, United Kingdom, Sept. 14-17, 1992.
- Katz, Y., Nishri, B., and Wygnanski, I. "The Delay of Turbulent Boundary Layer Separation by Oscillatory Active Control." AIAA Paper 89-0975, 1989.
- Kawai, H. "The Piezoelectricity of Polyvinylidene Fluoride." *Japan J. Applied Physics*, Vol. 8, 1968, pp. 975-976.
- Kim, J., Kline, S. J., and Johnston, J. P. "Investigation of a Reattaching Turbulent Shear Layer: Flow Over a Backward-Facing Step." *ASME J. Fluids Engineering*, Vol. 102, 1980, pp. 302-308.
- Kim, K. *A New Hue-Capturing Technique for the Quantitative Interpretation of Liquid Crystal Images Used in Convective Heat Transfer Studies*. Ph.D. Thesis, The Pennsylvania State University, Department of Aerospace Engineering, 1991.
- Klaase, P. Th. A. "Low-Frequency and Ultrasonic Applications of Piezoelectric PVDF-Films." *Ferroelectrics*, Vol. 60, 1984, pp. 215-225.
- Klein, E. J. "Liquid Crystals in Aerodynamic Testing." *Astronautics & Aeronautics*, Jul. 1968, pp. 70-73.
- Kline, S. J. and McClintock, F. A. "Describing Uncertainties in Single Sample Experiments." *ASME, Mechanical Engineering*, Vol. 75, 1953, pp. 3-8.
- Kobayakawa, M., Kondo, Y., and Suzuki, H. "Airfoil Flow Control at High Angle of Attack by Surface Oscillation." *IUTAM Symposium*, eds. R. Kawamura and Y. Aihara, Tokyo, Japan, 1992.
- Korkan, K. D., Griffiths, R. C. and Uellenberg, S. A. "Verification of the SM701 Airfoil Aerodynamic Characteristics Utilizing Theoretical Techniques." NAG1-1260-FDP, Presented at the XXII OSTIV Congress, Uvalde, TX, Jul. 1991.
- Latour, M. and Murphy, P. V. "Application of PVF₂ Transducers as Piezoelectric Vibrators for Marine Fouling Prevention." *Ferroelectrics*, Vol. 32, 1981, pp. 33-37.
- Liepmann, H. W., Brown, G. L., and Nosenchuck, D. M. "Control of Laminar-Instability Waves Using a New Technique." *J. Fluid Mechanics*, Vol. 118, 1982, pp. 187-200.
- Linville, J. G. "PVF₂ Models, Measurements and Devices." *Ferroelectrics*, Vol. 28, 1980, pp. 291-296.

- Lomas, C. G. *Fundamentals of Hot Wire Anemometry*. Cambridge University Press, New York, 1986.
- Malkiel, E. and Mayle, R. E. "Transition in a Separation Bubble." *J. Turbomachinery*, Vol. 118, Oct. 1996, pp. 752-759.
- Maltby, R. L. *Flow Visualization in Wind Tunnels Using Indicators*. AGARDograph 70, Apr. 1962.
- Martin, C. J. "The Non-Intrusive Measurement of Wall Shear Stress and Velocity Profiles in Vertical Annular Two Phase Flow." *AIChE Symposium Series Heat Transfer*, Niagara Falls, 1984.
- Mauldin, M. *Determination of the Thermophysical Triple Product of Heat Transfer Models Coated with Chiral Nematic Liquid Crystals*. Master's Thesis, The Pennsylvania State University, Department of Aerospace Engineering, 1996.
- McCroskey, W. J. and Durbin, E. J. "Flow Angle and Shear Stress Measurements Using Heated Films and Wires." *J. Basic Engineering*, Mar. 1972, pp. 46-52.
- Mee, D. J., Walton, T. W., Harrison, S. B., and Jones, T. V. "A Comparison of Liquid Crystal Techniques for Transition Detection." AIAA 91-0062, 29th Aerospace Sciences Meeting, Reno, NV, Jan. 7-10, 1991.
- MetraByte Corporation. *DASH-16 Manual*. Copyright 1984.
- Modest, Michael F. *Radiative Heat Transfer*. McGraw-Hill Series in Mechanical Engineering, New York, 1993, p. 773.
- Muirhead, V. U. and Saltzman, E. G. "Reduction of Aerodynamic Drag and Fuel Consumption for Tractor-Trailer Vehicles." *J. Energy* 3, 1979, pp. 279-284.
- Myer, Eric C. *An Investigation of the Sensitivity of a McCroskey Type Thin Film Shear Stress Gauge to Flow Direction*. Bachelor's Thesis, The Pennsylvania State University, Department of Aerospace Engineering, May 1988.
- Narayanan, M. A. Badri, Raghu, S., and Poddar, K. "Wall Shear Fluctuations in a Turbulent Boundary Layer." *AIAA Journal*, Vol. 22, No. 9, 1984, pp. 1336-1337.
- Neumann, R. D. and Hayes, J. R. "Introduction to Aerodynamic Heating Analysis of Supersonic Missiles." *AIAA Progress in Astronautics and Aeronautics, Tactical Missile Aerodynamics*, eds. M. J. Hemsch and J. N. Nielsen, Vol. 104, 1986.

- Nicks, O., Steen, G., Heffner, M. and Bauer, D. "Wind Tunnel Investigation and Analysis of the SM701 Airfoil." NAG1-1260-FDP, Presented at the XXII OSTIV Congress, Uvalde, TX, Jul. 1991.
- Nishioka, M., Asai, M., and Yoshida, S. "Control of Flow Separation by Acoustic Excitation." *AIAA Journal*, Vol. 28, No. 11, Nov. 1990, pp. 1909-1915.
- Nitsche, W., Mirow, P., Szodruch, J. "Piezo-electric Foils as a Means of Sensing Unsteady Surface Forces." *Experiments in Fluids*, Vol. 7, No. 2, 1989, pp. 111-118.
- den Ouden, C. and Hoogendoorn, C. J. "Local Convective-Heat-Transfer Coefficients for Jets Impinging on a Plate; Experiments Using a Liquid-Crystal Technique." *Proceedings of the Fifth International Heat Transfer Conference*, Vol. V., AIChE, New York, 1974, pp. 293-297.
- Parekh, D. E., Kibens, V., Glezer, A., Wiltse, J. M., and Smith, D. M. "Innovative Jet Flow Control: Mixing Enhancement Experiments." AIAA-96-0308, 34th Aerospace Sciences Meeting, Reno, NV, Jan. 15-18, 1996.
- Parsley, Dr. M. "The Use of Thermochromic Liquid Crystals in Research Applications, Thermal Mapping and Non-Destructive Testing." *Seventh IEEE SEMI-THERM Symposium*, 1991, pp. 53-58.
- Patankar, S. V. and Spalding, D. B. *Heat and Mass Transfer in Boundary Layers*. 1st ed., Morgan-Grampian, London, 1967.
- Pearman, G. T., Hokanson, J. L., and Meeker, T. R. "Design and Evaluation of a Contactless Piezoelectric Keyboard Using Polyvinylidene Fluoride as the Active Element." *Ferroelectrics*, Vol. 28, 1980, pp. 311-314.
- Poinsatte, P. E. and Van Fossen, G. J. "Convective Heat Transfer Measurements from a NACA 0012 Airfoil in Flight and in the NASA Lewis Icing Research Tunnel." AIAA-90-0199, 28th Aerospace Sciences Meeting, Reno, NV, Jan. 8-11, 1990.
- Press, W. H., Teukolsky, S. A., Vetterling, W. T., and Flannery, B. P. *Numerical Recipes in FORTRAN, The Art of Scientific Computing*. 2nd edition, Cambridge University Press, New York, 1992.
- Pucher, P. and Göhl, R. "Experimental Investigation of Boundary Layer Separation With Heated Thin-Film Sensors." *J. Turbomachinery*, Vol. 109, Apr. 1987, pp. 303-309.
- Rice, E. J. and Abbott, J. M. "Control of Flow Separation and Mixing by Aerodynamic Excitation." ICAS-90-5.3.3, *ICAS Proceedings*, 17th, Stockholm, Sweden, Sept. 9-14, 1990.

- Rice, E. J. and Zaman, K. B. M. Q. "Control of Shear Flows by Artificial Excitation." NASA TM-100201 and AIAA-87-2722, 11th Aeroacoustics Conference, Sunnyvale, CA, Oct. 19-21, 1987.
- Rivir, R. B., Johnston, J. P., and Eaton, J. K. "Heat Transfer on a Flat Surface Under a Region of Turbulent Separation." *J. Turbomachinery*, Vol. 116, Jan. 1994, pp. 57-62.
- Roshko, A. "On Drag and Shedding Frequency of Two-Dimensional Bluff Bodies." NACA-TN-3169, 1954.
- Schlichting, H. *Boundary-Layer Theory*. 6th edition, translated by J. Kestin, McGraw-Hill Book Company, New York, 1968.
- Simonich, J. C. and Moffat, R. J. "Liquid Crystal Visualization of Surface Heat Transfer on a Concavely Curved Turbulent Boundary Layer." *J. Engineering for Gas Turbines and Power*, Vol. 106, Jul. 1984, pp. 619-627.
- Somers, D. M., and Maughmer, M. D. "The SM701 Airfoil." Airfoils, Incorporated, State College, PA, Dec. 1990.
- Somers, Dan M., and Maughmer, Mark D. "The SM701 Airfoil: An Airfoil for World Class Sailplanes." *Technical Soaring*, Vol. XVI, No. 3, 1992, pp. 70-77.
- Toda, M. "Voltage-Induced Large Amplitude Bending Device - PVF₂ Bimorph - Its Properties and Applications." *Ferroelectrics*, Vol. 32, 1981, pp. 127-133.
- Uzol, Oğuz. Personal Communication. Sept. 1997.
- Vennemann, D. and Bütefisch, K. A. "The Application of Temperature-Sensitive Crystals to Aerodynamic Investigations." European Space Agency, ESRO-RR-77, translation of DLR-FB-73-121, 1973.
- Welty, J. R., Wicks, C. E., and Wilson, R. E. *Fundamentals of Momentum, Heat, and Mass Transfer*. Wiley & Sons, New York, 1984.
- White, F. M. *Fluid Mechanics*. 2nd edition, McGraw Hill, Inc., New York, 1986.
- White, F. M. *Viscous Fluid Flow*. 2nd edition, McGraw Hill, Inc., New York, 1991.
- Whitehead, L. A., Graham, D. J., Moore, F. A., Bolleman, B. J., Lake, R., and Dunwoody, A. B. "Investigation of Boundary Layer Flow Separation Control by Airfoil Surface Vibration." *Canadian Aeronautics and Space Journal*, Vol. 42, n. 4, Dec. 1996, pp. 213-219.

Wiedner, B. G. *Passage Flow Structure and Its Influence on Endwall Heat Transfer in a 90° Turning Duct.* Ph.D. Thesis, The Pennsylvania State University, Department of Aerospace Engineering, Aug. 1994.

Wiedner, B. G. and Camci, C. "A Technique for the Determination of Local Heat Flux on Steady State Heat Transfer Surfaces with Arbitrarily Specified Boundaries." *J. Heat Transfer*, Vol. 118, No. 4, Nov. 1996, pp. 1-8.

Wiedner, B. G. and Camci, C. "Passage Flow Structure and Its Influence on Endwall Heat Transfer in a 90° Turning Duct: Mean Flow and High Resolution Endwall Heat Transfer Experiments." *J. Turbomachinery*, Vol. 119, No. 1, Jan. 1997, pp. 39-50.

Winant, C. D. and Browand, F. K. "Vortex Pairing: The Mechanism of Turbulent Mixing-Layer Growth at Moderate Reynolds Number." *J. Fluid Mechanics*, Vol. 63, Part 2, 1974, pp. 237-255.

Yoo, J. Y. and Baik, S. J. "Redeveloping Turbulent Boundary Layer in the Backward-Facing Step Flow." *ASME J. Fluids Engineering*, Vol. 114, Dec. 1992, pp. 522-529.

Zaman, K. B. M. Q., Bar-Sever, A., and Mangalam, S. M. "Effect of Acoustic Excitation on the Flow over a Low-Re Airfoil." *J. Fluid Mechanics*, Vol. 182, Sept. 1987, pp. 127-148.

Zaman, K. B. M. Q. and McKinzie, D. J. "A Natural Low Frequency Oscillation in the Wake of an Airfoil Near Stalling Conditions." NASA TM-100213 and AIAA-88-0131, 26th Aerospace Sciences Meeting, Reno, NV, Jan. 11-14, 1988.

Zaman, K. B. M. Q. and McKinzie, D. J. "Control of Laminar Separation Over Airfoils by Acoustic Excitation." NASA TM-101379 and AIAA Paper 89-0565, 27th Aerospace Sciences Meeting, Reno, NV, Jan. 9-12, 1989.

Zhang, X., Stasiek, J., and Collins, M. W. "Novel Applications of Holographic Interferometry and Liquid Crystal Thermography in Low Speed Wind Tunnels." *Wind Tunnels and Wind Tunnel Test Techniques, Proceedings of the Conference*, Southampton, United Kingdom, Sept. 14-17, 1992.